UNIVERSITAT POLITÈCNICA DE VALÈNCIA

dma
Departament de Matemàtica Aplicada

Advances in Random Differential Equations: Computational Methods and Multidisciplinary Applications

PhD. Thesis

PhD Candidate
Vicente José Bevia Escrig

Supervisor
PhD Juan Carlos Cortés López

València, Autumn 2024

UNIVERSITAT
POLITÈCNICA
DE VALÈNCIA

Advances in Random Differential Equations: Computational Methods and Multidisciplinary Applications

Author: Vicente J. Bevia Escrig

Supervisor: PhD Juan Carlos Cortés López

The scientist does not study nature because it is useful to do so.
He studies it because he takes pleasure in it,
and he takes pleasure in it because it is beautiful.

Henri Poincaré

Al apoyo de todos mis buenos amigos y familia
a los largos cafés con David, Cristina, Nikita
a los partidos de básket con Elena, Clara y Marcos
a Carlos, su miel y sus ideas para arreglar el mundo
a las conversaciones acerca de la vida con Sorina por la tarde
a las gestiones y papeleos de Toni
a la inconmensurable ayuda y guía de Juan Carlos y Rafa
y, sobre todo, a la paciencia y apoyo de mi medio aguacate, Selene.

Declaration of Authorship

PhD Juan Carlos Cortés López, full professor at the Universitat Politècnica de València,

CERTIFIES that the present PhD thesis entitled: *Advances in Random Differential Equations: Computational Methods and Multidisciplinary Applications* has been performed under our supervision at the *Instituto Universitario de Matemática Multidisciplinar* in the Universitat Politècnica de València by Vicente J. Bevia Escrig. It constitutes his thesis dissertation to obtain the PhD degree in Mathematics.

In compliance with the current legislation, I authorize the presentation of this dissertation signing the present certificate.

Valencia - September 2024

JUAN CARLOS| CORTES| LOPEZ

Firmado digitalmente por JUAN CARLOS| CORTES|LOPEZ
Fecha: 2024.11.07 18:50:16 +01'00'

PhD Juan Carlos Cortés López

Resumen

La cuantificación de incertidumbre involucra diversos métodos y técnicas computacionales para abordar las brechas inherentes en la modelización matemática de fenómenos reales. Estos métodos son especialmente útiles para modelar procesos biológicos, físicos y sociales que contienen elementos que no pueden ser determinados con precisión. Por ejemplo, la tasa de transmisión de una enfermedad infecciosa o la tasa de crecimiento de un tumor están influidas por factores genéticos, ambientales o de comportamiento que no se comprenden completamente, introduciendo incertidumbres que afectan los resultados.

Esta tesis doctoral tiene como objetivo desarrollar y ampliar técnicas analíticas y computacionales para cuantificar la incertidumbre en sistemas de ecuaciones diferenciales aleatorias utilizando la función de densidad de probabilidad del sistema. Empleando el teorema de transformación de variables aleatorias y la ecuación de Liouville (continuidad), abordamos problemas de cuantificación de incertidumbre hacia adelante e inversos en sistemas aleatorios con datos reales. También diseñamos un método computacional para estimar eficientemente la densidad de probabilidad de un sistema resolviendo la ecuación de Liouville mediante aceleración de GPU. Finalmente, examinamos la evolución de la incertidumbre en una clase de sistemas forzados por impulsos, proporcio-

nando nuevos conocimientos sobre la dinámica de sus funciones de densidad de probabilidad.

Resum

La quantificació de la incertesa implica diversos mètodes i tècniques computacionals per a abordar les llacunes inherents en la modelització matemàtica de fenòmens del món real. Aquests mètodes són especialment valuosos per a modelar processos biològics, físics i socials que contenen elements que no poden ser determinats amb precisió. Per exemple, la taxa de transmissió d'una malaltia infecciosa o la taxa de creixement d'un tumor estan influïdes per factors genètics, ambientals o de comportament que no es comprenen completament, introduint incerteses que afecten els resultats.

Aquesta tesi doctoral té com a objectiu desenvolupar i ampliar tècniques analítiques i computacionals per a quantificar la incertesa en sistemes d'equacions diferencials aleatòries utilitzant la funció de densitat de probabilitat del sistema. Mitjançant el teorema de transformació de variables aleatòries i l'equació de Liouville (continuïtat), abordem problemes de quantificació de la incertesa cap avant i inversos en sistemes aleatoris amb dades reals. També dissenyem un mètode computacional per a estimar eficientment la densitat de probabilitat d'un sistema resolent l'equació de Liouville amb acceleració de GPU. Finalment, examinem l'evolució de la incertesa en una classe de sistemes forçats per impulsos, proporcionant noves perspectives sobre la dinàmica de les seues funcions de densitat de probabilitat.

Abstract

Uncertainty quantification involves various methods and computational techniques to address inherent gaps in the mathematical modeling of real-world phenomena. These methods are particularly valuable for modeling biological, physical, and social processes that contain elements that cannot be precisely determined. For example, the transmission rate of an infectious disease or the growth rate of a tumor is influenced by genetic, environmental, or behavioral factors that are not fully understood, introducing uncertainties that impact outcomes.

This PhD thesis aims to develop and extend analytical and computational techniques for quantifying uncertainty in random differential equation systems using a system's probability density function. By employing the random variable transformation theorem and the Liouville (continuity) equation, we tackle both forward and inverse uncertainty quantification problems in random systems with real-world data. We also design a computational method to efficiently estimate a system's probability density by solving the Liouville equation with GPU acceleration. Finally, we examine uncertainty evolution in a class of impulse-forced systems, providing new insights into the dynamics of their probability density functions.

Contents

Acronyms

AMR Adaptive Mesh Refinement. 71–73, 82, 86, 88, 91, 99

IVP Initial Value Problem. 59, 96, 126, 145–147, 149–151, 155, 157, 163, 182

ODE Ordinary Differential Equation. 18, 20, 69, 77–79, 81, 86, 91, 94, 156–158, 162

PDE Partial Differential Equation. 4, 7, 14–16, 18, 20, 27, 59–61, 70, 77–79, 81, 115, 117, 120, 129, 131, 133, 163, 178, 184

PDF Probability Density Function. xxiv, xxv, xxvii, xxix, 3, 5, 13–20, 22, 23, 26, 27, 29, 31–35, 37, 38, 41, 42, 45, 50, 51, 56, 57, 59–63, 70, 71, 79, 82–85, 87, 88, 90–93, 95–99, 103, 105, 106, 115, 117–119, 121–126, 129, 132–135, 138, 144, 151–155, 157–159, 162–165, 167, 171, 172, 177, 178, 180–182, 184, 186, 187

PME Principle of Maximum Entropy. 4, 22–24, 51, 57, 59, 124, 129, 131

RBF Radial Basis Function. 71, 73–77, 80–82, 88, 89, 91, 95, 96, 99, 105

RDE Random Differential Equation. 2, 3, 5, 11, 12, 14–16, 19, 20, 26, 69–71, 84, 93, 107, 144, 156, 165, 177, 178, 180, 181, 186, 189

RVT Random Variable Transformation. 4, 5, 14, 15, 17, 19, 27, 30, 31, 115, 117, 118, 121, 152, 154, 162, 177, 178, 180, 189, 191

SDE Stochastic Differential Equation. 2, 14

List of Figures

List of Tables

Chapter 1

Introduction

"The noblest pleasure is the joy of understanding". This celebrated quote is attributed to Leonardo da Vinci and is a shared experience among most scientists. Understanding the inner workings of the world around us is an everlasting source of intellectual pleasure, curiosity, and imagination. It is the fuel that has powered most scientific endeavors, resulting in discoveries and inventions that have greatly influenced our world.

Mathematical models have long been the main tool used to tackle the deep questions that arise in science and engineering. One of the most powerful tools developed in this regard is continuous-time dynamical systems, specifically differential equation systems. Complex phenomena such as cloud evolution in atmospheric physics, population growth in ecology, neuron activation in biology, or even engineering systems such as spring-damper systems in a vehicle, are non-stationary. Differential equation systems describe a system's rate of change, allowing us to understand and predict its evolution. Most phenomena can be mathematically described as a function evolving smoothly with respect to time, which solves the corresponding differential equation.

Our understanding of nature is also non-deterministic. Dynamical systems consist of an input, a set of parameters, and an output. When analyzing and predicting the behavior of a real-world system, one must obtain a set of measurements to calibrate the model parameters so that the dynamical system output closely resembles the measurement data. However, having a perfect fit between the model output and the measurements is impossible. The reason behind this impossibility can be classified into two categories [1, 2]:

- Mathematical models usually simplify real-world systems, leaving out some variables that, unawarely, may affect the system's evolution. This is usually termed as *epistemic, or structural uncertainty.*
- Measurement devices have error tolerances, implying that whatever measurement has been taken to obtain a given parameter or initial condition, one must consider a given amount of uncertainty. Also, some models include variables that cannot be directly measured or present high variability. These facts entail that the information given by the mathematical model must also account for uncertainty in model parameters (initial/boundary conditions, source term, and/or coefficients). This is usually termed *aleatoric uncertainty.*

Therefore, to have a truly accurate and realistic model of a real-world system, one has to quantify all the uncertainties appearing in the model. One mainly distinguishes two types of differential equations with uncertainty: Stochastic Differential Equations (SDEs) and Random Differential Equations (RDEs). The former term is reserved for differential equations driven by white noise (the formal derivative of the Wiener process) while the latter term refers to those differential equations driven by other types of random inputs, such as colored noise. The rigorous handling of SDEs requires special mathematical tools like Itô or Malliavin stochastic calculus [3–7]. Under this approach, noise is prefixed by specific patterns like Gaussian or Lévy stochastic processes. SDEs have been particularly useful when modeling phenomena whose dynamics are affected by irregular fluctuations, such as vibrations in Mechanics, or thermal noise in Thermodynamics [8, Ch. 5], but they have demonstrated to be particularly fruitful in Finance [9, 10].

The latter term, RDEs, allows for a more natural and flexible approach when modeling uncertainties since they permit assigning appropriate probability distributions to each model parameter (initial/boundary conditions, external source, and/or coefficients), reflecting the intrinsic random features of the models more accurately [2, 11–14]. In this setting, the deterministic input parameters of the equation (initial and/or boundary conditions, forcing term, and coefficients) are substituted by their respective random counterpart: random variables and stochastic processes. A main advantage of RDEs is that a wide range of probability distributions can be allocated for input parameters. This key fact has stimulated the extensive application of RDEs in dealing with real applications where uncertainties play a major role in properly describing the dynamics of the corresponding phenomenon under analysis using many techniques, including generalized polynomial chaos, collocation methods, random Fröbenius expansions, equivalent linearization, perturbation techniques, etc., [2, 11, 12, 14]. This thesis focuses on developing new techniques to study RDEs and their application to study some relevant mathematical models.

Aside from the rigorous calculation of the solution of the RDE, which is a stochastic process, many contributions also focus on the computation of its mean and variance functions because of the great statistical information they provide. However, a more significant goal than computing one-dimensional moments of the solution is the determination of the First Probability Density Function (1-PDF), or simply PDF, of the solution [12, Ch.3]. The PDF defines a distribution function for the stochastic process at a given instant, which defines much probabilistic information about the solution process. The 1-PDF permits computing any one-dimensional higher moment of the solution provided they exist as well as the probability that the solution varies within any specific interval of interest.

This thesis adds knowledge and practical computational tools for quantifying uncertainty in RDEs based on the corresponding 1-PDF. The tools built are then applied to multiple examples to show their versatility and potential. It also fills a knowledge gap in the case of delta-impulsive systems, both additive and multiplicative.

THESIS OUTLINE

This PhD thesis is structured in eight chapters. To follow the connecting thread in this dissertation, we write a motivation at the beginning of each chapter.

First, in Chapter 2 we introduce some notation and concepts that are repeatedly used in the thesis. This includes probabilistic concepts, the Random Variable Transformation (RVT) theorem and the Liouville Partial Differential Equation (PDE), or simply Liouville equation. Regarding the latter, we also include the main idea that will be used to compute its solution. Finally, we end with the definition of a prediction region and the Principle of Maximum Entropy (PME) that will be useful when fitting a probability density function to real data.

Then, in Chapter 3 we perform a comprehensive uncertainty quantification analysis of the randomized Gompertz model by deriving an explicit expression for the first probability density function of its solution's stochastic process. The analysis includes calculating key probabilistic characteristics, such as the time distribution until the solution reaches a specific value and the stationary distribution of the solution. The theoretical findings are then applied to two examples: one of a numerical nature and another involving real-world data to model the weight dynamics of a species.

In Chapter 4, we examine the random Baranyi–Roberts model, which characterizes the dynamics of two interacting cell populations. The initial conditions are treated as random variables, with their distributions determined using sample data and the PME. A finite volume scheme is employed to numerically approximate the probability density function of the solution through the Liouville equation. Using this framework, we develop an optimization procedure to identify the optimal parameter values for the Baranyi–Roberts model, ensuring that the system's expectation align with the sample data.

Then, Chapter 5, motivated by the insights from the attempt to devise an efficient Liouville solver described in the previous chapter, presents and analyzes a numerical approach to efficiently solve the Liouville equation in the context

of RDEs using GPU computing. This method combines wavelet compression-based adaptive mesh refinement, Lagrangian particle methods, and radial basis function interpolation to create a versatile algorithm applicable to multiple dimensions. We discuss the advantages and limitations of this algorithm. To demonstrate its effectiveness, we compute the PDF for some 2D and 3D random ODE systems with applications in physics and epidemiology.

In Chapter 6, we explore the random generalized logistic differential equation. We begin by constructing its solution rigorously using the sample-path approach and mean-square calculus. Next, we derive the PDF at each time instant by applying the RVT technique and solving the associated Liouville equation. We also demonstrate that, under specific conditions, the stochastic solution and its density function converge to the corresponding solution and density function of the logistic and Gompertz models, respectively. The chapter concludes with examples that combine the computational techniques from the previous chapter to construct reliable approximations of the PDF of the stochastic solution, including an application to a real-world problem.

Finally, in Chapter 7, we study a general class of random differential equations with Dirac-delta forcing at a finite number of time instants via its PDF. We consider the case of additive impulses and state-multiplicative impulses. We combine the Liouville equation and the random variable transformation method to conduct our study. Finally, all our theoretical findings are illustrated on two stochastic models, widely used in mathematical modeling, for which numerical simulations are carried out using the computational approach described in Chapter 5.

Finally, I would like to highlight that this thesis was developed as part of the objectives of the following Spanish competitive research project under the supervision of one of its two principal investigators: *Ecuaciones Diferenciales Aleatorias. Cuantificación de la Incertidumbre y Aplicaciones (Random Differential Equations. Uncertainty Quantification and Applications).* PID2020-115270GB-I00. IPs: Juan Carlos Cortés López and Rafael Villanueva Micó. Agencia Estatal de Investigación. I also highlight that I was awarded the

doctorate scholarship granted by Programa de Ayudas de Investigación y Desarrollo (PAID-21), Universitat Politècnica de València (UPV).

Chapter 2

Methodology

This chapter will give a brief theoretical overview of the main methods used in the thesis. The following chapters will give analytical and computational details about their implementation. We first remind some notation regarding measure theory, and probability theory specifically, that will be useful. We assume that the reader is familiarized with basic topics in Lebesgue integration theory and PDEs.

2.1 Probability concepts

We will begin by fixing some notation and concepts that will be needed to successfully follow the theoretical development of the current thesis. To do so, we follow Loève's introduction from [15, Ch. 3] and some key ideas from Soong's book [12]. Note that probability theory is a subset of measure theory, so most notation and ideas are shared with the well-known Lebesgue measure theory in $\mathbb{R}^d$, d positive integer.

Definition 2.1.1. *A **probability space** $(\Omega, \mathcal{F}, \mathbb{P})$ consists of a **sample space** or **sure event** Ω, a non-empty σ-algebra $\mathcal{F}$ of **events** and the **probability measure** $\mathbb{P} : \mathcal{F} \to [0, 1]$. Without any loss of generality, we assume that the space is complete; that is, every subset of a null event is also a null event. If not, we can complete the space by adding the required sets.*

Definition 2.1.2. *A **random variable** $X : \Omega \to \mathbb{R}$ is a function such that $X^{-1}(B) \in \mathcal{F}, \forall B \in \mathcal{B}$, where $\mathcal{B}$ is the Borel σ-algebra on $\mathbb{R}$ with its usual topology.*

Definition 2.1.3. *A **random vector** $\mathbf{X} = (X_1, \ldots, X_d) : \Omega \to \mathbb{R}^d$ is a function such that each of its components X_i, $i \in \{1, \ldots, d\}$ is a random variable.*

As in the case of the classical Lebesgue theory, we can define the integral operator for probability spaces.

Definition 2.1.4. *The **expectation** of a random variable X as the integral of X in the sure event Ω respect to the underlying probability measure $\mathbb{P}$. That is:*

$$\mathbb{E}[X] := \int_{\Omega} X(\omega) \mathrm{d}\mathbb{P}(\omega).$$

Since the expectation is defined as an integral respect to a measure, we can build norms in the probability space as follows:

Definition 2.1.5. *Given a random variable X, we define its **p-th moment** as the expectation of $|X|^p$. This naturally defines a norm and a normed space, respectively, as follows:*

$$\|X\|^p_{\mathrm{L}^p(\Omega,\mathbb{P})} := \mathbb{E}[|X|^p] = \int_\Omega |X(\omega)|^p \mathrm{d}\mathbb{P}(\omega).$$
$$\mathrm{L}^p(\Omega,\mathbb{P}) = \left\{X : \Omega \to \mathbb{R} \,|\, \|X\|_{\mathrm{L}^p(\Omega,\mathbb{P})} < \infty\right\}, \quad p \in [1,\infty).$$

For $X \in \mathrm{L}^p(\Omega,\mathbb{P})$, we say that X is a ***p-th order random variable****.*

In the case, $p = \infty$, we have the following space and norm, respectively:

$$\mathrm{L}^\infty(\Omega,\mathbb{P}) = \{X : \Omega \to \mathbb{R} \,|\, \exists M > 0, \mathbb{P}[|X| < M] = 1\},$$
$$\|X\|_{\mathrm{L}^\infty(\Omega,\mathbb{P})} = \inf\{M > 0 \,|\, \mathbb{P}[|X| < M] = 1\}.$$

For $X \in \mathrm{L}^\infty(\Omega,\mathbb{P})$, we say that X is an ***essentially bounded random variable****.*

In the case of random vectors, we define their respective norms as $\|\mathbf{X}\|_{\mathrm{L}^p_d(\Omega,\mathbb{P})} = \max\{\|X_i\|_{\mathrm{L}^p(\Omega,\mathbb{P})} : 1 \le i \le d\}$.

Note that, since $(\Omega,\mathcal{F},\mathbb{P})$ is a finite measure space, we have $\mathrm{L}^p \subseteq \mathrm{L}^q$, when $p \ge q$. For example, if we consider a random variable such that $\mathbb{E}[|X|^2] < +\infty$, that means $\mathbb{E}[|X|] < +\infty$ and thus this random variable has finite mean and variance since $\mathbb{V}[X] = \mathbb{E}[X^2] - \mathbb{E}^2[X]$. Throughout the thesis, we will assume (unless specified otherwise) that random variables live in $\mathrm{L}^2(\Omega,\mathbb{P})$ (therefore, d-dimensional random vectors will live in $\mathrm{L}^2_d(\Omega,\mathbb{P})$).

With this information we can now write the definitions of limits of random variables in their probability space.

Definition 2.1.6. *Consider a sequence of random variables $\{X_k\}_{k\in\mathbb{N}}$ defined in the same probability space $(\Omega,\mathcal{F},\mathbb{P})$. We have the following convergence types:*

- *The sequence* ***converges in probability*** *to a random variable X if, for any $\varepsilon > 0$,*

$$\mathbb{P}[|X_n - X| \ge \varepsilon] \xrightarrow[n\to+\infty]{} 0. \tag{2.1.1}$$

- *The sequence* ***converges almost surely (a.s)*** *to a random variable X if for every $\varepsilon > 0$,*

$$\mathbb{P}\left[\bigcup_{k\geq n}\{|X_k - X| \geq \varepsilon\}\right] \xrightarrow[n\to+\infty]{} 0. \tag{2.1.2}$$

  Equivalently, we can rewrite this as follows:

$$\mathbb{P}\left[\left\{\omega \in \Omega : \lim_{n\to+\infty} X_n(\omega) = X(\omega)\right\}\right] = 1. \tag{2.1.3}$$

- *The sequence* ***converges in the p-th moment****, for $p \in [1, \infty)$ moment if*

$$\lim_{n\to+\infty} \|X_n - X\|_{\mathrm{L}^p(\Omega,\mathbb{P})} = \lim_{n\to+\infty} \mathbb{E}[|X_n - X|^p] = 0. \tag{2.1.4}$$

  A special case we will consider is $p = 2$, called ***mean-square convergence****.*

Almost sure and mean-square convergence implies convergence in probability, but mean-square and almost sure convergence do not imply each other in general [12, Fig. 4.1].

Definition 2.1.7. *Given $\mathcal{T} \subset \mathbb{R}$, a* ***real-valued stochastic process*** *is a non-countable family of real-valued random vectors indexed by elements of $\mathcal{T}$; that is,*

$$\{\mathbf{X} : \mathcal{T} \times \Omega \to \mathbb{R}^n : t \in \mathcal{T}, \omega \in \Omega\}, \quad \mathbf{X}(t, \cdot) \text{ is a random vector } \forall t \in \mathcal{T}.$$

In practice, $\mathcal{T} = [t_1, t_2]$, $0 \leq t_1 < t_2 \leq \infty$ (for convenience, we interpret the parameter t as time, so we assume it is nonnegative). Furthermore, if $\mathbf{X}(t, \cdot) \in \mathrm{L}^2_d(\Omega, \mathbb{P})\, \forall t \in \mathcal{T}$, we say that it is **a second order stochastic process**. Given this kind of stochastic process, we can talk about the *continuity* and *differentiability* of stochastic processes.

Definition 2.1.8. *A stochastic process $\mathbf{X}(t, \omega)$ is* ***sample continuous****, or* ***pathwise continuous*** *if its sections, $X_{\tilde{\omega}}(t) := X(t, \tilde{\omega}) : \mathcal{T} \to \mathbb{R}^d$ are continuous (in the classical, deterministic sense) for $\mathbb{P}$-almost every fixed $\tilde{\omega} \in \Omega$.*

Likewise, it will be ***sample differentiable****, or* ***pathwise differentiable*** *if its sections are differentiable for $\mathbb{P}$-almost every sample.*

See [12, App. A.1, A.2] for a deeper consideration of sample calculus. However, the idea is simple: a stochastic process is pathwise continuous, or pathwiseC^1, or verifies any other property in the pathwise sense, if the corresponding deterministic property is verified for almost every sample.

Another important definition is continuity and differentiability in the $\mathrm{L}^p_d(\Omega, \mathbb{P})$ spaces, which we now define.

Definition 2.1.9. *A stochastic process $\mathbf{X}(t, \cdot) \in \mathrm{L}^p_d(\Omega, \mathbb{P})$, $t \in \mathcal{T}$, is* ***continuous in the*** L^p ***sense*** *if*

$$\lim_{h \to 0} \|\mathbf{X}(t+h) - \mathbf{X}(t)\|_{\mathrm{L}^p_d(\Omega,\mathbb{P})} = 0. \tag{2.1.5}$$

Likewise, we say that it is ***differentiable in the*** L^p ***sense*** *if there exists a stochastic process, which we denote by $\frac{\mathrm{d}\mathbf{X}}{\mathrm{d}t}(t, \cdot) \in \mathrm{L}^p_d(\Omega, \mathbb{P})$, such that*

$$\lim_{h \to 0} \left\| \frac{\mathbf{X}(t+h) - \mathbf{X}(t)}{h} - \frac{\mathrm{d}\mathbf{X}}{\mathrm{d}t}(t) \right\|_{\mathrm{L}^p_d(\Omega,\mathbb{P})} = 0. \tag{2.1.6}$$

In the specific case of $p = 2$, we say that a process is **mean square continuous** and **mean square differentiable**, respectively.

2.1.1 Random differential equations

With all the previous information, we can now formulate an RDE *model*. If not stated otherwise, when speaking of a generic RDE, we will consider an RDE system such that

- The vector-valued function $\mathbf{v}(\cdot, t) : \mathbb{R}^d \longrightarrow \mathbb{R}^d$, which we call the ***(vector) field of the RDE***, is assumed to be a Lipschitz-continuous function, uniformly in $t \in [t_0, \infty)$, and continuous and bounded in t. This way, we can assume certain existence and uniqueness properties (see [16–18]).

- $\mathbf{X}(t) = \mathbf{X}(t, \omega)$, $t \geq t_0$, $\omega \in \Omega$ is a stochastic process verifying:

$$\begin{cases} \dfrac{\mathrm{d}\mathbf{X}}{\mathrm{d}t}(t) &= \mathbf{v}(\mathbf{X}(t), t), \quad t > t_0, \\ \\ \mathbf{X}(t_0) &= \mathbf{X}_0 \in \mathrm{L}^2_d(\Omega, \mathbb{R}^d). \end{cases} \tag{2.1.7}$$

  The sense in which the stochastic process verifies the RDE system will be detailed in each specific problem. The pathwise notion is the strongest and the usual one in a computational setting [8, 12, 19–21]. Unless specified otherwise, we will work with this definition, although the mean square notion is also of great theoretical value.

One may also consider a generic RDE with a finite number of random parameters in its formulation. In this case, we consider the generic RDE to verify:

- The vector-valued function $\mathbf{v}(\cdot, t, \mathbf{A}) : \mathbb{R}^d \longrightarrow \mathbb{R}^d$ now depends on the samples, or realizations, of the parameter random vector. We will assume that the event $E = E_1 \cap E_2$, where

  $$E_1 = \{\omega \in \Omega : \mathbf{v}(\cdot, t, \mathbf{A}(\omega)) \text{ is Lipschitz in } \mathbb{R} \text{ uniformly in } t\},$$
  $$E_2 = \{\omega \in \Omega : \mathbf{v}(x, \cdot, \mathbf{A}(\omega)) \text{ is continuous in } [t_0, \infty) \text{ for all } x \in \mathbb{R}\},$$

  has probability 1, i.e., $\mathbb{P}[E] = 1$.
- $\mathbf{X}(t) = \mathbf{X}(t, \omega)$, $t \geq t_0$, $\omega \in \Omega$ is a stochastic process verifying:

$$\begin{cases} \dfrac{\mathrm{d}\mathbf{X}}{\mathrm{d}t}(t) &= \mathbf{v}(\mathbf{X}(t), t, \mathbf{A}), \quad t > t_0, \\ \\ \mathbf{X}(t_0) &= \mathbf{X}_0 \in \mathrm{L}^2_d(\Omega, \mathbb{R}^d), \end{cases} \tag{2.1.8}$$

  where $\mathbf{A} \in \mathrm{L}^2_m(\Omega, \mathbb{P})$ is a real-valued random vector. The same comment about the pathwise notion applies to this case.

2.2 Probability distribution

Let us first consider the definition of the PDF of a random variable or vector. Recall from Theorem 2.1.2 that, given a probability space $(\Omega, \mathcal{F}, \mathbb{P})$, a random variable X defined in that space must verify $X^{-1}(B) \in \mathcal{F}$ for any Borel-measurable set B. This means that $\mathbb{P}(X^{-1}(B)) \in [0,1]$. This motivates the following definitions.

Definition 2.2.1. *Given a random vector* $\mathbf{X}$ *in the complete probability space* $(\Omega, \mathcal{F}, \mathbb{P})$*, we define the* ***law, or distribution, of*** $\mathbf{X}$*, denoted by* $\mu_{\mathbf{X}} : \mathcal{B}_d \to [0,1]$*, as the push-forward of* $\mathbb{P}$ *by* $\mathbf{X}$*; that is*

$$\mu_{\mathbf{X}}(B) := \mathbf{X}_{\#}\mathbb{P}(B) := \mathbb{P}[\mathbf{X}^{-1}(B)], \quad B \in \mathcal{B}_d.$$

If $\mu_{\mathbf{X}}$ *happens to be absolutely continuous with respect to some measure* $\boldsymbol{m}$ *in* $\mathbb{R}^d$*, the Radon-Nykodym theorem [15, Ch. 2, Secs. 8B, 8C] then guarantees that we can find an* $\boldsymbol{m}$*-integrable function* $f_{\mathbf{X}}$ *such that*

$$\mu_{\mathbf{X}}(B) = \int_B f_{\mathbf{X}}(\mathbf{x}) \mathrm{d}\boldsymbol{m}(\mathbf{x}).$$

Now we have the following two common situations:

- *If* $\boldsymbol{m} = \mathcal{L}_d$*, which is the classical Lebesgue measure in* $\mathbb{R}^d$*, then we say that* $\mathbf{X}$ *is an* ***absolutely continuous random vector****, and* f *is called the* ***probability density function (PDF) of*** $\mathbf{X}$*.*
- *If* $\boldsymbol{m}$ *is the counting measure, then* $\mathbf{X}$ *is an* ***discrete random vector****, and* f *is called the* ***probability mass function (PMF) of*** $\mathbf{X}$*.*

In the case of random variables, since the usual topology for $\mathbb{R}$ *is defined by open intervals, we can also define the* ***cumulative density function (CDF)*** *by*

$$F_X(x) := \mu_X((-\infty, x]) = \mathbb{P}[X^{-1}(-\infty, x]].$$

2.2.1 Probability density function evolution

Obtaining the PDF of a stochastic process has been classically done via Monte Carlo sampling. The calculation of the 1-PDF at a certain time instant via Monte-Carlo sampling consists of numerically obtaining samples of the random variables appearing in the RDE and then simulating their evolution up to the corresponding time to build the histogram that represents the 1-PDF at the desired time [22]. This method is widely used in RDEs, SDEs, random PDEs, and stochastic PDEs, among others, because it is fairly simple to implement in its naive version. However, it is also true that many samples must be used to obtain an accurate, smooth representation of the PDF [23, 24]. Nevertheless, improved Monte-Carlo techniques, such as variance-reduction, multi-level, etc., have been successfully designed to speed up the raw Monte-Carlo method [25].

Random Variable Transformation theorem

Another well-known method, the RVT theorem, is an analytical method that works directly over the densities of the random variables involved in the RDE. In fact, the RVT theorem gives a closed formula of the 1-PDF at any time instant. The theorem can be stated as follows:

Theorem 2.2.2. *[12, 26] (**RVT theorem**) Let* $\mathbf{X}, \mathbf{Y} : \Omega \longrightarrow \mathbb{R}^m$ *be two random vectors with PDFs* $f_{\mathbf{X}}$ *and* $f_{\mathbf{Y}}$*, respectively. Assume that there is a one-to-one* C^1 *mapping* $\mathbf{h} : \mathbb{R}^m \longrightarrow \mathbb{R}^m$*, such that* $\mathbf{X} = \mathbf{h}(\mathbf{Y})$ *with* $\left|\frac{\partial h}{\partial \mathbf{Y}}(\mathbf{y})\right| \neq 0$ *for all* $\mathbf{y}$*. Then, denoting* $\mathbf{h}^{-1}$ *as the inverse mapping of* $\mathbf{h}$*,*

$$f_{\mathbf{X}}(\mathbf{x}) = f_{\mathbf{Y}}(\mathbf{h}^{-1}(\mathbf{x})) \left| \frac{\partial \mathbf{h}^{-1}}{\partial \mathbf{x}}(\mathbf{x}) \right|, \tag{2.2.1}$$

where $\left|\frac{\partial \mathbf{h}^{-1}}{\partial \mathbf{x}}(\mathbf{x})\right|$ *denotes the absolute value of the determinant of the Jacobian matrix.*

Note that, in essence, (2.2.1) is a change of measure formula. In the specific application to RDEs, the mapping h is, in fact, the time-wise and pathwise flow of the differential equation; that is, a function $\Phi(\cdot\,; t_0, \mathbf{X}_0(\omega)) : [t_0, +\infty) \to \mathbb{R}^d$

that verifies (2.1.7) for $\mathbb{P}$-almost every $\omega \in \Omega$. Particularly, for every $t \geq t_0$ we have $\mathbf{X}(t,\omega) = h(\mathbf{X}_0(\omega)) = \Phi(t; t_0, \mathbf{X}_0(\omega))$. Therefore, (2.2.1) says that the density of $\mathbf{X}(t,\cdot)$ can be obtained as the Radon-Nykodym derivative (respect to the Lebesgue measure) of the *push-forward* measure obtained via the flow function $\mathbf{v}(\cdot\,,t)$, of the measure associated with the density of $\mathbf{X}_0(\cdot)$ (see Figure 2.1, [27, Ch. 3]).

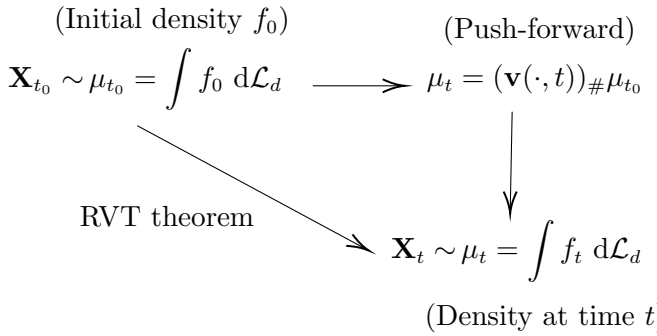

Figure 2.1: Schematic representation of the RVT theorem application in RDEs. $\mathcal{L}_d$ denotes the Lebesgue measure in the appropriate $\mathbb{R}^d$ space.

This analytical approach provides great insight into the random dynamics of the problem's solution. This method has been successfully applied to determine the 1-PDF of many RDEs ([28–34], random difference equations [33, 35], and random PDEs [36]). The RVT method has been demonstrated to be very useful to compute approximations of the 1-PDF of the aforementioned type of random equations in combination with other techniques such as Karhunen-Loève expansions [37, 38], Fröbenius expansions [39], differential transform method [40], the homotopy method [41], numerical schemes [42, 43], etc. However, it relies on the knowledge of a closed-form or *friendly* analytical solution of the corresponding RDE [44, 45] solution and its inverse respect to the initial condition term, which is often impossible to obtain analytically.

The Liouville equation

Another approach, which is the main tool used in this thesis, is based on the Liouville, or Continuity, Equation [12, 46–50]. The Liouville equation is a fundamental PDE in classical mechanics and statistical physics and plays a crucial role in applied mathematics due to its significance in understanding dynamic systems where certain quantities are conserved through the evolution of the system [51–55]. This equation describes the time evolution of a density function in the phase space of a dynamical system, which characterizes the probabilistic behavior of a collection of particles or a continuous medium. The Liouville equation appears in various disciplines in different forms; for example, in fluid dynamics, it describes the conservation of mass and momentum of a certain fluid for compressible flows; in plasma physics, it is instrumental in understanding the behavior of ionized gases and the dynamics of charged particles. Since the PDF of an RDE satisfies the Liouville equation, an alternative to calculate the PDF consists in solving this equation analytically or numerically (see [12, Th. 6.2.2], [46, Th. 4.4]).

The main result upon which we set our work is the following:

Theorem 2.2.3. *[12, 46, 56] Consider the RDE* (2.1.7) *with the assumed conditions on the vector field* $\mathbf{v}(\cdot, t)$*. Let* $\mathcal{D} \subseteq \mathbb{R}^d$ *be a positively invariant set for the RDE; i.e.* $\{\mathbf{X}([t_0, \infty), \omega)\}_{\omega \in \Omega} \subset \overline{\mathcal{D}}$*,* $\mathbb{P}$*-almost surely. Then, the 1-PDF of the stochastic process* $\mathbf{X}(t)$*, denoted by* $f = f_{\mathbf{X}(t)}$*, verifies the Liouville PDE:*

$$\begin{cases} \partial_t f(\mathbf{x}, t) + \nabla_{\mathbf{x}} \cdot [\mathbf{v}\, f](\mathbf{x}, t) = 0, \quad \mathbf{x} \in \mathcal{D}, \quad t > t_0, \\ f(\mathbf{x}, t_0) = f_0(\mathbf{x}), \quad x \in \overline{\mathcal{D}}, \\ f(\mathbf{x}, t)\mathbf{v}(\mathbf{x}, t) \cdot \mathbf{n}(\mathbf{x}) = 0, \quad x \in \partial\mathcal{D}, \quad t \geq t_0, \end{cases} \tag{2.2.2}$$

where f_0 *is the PDF of* $\mathbf{X}_0$*,* $\mathbf{n}$ *is the normal vector of the boundary and* $\nabla_{\mathbf{x}}$ *and* $\nabla_{\mathbf{x}} \cdot$ *denote the gradient and divergence operators, respectively. Also,* $\overline{\mathcal{D}} = \mathcal{D} \cup \partial\mathcal{D}$*.*

Note that the last condition (homogeneous Neumann conditions at the boundary) is only considered wherever $\partial\mathcal{D}$ is bounded. Unless specified, we will assume that $\partial\mathcal{D}$ is, at least, piece-wise C^1, and that f_0 is integrable and C^1 inside its support.

Theorem 2.2.3 and the RVT theorem are very closely related: Every solution of the Liouville equation is of the form described by the RVT theorem (the push-forward of a measure), and functions of the form described by the RVT theorem verify the Liouville equation. For some of the different proofs of Theorem 2.2.3 and the relationship with the RVT Theorem 2.2.2, see Appendices A and B. Despite the connection between the two, the Liouville equation allows for a broad application in practice due to a fundamental property discussed in the following section. Under the conditions of the theorem, the Liouville equation can be verified in the weak or strong sense depending on the regularity of the initial density f_0. However, in this thesis we only deal with the strong solution of the Liouville equation.

Solving the Liouville equation

Solving the Liouville equation analytically to obtain a PDF requires a similar effort to using the RVT theorem. Furthermore, using a numerical method for the Liouville equation avoids the limitation of the RVT theorem: Needing some sort of closed-form expression or approximation of the solution stochastic process. However, finding a general method for solving this equation is not straightforward by any means.

For the time being, we will make a slight notation abuse in this section: I will write $\Phi(t;\cdot,\mathbf{a}) = \Phi(t;t_0,\cdot)$, and $\Phi(t) = \Phi(t;\cdot,\mathbf{a})$ as well. This notation usage will be brief, and I believe it does not lead to confusion.

Let us first give some insight into the special form of the Liouville equation. Consider (2.2.2), and let us consider the random parameter case of the Liouville equation from Equation (2.1.8). If

$$\mathbb{P}[\{\omega \in \Omega : \mathbf{v}(\cdot,t,\mathbf{A}(\omega)) \in C^1(\mathcal{D}),\, \forall t \geq t_0\}] = 1,$$

then, for almost any realization $\mathbf{a}$ of $\mathbf{A}$, Equation (2.2.2) can be written as

$$\partial_t f(\mathbf{x}, t \,|\, \mathbf{a}) + \mathbf{v}(\mathbf{x}, t, \mathbf{a}) \cdot \nabla_{\mathbf{x}} f(\mathbf{x}, t \,|\, \mathbf{a}) = -f(\mathbf{x}, t \,|\, \mathbf{a}) \nabla_{\mathbf{x}} \cdot \mathbf{v}(\mathbf{x}, t, \mathbf{a}), \tag{2.2.3}$$

for $\mathbf{x} \in \mathcal{D}$, $t > t_0$, and its solution can be analyzed through its characteristic equations [47, 56, 57]. These curves describe the time evolution of a particle, whose trajectory is $\Phi(t) = (\phi_1, \ldots, \phi_d) \in \mathbb{R}^d$, in phase space and the value of the desired PDE solution at that particle's position. These equations form a system of Ordinary Differential Equations (ODEs), which are given by

$$\begin{aligned} \frac{\mathrm{d}}{\mathrm{d}t}\Phi(t) &= \mathbf{v}(\Phi(t), t, \mathbf{a}), & \Phi(0) &= \mathbf{x}_0, \\ \frac{\mathrm{d}}{\mathrm{d}t} f(\Phi(t), t \,|\, \mathbf{a}) &= -f(\Phi(t), t \,|\, \mathbf{a}) \nabla_{\mathbf{x}} \cdot \mathbf{v}(\Phi(t), t, \mathbf{a}), & f(\Phi(0), 0 \,|\, \mathbf{a}) &= f_0(\mathbf{x}_0), \end{aligned} \tag{2.2.4}$$

where $\mathbf{x}_0$ is a generic point in $\mathcal{D}$, which represents the initial position of the particle to be simulated. The first equation defines the time evolution of the particle's position, whereas the last equation in (2.2.4) defines the evolution of the PDF value in the considered particle. Now, the characteristic curves, which form the solution of the characteristic equations (2.2.4), are defined by

$$\Phi(t;\, \mathbf{x}_0, \mathbf{a}) = \mathbf{x}_0 + \int_{t_0}^{t} \mathbf{v}(\Phi(s;\, \mathbf{x}_0, \mathbf{a}), s, \mathbf{a}) \mathrm{d}s, \quad t \geq t_0, \tag{2.2.5}$$

$$f(\Phi(t;\, \mathbf{x}_0, \mathbf{a}), t \,|\, \mathbf{a}) = f_0(\mathbf{x}_0) \exp\left(- \int_{t_0}^{t} \nabla_{\mathbf{x}} \cdot \mathbf{v}(\Phi(s;\, \mathbf{x}_0, \mathbf{a}), s, \mathbf{a}) \mathrm{d}s \right), \quad t \geq t_0, \tag{2.2.6}$$

where $\Phi(t;\, \mathbf{x}_0, \mathbf{a})$ denotes the characteristic curve at time t, starting at $\mathbf{x}_0$, with parameter values $\mathbf{a}$.

It is well known that the flow function of an ODE with a "sufficiently regular" vector field (for example, Lipschitz in space, continuous in time) is differentiable. As a simple consequence of the inverse function theorem, wherever the vector field is non-zero, and the flow function has continuous derivatives, one can define its inverse function, which will be differentiable (see [58, Th. 1.1.7] for more details). Mathematically, it is a differentiable function $\Psi(t; \mathbf{x}, \mathbf{a})$ such

that $\Phi(t; \Psi(t; \mathbf{x}, \mathbf{a}), \mathbf{a}) = \mathbf{x}$. This function is called the *inverse flow* function. See Figure 2.2 for a graphical representation of both functions.

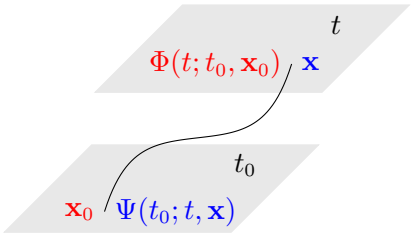

Figure 2.2: The flow function (red) gives the position $\mathbf{x}$ at time t of the characteristic curve starting at $\mathbf{x}_0$. The inverse flow function (blue) gives the point where the curve must start, $\mathbf{x}_0$, so that it is located at $\mathbf{x}$ at time t.

With the notion of the inverse flow in mind, we can now write (2.2.6) as

$$f(\mathbf{x}, t \,|\, \mathbf{a}) = f_0(\Psi(t; \mathbf{x}, \mathbf{a})) \exp\left(- \int_{t_0}^{t} \nabla_{\mathbf{x}} \cdot \mathbf{v}(\Phi(s; \Psi(t; \mathbf{x}, \mathbf{a}), \mathbf{a}), s, \mathbf{a}) \mathrm{d}s \right). \tag{2.2.7}$$

Note that Equation (2.2.7) actually defines a change of variables and, together with Equation (2.2.6) and the relation we have with the RVT theorem, we have

$$\int_{\mathbb{R}^n} f(\mathbf{x}, t \,|\, \mathbf{a}) \mathrm{d}\mathbf{x} = \int_{\mathbb{R}^n} f_0(\mathbf{x}) \mathrm{d}\mathbf{x} = 1, \tag{2.2.8}$$

for all $t \geq 0$ and $\mathbf{a}$. Finally, the PDF of the RDE solution (independent of parameter realizations) is finally obtained by marginalizing the joint PDF of both the solution and the random parameter vector $\mathbf{A}$, which, using the definition for the conditional PDF, can be written as

$$f(\mathbf{x}, t) = \int_{\mathbb{R}^m} f(\mathbf{x}, t \,|\, \mathbf{a}) f_{\mathbf{A}}(\mathbf{a}) \mathrm{d}\mathbf{a} = \mathbb{E}_{\mathbf{A}}[f(\mathbf{x}, t \,|\, \mathbf{A})], \tag{2.2.9}$$

where $f_{\mathbf{A}}$ is the joint PDF of the random vector parameters $\mathbf{A}$ and $\mathbb{E}_{\mathbf{A}}$ denotes the expectation operator with respect to $\mathbf{A}$. This shows that the PDF can be obtained by calculating (2.2.7) for all realizations $\mathbf{a}$ of $\mathbf{A}$ and then averaging. Furthermore, when computational techniques are required for this task,

expression (2.2.9) allows the use of either quadrature formulas [59] or Monte Carlo integration strategies [22–24, 60].

The characteristic equations give a particle's point of view about the evolution of the system. However, although the PDE is transformed into a family of ODEs, the task at hand for obtaining the solution is still complicated. There are several methods to obtain a numerical approach for deterministic PDEs, e.g., finite difference methods (FDM), finite volume methods (FVM), and finite element methods (FEM). However, these methods suffer when simulating convection/transport-dominated problems because of the incorrect introduction of numerical dissipation. Furthermore, the computational complexity of grid-based methods grows exponentially with the problem dimensionality. Designing the numerical approach is one of the main topics of the thesis and will be fully detailed in Chapter 5.

2.3 Prediction region

Finding an appropriate definition for a prediction region has been a long-standing question that still remains open. Classically, in 1D RDEs, a prediction region is built by simulating the evolution of several samples from the initial condition and then building the sample quantiles (usually an interval centered at the mean and whose width is given by a multiple of the standard deviation of the samples). However, there is no natural way to generalize this concept in higher dimensions; building a *natural* confidence region is not trivial or straightforward.

Since we are interested in obtaining the PDF of the solution stochastic process, we will consider a special kind of prediction region, one that is greatly defined by the structure of the PDF. But first, let us consider the following lemma with its short proof:

Lemma 2.3.1. *Let* $\alpha \in [0,1]$ *and consider a PDF* $f \in \mathrm{L}_1 \cap \mathrm{C}_0$*, such that* $\{\mathbf{x} : f(\mathbf{x}) = \lambda\}$ *is a Lebesgue-null set for all* $\lambda \in (0, \|f\|_\infty]$*. Consider* J :

$[0, \|f(\cdot,t)\|_\infty] \to [0,1]$ *defined as*

$$J(\lambda) = \int_{\{f \geq \lambda\}} f(\mathbf{x})\mathrm{d}\mathbf{x} = \mu_f(\{f \geq \lambda\}), \tag{2.3.1}$$

where $\{f \geq \lambda\} := \{\mathbf{x} : f(\mathbf{x}) \geq \lambda\}$. *Then, there exists a* λ^* *such that* $J(\lambda^*) = 1 - \alpha$.

Proof. We are going to prove that function J is continuous and monotone. The result will then follow trivially.

Let $0 \leq \lambda_1 < \lambda_2 = \lambda_1 + h \leq \|f\|_\infty$. Firstly, it is clear that J is monotonically decreasing. Indeed, since $f \geq 0$, μ_f is a non-negative measure. Therefore,

$$\{f \geq \lambda_2\} \subset \{f \geq \lambda_1\} \Rightarrow \mu_f(\{f \geq \lambda_2\}) \leq \mu_f(\{f \geq \lambda_1\}),$$

and thus, $J(\lambda_1) > J(\lambda_2)$.

Now, regarding continuity, let us consider $\lambda_1 > 0$. We have

$$|J(\lambda_1) - J(\lambda_2)| = \left| \int_{\{\lambda_1 \leq f \leq \lambda_1 + h\}} f(\mathbf{x})\mathrm{d}\mathbf{x} \right| \tag{2.3.2}$$

$$= \int_{\mathbb{R}} f(\mathbf{x})\, \mathbf{1}_{\{\lambda_1 \leq f \leq \lambda_1 + h\}}(\mathbf{x})\mathrm{d}\mathbf{x} \tag{2.3.3}$$

$$= \mu_f(\{\lambda_1 \leq f \leq \lambda_1 + h\}). \tag{2.3.4}$$

Since $f \in \mathrm{L}^1$, the dominated convergence theorem applies and we can take limits inside the integral at (2.3.3), giving:

$$\lim_{h \to 0} |J(\lambda_1) - J(\lambda_1 + h)| = \mu_f(\{f = \lambda_1\}) = 0 \tag{2.3.5}$$

because $\mu_f << \mathcal{L}_d$; that is, the measure generated by f is absolutely continuous respect to the Lebesgue measure (by construction), and we considered f such that $\{f = \lambda_1\}$ had zero Lebesgue measure. Therefore, J is continuous in $(0, \|f\|_\infty]$.

In the $\lambda = 0$ case, note that J is monotonically decreasing and upper bounded by $J(0) = 1$. Thus, it is convergent by the monotone convergence theorem. As a result, J is continuous in $[0, \|f\|_\infty]$.

Finally, by Weierstrass' extreme value theorem a continuous function in a compact interval achieves any value between its minimum and maximum (both included). In particular, it reaches $1 - \alpha$ at some λ^*. □

Now we may consider the following prediction region definition:

Definition 2.3.2. *We define the PDF-induced α-level prediction region as*

$$\mathcal{P}^\alpha := \{\mathbf{x} \in \mathcal{D} \,:\, f(\mathbf{x}) \geq \lambda^*\}, \tag{2.3.6}$$

where λ^* is obtained by the previous lemma (2.3.1)*.*

Note that, since the function J as defined in Lemma 2.3.1 is continuous and monotone, we may apply the bisection method to numerically compute the λ^* value that defines $\mathcal{P}^\alpha$. This method will be used extensively in Chapters 5 to 7 to compute the prediction regions in the different models.

2.4 Principle of maximum entropy

The PME allows us to assign statistical distributions to some variables. It is based on maximizing the mathematical concept of *differential entropy*, which is a measure defining the lack of knowledge of a random variable. It will be a key part of Chapters 4 and 6.

Given a random variable Y, with its associated PDF f_Y, the *differential entropy* or *Shannon's entropy* is given by

$$S_Y(f) = -\int_{\mathcal{D}(Y)} f(y) \log f(y) \mathrm{d}y,$$

where $\mathcal{D}(Y)$ is the domain of the random variable Y (see [61, Sec. 2.2]). This value quantifies the loss of information of a random variable; the less the

information, the higher the entropy. In the extant literature, several chapters have applied PME to reliable statistical distributions for random variables (see [62–64]).

To assign reliable probabilistic distributions to a random variable, Y, the PME seeks for a PDF, f_Y, by maximizing the functional $S_Y(f)$ subject to the available information for the unknown random variable such as the domain $\mathcal{D}(Y)$, its integral is the unit ($m_0 = 1$), the mean m_1 and other available higher moments m_k, $k = 2, \ldots, K$. Specifically, one solves the following optimization problem

$$\begin{aligned} \text{maximizing} \qquad & -\int_{\mathcal{D}(Y)} f_Y(y) \log f_Y(y) \mathrm{d}y, \\ \text{subject to} \qquad & \int_{\mathcal{D}(Y)} y^k f_Y(y) \mathrm{d}y = m_k, \qquad k = 0, 1, \ldots, K, \end{aligned}$$

where m_k are the k-order moments, which usually are known by metadata, samples, etc.

The general form of the density, f_Y, maximizing $S_Y(f)$ given $\{m_i\}_{i=0}^K$, is given by

$$f_Y(y) = \exp\left\{-1 - \sum_{k=1}^{K} \lambda_k y^k\right\}, \quad y \in \mathcal{D}(Y), \tag{2.4.1}$$

where the set $\{\lambda_k\}_{k=0}^K$ are called *the Lagrange multipliers* for the optimization problem (see [65, Th. 1, Ch.8]).

In our setting, the PME will be applied to assign a reliable density to the 2D sample data at time $t = 0$, i.e., the two-dimensional vector of initial conditions. According to the experimental procedure described at [66], cell densities grow in separate cultures before being introduced in the same culture. Therefore, it is logical to assume that the two initial random variables in system (4.0.1)-(4.0.2), which model the densities' time evolution in mixed culture, have statistically independent densities. Therefore, the joint PDF, represented by f_0 in the Liouville equation (2.2.2), can be expressed by $f_0(x_1, x_2) = f_{0,1}(x_1) f_{0,2}(x_2)$

for all $(x_1, x_2) \in \mathcal{D}$. In our application, we will determine both $f_{0,1}$ and $f_{0,2}$ by separately using the PME in each cell culture population.

Chapter 3

The Gompertz model subject to random fluctuations in all its parameters

In this chapter, we present a complete uncertainty quantification analysis of the randomized Gompertz model via the computation of an explicit expression to the first probability density function of its solution stochastic process, taking advantage of the Liouville-Gibbs theorem for dynamical systems. The stochastic analysis is completed by computing other important probabilistic information of the model, such as the time distribution until the solution reaches an arbitrary value of specific interest and the stationary distribution of the solution. Finally, we apply all our theoretical findings to two examples, the first of numerical nature and the second to model the dynamics of weight of a species using real-world data.

Some important mathematical models that have been extensively studied to describe population dynamics include the Malthusian, Verhulstian/Logistic, and Gompertzian models [67]. Although simple, these models serve as cornerstones for developing more sophisticated mathematical models aimed at describing the dynamics of various components of complex biological systems [68, 69]. Motivated by these facts, several interesting extensions of the aforementioned deterministic growth population models to stochastic scenarios have been proposed. It is important to note that these extensions depend on the mathematical properties of the random/stochastic noise introduced into the corresponding deterministic model to formulate its stochastic counterpart.

In the context of SDEs, the classical Malthusian, Verhulstian, and Gompertzian models have been studied and applied to model a variety of problems like the price of a stock, the asymptotic analysis of equilibrium states for a single species and tumor cell growth, for example (see [10, 70, 71] and references therein, respectively). Whereas in the setting of RDEs both Malthusian and Verhulstian models have also been extensively studied, see for instance [72] and [44, 73–75], respectively. However, to the best of our knowledge, the randomized Gompertz model has not yet been studied in the framework of RDEs.

This chapter is organized as follows. First, we remind and adapt the main results related to the Liouville-Gibbs theorem that will be required to determine a closed-form expression of the 1-PDF of the solution of the randomized Gompertz model. This is done in Subsection 3.1.1. Section 3.1 is completed by computing both the distribution of time until a certain number of individual/particles reaches a prefixed level (Subsection 3.1.2) and the stationary distribution of the solution (Subsection 3.1.3). In Section 3.2, all the theoretical results established in Section 3.1 are illustrated via two examples. Conclusions are shown in Section 3.2.

We finish this section pointing out that throughout this chapter the exponential function will be denoted by e or exp, interchangeably.

3.1 The randomized Gompertz model

This section is addressed to determine the main probabilistic properties of the randomized Gompertz model, namely, the 1-PDF of its solution stochastic process, the distribution of the time until a certain number of the individuals (also termed particles, depending upon the context of the problem) reaches a prefixed level and, finally, the stationary distribution. All this crucial information is presented in the following subsections. The main mathematical tools that will be applied to conduct our subsequent study are the Liouville PDE and the so-called RVT theorem. The former is required to determine the 1-PDF of the randomized Gompertz model, and the latter to compute both the distribution of the time and the stationary distribution.

3.1.1 Computing the 1-PDF of the randomized Gompertz model

The aim of this subsection is to obtain an explicit expression for the 1-PDF, $f(t,n)$, of the following Gompertz model

$$\begin{cases} N'(t) = N(t)[C - B\ln(N(t))], \quad t > t_0 \geq 0, \\ N(t_0) = N_0, \end{cases} \tag{3.1.1}$$

where N_0, B and C are second-order random variables and the unknown $N(t)$ is a second-order stochastic process. Here, $N(t)$ can represent the number of cells/organisms, weight, or other biological magnitudes, being N_0 its initial value at the time instant t_0. Parameters $B > 0$ and $C > 0$ represent the growth rate (division rate in the case of cells) of the system and the difference between the growth and "dampening factor" rates (death rate in the case of cells), respectively [76]. Observe that according to the development exhibited in Chapter 2, comparing (3.1.1) with the general problem (2.1.7) and its notation, now $n = 1$ ($\mathbf{X}(t) \equiv X(t) = N(t)$), $m = 2$ ($\mathbf{A} = (B, C)$) and $\mathbf{v}(t, \mathbf{X}(t), \mathbf{A}) = g(t, N(t), B, C) = N(t)\,[C - B\ln(N(t))]$. Using the notation $n = n(t)$, the

Liouville-Gibbs equation (2.2.2) writes

$$\begin{cases} \dfrac{\partial f(t,n,b,c)}{\partial t} + \nabla \cdot \left(f(t,n,b,c)\, n(c - b\ln(n)) \right) = 0, \quad t > t_0, \quad n > 0, \\ f(t_0,n,b,c) = f_0(n_0,b,c), \end{cases}$$

where f_0 is the joint density of the random variables N_0, B and C.

To obtain the solution by expression (2.2.7), we need to calculate the divergence term and function $n(t) = h(t,n_0,b,c)$. On the one hand, $g(t,n) = n(c - b\ln(n))$, so its divergence with respect to the "spatial" components is its derivative with respect to n, i.e.,

$$\nabla \cdot g(t,n) = c - b(\ln(n) + 1).$$

On the other hand, it is well-known that the solution of the Gompertz model (3.1.1) is given by

$$n = h(t,n_0,b,c), \quad \text{where} \quad h(t,n_0,b,c) = \mathrm{e}^{-\frac{c\left(\mathrm{e}^{-b(t-t_0)}-1\right)}{b}} n_0^{\mathrm{e}^{-b(t-t_0)}}. \tag{3.1.2}$$

Therefore, solving for n_0 gives

$$n_0 = h^{-1}(t,n,b,c) = n^{\mathrm{e}^{b(t-t_0)}} \mathrm{e}^{-\frac{c}{b}(\mathrm{e}^{b(t-t_0)}-1)}. \tag{3.1.3}$$

And so, we obtain

$$\begin{aligned} f(t,n,b,c) &= f_0(h^{-1}(t,n,b,c),b,c) \cdot \\ &\quad \exp\left\{ -\int_{t_0}^{t} c - b(\ln(h(t,n_0,b,c)) + 1)\, \mathrm{d}s \right\} \Big|_{n_0 = h^{-1}(t,n,b,c)} \\ &= f_0(h^{-1}(t,n,b,c),b,c) \exp\left(\eta(t,n,b,c)\right), \end{aligned} \tag{3.1.4}$$

where, after calculating the integral and performing its evaluation at $n_0 = h^{-1}(t, n, b, c)$ given by (3.1.3), one gets

$$\begin{aligned}\eta(t,n,b,c) &= b(t-t_0) + \tfrac{c}{b}\left(\mathrm{e}^{b(t-t_0)}-1\right) + ct\mathrm{e}^{b(t-t_0)} \\ &\quad - \left(\mathrm{e}^{b(-t+t_0)}(1+bt)-1\right)\ln\left[\mathrm{e}^{-\frac{c\left(-1+\mathrm{e}^{b(t-t_0)}\right)}{b}} n^{\mathrm{e}^{b(t-t_0)}}\right] \\ &\quad + bt\ln\left[\mathrm{e}^{-\frac{c\left(-1+\mathrm{e}^{b(-t+t_0)}\right)}{b}}\left(\mathrm{e}^{-\frac{c\left(-1+\mathrm{e}^{b(t-t_0)}\right)}{b}} n^{\mathrm{e}^{b(t-t_0)}}\right)^{\mathrm{e}^{b(-t+t_0)}}\right].\end{aligned} \tag{3.1.5}$$

Finally, we apply expression (2.2.9) to determine the PDF of the solution stochastic process of the randomized Gompertz model (3.1.1) by marginalizing

$$f(t,n) = \int_{\mathbb{R}^2} f(t,n,b,c)\,\mathrm{d}b\,\mathrm{d}c, \tag{3.1.6}$$

where $f(t, n, b, c)$ is given by (3.1.3)–(3.1.5). In the case that the N_0, B and C are independent random variables, then $f_0(n_0, b, c) = f_{n_0}(n_0)f_B(b)f_C(c)$ and (3.1.4) writes

$$f(t,n,b,c) = f_{N_0}(h^{-1}(t,n,b,c))f_B(b)f_C(c)\exp\left(\eta(t,n,b,c)\right). \tag{3.1.7}$$

Finally, observe that once the 1-PDF $f(t, n)$ has been determined, the computation of the one-dimensional moments turns out easily, provided they exist. For instance, the mean and the standard deviation are given by

$$\mu_N(t) = \mathbb{E}[N(t)] = \int_{\mathbb{R}} nf(t,n)\,\mathrm{d}n, \tag{3.1.8}$$

and

$$\sigma_N(t) = \sqrt{\int_{\mathbb{R}} n^2 f(t,n,b,c)\,\mathrm{d}n - (\mu_N(t))^2}, \tag{3.1.9}$$

respectively.

3.1.2 The distribution of the time until a certain number of individuals reaches a prefixed level

The Gompertz model describes the dynamics of $N(t)$ over the time t. In this setting, a crucial question that often arises in research is to determine when $N(t)$ reaches a specific value of interest, say ρ_N. In other words, we may be interested in determining the time instant $T_{\rho_N} := T$ such that $N(t) = \rho_N$. In our context, $N(t) = N(t; N_0, B, C)$ depends on model parameters N_0, B, and C, which are random variables, so the time T is also a random variable. Hereinafter, we derive the distribution of T under very general hypotheses on N_0, B, and C taking advantage of the RVT method stated in Theorem 2.2.2.

To this end, let us fix a value $\rho_N > 0$. Then, the solution (3.1.2) can be expressed as (observe that for convenience, the model parameters and time are written using capital letters since now they are interpreted as random variables)

$$\rho_N = \mathrm{e}^{-\frac{C\left(\mathrm{e}^{-B(T-t_0)}-1\right)}{B}} N_0^{\mathrm{e}^{-B(T-t_0)}}.$$

According to Theorem 2.2.2 with $k = 3$, let us consider the following identification $\mathbf{V} = (V_1, V_2, V_3) = (N_0, B, C)$ and $\mathbf{W} = (W_1, W_2, W_3)$ with the following transformation $\mathbf{r} : \mathbb{R}^3 \longrightarrow \mathbb{R}^3$ whose components $r_i(\mathbf{v})$, $i = 1, 2, 3$, are given by

$$\begin{aligned} w_1 &= r_1(\mathbf{v}) = t = t_0 - \tfrac{1}{b} \ln\left(\tfrac{\ln(\rho_N) - \frac{c}{b}}{\ln(n_0) - \frac{c}{b}}\right), \\ w_2 &= r_2(\mathbf{v}) = b, \\ w_3 &= r_3(\mathbf{v}) = c. \end{aligned}$$

Now, we compute the inverse mapping of $\mathbf{r}$: $\mathbf{s}(\mathbf{w}) = \mathbf{r}^{-1}(\mathbf{v})$, whose components s_i, $1 \leq i \leq 3$, are

$$\begin{aligned} n_0 &= s_1(\mathbf{w}) = \rho_N^{\mathrm{e}^{w_2(w_1-t_0)}} \mathrm{e}^{-\frac{w_3}{w_2}(\mathrm{e}^{w_2(w_1-t_0)}-1)}, \\ b &= s_2(\mathbf{w}) = w_2, \\ c &= s_3(\mathbf{w}) = w_3. \end{aligned}$$

The absolute value of the jacobian of this transformation $\mathbf{s}$ is

$$|J| = \left| \det \begin{bmatrix} \frac{\partial n_0}{\partial w_1} & 0 & 0 \\ \frac{\partial n_0}{\partial w_2} & 1 & 0 \\ \frac{\partial n_0}{\partial w_3} & 0 & 1 \end{bmatrix} \right| = \left| \frac{\partial n_0}{\partial t}(w_1, w_2, w_3) \right| \tag{3.1.10}$$

$$= \rho_N^{\mathrm{e}^{w_2(w_1-t_0)}} \mathrm{e}^{-\frac{w_3}{w_2}(\mathrm{e}^{w_2(w_1-t_0)}-1)} |w_2 \ln(\rho_N) - w_3| \mathrm{e}^{w_2(w_1-t_0)}. \tag{3.1.11}$$

Therefore, applying Theorem 2.2.2 the distribution of time T for a given value ρ_N of N is given by

$$f_T(t, \rho_N) = \tag{3.1.12}$$
$$\int_{\mathbb{R}^2} f_0(\rho_N^{\mathrm{e}^{b(t-t_0)}} \mathrm{e}^{-\frac{c}{b}(\mathrm{e}^{b(t-t_0)}-1)}, b, c) \rho_N^{\mathrm{e}^{b(t-t_0)}} \mathrm{e}^{-\frac{c}{b}(\mathrm{e}^{b(t-t_0)}-1)} |b \ln \rho_N - c| \mathrm{e}^{b(t-t_0)} \, \mathrm{d}b \, \mathrm{d}c,$$

where $f_0(n_0, b, c)$ denotes the joint PDF of the random vector (N_0, B, C). If we assume independence between the model parameters N_0, B and C, f_0 would factorize as the product of the corresponding marginals f_{N_0}, f_B and f_C.

An important information that will be utilized later in the Example 3.2.2 is the average time of random variable $T := T_{\rho_N}$ for a fixed value of ρ_N. This quantity is now straightforwardly obtained once the PDF of T has been determined,

$$\mu_T(\rho_N) := \mathbb{E}[T_{\rho_N}] = \mathbb{E}[T] = \int_{\mathbb{R}} t f_T(t, \rho_N) \, \mathrm{d}t = \int_{t_0}^{+\infty} t f_T(t, \rho_N) \, \mathrm{d}t, \tag{3.1.13}$$

where $f_T(t, \rho_N)$ is given by (3.1.12).

3.1.3 Stationary distribution of the solution

In this section, we will take advantage of the RVT theorem to calculate the probability distribution of the stationary state. Taking limits as $t \to \infty$ in expression (3.1.2), it is straightforward to check that the steady-state of the randomized Gompertz model is the random variable $N^* = \mathrm{e}^{C/B}$. To compute its PDF we will apply Theorem 2.2.2 with $k = 2$, $\mathbf{V} = (V_1, V_2) = (B, C)$, $\mathbf{W} = (W_1, W_2)$ and the following deterministic mapping, $\mathbf{r} : \mathbb{R}^2 \to \mathbb{R}^2$, $\mathbf{r}(\mathbf{v}) =$

$(r_1(\mathbf{v}), r_2(\mathbf{v}))$ where

$$w_1 = r_1(\mathbf{v}) = \mathrm{e}^{c/b}, \qquad w_2 = r_2(\mathbf{v}) = b.$$

Then, its inverse mapping, $\mathbf{s} : \mathbb{R}^2 \to \mathbb{R}^2$, is

$$b = s_1(\mathbf{w}) = w_2, \qquad c = s_2(\mathbf{w}) = w_2 \ln(w_1).$$

The absolute value of the Jacobian of mapping $\mathbf{s}$ can be easily calculated

$$|J_2| = \left| \det \begin{bmatrix} 0 & \frac{w_2}{w_1} \\ 1 & \ln(w_1) \end{bmatrix} \right| = \left| -\frac{w_2}{w_1} \right| = \frac{w_2}{w_1}.$$

The last equality holds because both $\mathbb{P}\left[\{\omega \in \Omega : \mathrm{e}^{c(\omega)/b(\omega)} > 0\}\right] = 1$ and $\mathbb{P}\left[\{\omega \in \Omega : b(\omega) > 0\}\right] = 1$. Therefore, the PDF of the random vector (N^*, B) is

$$f_{N^*,B}(w_1, w_2) = f_{B,C}\left(w_2, w_2 \ln(w_1)\right) \frac{w_2}{w_1}. \tag{3.1.14}$$

Since we are assuming that the PDF f_0 of model parameters, (N_0, B, C), is known, then the PDF of random vector (B, C) is given by

$$f_{B,C}(b, c) = \int_{\mathbb{R}} f_0(n_0, b, c)\, \mathrm{d}n_0.$$

So, applying this in (3.1.14) and taking into account that $w_1 = n^*$ and $w_2 = b$, one obtains

$$f_{N^*,B}(n^*, b) = \frac{b}{n^*} \int_{\mathbb{R}} f_0(n_0, b, b \ln(n^*))\, \mathrm{d}n_0.$$

Finally, we can determine the PDF of the stationary state marginalizing this distribution with respect to the random variable B. This yields

$$f_{N^*}(n^*) = \frac{1}{n^*} \int_{\mathbb{R}} \int_{\mathbb{R}} b\, f_0(n_0, b, b \ln(n^*))\, \mathrm{d}n_0\, \mathrm{d}b. \tag{3.1.15}$$

In the usual case where all input parameters are independent random variables, the previous expression can be simplified as

$$f_{N^*}(n^*) = \frac{1}{n^*} \int_{\mathbb{R}} b f_B(b)\, f_C(b \ln(n^*)))\, \mathrm{d}b, \tag{3.1.16}$$

since $f_0(n_0, b, b\ln(n)) = f_{N_0}(n_0) f_B(b) f_C(b\ln(n))$ (where f_{N_0}, f_B and f_C denote the PDFs of random variables N_0, B and C, respectively) and f_{N_0} has unit mass; that is, $\int_{\mathbb{R}} f_{N_0}(n_0)\, \mathrm{d}n_0 = 1$.

Remark 3.1.1. *Observe that since C is a positive random variable, in practice, the domain of integration in* (3.1.16) *must be calculated taking into account that the term $b\ln(n^*)$ must be positive. Even more, since B is also a positive random variable, then $N^*(\omega) > 1$ for all $\omega \in \Omega$. This fact will be used later in Example 3.2.2.*

3.2 Examples

In this section, we present two examples. Example 3.2.1 is devised to illustrate the application of the theoretical results established throughout Section 3.1 considering statistical dependence/independence of model parameters N_0, B, and C. The nature in this example is just numerical. We complete this section, including a second example where we show how to describe the dynamics of a biological process using real data via the Gompertz model. In both examples, we calculate the 1-PDF of the solution stochastic process, its mean and standard deviation functions together with confidence intervals, as well as the stationary distribution. Additionally, we compute the PDF the random variable time as defined in Section 3.1.2.

Example 3.2.1. *In this numerical example, we will examine two scenarios with respect to the dependence/independence of model parameters N_0, B, and C and their impact on the Gompertz model output. To this end, we will first consider that the random vector (N_0, B, C) has a Multinormal distribution whose variance-covariance matrix, say Σ, is non-diagonal (so, N_0, B and C are dependent random variables) and, secondly, when Σ is diagonal (so, N_0, B and C are independent random variables). Then, we show how the 1-PDF*

of the solution stochastic process, the mean and standard deviation functions, the PDF of the time random variable, and the stationary distribution change in each scenario.

- *Scenario 1 (dependence): The random vector* (N_0, B, C) *has a Multinormal distribution truncated to* $T = \mathbb{R}^+ \times \mathbb{R}^+ \times \mathbb{R}^+$, $(N_0, B, C) \sim \mathrm{N}_T(\boldsymbol{\mu}, \boldsymbol{\Sigma})$, *with the following mean vector and variance-covariance matrix*

$$\boldsymbol{\mu} = (0.8, 1, 1.5), \quad \boldsymbol{\Sigma} = \frac{1}{10}\begin{bmatrix} 1 & 0 & 1 \\ 0 & 1.2 & 1 \\ 1 & 1 & 2 \end{bmatrix}, \tag{3.2.1}$$

respectively. Then, the PDF of random vector (N_0, B, C) *is* $f_0(n_0, b, c) =$

$$\begin{cases} 0.001676\, \mathrm{e}^{-25b^2-30c^2+b(15+50c-50n_0)+(16-35n_0)n_0+c(-8+60n_0)} & n_0, b, c > 0, \\ 0 & \textit{otherwise.} \end{cases} \tag{3.2.2}$$

- *Scenario 2 (independence): The random vector* (N_0, B, C) *has a Multinormal distribution truncated to* $T = \mathbb{R}^+ \times \mathbb{R}^+ \times \mathbb{R}^+$, $(N_0, B, C) \sim \mathrm{N}_T(\mu, \Sigma)$, *with the following mean vector and variance-covariance matrix*

$$\boldsymbol{\mu} = (0.8, 1, 1.5), \quad \boldsymbol{\Sigma} = \frac{1}{10}\begin{bmatrix} 1 & 0 & 0 \\ 0 & 1.2 & 0 \\ 0 & 0 & 2 \end{bmatrix}, \tag{3.2.3}$$

respectively. Then, the PDF of random vector (N_0, B, C) *is* $f_0(n_0, b, c) = f_{N_0}(n_0) f_B(b) f_C(c) =$

$$\begin{cases} 1.30656\, \mathrm{e}^{-4.17(-1+b)^2-2.5(-1.5+c)^2-5(-0.8+n_0)^2} & n_0, b, c > 0, \\ 0 & \textit{in other case.} \end{cases} \tag{3.2.4}$$

In Figure 3.1, we show the 1-PDF, $f(t, n)$, *of the solution stochastic process for different time instants in the interval* $[0, 1]$ *in both scenarios. To compute* $f(t, n)$ *in the scenario 1, we have used expressions* (3.1.6) *together with* (3.1.3)–(3.1.5) *where* f_0 *is given by* (3.2.2). *While to compute* $f(t, n)$ *in the scenario 2, we have applied* (3.1.6), (3.1.3), (3.1.5) *and* (3.1.7) *where* f_0 *is given by* (3.2.4). *From this graphical representation, we can observe that the*

1-PDF corresponding to scenario 2 is more leptokurtic than in scenario 1. This fact is in agreement with the results shown in Figure 3.2 where the expectation (calculated via (3.1.8)*) and the standard deviation (calculated via* (3.1.9)*) in each scenario are compared. In Figure 3.2, we see that the variability of the solution is, in general, greater considering dependent random inputs (scenario 1). We observe that near the time instant* $t = 1$*, the variability in the dependent case is smaller than in the independent one. This fact can be explained from Figure 3.3 since at* $t = 1$*, we see that the right-tail of the PDF,* $f(n, 1)$*, obtained in scenario 2 is heavier than in scenario 1.*

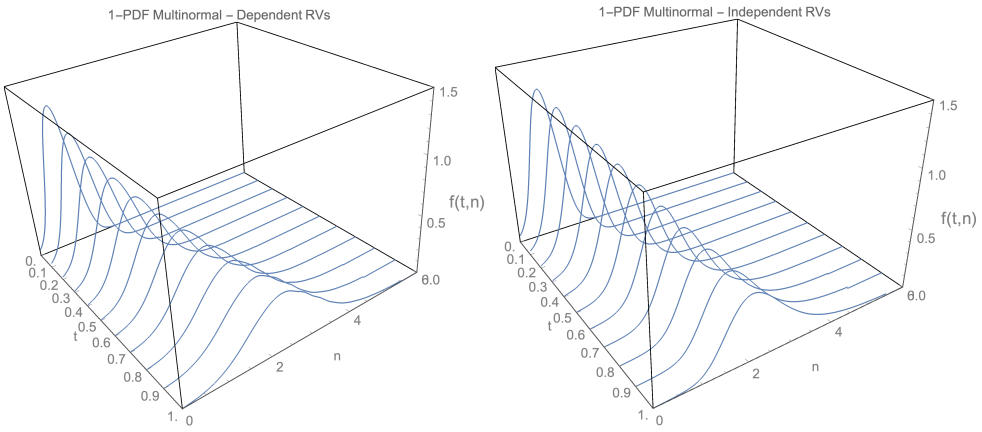

Figure 3.1: 1-PDF of the solution stochastic process, $f(t, n)$, of the Gompertz model (3.1.1) whose input is a multinormal distribution $(N_0, B, C) \sim \mathrm{N}_T(\boldsymbol{\mu}, \boldsymbol{\Sigma})$, at different time instants in the interval $[0, 1]$, in both scenarios. Left (scenario 1-dependent random variables): $\boldsymbol{\mu}$ and $\boldsymbol{\Sigma}$ are given by (3.2.1). Right (scenario 2-independent random variables): $\boldsymbol{\mu}$ and $\boldsymbol{\Sigma}$ are given by (3.2.3). Example 3.2.1.

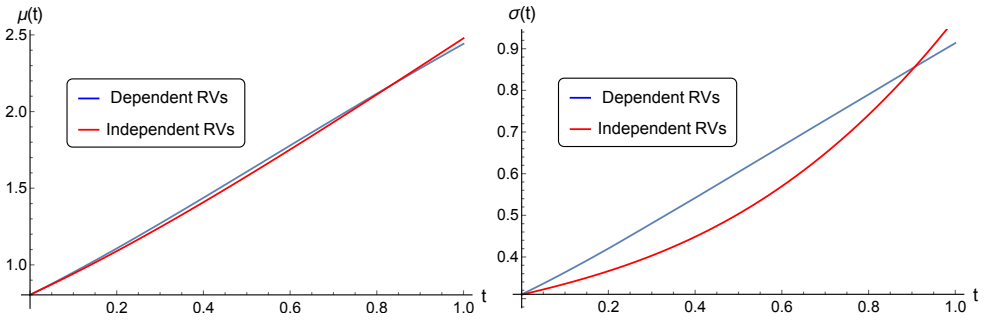

Figure 3.2: Expectation (left), $\mu(t)$, and standard deviation (right), $\sigma(t)$, in scenario 1 (dependent random variables) and in scenario 2 (independent random variables) in the time interval $[0, 1]$. Example 3.2.1.

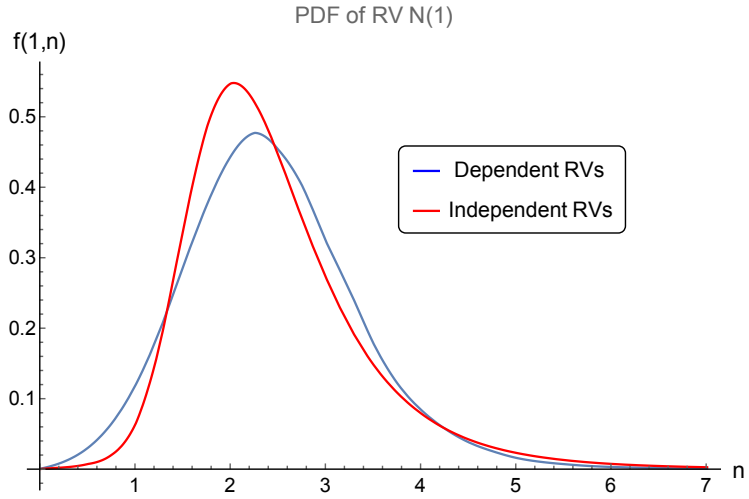

Figure 3.3: PDF of the solution stochastic process in the time instant $t = 1$, $f(1, n)$, in scenario 1 (dependent random variables) and in scenario 2 (independent random variables). Example 3.2.1.

According to Subsection 3.1.2, we can also compute the PDF of the time T until a certain number of individuals/particles reach a fixed value, ρ_N. In Figure 3.4 we show the PDF of T for different values of $\rho_N \in \{1, 1.25, 1.5, 1.75, 2, 2.25, 2.50\}$. By applying (3.1.13)*, in Table 3.1 we collect the expectation of T for the different values of ρ_N in scenarios 1 and 2. To carry out computations, we have used expressions* (3.1.13) *and* (3.1.12)*, taking f_0 the PDF defined in* (3.2.2) *(in scenario 1) and* (3.2.4) *(in scenario 2). With data chosen in our numerical experiments, we observe that in the case of independent random inputs (scenario 2), the time $\mu_T(\rho_N)$ needed to reach each prefixed value ρ_N is smaller than in the dependent case (scenario 1).*

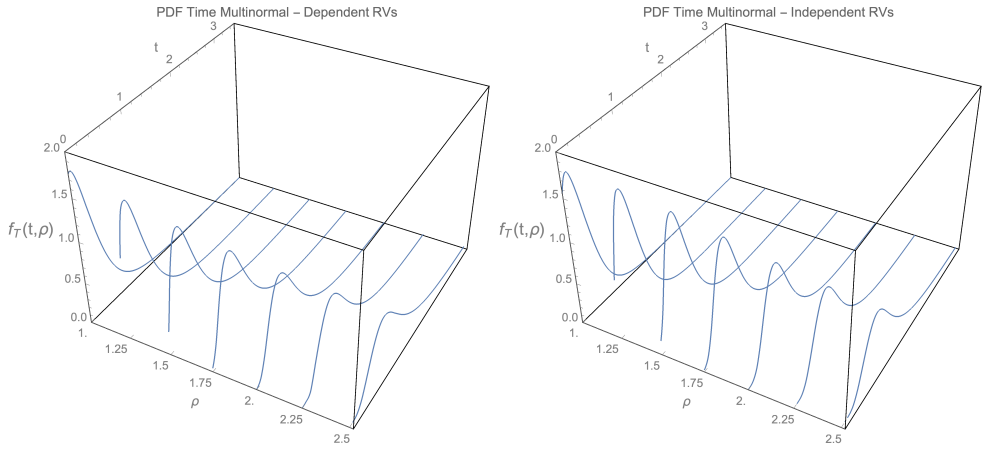

Figure 3.4: PDF of the time T until a given number of individuals reach a fixed value $\rho = \rho_N \in \{1, 1.25, 1.5, 1.75, 2, 2.25, 2.50\}$. Left (scenario 1-dependent random variable). Right (scenario 2-independent random variables). Example 3.2.1.

ρ_N	1	1.25	1.5	1.75	2	2.25	2.5
$\mu_T(\rho_N)$ Dep.	0.232	0.414	0.592	0.774	0.967	1.173	1.386
$\mu_T(\rho_N)$ Indep.	0.169	0.359	0.551	0.745	0.934	1.106	1.255

Table 3.1: Expectation of the time needed to reach certain fixed values, $\rho_N \in \{1, 1.25, 1.5, 1.75, 2, 2.25, 2.50\}$ in scenario 1 (dependent random variables) and in scenario 2 (independent random variables). Example 3.2.1.

Finally, we compute the distribution of the stationary state $N^* = \mathrm{e}^{C/B}$*, using the results derived in Subsection 3.1.3. In Figure 3.5 we have plotted the PDF of* N^**,* $f_{N^*}(n^*)$ *from expressions* (3.1.15) *(scenario 1) and* (3.1.16) *(scenario 2). In this latter case, observe that* f_B *and* f_C *correspond to the PDF of the following Gaussian random variables* $B \sim \mathrm{N}(\mu_B = 1; \sigma_B^2 = 12/100)$ *and* $C \sim \mathrm{N}(\mu_C = 15/10; \sigma_C^2 = 2/10)$*. From Figure 3.5, we observe that in this particular case, the stationary corresponding to scenario 2 has a heavier right tail.*

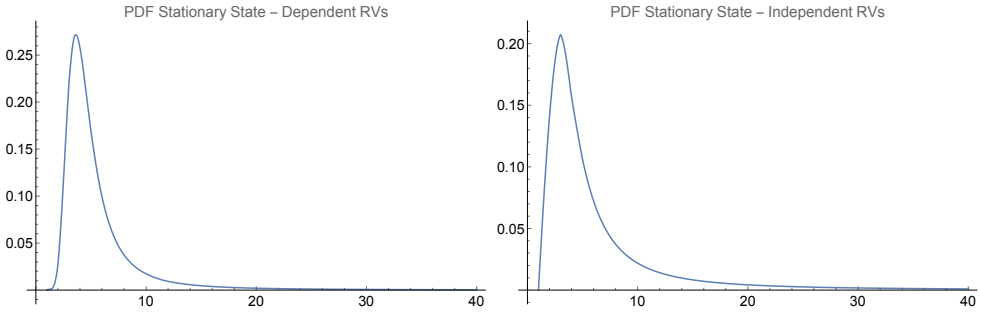

Figure 3.5: PDFs of the stationary state for each scenario. Left: scenario 1-dependent random variables. Right: scenario 2-independent random variables. Example 3.2.1.

Example 3.2.2. *In real applications, the Gompertz model is used to explain the dynamics of data that has been sampled. This model has been used to explain the growth of species, tumors, etc., via measurements like weight, volume, etc. In this example, we use data corresponding to weight measurements, in kilograms, for a randomly bred male Pearl Gray Guinea Fowl population during 23 consecutive days [77]. We have assumed that model parameters are independent random variables, and, for them, we choose the following distributions:*

$N_0 \sim \mathrm{U}([0.019779, 0.032472])$ (*uniform distribution*),
$B \sim \mathrm{G}(3841.397958, 0.000057)$ (*gamma distribution*),
$C \sim \mathrm{N}|_T(0.105982, 0.002643)$ (*truncated normal distribution in* $T = [0.09, 0.12]$).

Now, we justify the selection made for the above-mentioned distributions of each model input. We will assume independence between N_0*,* B*, and* C *since,*

from a computational point of view, this assumption simplifies the calculations. Anyway, the subsequent computations may be carried out in the case that input parameters are statistically dependent, as was shown in Example 3.2.1. For the sake of clarity, down below, we explain, in several steps, the underlying reasoning for selecting the probability distribution of each model input as well as how we have calculated their corresponding parameters.

Step 1: Initially, the model inputs whose information is more limited are B and C. We only know that both are positive. So, we are going to assign them positive distributions having certain flexibility (specifically, having two degrees of freedom, i.e., two parameters, and whose respective shape's density probability varies with such parameters) so that we can better capture their intrinsic uncertainty. Specifically, we will assume that B has a Gamma distribution with parameters $b_1, b_2 > 0$, $B \sim \mathrm{G}(b_1, b_2)$, and C has a Normal distribution with mean, $\mu > 0$, and standard deviation, $\sigma > 0$, truncated in certain interval $T \subset \mathbb{R}^+$, $\mathrm{N}|_T(\mu, \sigma)$. For the initial condition N_0 we will assume that it has a Uniform distribution in the interval $[n_{0,1}, n_{0,2}]$. These six parameters (b_1, b_2), (μ, σ) and $(n_{0,1}, n_{0,2})$ together with the interval T will be determined later.

Step 2: We first calculate (deterministic) values for model inputs n_0, b, and c that best fit, in the mean square sense, the sampled data. We have used the command "NonlinearModelFit" (by Mathematica software) that provides the estimates of model inputs and their errors,

$$\begin{array}{rclrcl} n_0 &=& 0.026615, & \epsilon_{n_0} &=& 0.000776, \\ b &=& 0.226409, & \epsilon_b &=& 0.003654, \\ c &=& 0.1046, & \epsilon_c &=& 0.002296. \end{array}$$

These (deterministic) estimates will be used later to determine the parameters, $(n_{0,1}, n_{0,2})$, (b_1, b_2) and (μ, σ), of the probability distributions, assigned in Step 1, to each model input N_0, B and C, respectively. Specifically, we will consider that the previous values for (n_0, ϵ_{n_0}), (b, ϵ_b) and (c, ϵ_c) represent (approximately) their means and standard deviations, respectively. As, initially, we are assuming that C has a Normal distribution with mean $c = 0.1046$ and standard deviation $\epsilon_c = 0.002296$,

truncated a certain interval T to be determined, we take T large enough so that it contains its total probability density. We will take, for example, $T = (0.09, 0.12)$ since $P[\{\omega \in \Omega : 0.09 < C(\omega) < 0.12\}] \approx 1$, i.e.

$$\int_{0.09}^{0.12} \frac{1}{\sqrt{2\,\pi\, 0.002296^2}}\, \mathrm{e}^{-\frac{1}{2}\left(\frac{c-0.1046}{0.002296}\right)^2}\, \mathrm{d}c \approx 1.$$

Step 3: Now, we will determine the parameters $(n_{0,1}, n_{0,2})$, (b_1, b_2) and (μ, σ) by minimizing the mean square error between sampled data, n_j, $0 \leq j \leq 22$, and the expectation of the solution stochastic process $N(t) = N(t; n_{0,1}, n_{0,2}, b_1, b_2, \mu, \sigma)$ evaluated at the time instants $t = t_j$, $0 \leq j \leq 22$:

$$\min_{n_{0,1}, n_{0,2}, b_1, b_2, \mu, \sigma > 0} \mathrm{E}(n_{0,1}, n_{0,2}, b_1, b_2, \mu, \sigma) = \sum_{j=0}^{22} \left(\mathbb{E}\left[N(t_j; n_{0,1}, n_{0,2}, b_1, b_2, \mu, \sigma)\right] - n_j\right)^2, \tag{3.2.5}$$

where the above expectation is computed using expression (3.1.8)*. In order to calculate the minimum of the above error function* E*, we have used the Nelder-Mead algorithm. Nelder-Mead is a simplex-type method that requires an initial value (seed) to apply it. We use the deterministic information shown in Step 2 to set the starting values that, hereinafter, will be denoted by $(n_{0,1}^0, n_{0,2}^0)$, (b_1^0, b_2^0) and (μ^0, σ^0). The starting values for random variable C match, obviously, the mean and standard deviation calculated via the deterministic fitting shown in Step 2, so $\mu^0 = 0.1046$ and $\sigma^0 = 0.002296$. For N_0, we calculate $(n_{0,1}^0, n_{0,2}^0)$ using the Moment Matching Method [78] for the mean and the variance of a Uniform distribution,*

$$0.026615 = \mathbb{E}[N_0] = \frac{n_{0,1}^0 + n_{0,2}^0}{2}, \qquad 0.000776^2 = \mathbb{V}[N_0] = \frac{(n_{0,2}^0 - n_{0,1}^0)^2}{12}.$$

Solving the above nonlinear system, we obtain $n_{0,1}^0 = 0.020285$ and $n_{0,2}^0 = 0.032944$. Similarly, we calculate the estimates $b_1^0 = 3838.25$ and $b_2^0 =$

0.000059 *solving the system*

$$0.226409 = \mathbb{E}[B] = b_1^0 b_2^0, \qquad 0.003654^2 = \mathbb{V}[B] = b_1^0 \left(b_2^0\right)^2.$$

With this starting value, the error is $\mathrm{E}(n_{0,1}^0, n_{0,2}^0, b_1^0, b_2^0, \mu^0, \sigma^0) = 0.011507$. *After minimizing the objective function* (3.2.5), *we obtain*

$$\begin{array}{rclrclrcl} n_{0,1}^* & = & 0.019779, & n_{0,2}^* & = & 0.032472, & b_1^* & = & 3841.297958, \\ b_2^* & = & 0.000057, & \mu^* & = & 0.105982, & \sigma^* & = & 0.002643, \end{array}$$

being the error 0.006635.

In Figure 3.6, we show the data (points), the mean of the solution (solid curve), and the confidence interval (dotted curves). The mean, $\mu_N(t)$, *has been calculated by* (3.1.8) *and* (3.1.3)–(3.1.6), *being* $f_0(n_0, b, c) = f_{N_0}(n_0) f_B(b) f_C(c)$ *and*

$$f_{N_0}(n_0) = \begin{cases} 78.7836, & \text{if } \ n_0 \in [0.019779, 0.032472], \\ 0, & \text{otherwise,} \end{cases}$$

$$f_B(b) = \begin{cases} 4.119667 \cdot 10^{4203}\, \mathrm{e}^{-17542.9b}\, b^{3840.4}, & \text{if } \ b > 0, \\ 0, & \text{otherwise,} \end{cases}$$

$$f_C(c) = \begin{cases} 150.943\, \mathrm{e}^{-71577.4(-0.105982+c)^2}, & \text{if } \ 0.09 < c < 0.12, \\ 0, & \text{otherwise,} \end{cases}$$

and $t_0 = 0$. *The confidence interval has been calculated by* $\mu_N(t) \pm 1.96\sigma_N(t)$ *where* $\sigma_N(t)$ *has been calculated via* (3.1.9). *From Figure 3.6, we can see that this confidence interval captures very well the uncertainty of sample data. In Figure 3.7, we show the evolution of the 1-PDF,* $f(t, n)$, *of the solution stochastic process,* $N(t)$, *together with the data (points), mean (solid curve) and confidence intervals (dotted curves). We observe that variability slightly increases as time goes on in agreement with the fitting shown in Figure 3.6.*

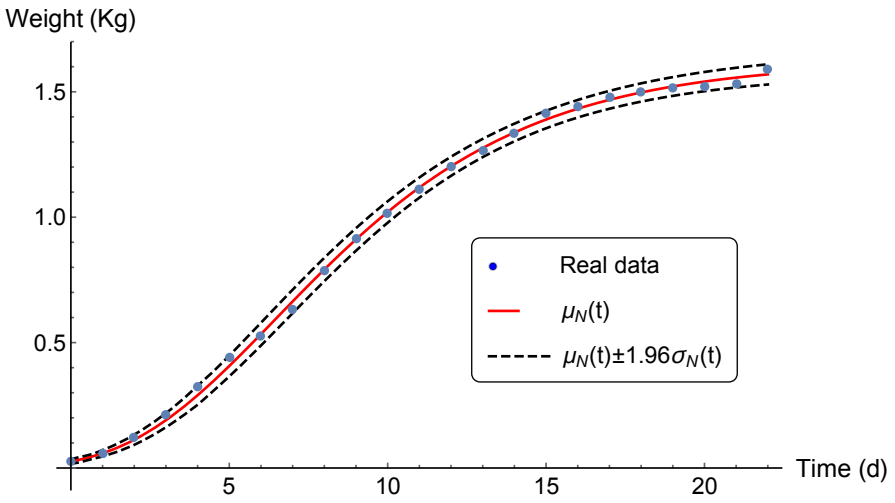

Figure 3.6: Model fitting: Sample data (points), expectation function (solid curve) and confidence interval (dotted curves) centered in the mean $\mu_N(t)$ and radius $1.96\,\sigma_N(t)$, being $\sigma_N(t)$ the standard deviation function. Example 3.2.2.

Now, using expression (3.1.12)*, in Figure 3.8, we show the PDF of random variable time T (in days) until the Pearl Gray Guinea Fowl species has a prefixed weight $\rho = \rho_N$ (in kilograms). In Table 3.2, we collect the expected value of T for different values of $\rho = \rho_N$ using expression* (3.1.13)*. According to these values, for example, it is expected that after* 9 *or* 10 *days, the species will weigh* 1 *kg. It is worthwhile pointing out that the numerical values shown in Table 3.2 agree with the graphical representation shown in Figure 3.8.*

ρ_N	0.25	0.5	0.75	1	1.25	1.50
$\mu_T(\rho_N)$	3.628197	5.746689	7.682120	9.719286	12.575619	18.112325

Table 3.2: Expected time ($\mu_T(\rho_N)$, measured in days, needed for the weight to reach certain prefixed values (ρ_N), measured in kilograms. Example 3.2.2.

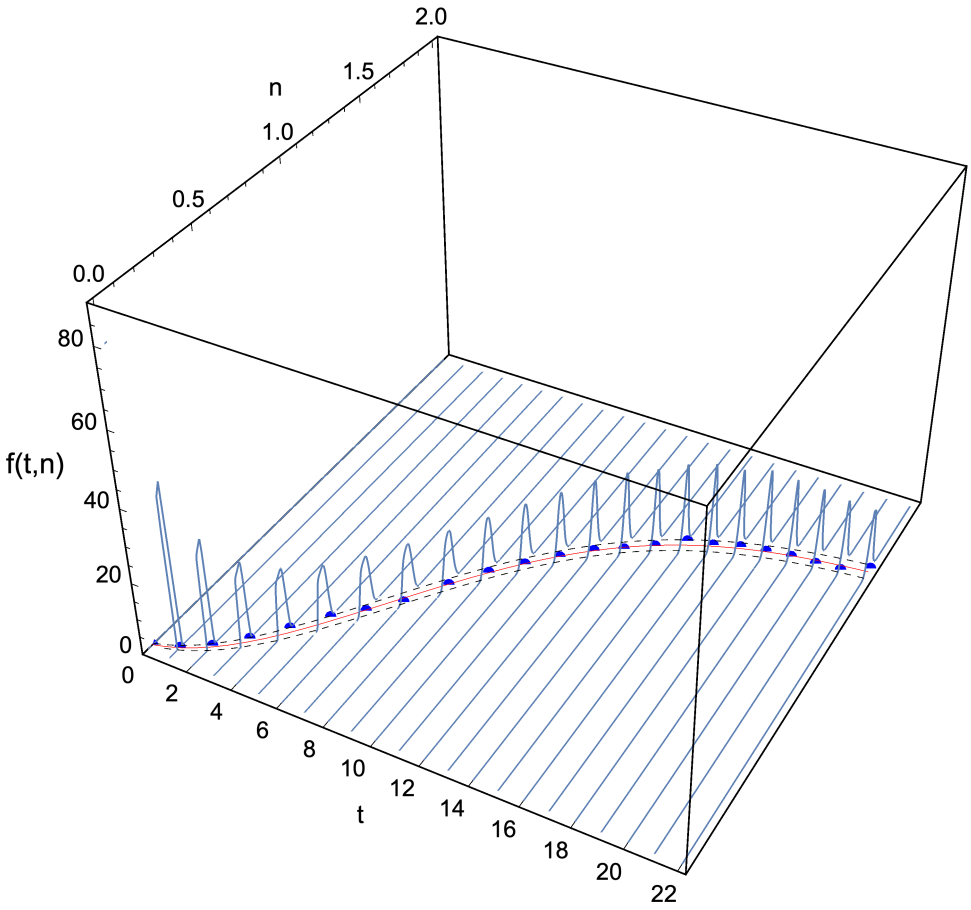

Figure 3.7: Representation of the 1-PDF, $f(t, n)$ of the solution stochastic process, $N(t)$, for fixed time values. In the horizontal plane $t - f(t, n)$, we have projected the plot shown in Figure 3.6. Example 3.2.2.

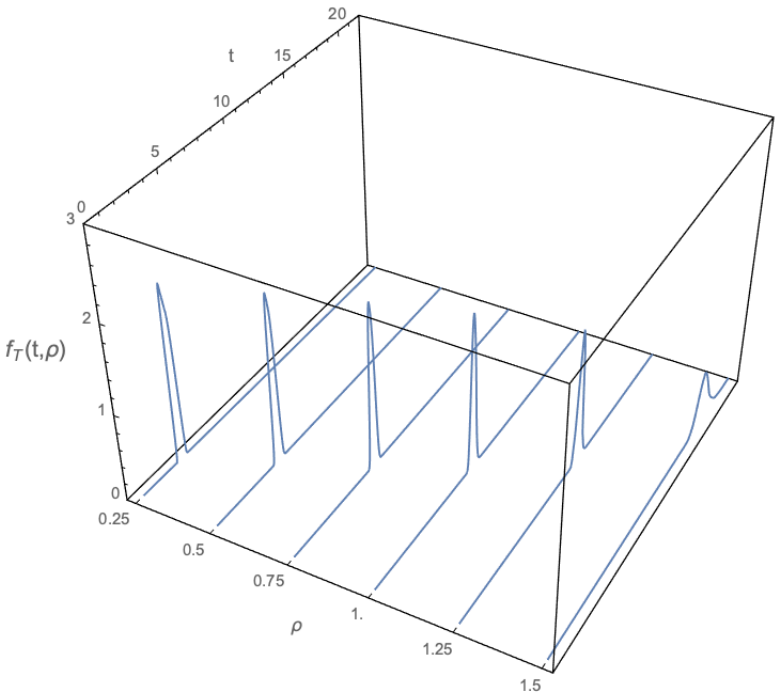

Figure 3.8: Graphical representation of the PDF of the random variable time T for the prefixed values of $\rho = \rho_N$ shown in Table 3.2. Example 3.2.2.

We conclude this example calculating, from expression (3.1.16)*, the PDF of the asymptotic state,* $N^* = \mathrm{e}^{C/B}$*,*

$$f_{N^*}(n^*) = \begin{cases} \displaystyle\int_{0.09/\ln(n^*)}^{0.12/\ln(n^*)} \frac{1}{n^*}\left(a_1 \cdot 10^{a_2} b^{a_3}\, \mathrm{e}^{-a_4 b - a_5(-a_6 + b\ln(n^*))^2}\right) \mathrm{d}b, & \text{if } n^* > 1, \\ 0, & \text{otherwise.} \end{cases}$$

where $a_1 = 6.218349$*,* $a_2 = 4025$*,* $a_3 = 2840.4$*,* $a_4 = 17543.9$*,* $a_5 = 71577.4$ *and* $a_6 = 0.105982$*. Observe that, using Remark 3.1.1, the domain of integration has been determined so that* $b\ln(n^*) \in (0.09, 0.12)$*, taking into account that* $B > 0$ *(recall that it has a Gamma distribution). In Figure, 3.9 we show the PDF of the equilibrium,* $f_{N^*}(n^*)$*, as well as its mean,*

$$m^* = \int_{\mathbb{R}} n^* f_{N^*}(n^*)\,\mathrm{d}n^* = 1.622966, \tag{3.2.6}$$

and the confidence interval

$$\begin{gathered} [m^* - 1.96\,\sigma^*, m^* + 1.96\,\sigma^*] = [1.577268, 1.668664], \\ \sigma^* = \sqrt{\textstyle\int_{\mathbb{R}} (n^*)^2 f_{N^*}(n^*)\,\mathrm{d}n^* - (m^*)^2} = 0.023315. \end{gathered} \tag{3.2.7}$$

For the sake of clarity, in Figure 3.10, we show a graphical representation of the model fitting together with the equilibrium, including the means and confidence intervals. We can observe that for a finite time (until $t = 22$*), the diameter of the confidence interval increases slowly. It is expected that its maximum diameter will be reached as* $t \to \infty$*, so the confidence interval graphically represented for the equilibrium accounts for this quantity. This quantifies the maximum expected uncertainty.*

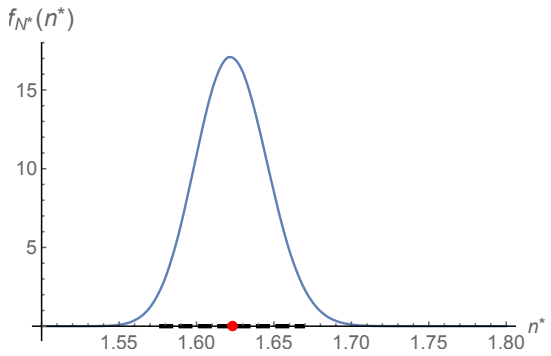

Figure 3.9: PDF of the equilibrium random variable $N^* = \mathrm{e}^{C/B}$. In the horizontal axis, the mean (point) and the confidence interval (dashed lines) are indicated. They have been calculated by (3.2.6) and (3.2.7), respectively. Example 3.2.2.

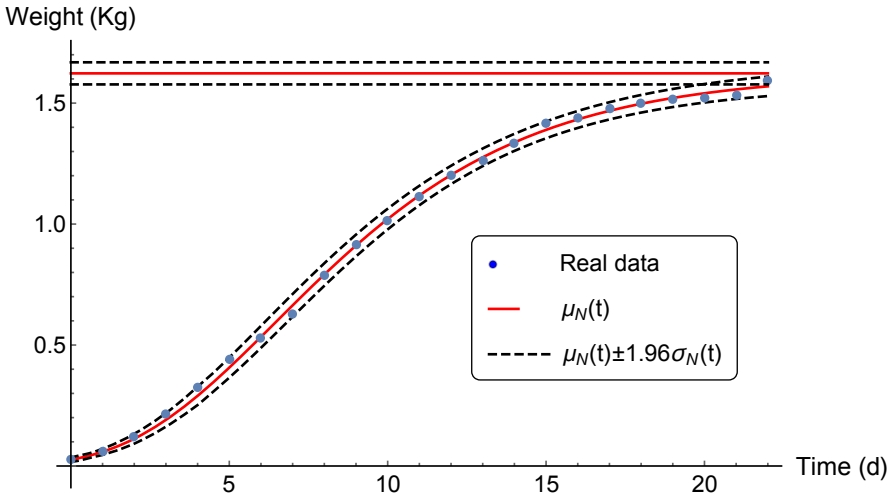

Figure 3.10: Graphical representation of the model fitting together with the equilibrium including the means (solid lines), confidence intervals (dotted lines) and data (points). Example 3.2.2.

Conclusions

In this chapter we have studied, from a probabilistic standpoint, the fully randomized Gompertz model. This important model plays a key role in describing the dynamics of biological and biophysical parts of complex systems, which often involve uncertainties. The study has been conducted under very general hypotheses regarding the probability distributions of model parameters, which confers a wide range of applicability to our theoretical findings. The numerical experiments and modeling carried out in our examples show very good results.

Publications

The results presented in this thesis chapter have been published in [26]. In regard to this chapter, the PhD candidate has contributed by working on its complete development with more emphasis on the theoretical results and preparing the visualization of the numerical examples.

Chapter 4

Random microbial growth in a competitive environment

The Baranyi–Roberts model describes the dynamics of the volumetric densities of two interacting cell populations. We randomize this model by considering that the initial conditions are random variables whose distributions are determined by using sample data and the Principle of Maximum Entropy. Because the exact solution of this equation is unaffordable, we use a finite volume scheme to numerically approximate the solution's probability density function via the Liouville equation. Based on this, we design an optimization procedure to determine the optimal parameter values of the Baranyi–Roberts model so that the expectation fits the sample data.

As described in [66], the Baranyi-Roberts model can be used to describe growth that comprises several phases: lag phase, exponential phase, deceleration phase, and stationary phase. The system can be seen as a generalization of a family of multi-species interaction systems (see [79]). These systems can be classified as competition, mutualism, and predation systems (see [80, 81]). The Baranyi-Roberts model assumes that cell growth accelerates as cells adjust to new growth conditions and then decelerates as resources are depleted. When modeling growth in a mixed culture, we assume that interactions between strains are density-dependent, for example, due to resource competition. The Baranyi-Roberts model is given by the following non-autonomous and nonlinear system of differential equations

$$\frac{\mathrm{d}N_1}{\mathrm{d}t} = \alpha_1(t)\, r_1\, N_1 \left(1 - \frac{N_1^{\nu_1}}{K_1^{\nu_1}} - c_2 \frac{N_2^{\nu_2}}{K_1^{\nu_1}}\right), \quad N_1(0) = N_1^0, \tag{4.0.1}$$

$$\frac{\mathrm{d}N_2}{\mathrm{d}t} = \alpha_2(t)\, r_2\, N_2 \left(1 - \frac{N_2^{\nu_2}}{K_2^{\nu_2}} - c_1 \frac{N_1^{\nu_1}}{K_2^{\nu_2}}\right), \quad N_2(0) = N_2^0, \tag{4.0.2}$$

where $N_1 > 0$ and $N_2 > 0$ are the densities of cell populations 1 and 2, respectively; $r_i > 0$ are the respective specific growth rates, $K_i > 0$ are the maximum densities and $\nu_i > 0$ are the deceleration parameters. The parameters $c_i > 0$ are the competition coefficients, and the adjustment functions, α_1, $\alpha_2 : [0, +\infty) \to (0, 1]$, which describe the fraction of the population that has adjusted to the new growth conditions by time t, may be chosen as constant functions or may be chosen to be the ones given by Baranyi and Roberts (see [66] and references therein) $\alpha_i(t) = q_{0,i}/(q_{0,i} + \mathrm{e}^{-m_i\, t})$, where $q_{0,i}$ characterizes the physiological states of the initial populations and m_i are the rates at which the physiological states adjust to the new growth conditions. As the aim of the present chapter is to introduce randomness in the foregoing model, for the sake of simplicity in this first stage, we shall assume that $\alpha_1(t) = \alpha_2(t) = 1$ for all $t \geq 0$.

In this chapter we present a procedure to quantify uncertainty in the Baranyi-Roberts model, with random parameters, and calibrated with real data. In particular, we apply classical *Donor Cell Upwind* (DCU) finite volume scheme [82, Ch. 20] to calculate the 1-PDF as the solution to the Liouville equation.

The 1-PDF is approximated by numerically solving the corresponding Liouville equation assuming that the initial conditions are random variables. The study is conducted using real test data taken from [66]. We will determine suitable parametric probability distributions for the random initial conditions by applying the PME (see Chapter 2). These distributional parameters, together with the other model parameters, will be calculated using a tailor-made procedure based on the application of an optimization algorithm named Particle Swarm Optimization (PSO) (see [83]). Afterward, we calculate predictions of the expectation of the aforementioned biological model at different time instants. These predictions are constructed thanks to the previous approximation of the 1-PDF of the solution.

This chapter is organized as follows. In Section 4.1, we investigate some interesting dynamic and asymptotic information about the Baranyi-Robters model, as well as the PDF of its solution. Afterward, in Section 4.2, we review the mathematical background of the PME and how it is applied to the present study. In Sections 4.3-4.5, we present the procedure and the numerical results obtained in our study. Finally, we draw our main conclusions as well as some remarks on future work in Section 4.6.

4.1 Model analysis

Despite the classical and well-studied nature of multi-species interaction systems, finding stability properties of (4.0.1)-(4.0.2) is not trivial by any means. We have been able to obtain an asymptotic stability result through system linearization. However, numerical simulations show that the unique interior equilibrium point for the system (4.0.1)-(4.0.2) is a globally asymptotically stable point, and its attraction region is the entire initial set $\mathcal{D} := [0, 1] \times [0, 1]$ except for the other 3 trivial equilibrium points (see Figures 4.1 and 4.2). In

particular,

$$0 = r_1 N_1 \left(1 - \frac{N_1^{\nu_1}}{K_1^{\nu_1}} - c_2 \frac{N_2^{\nu_2}}{K_1^{\nu_1}}\right), \tag{4.1.1}$$

$$0 = r_2 N_2 \left(1 - \frac{N_2^{\nu_2}}{K_2^{\nu_2}} - c_1 \frac{N_1^{\nu_1}}{K_2^{\nu_2}}\right) \tag{4.1.2}$$

has 3 trivial solutions, $(0,0)$, $(K_1,0)$ and $(0,K_2)$. But there is another one in the interior of $\mathcal{D}$, which can be found through a numerical root finder. Figures 4.1 and 4.2 show the vector field and how the parameters affect the dynamics of the system.

Let us analyze the asymptotic behavior of the Baranyi-Roberts system (4.0.1)-(4.0.2). Let $\mathbf{x}^\infty$ be its unique interior equilibrium point. Let the flow function $\mathbf{v} = (v_1, v_2) : \mathcal{D} \to \mathbb{R}^2$ be defined as

$$\mathbf{v}(x_1, x_2) = \begin{bmatrix} r_1\, x_1 \left(1 - \frac{x_1^{\nu_1}}{K_1^{\nu_1}} - c_2 \frac{x_2^{\nu_2}}{K_1^{\nu_1}}\right) \\ r_2\, x_2 \left(1 - \frac{x_2^{\nu_2}}{K_2^{\nu_2}} - c_1 \frac{x_1^{\nu_1}}{K_2^{\nu_2}}\right) \end{bmatrix} \tag{4.1.3}$$

whose differential matrix at $\mathbf{x}^\infty = (x_1^\infty, x_2^\infty)$ is

$$\mathrm{D}\mathbf{v}(\mathbf{x}^\infty) = \begin{bmatrix} -r_1\,\nu_1 \frac{(x_1^\infty)^{\nu_1}}{K_1^{\nu_1}} & -r_1\, c_2\, \nu_2 \frac{x_1^\infty (x_2^\infty)^{\nu_2 - 1}}{K_1^{\nu_1}} \\ -r_2\, c_1\, \nu_1 \frac{x_2^\infty (x_1^\infty)^{\nu_1 - 1}}{K_2^{\nu_2}} & -r_2\,\nu_2 \frac{(x_2^\infty)^{\nu_2}}{K_2^{\nu_2}} \end{bmatrix}. \tag{4.1.4}$$

Notice that, to calculate the matrix $\mathrm{D}\mathbf{v}(\mathbf{x}^\infty)$, we have first computed ∇v_1 and ∇v_2 at $\mathbf{x}^\infty$ and we have then applied the equilibrium condition given by Equations (4.1.1)-(4.1.2).

Lyapunov's indirect method [84, Sec. 3.3] consists in studying the asymptotic behavior of a system by analyzing the asymptotic behavior of its linearized counterpart. It is widely used when studying highly nonlinear systems where using Lyapunov functions may not be useful (see [84] and references therein). The result may be stated in our case as follows:

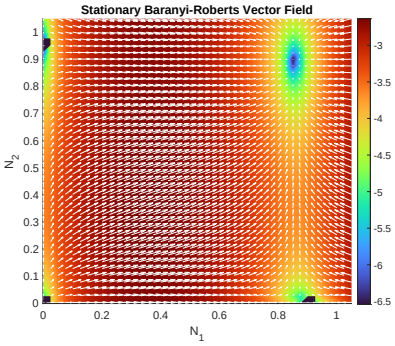

(**a**) Growth parameters: $r_1 = 0.82$, $r_2 = 0.55$. There is faster growth for N_1. Therefore, we can see a more horizontally aligned vector field.

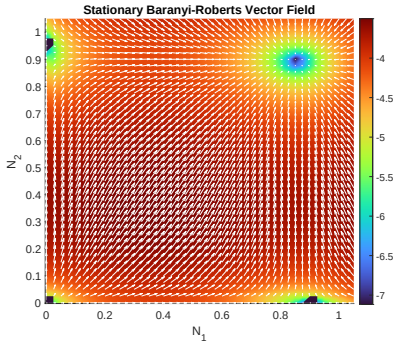

(**b**) Growth parameters: $r_1 = 0.2$, $r_2 = 0.55$. There is faster growth for N_2. Therefore, we can see a more vertically aligned vector field.

Figure 4.1: Comparison of the flow function $\mathbf{v}(\cdot)$ and its log-magnitude, $\log(\|\mathbf{v}(\cdot)\|_2)$, given by the Baranyi-Roberts system (4.0.1)-(4.0.2) with the set of parameters described in each figure, and $K_1 = 0.9$, $K_2 = 0.95$, $\nu_1 = 0.3$, $\nu_2 = 0.15$, $c_1 = 0.01$, $c_2 = 0.015$ in both figures. In darker color, the 4 equilibrium points given by the solutions of the nonlinear system (4.1.1)-(4.1.2).

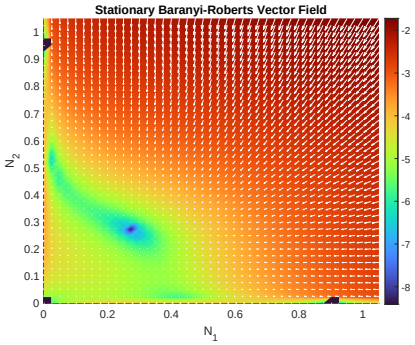

(**a**) Competition parameters: $c_1 = 0.25$, $c_2 = 0.35$. There is greater competition between N_1 and N_2. Therefore, the equilibrium is obtained closer to the origin than in the case of the previous Figure.

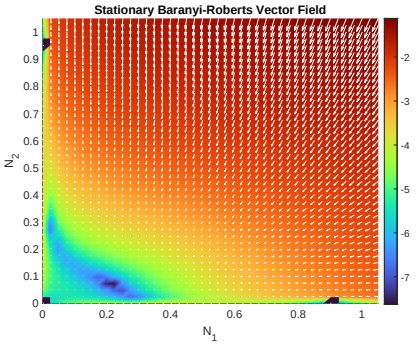

(**b**) Growth parameters: $c_1 = 0.5$, $c_2 = 0.5$. There is a very high competition between N_1 and N_2. Therefore, the equilibrium is obtained very close to the origin.

Figure 4.2: Comparison of the flow function $\mathbf{v}(\cdot)$ and its log-magnitude, $\log(\|\mathbf{v}(\cdot)\|_2)$, given by the Baranyi-Roberts system (4.0.1)-(4.0.2) with the set of parameters described in each figure, and $K_1 = 0.9$, $K_2 = 0.95$, $\nu_1 = 0.3$, $\nu_2 = 0.15$, $r_1 = 0.2$, $r_2 = 0.55$ in both figures. In darker color the 4 equilibrium points given by the solutions of the nonlinear system (4.1.1)-(4.1.2).

Theorem 4.1.1. *([84, Th. 3.7]). Let $\mathbf{x}^\infty$ be an equilibrium point for the nonlinear system*

$$\dot{\mathbf{x}} = \mathbf{v}(\mathbf{x}),$$

where $\mathbf{v} : \mathcal{D} \to \mathbb{R}^n$ and $\mathcal{D}$ is a neighborhood of the equilibrium point. Let

$$A = \mathrm{D}\mathbf{v}(\mathbf{x}^\infty).$$

Then, denoting $\Re$ as the real part of a complex number, the following statements are verified:

1. *The equilibrium point is stable if $\Re(\beta_i) < 0$ for all eigenvalues β_i of A.*
2. *The equilibrium point is unstable if $\Re(\beta_i) > 0$ for one or more of the eigenvalues of A.*

In our case, the eigenvalues for the matrix $\mathrm{D}\mathbf{v}(\mathbf{x}^\infty)$ can be obtained as

$$\beta = \frac{\mathrm{Tr}\,(\mathrm{D}\mathbf{v}(\mathbf{x}^\infty)) \pm \sqrt{(\mathrm{Tr}\,(\mathrm{D}\mathbf{v}(\mathbf{x}^\infty)))^2 - 4\,\mathrm{Det}(\mathrm{D}\mathbf{v}(\mathbf{x}^\infty))}}{2},$$

where Tr denotes the trace of the matrix, and Det denotes the determinant of the matrix. It can be easily seen, by using Equation (4.1.4), that $\mathrm{Tr}\,(\mathrm{D}\mathbf{v}(\mathbf{x}^\infty))$ is negative for any set of admissible parameters. However, we can prove that the determinant is positive only in certain cases. Indeed,

$$\begin{aligned}\mathrm{Det}(\mathrm{D}\mathbf{v}(\mathbf{x}^\infty)) &= r_1\, r_2\, \nu_1\, \nu_2 \frac{(x_1^\infty)^{\nu_1}(x_2^\infty)^{\nu_2}}{K_1^{\nu_1} K_2^{\nu_2}} - r_1\, r_2\, c_1\, c_2\, \nu_1\, \nu_2\, \frac{(x_1^\infty)^{\nu_1}(x_2^\infty)^{\nu_2}}{K_1^{\nu_1} K_2^{\nu_2}} \\ &= r_1\, r_2\, \nu_1\, \nu_2\, \frac{(x_1^\infty)^{\nu_1}(x_2^\infty)^{\nu_2}}{K_1^{\nu_1} K_2^{\nu_2}}(1 - c_1\, c_2).\end{aligned}$$

It is obvious that the determinant's sign will depend on the sign of $1 - c_1\, c_2$. Therefore, if $c_1\, c_2 < 1$, Theorem 4.1.1 assures that $\mathbf{x}^\infty$ is a stable equilibrium point. It can be checked that all the cases seen in Figures 4.1a-4.2b verify this last inequality (see the parameters' values in the captions).

The previous information about the asymptotic state of the Baranyi-Roberts system (4.0.1)-(4.0.2) also shows what happens in the random case. which we see and prove in the following result.

Lemma 4.1.2. *Let $U \subseteq \mathcal{D}$ be the local region of attraction of $\mathbf{x}^\infty$ given by Theorem 4.1.1*[1]*. Consider $\mathbf{X}_0 := (N_1^0, N_2^0)$ a random vector truncated in the system's domain $\mathcal{D}$ as defined previously. Assume, without loss of generality, $\int_U f_0(\mathbf{x})\mathrm{d}\mathbf{x} = 1$. Then the asymptotic state of $f(\cdot, t)$ will be the Dirac delta function centered at $\mathbf{x}^\infty$, $\delta_{\mathbf{x}^\infty}$ ([85, Less. 27]), in the sense of distributions.*

Proof. First, we know from Theorem 2.2.1

$$1 = \int_U f_0(\mathbf{x})\mathrm{d}\mathbf{x} = \mathbb{P}[\mathbf{X}_0^{-1}(U)] = \mathbb{P}[\{\omega \in \Omega : \mathbf{X}_0(\omega) \in U\}],$$

and, since U is a local region of attraction, we know that every curve starting inside U will converge asymptotically to $\delta_{\mathbf{x}^\infty}$. Let $\mathbf{X}(t, \omega) := \mathbf{X}(t, \mathbf{X}_0(\omega))$. Then

$$\mathbb{P}\left[\left\{\omega \in \Omega : \lim_{t\to+\infty} \mathbf{X}(t, \omega) = \mathbf{x}^\infty\right\}\right] = 1.$$

Now, using that almost sure convergence implies convergence in distribution and the *Portmanteau lemma*, we get (see [86]):

$$\mathbb{E}[\phi(\mathbf{X}(t, \cdot))] \xrightarrow[t\to+\infty]{} \mathbb{E}[\phi(\mathbf{x}^\infty)] \iff \int_\Omega \phi(\mathbf{X}(t, \omega))\mathrm{d}\mathbb{P}(\omega) \xrightarrow[t\to+\infty]{} \phi(\mathbf{x}^\infty). \tag{4.1.5}$$

for all bounded, continuous functions ϕ. Now, because the Baranyi-Roberts model in Eqs. (4.0.1) and (4.0.2) verifies the conditions of the Liouville equation Theorem Theorem 2.2.3, we know that $\mathbf{X}(t, \cdot)$ admits a PDF at every $t \geq t_0$. Therefore, Eq. (4.1.5) can be rewritten as:

$$\int_\Omega \phi(\mathbf{X}(t, \omega))\mathrm{d}\mathbb{P}(\omega) \xrightarrow[t\to+\infty]{} \phi(\mathbf{x}^\infty) \iff \int_U \phi(\mathbf{x}) f(\mathbf{x}, t)\mathrm{d}\mathbf{x} \xrightarrow[t\to+\infty]{} \int_U \phi(\mathbf{x})\delta_{\mathbf{x}^\infty}(\mathbf{x})\mathrm{d}\mathbf{x},$$

which proves convergence in the sense of distributions. □

[1] Numerical computations show that the interior equilibrium point is globally stable; we will not seek the exact attraction region. We will only use the fact that Theorem 4.1.1 guarantees the existence of an attraction region.

4.2 Assigning reliable probability distributions to the initial conditions

To assign reliable probabilistic distributions to a random variable, Y, we will use the PME as described in Chapter 2. Recall that the PME seeks for a PDF, f_Y, by maximizing the functional $S_Y(f)$ subject to the available information for the unknown random variable such as the domain $\mathcal{D}(Y)$, its integral is the unit ($m_0 = 1$), the mean m_1 and other available higher moments m_k, $k = 2, \ldots, K$. Using the closed-form solution for the density, we have the following problem:

$$\begin{aligned} &\text{for} && f_Y(y) = \exp\left\{-1 - \sum_{k=1}^{K} \lambda_k y^k\right\}, \quad y \in \mathcal{D}(Y), \\ &\text{minimizing} && \left|\int_{\mathcal{D}(Y)} y^k f_Y(y)\mathrm{d}y - m_k\right|, \qquad k = 0, 1, 2, \end{aligned}$$

where m_k are the k-order moments, among all possible Lagrange multipliers $(\lambda_0, \lambda_1, \lambda_2) \in \mathbb{R}^3$.

In our setting, the PME will be applied to assign a reliable density to the 2D sample data at time $t = 0$, i.e., the two-dimensional vector of initial conditions. According to the experimental procedure described at [66], cell densities grow in separate cultures before being introduced in the same culture. Therefore, it is logical to assume that the two initial random variables in system (4.0.1)-(4.0.2), which model the densities' time evolution in mixed culture, have statistically independent densities. Therefore, the joint PDF, represented by f_0 in the Liouville equation (2.2.2), can be expressed by $f_0(x_1, x_2) = f_{0,1}(x_1) f_{0,2}(x_2)$ for all $(x_1, x_2) \in \mathcal{D}$. In our application, we will determine both $f_{0,1}$ and $f_{0,2}$ by separately using the PME in each cell culture population.

4.3 Application to study microbial growth in a competitive environment

This section is devoted to applying the theoretical findings described above to study the growth of two microbial strains that compete for the same resources and space.

It is important to note that to measure the volumes and densities of microbial strains, electronic devices may have certain measurement errors. To account for this error, multiple measurements of the densities have been carried out (see [66, Sec. Materials and Methods] for more details). Table 4.1 collects the mean and the standard deviation of all volumetric density measurements for the two microbial strains (denoted by *Green Strain* and *Red Strain*) at different time instants.

Time (t_i) hours	Mean ($m_{1,i}$) *Green Strain*	St. Dev.($\sigma_{1,i}$) *Green Strain*	Mean ($m_{2,i}$) *Red Strain*	Std Dev.($\sigma_{2,i}$) *Red Strain*
$t_0 = 0$	0.2864	0.0088	0.2298	0.0054
$t_1 = 0.2325$	0.3078	0.0094	0.2456	0.0060
$t_2 = 0.46503$	0.3310	0.0100	0.2699	0.0058
$t_3 = 0.6975$	0.3544	0.0098	0.2982	0.0057
$t_4 = 1.014$	0.3827	0.0093	0.3276	0.0066

Table 4.1: Mean and variance of the optical densities (OD) at different time instants of the two *E. Coli* strains in mono-culture growth [66, Experiment B].

Using the Baranyi-Roberts dynamical system described in (4.0.1)-(4.0.2), we study how the *Green Strain* and *Red Strain* compete in the same culture medium. Since the objective of this chapter is to illustrate the applicability of the proposed method in a real scenario, we will assume that the data collected in Table 4.1 shows data from cells in a competitive mixed-culture, despite not being the case. As it can be observed in Table 4.1, our data has intrinsic uncertainty given by measurement errors (*epistemic uncertainty*), so it seems reasonable to consider a randomized model. To do so, some of the model parameters are treated as random variables instead of deterministic values.

In this chapter, we perform a first step in the spirit of introducing uncertainties in the Baranyi-Roberts model by considering that the initial conditions, N_1^0 and N_2^0, of the Initial Value Problem (IVP) (4.0.1)-(4.0.2) are independent random variables. They represent, respectively, the initial volumetric density of the *Green Strain* and *Red Strain*, which have been introduced in the culture medium. Then, taking into account the values of the means, $m_{1,i}$ and $m_{2,i}$ and of the standard deviations, $\sigma_{1,i}$ and $\sigma_{2,i}$, $i = 0, \ldots, 4$ (equivalently of the first and second moments) of N_1^0 and N_2^0 (see Table 4.1), we have applied the PME method to assign probability distributions, $f_{N_1^0}$ and $f_{N_2^0}$, to N_1^0 and N_2^0, respectively. This yields

$$f_{N_1^0}(x) = e^{-1-\lambda_0^{N_1^0}-\lambda_1^{N_1^0}x-\lambda_1^{N_1^0}x^2}, \quad x \in [0,1], \tag{4.3.1}$$

$$f_{N_2^0}(y) = e^{-1-\lambda_0^{N_2^0}-\lambda_1^{N_2^0}y-\lambda_1^{N_2^0}y^2}, \quad y \in [0,1], \tag{4.3.2}$$

where the values for the coefficients are given in Table 4.2. Therefore, the joint PDF, $f_0(x, y)$, of the initial condition of the Baranyi-Roberts system (4.0.1)-(4.0.2) is $f_0(x, y) = f_{N_1^0}(x) f_{N_2^0}(y)$.

$\lambda_0^{N_1^0}$	440.89	$(7.0067 \cdot 10^{-7})$	$\lambda_0^{N_2^0}$	471.01	$(1.6053 \cdot 10^{-6})$
$\lambda_1^{N_1^0}$	-3112.29	$(3.8798 \cdot 10^{-6})$	$\lambda_1^{N_2^0}$	-4142.74	$(2.0184 \cdot 10^{-7})$
$\lambda_2^{N_1^0}$	5434.25	$(1.6064 \cdot 10^{-5})$	$\lambda_2^{N_2^0}$	9014.1	$(2.8044 \cdot 10^{-5})$

Table 4.2: Lagrange multipliers and their respective errors for the PME problem. Error with respect to the mean and variance of the data, as described in Section 4.2, has been minimized using the `fsolve` built-in algorithm in MATLAB ®.

Now that the joint PDF of the initial conditions of IVP (4.0.1)-(4.0.2) has been determined, we can apply Theorem 2.2.3, which asserts that the solution of the PDE given in Eqs. (2.2.2) and (2.2.3) defines the 1-PDF of the solution stochastic process of the Baranyi-Roberts system. Unfortunately, a closed form of the solution of the Liouville PDE is not affordable in our case. So, we have used the *Donor Cell Upwind* DCU numerical scheme to approximate the solution of that PDE for every fixed time instant t. This numerical scheme is given by

$$f_{i,j}^{n+1} = f_{i,j}^{n} - \frac{\Delta t}{\Delta x}(v_1(x_i, y_j, t_n)^+ (f_{i,j}^{n} - f_{i-1,j}^{n}) + v_1(x_i, y_j, t_n)^- (f_{i+1,j}^{n} - f_{i,j}^{n})) \tag{4.3.3}$$

$$- \frac{\Delta t}{\Delta y}(v_2(x_i, y_j, t_n)^+ (f_{i,j}^{n} - f_{i,j-1}^{n}) + v_2(x_i, y_j, t_n)^- (f_{i,j+1}^{n} - f_{i,j}^{n})) \tag{4.3.4}$$

$$+ f_{i,j}^{n} \operatorname{Div}_{\mathbf{x}} \mathbf{v}(x_i, y_j, t_n), \tag{4.3.5}$$

where $\mathbf{x} = (x, y)$, $f_{i,j}^{n} = f(x_i, y_j, t_n)$, $u^+ = \max\{u, 0\}$ and $u^- := \min\{u, 0\}$. Stability and convergence properties of this numerical scheme are analyzed in [82, Chap. 20]. Most finite volume schemes developed for 2D hyperbolic PDEs are modified versions of the DCU, by adding *correction terms*, *flux limiters* and/or *reconstruction algorithms* in order to control the dissipation loss or possible instabilities from such a simple scheme and obtain very sharp and exact solutions in very few time-steps. The main advantage of the DCU scheme (4.3.3)-(4.3.5) is that it is very easily implemented and that it is very fast due to the fact that no extra terms are involved in the computation. The *Courant-Friedrichs-Lewy* (CFL) conditions are the space and time discretization size conditions used in every PDE numerical solver in order to assure stability and convergence of the numerical method to the true solution of the problem. In the particular case of the DCU scheme, the following CFL condition must be verified

$$\frac{\Delta t}{\Delta x} + \frac{\Delta t}{\Delta y} < 1,$$

where Δx, Δy and Δt refer to the size of the space meshing in the x-direction, the size of the meshing in the y-direction, and the time meshing, respectively. In our computations, we have chosen $\frac{\Delta t}{\Delta x} = \frac{\Delta t}{\Delta y} = 0.475$, and $\Delta x = \Delta y = 0.0067$. Once the numerical scheme to approximate the 1-PDF of the solution stochastic process of the Baranyi-Roberts model has been constructed, we will proceed to seek the model parameter values that best describe the data shown in Table 4.1. As indicated in the Introduction section, this has been done by applying an optimization technique called PSO. In the next section, we explain the procedure.

4.4 Computational procedure design

The PSO is a bioinspired optimization method since it operates using similar rules as the behavior of swarms of birds that try to explore and exploit a certain region to find food (see [83]). The PSO algorithm basically generates a family of possible solutions (swarm of birds) in the given parametrical search space so that it evolves over every iteration to minimize the Fitness Function (FF). In our context, we apply PSO algorithm only to determine growth parameters r_1 and r_2, while the rest of model parameters (K_1, K_2, v_1, v_2, c_1 and c_2) have been taken from [66] (see Table 4.3).

For a given pair of growth parameters r_1 and r_2, the FF is defined by the following steps:

Step 1: Compute a discrete approximation of the 1-PDF at the time instants $t_n \in \mathcal{T} = \{0, 0.2325, 0.4652, 0.6975, 1.0014\}$, (in hours) by numerically solving the Liouville-Gibbs PDE, in the region $(0,1) \times (0,1)$, using the DCU scheme (4.3.3)-(4.3.5). We take the joint PDF given by the product of (4.3.1) and (4.3.2), with the parameters in Table 4.2, as the initial condition. We also consider null Neumann boundary conditions and the meshing parameters seen at the end of the previous section. This step gives a set of discrete values for each time instant $\{f^n_{i,j}\}_{i,j,n}$. We use the notation of (4.3.3)-(4.3.5).

Step 2: Compute the means at each time instant, $\mathbb{E}[N_1(t_n)]$ and $\mathbb{E}[N_2(t_n)]$, using the values of $\{f^n_{i,j}\}_{i,j}$ and the *composite 1/3 Simpson's rule* (see [87, Chap. 25]) in each integration dimension.

Step 3: Once the means for $t_n \in \mathcal{T}$ have been computed, that is $\mathbb{E}[N_1(t_n)]$ and $\mathbb{E}[N_2(t_n)]$, we obtain the total error, denoted by FF, where each summand is the relative error between the aforementioned means and the sample data, $m_{1,i}$ and $m_{2,i}$, shown in Table 4.1,

$$FF = \sum_{i=0}^{4} e_i, \tag{4.4.1}$$

where

$$e_i = \frac{Err(t_i)}{\|(m_{1,i}, m_{2,i})\|_2} \text{ and } Err(t_i) = \|(\mathbb{E}[N_1(t_i)], \mathbb{E}[N_2(t_i)]) - (m_{1,i}, m_{2,i})\|_2. \tag{4.4.2}$$

Once the fitness function FF has been defined, we apply the PSO algorithm to seek suitable growth parameters r_1 and r_2 minimizing it.

4.5 Results

This section is aimed at showing the results obtained by implementing the procedure described in the previous section.

We recall that the objective is to find the optimal values of r_1 and r_2 so that the mean of the PDF given by the numerical scheme and the empirical mean of the data are as close as possible. To do so, we have used the built-in MATLAB function `particleswarm` to minimize FF, defined through the 3 steps described in Section 4.4.

In order to avoid the effect of randomness coming from generating the initial positions of the particles in the PSO algorithm, multiple different procedures have been executed at the same time. The obtained results are close enough to guarantee we can neglect the above-mentioned effect of randomness.

	K_i	r_i	ν_i	c_i
Green Strain ($i = 1$)	0.6280	0.5382	1.4610	0.2
Red Strain ($i = 2$)	0.6190	0.5113	2.4840	0.25

Table 4.3: Parameters for the Baranyi-Roberts system after performing the optimization procedure. Note that we have only determined the growth parameters r_1 and r_2 while the other have been taken from [66, Experiment B].

The procedure with the best results takes over 7 hours to reach a suitable minimum for the FF. The procedure has been carried out on an Ubuntu 16.04.7 LTS-based computer with a quad-core, 16-thread Intel Xeon E5-4620

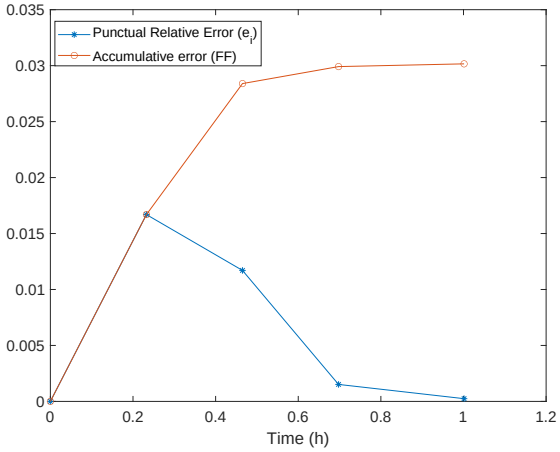

Figure 4.3: Punctual and accumulative errors e_i and FF defined by (4.4.2) and (4.4.1), respectively.

processor with 512 GB of RAM. The values of the optimized parameters, r_1 and r_2, are shown in Table 4.3.

Figure 4.3 shows the punctual and accumulative errors given, respectively, by e_i and FF defined in expressions (4.4.2) and (4.4.1), at the time instants $t \in \mathcal{T} = \{0, 0.2325, 0.4652, 0.6975, 1.014\}$, measured in hours. We observe the relative error decreases as time goes on. Figures 4.4 and 4.5 show the vector field for the parameters in Table 4.3. In Figures 4.6a and 4.6b we have performed a graphical comparison between the sampled data and the approximation obtained by our stochastic model for both Green and Red Strains. From both plots we observe a very good fitting. Furthermore, we can see the time evolution of the joint PDF of the solution stochastic process in Figures 4.7a-4.7e. However, as it can be seen in Figures 4.7a-4.7e, the maximum height of the joint PDF decreases very rapidly (observe the magnitude of the lateral

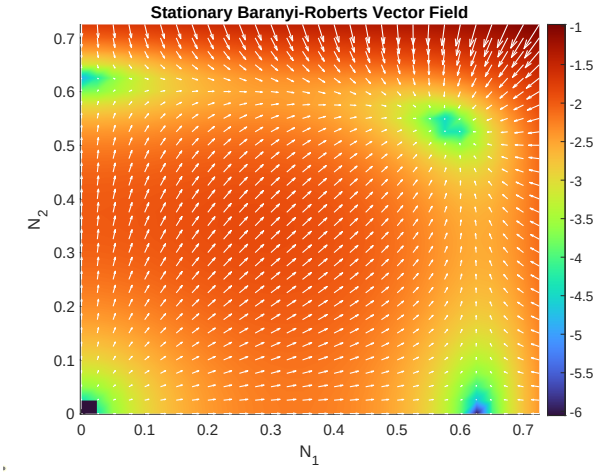

Figure 4.4: Flow function, $\mathbf{v}(\cdot)$, and its log-magnitude, $\log(\|\mathbf{v}(\cdot)\|_2)$, given by the Baranyi-Roberts system (4.0.1)-(4.0.2) and the optimized parameters in Table 4.3. In darker color, the 4 equilibrium points given by the solutions of the nonlinear system (4.1.1)-(4.1.2).

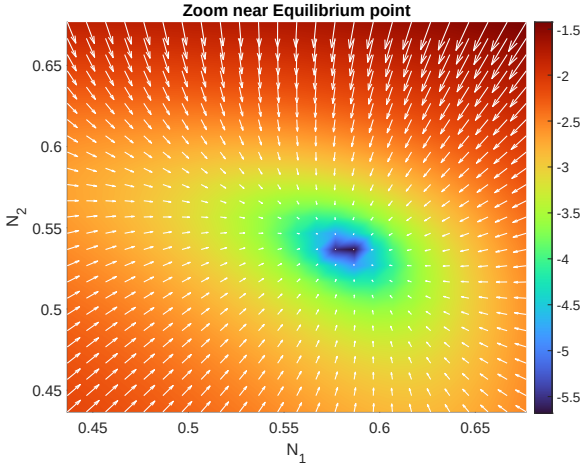

Figure 4.5: Zoomed-up view of Figure 4.4 in a neighborhood of the interior equilibrium point $\mathbf{x}^{\infty} = (0.5820, 0.5366)$. We can see how it clearly attracts all the points surrounding the equilibrium point.

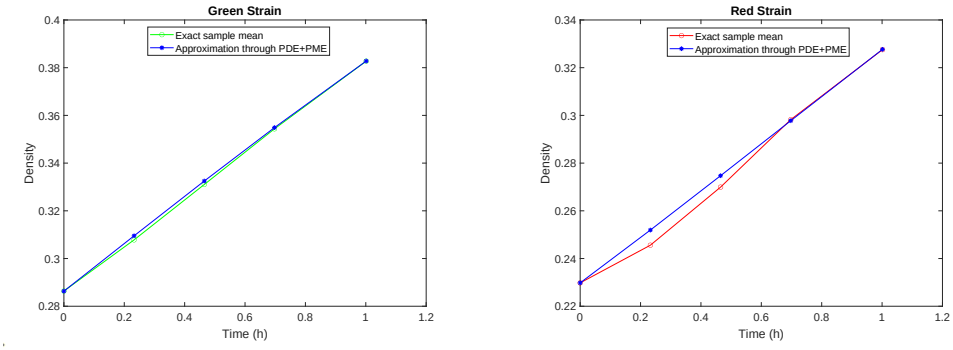

(**a**) Green Strain comparison

(**b**) Red Strain comparison.

Figure 4.6: Visual comparison of the sample mean of each Strain data set from Table 4.1 with the mean computed by procedure described in Section 4.4.

colored bar), which means that the variance of the solution increases from diffusion, probably due to the DCU numerical scheme's nature.

Predicting or extrapolating the dynamics of complex and highly parameterizable systems with randomness is a very difficult task. In our model setting, and after the previous validation process, we are interested in predicting the volumetric density of both strains of bacteria since such future projections allow us to control the biological culture. In Figures 4.8a and 4.8b, we show the predictions for Green and Red Strains over the time instants $t_6 = 1.234$, $t_7 = 1.466$, $t_8 = 1.839$ and $t_9 = 2.0716$ hours. Comparing these figures with the ones collected in [66, Experiment B], we observe the stochastic model is able to capture the dynamics of volumetric density for the two strains of bacteria. This result has been obtained by only considering randomness in the initial conditions and adjusting the model parameters r_1 and r_2.

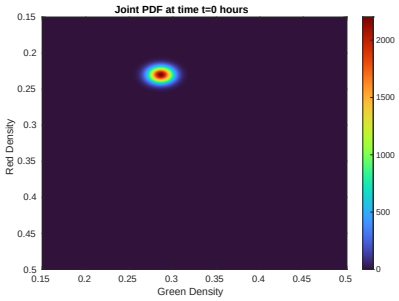

(**a**) Initial time: 0 hours. This function is the one obtained by the PME, as described in Section 4.2.

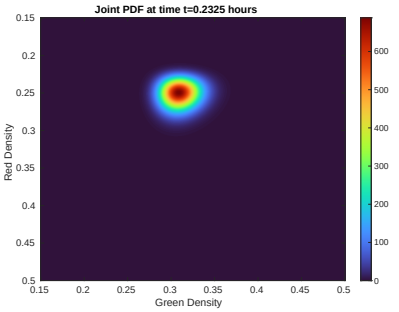

(**b**) Second time instant: nearly 14 minutes elapsed.

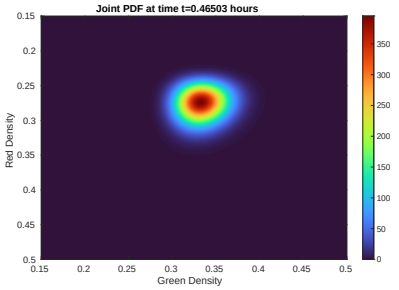

(**c**) Third time instant: nearly 28 minutes elapsed.

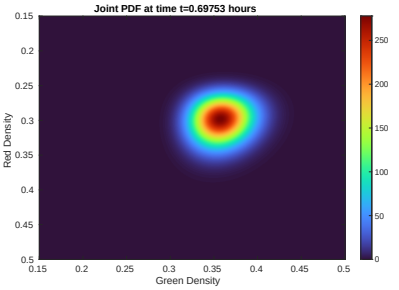

(**d**) Fourth time instant: nearly 42 minutes elapsed.

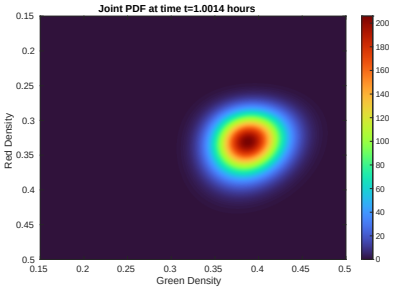

(**e**) Fifth time instant: over 1 hour elapsed.

Figure 4.7: Joint 1-PDF evolution of the solution stochastic process in every time instant given by data from Table 4.1. It can be seen how variance, which is reflected by the width/height ratio, grows. Take into account that the color bar is not fixed and, therefore, it re-scales itself at every time instant.

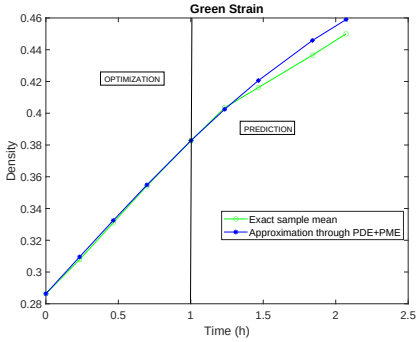

(**a**) Mean path of the solution stochastic process for the green strain.

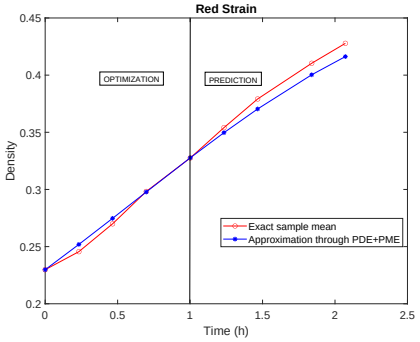

(**b**) Mean path of the solution stochastic process for the red strain.

Figure 4.8: Optimization, as computed in Section 4.4, and prediction of the mean paths of the solution stochastic process. The available data spans over 2 hours of measurements.

4.6 Conclusion

In this chapter, a procedure to quantify uncertainty in random dynamical systems has been defined and applied to a biological model. Specifically, we have used the classical Liouville equation, whose solution at every instant has been obtained using a finite volume numerical scheme. Using real data from experiments performed in the literature and the Principle of Maximum Entropy, we have assigned a reliable probability density to the initial condition of the dynamical system. We have successfully optimized two key model parameters, representing the growth rates of both types of strains of bacteria so that the mean of the solution stochastic process is as close as possible to the real sample mean. The optimal values were obtained using the Particle Swarm Optimization algorithm.

Publications

The results presented in this thesis chapter have been published in [57]. Regarding this chapter, the PhD candidate has contributed by working on its complete development with more emphasis on the theoretical results and preparing the visualization of the numerical examples.

Chapter 5

A GPU-accelerated Lagrangian particle method for solving the Liouville equation

Motivated by the insights from the attempt to devise an efficient Liouville solver described in the previous chapter, we now present and analyze a numerical approach to efficiently solve the Liouville equation in the context of RDEs using GPU computing. Our method combines wavelet compression-based adaptive mesh refinement, Lagrangian particle methods, and radial basis function interpolation to create a versatile algorithm applicable to multiple dimensions. We discuss the advantages and limitations of this algorithm. To demonstrate its effectiveness, we compute the probability density function for some 2D and 3D random ODE systems with applications in physics and epidemiology.

5.1 Introduction

In Chapter 4, we applied a classical numerical method, an FVM approach, to study the evolution of the PDF associated to a two-dimensional RDE system. This example showed the main advantage of the Liouville equation over other methods discussed in Chapter 2: the possibility to use deterministic numerical methods to quantify the system's uncertainty evolution via its PDF. However, it also showed two limitations that we aim to overcome in this chapter.

The first limitation is widely known in computational physics: grid-based methods, such as finite difference, finite volume or finite element methods, introduce artificial diffusion in convection-dominated problems (where there is a relatively weak diffusion effect in the system). Another limiting factor is that every degree of freedom in a physical system, that is, every equation in an RDE system, translates into a spatial dimension of the Liouville equation. Considering the computational cost and memory requirements needed to solve PDEs in dimensions higher than 2 with standard grid-based methods, it is understandable that the use of the equation was reduced only to the theoretical or academic realm.

However, computer science has taken huge leaps in performance in the last decades, especially since General Purpose Graphical Processing Units (GPGPUs, or simply GPUs) have become available for scientific simulation. Indeed, GPU-based simulation has become a standard practice in fields such as machine learning, computational physics, and meteorology, where simulations can take a huge advantage of their highly parallel architecture and energy efficiency. Because of the special nature of the Liouville equation, which will be exploited throughout the current chapter, GPU-based solvers can become a powerful ally for the efficient use of the Liouville equation in realistic scenarios, reducing computation times from hours to a few minutes or even seconds.

This chapter is structured as follows: In Section 5.2, we provide a mathematical discussion of the methods used to design an efficient GPU-based Liouville equation numerical solver. In Section 5.3, we discuss the details of the computational setup of each mathematical tool described in Section 5.2. Finally, in

Section 5.4, we demonstrate the applicability of our Liouville equation numerical solver by applying it to several relevant mathematical models formulated with random differential equations.

Remark 5.1.1. *Throughout this chapter, we will use a different notation, for clarity. The PDF and the general RDE system will be referred to as*

$$\rho_t := \rho(t,\cdot) = \rho_{\mathbf{X}(t)}(t,\cdot), \quad \mathbf{v}_t := \mathbf{v}(t,\cdot),$$

respectively. Unless specified, we assume both are defined in the RDE system's positively invariant set $\mathcal{D}$.

5.2 Methods

In this section, we discuss the mathematical basis used in the design of our Liouville numerical solver, which is based on 3 main techniques: (1) adaptive mesh refinement, (2) Radial Basis Function (RBF) interpolation and remeshing, (3) Lagrangian particles and characteristic curves. The first two techniques are discussed in a general setting; in the third subsection, we will also show how we combine all techniques to form our solver.

5.2.1 Adaptive mesh refinement

The evolution of the PDF of an RDE's solution can undergo large changes in its variance throughout the simulation. For example, it may start as a very narrow function because there is little uncertainty at the system's initial state. Likewise, the asymptotic state of the system may be deterministic, so the PDF will converge to a Dirac delta. Evolving the PDF with enough resolution to capture those low-variance situations will allow for better accuracy but at a prohibitive computational cost. In contrast, a lower resolution will give a faster simulation but lower accuracy, especially in low-variance cases.

Adaptive Mesh Refinement (AMR) delivers the best of both worlds: it allows to evolve in greater detail only where needed while keeping the global computational cost as low as possible for faster simulation and lower computational

memory requirements. There are many possibilities to perform AMR (patch, block, structured, unstructured, Cartesian, etc. see [88]), but they share the same philosophy: setting a finer grid where the gradient of the solution is larger. One possible way to do this, which we have chosen, is the Wavelet-compression-based AMR in a Cartesian grid [89]. This AMR approach method allows for a fast, easily parallelizable, and memory-efficient technique for the use cases of the numerical procedure described in this chapter.

Wavelet transforms are widely used in audio, image, and video compression [90, 91]. Mathematically, the wavelet transform allows representing square-integrable functions with an orthonormal L^2 basis, whose spanned space form a set of nested orthogonal spaces:

$$\mathrm{L}^2(\mathbb{R}) = V_{L_0} \oplus W_{L_0} \oplus \ldots \oplus W_L, \quad W_l \subset W_{l+1},$$

where V_{L_0} is the *approximation* space at level L_0, whose base we denote by f^{L_0}, and the collection of nested subspaces $\{W_l\}_{l=L_0}^{L}$ are the detail spaces. Each W_l is generated by dilation and translation of a wavelet function g; that is

$$g_k^l(x) = 2^{l/2}\, g(2^l x - k), \quad \forall x \in \mathbb{R}, \tag{5.2.1}$$

and $\{g_k^l\}_j$ form an $\mathrm{L}^2(\mathbb{R})$-orthonormal basis of W_l.

When applied to AMR, some remarks must be made. In one dimension, we have one grid point associated with the wavelet function (detail coefficient) and one with the scaling function (approximation coefficient), which will become the detail coefficient at the next coarser level. In higher dimensions, we will have $2^d - 1$ grid points associated with detail coefficients and one with the approximation coefficient. At the next coarser level, $2^d - 1$ points associated with approximation coefficients will be associated with detail coefficients. Therefore, we will refer to *detail points at level l* when referring to points associated with a detail coefficient at the refinement level l. We use the tensor product of one-dimensional wavelets to handle the multidimensional case.

We can now write out the wavelet compression refinement procedure rigorously. Let $u : \mathbb{R}^d \to \mathbb{R}$ be the function to be compressed. Let $\{u_i := u(\mathbf{x}^i)\}_{i=1}^{2^{dL}}$

be a vector comprised of the finest discretization of u at level L; that is, u evaluated at the equispaced grid $\mathcal{G} := \{\mathbf{x}^i\}_{i=1}^{2^{dL}}$. Then, we can represent each point as:

$$u_i = \sum_{k=1}^{2^{dL_0}} a_k f_k^{L_0}(\mathbf{x}^i) + \sum_{l=L_0+1}^{L} \sum_{k=1}^{2^{dl}} \sum_{\mu=1}^{2^d-1} d_k^{l,\mu} g_k^{l,\mu}(\mathbf{x}^i). \tag{5.2.2}$$

We will only advect the particles where the corresponding detail coefficient is above a pre-established threshold $\varepsilon > 0$; that is, we will obtain the characteristic curves defined by the solution to (5.2.9) at all points in $\mathcal{G}_A := \bigcup_{l=L_0+1}^{L} \mathcal{G}_l$, where

$$\mathcal{G}_l := \{\mathbf{x}^i \in \mathcal{G} \,:\, \mathbf{x}^i \in \mathrm{supp}(g_k^{l,\mu}), \quad |d_k^{l,\mu}| \geq \varepsilon, \quad k = 1, \ldots, 2^{dl},\, \mu = 1, \ldots, 2^d - 1\}.$$

Fig. 5.1 shows the scheme of a wavelet cube in 3D; however, we can also see the structure in lower dimensions. In 1D, the wavelet transform would consist of the vertices $\{a_k, d_k^{l,1}\}$. In 2D, the wavelet transform would have $\{a_k, d_k^{l,1}, d_k^{l,2}, d_k^{l,3}\}$. Note that the nodes that form a certain refinement level are every other node from the previous, finer level. The nodes that do not pass to the next refinement level are associated with detail coefficients; that is, the nodes that belong to $\mathcal{G}_l$ are a subset of those not considered in the following coarser level.

5.2.2 RBF interpolation and remeshing

One of the main strengths of Lagrangian methods is that they are meshless methods; particles are not explicitly required to be set on a grid. However, as explained in [92, 93], it is advisable to use an underlying mesh because it can greatly improve the simulation's quality. This implies performing "scattered" data interpolation because of the irregular particle spatial distribution after the AMR step. Many kinds of interpolation techniques exist for scattered data in multiple dimensions; we have based our interpolation procedure on Wendland's Compactly Supported Radial Basis Functions (CS-RBF, see [94, 95] for the definition and some comments on the advantages of this approach).

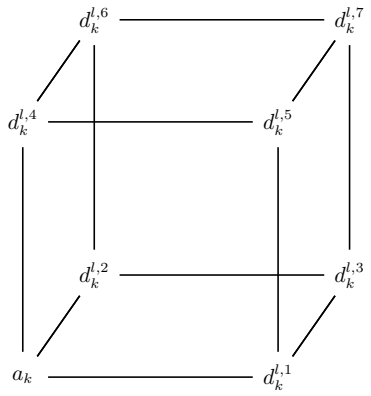

Figure 5.1: Illustrative scheme on the location of approximation/detail coefficients for a 3D wavelet transform. Compare with Eq. (5.2.2).

Let $\mathcal{X} := \{\mathbf{x}^i\}_{i=1}^N \subset \mathcal{D} \subseteq \mathbb{R}^d$ be a set of points and $\mathbf{u} = (u_i := u(\mathbf{x}^i))_{i=1}^N$ the values of a given function $u : \mathcal{D} \to \mathbb{R}$ at the aforementioned locations. CS-RBF interpolation consists of a function $s_{u,\mathcal{X}}$ defined by the linear combination of a compactly supported, radially symmetric kernel, which we denote $\sigma : [0,\infty) \to [0,\infty)$, centered at each particle location $\mathbf{x}^i$, and a set of weights $\Lambda = (\lambda_1, \ldots, \lambda_N)$ such that

$$u(\mathbf{x}) \simeq s_{u,\mathcal{X}}(\mathbf{x}) := \sum_{k=1}^{N} \sigma\left(\frac{\|\mathbf{x} - \mathbf{x}^k\|}{r}\right) \lambda_k = \sigma(\mathbf{x})\Lambda, \tag{5.2.3}$$

where r is the support radius of the RBF kernel and

$$s_{u,\mathcal{X}}(\mathbf{x}^i) = \sigma(\mathbf{x}^i)\Lambda = u_i, \quad \forall\, i = 1, \ldots, N.$$

In matrix terms, this last condition amounts to solving the following linear system

$$\begin{bmatrix} \sigma(\mathbf{x}^1) \\ \sigma(\mathbf{x}^2) \\ \vdots \\ \sigma(\mathbf{x}^N) \end{bmatrix} \Lambda = \underbrace{\begin{bmatrix} \sigma\left(\frac{\|\mathbf{x}^1-\mathbf{x}^1\|}{r}\right) & \sigma\left(\frac{\|\mathbf{x}^1-\mathbf{x}^2\|}{r}\right) & \dots & \sigma\left(\frac{\|\mathbf{x}^1-\mathbf{x}^N\|}{r}\right) \\ \sigma\left(\frac{\|\mathbf{x}^2-\mathbf{x}^1\|}{r}\right) & \sigma\left(\frac{\|\mathbf{x}^2-\mathbf{x}^2\|}{r}\right) & \dots & \sigma\left(\frac{\|\mathbf{x}^2-\mathbf{x}^N\|}{r}\right) \\ \vdots & \vdots & \ddots & \vdots \\ \sigma\left(\frac{\|\mathbf{x}^N-\mathbf{x}^1\|}{r}\right) & \sigma\left(\frac{\|\mathbf{x}^N-\mathbf{x}^2\|}{r}\right) & \dots & \sigma\left(\frac{\|\mathbf{x}^N-\mathbf{x}^N\|}{r}\right) \end{bmatrix}}_{=:A_\sigma} \begin{bmatrix} \lambda_1 \\ \lambda_2 \\ \vdots \\ \lambda_N \end{bmatrix} = \begin{bmatrix} u_1 \\ u_2 \\ \vdots \\ u_N \end{bmatrix}. \tag{5.2.4}$$

This matrix has very desirable properties for our purposes. For example, it is symmetric. Also, using any of the functions defined in Iske [94, Table 3.2] returns a positive definite interpolation matrix, guaranteeing that the interpolation problem is well-posed and allowing the use of efficient iterative methods such as the conjugate gradient method. Furthermore, since the RBF kernels are compactly supported, the interpolation matrix will be sparse, which will be helpful when the number of particles is large.

Despite the versatility of this kind of interpolation scheme in a high-dimensional space, there are some drawbacks. The main issue is that the kernel support radius r must be chosen *a priori*. Specifically, the condition number of the interpolation matrix and its error are given by the following relations (see [96]):

$$\operatorname{cond}_2(A_\sigma) \leq C q_{\mathcal{X}}^{-d-2k-1}, \quad q_{\mathcal{X}} := \min\{\|\mathbf{x}^i - \mathbf{x}^j\|_2 \,:\, i \neq j\}, \tag{5.2.5}$$

$$\|u - s_{u,\mathcal{X}}\|_{\mathrm{L}^\infty(\mathcal{D})} \leq C(u)\eta^{k+1/2}, \quad \eta = \sup\left\{\min_{i\in\{1,\dots,N\}} \|\mathbf{x} - \mathbf{x}^i\| \,:\, \mathbf{x} \in \mathcal{D}\right\}, \tag{5.2.6}$$

d denotes the spatial dimension, and k is related to the smoothness of the interpolation kernel. Also, η, which is the *covering density* of the points with respect to the domain $\mathcal{D}$. On the one hand, the accuracy bound (5.2.6) is determined by the covering density of the points in space; obviously, more points covering the domain will result in a more accurate interpolation. On the other hand, the matrix condition relation (5.2.5) shows that particles being

very close to each other, will negatively affect the condition of the interpolation matrix, resulting in numerical instabilities and deteriorated convergence.

A crucial goal for our purposes is to have a fast and accurate interpolation scheme, which means trying to find a balance between the matrix condition number and the interpolation accuracy. Therefore, we must balance the number (and closeness) of RBFs and their support radius. Choosing a small radius will help in iteration speed when solving the linear system (5.2.4); in this case, any given particle affects a small number of neighboring particles. Unfortunately, having a small radius could result in a *bed-of-nails interpolant* (see Fig. 5.2). Contrarily, a very big radius will negatively affect iteration speed and matrix condition number (see also [97, Pg. 6]). Although there is no definite choice of optimal RBF radius, taking $\sim 5h$ as a starting RBF radius is recommended, subject to further adjustments (see [94]).

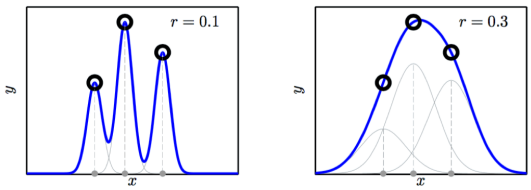

Figure 5.2: RBF interpolation in two cases: (left) small radius, also called *bed-of-nails interpolant* and (right) large radius. Image taken from [98].

RBFs can also be very useful for remeshing a function whose values are known at scattered points in a domain. Indeed, if we know the RBF weights of such a function (Λ in (5.2.3)), we can represent a function at a grid (regular or not). One must find the distance between the grid nodes, denoted by $\{\mathbf{x}^i_{\text{Grid}}\}_{i=1}^{NG}$, and the advected particles and multiply the *interpolation* matrix with the weight

vector Λ. Mathematically,

$$\begin{bmatrix} \sigma\left(\frac{\|\mathbf{x}^1_{\text{Grid}}-\mathbf{x}^1\|}{r}\right) & \sigma\left(\frac{\|\mathbf{x}^1_{\text{Grid}}-\mathbf{x}^2\|}{r}\right) & \dots & \sigma\left(\frac{\|\mathbf{x}^1_{\text{Grid}}-\mathbf{x}^N\|}{r}\right) \\ \sigma\left(\frac{\|\mathbf{x}^2_{\text{Grid}}-\mathbf{x}^1\|}{r}\right) & \sigma\left(\frac{\|\mathbf{x}^2_{\text{Grid}}-\mathbf{x}^2\|}{r}\right) & \dots & \sigma\left(\frac{\|\mathbf{x}^2_{\text{Grid}}-\mathbf{x}^N\|}{r}\right) \\ \vdots & \vdots & \ddots & \vdots \\ \sigma\left(\frac{\|\mathbf{x}^{NG}_{\text{Grid}}-\mathbf{x}^1\|}{r}\right) & \sigma\left(\frac{\|\mathbf{x}^{NG}_{\text{Grid}}-\mathbf{x}^2\|}{r}\right) & \dots & \sigma\left(\frac{\|\mathbf{x}^{NG}_{\text{Grid}}-\mathbf{x}^N\|}{r}\right) \end{bmatrix} \begin{bmatrix} \lambda_1^* \\ \lambda_2^* \\ \vdots \\ \lambda_N^* \end{bmatrix} = \begin{bmatrix} u_1 \\ u_2 \\ \vdots \\ u_{NG} \end{bmatrix}, \tag{5.2.7}$$

where NG denotes the number of nodes at the underlying regular grid.

5.2.3 Lagrangian methods and characteristic curves

Lagrangian methods refer to a family of numerical methods for solving PDEs that consider the solution field as a family of particles evolved through time in an invariant domain of the ODE, which corresponds to the spatial domain of the PDE [99]. The equations that govern the evolution of each particle are known as *characteristic equations*, and their solutions are called *characteristic curves* [47, Sec. 3.2]. Lagrangian methods focus on each particle's position and its value rather than the information that a given position in space may give of the solution, which is the nature of so-called *Eulerian* methods [100, 101]. We now list some pros of the characteristic equation approach:

- Particle methods do not add artificial numerical dissipation (see [57, 102, 103]).
- They are easily parallelizable, computationally speaking.
- Contrarily to grid-based methods such as Finite Differences, Finite Volumes, and Finite Elements, particle methods do not have a grid-size-forced CFL time step limit. This allows performing simulations with a lower number of time-steps, thus reducing the time needed for simulation and the computational burden. Instead, the time step limitation is determined by the accuracy of the numerical integrator used to obtain the characteristic curves and the interpolation scheme used to re-mesh particles onto the underlying grid. For example, for RBF interpolation, the limitation is set by the property that the basis functions should overlap (see [89, 104]). For example, if the dynamics are very complex or

separate particles rapidly, we will have to re-interpolate more frequently, thus limiting the time step used for the numerical integrator.

- The spatial dimension does not explicitly determine the computational complexity of the particle approach; instead, it is given by the number of particles and the re-interpolation step, (although the interpolation step does depend on the phase space dimension, there are efficient interpolation schemes, such as RBFs).

Now, let us detail what was first exposed in Chapter 2 about the characteristic curves and characteristic equations. Mathematically, if we denote the characteristic curve at time t, starting at $(t_0, \mathbf{x}^0)$ by $\Phi(t) := \Phi(t\,;\, t_0, \mathbf{x}^0)$, then Lagrangian methods study the dynamic behavior of $\rho_t(\Phi(t))$. If we take the time derivative of the composed function, the chain rule gives

$$\frac{\mathrm{d}}{\mathrm{d}t}\rho_t(\Phi(t)) = \partial_t\rho_t(\Phi(t)) + \nabla_{\mathbf{x}}\rho_t(\Phi(t)) \cdot \frac{\mathrm{d}\Phi}{\mathrm{d}t}(t) = L(t, \mathbf{x}, \rho_t, \ldots), \tag{5.2.8}$$

where the terms $\frac{\mathrm{d}\Phi}{\mathrm{d}t}(t)$ and L will vary depending on the specific problem. Some well-known examples are the Boltzmann, Navier-Stokes equations and other general conservation laws. Equation (5.2.8) shows that the Lagrangian approach transforms a PDE into a family of systems of ODEs. Comparing the Liouville equation (2.2.3), and (5.2.8), we can identify the corresponding terms, yielding the following system of characteristic equations:

$$\begin{aligned}
\frac{\mathrm{d}}{\mathrm{d}t}\phi_1(t) &= (\mathrm{v}_1)_t(\Phi(t)), \quad \phi_1(0) = \mathrm{x}_1^0, \\
&\vdots \\
\frac{\mathrm{d}}{\mathrm{d}t}\phi_d(t) &= (\mathrm{v}_d)_t(\Phi(t)), \quad \phi_d(0) = \mathrm{x}_d^0, \\
\frac{\mathrm{d}}{\mathrm{d}t}\rho_t(\Phi(t)) &= -\rho_t(\Phi(t))\nabla_{\mathbf{x}} \cdot \mathbf{v}_t(\Phi(t)), \quad \rho_0(\Phi(0)) = f_0(\Phi^0),
\end{aligned} \tag{5.2.9}$$

where $\mathbf{x}^0 = (x_1^0, \ldots, x_d^0)$ is a point in $\mathcal{D}$, which represents the initial position of the particle to be simulated and $\mathbf{v}_t = ((\mathrm{v}_1)_t, \ldots, (\mathrm{v}_d)_t)$ is the vector field from (2.2.3). Accordingly, the first d equations define the time evolution of

the particle, whereas the last equation in (5.2.9) defines the evolution of the PDF value of the considered particle.

This system of ODEs is easily solvable by numerical methods such as the well-known 4th order Runge Kutta integrator [105]. However, note that we can solve the last equation exactly:

$$\rho_t(\Phi(t\,;\,t_0,\,\mathbf{x}^0)) = \rho_0(\mathbf{x}^0)\exp\left(-\int_{t_0}^{t}\nabla_{\mathbf{x}}\cdot\mathbf{v}_s(\Phi(s;\mathbf{x}^0))\mathrm{d}s\right). \tag{5.2.10}$$

And in terms of the *inverse flow* function Ψ[1] we may rewrite (5.2.10) as

$$\rho_t(\mathbf{x}) = \rho_0(\Psi(t\,;\mathbf{x}))\exp\left(-\int_{t_0}^{t}\nabla_{\mathbf{x}}\cdot\mathbf{v}_s(\Phi(s\,;\,\Psi(t\,;\mathbf{x})))\mathrm{d}s\right). \tag{5.2.11}$$

The Liouville Equation (2.2.3) is a quasi-linear PDE, which means that the superposition principle applies: if every element of a family of functions approximates the Liouville equation, then any finite linear combination of these functions will also approximate the equation. Let us consider a set of N particles $\{\mathbf{x}^k\}_{k=1}^N$, also $r>0$, and let us represent the PDF we search for in the following way:

$$\rho_t(\mathbf{x}) \simeq \sum_{k=1}^{N}\underbrace{\lambda_t^k\sigma\left(\frac{\|\mathbf{x}-\Phi(t;\mathbf{x}^k)\|}{r}\right)}_{\zeta_t^k(\mathbf{x})} =: s_t^N(\mathbf{x}). \tag{5.2.12}$$

Clearly, the ζ_t^k functions do not satisfy the Liouville equation in general (in fact, only when $\nabla_{\mathbf{x}}\cdot\mathbf{v}_t$ is constant). From (5.2.10), we have that ζ_t^k satisfies

[1] Recall from Chapter 2 that this a differentiable function such that: $\Psi(t_0)=\Phi(t)=\mathbf{x}$ and $\Psi(t)=\mathbf{x}^0$, with $\Psi(s\,;\,\mathbf{x})=\Phi(t-s+t_0\,;\,t_0,\mathbf{x}^0)$, where $\Phi(t)$ is the *forward flow* of the system.

the Liouville equation along the characteristics $\Phi(t;\mathbf{x}^k)$ if and only if

$$\begin{aligned}\overbrace{\lambda_t^k\,\sigma\left(\frac{\|\Phi(t;\mathbf{x}^k)-\Phi(t;\mathbf{x}^k)\|}{r}\right)}^{=\text{const.}} =& \overbrace{\lambda_0^k\,\sigma\left(\frac{\|\mathbf{x}^k-\mathbf{x}^k\|}{r}\right)}^{=\text{const.}}\times \\ & \exp\left(-\int_0^t \nabla_{\mathbf{x}}\cdot\mathbf{v}_s(\Phi(s;\mathbf{x}^k))\mathrm{d}s\right) \iff \\ \lambda_t^k =& \lambda_0^k \exp\left(-\int_0^t \nabla_{\mathbf{x}}\cdot\mathbf{v}_s(\Phi(s;\mathbf{x}^k))\mathrm{d}s\right).\end{aligned}$$

Therefore, defining each λ_t^k in this way allows us to track the evolution of ρ_t using the values of $\zeta_t^k(\Phi(t;\mathbf{x}^k))$, as will be detailed in Section 5.3. Some notes about the accuracy of this method will be given in Remark 5.2.1.

By trivial evaluation and substitutions using the information from Eq. (5.2.11), and Eq. (5.2.12) for $t=0$ (RBF interpolation of the initial condition), we can get a pointwise error function between the exact solution and the RBF approximation ignoring integrator error for both Φ and Ψ. This is also reasonable because we do not consider the implementation of Ψ in our numerical method. Therefore, this function allows for *qualitative* information about the method's behavior. Consider $\mathbf{z}\in\mathcal{D}$, then

$$
\begin{aligned}
&|\rho_t(\mathbf{z}) - s_t^N(\mathbf{z})| \leq \\
&\exp\left\{-\int_0^t \nabla_{\mathbf{x}} \cdot \mathbf{v}_s(\Phi(s;\Psi(t;\mathbf{z})))\mathrm{d}s\right\} \times \\
&\qquad \left|\rho_0(\Psi(t;\mathbf{z})) - \sum_{\mathbf{x}\in\{\mathbf{x}^k\}_{k=1}^N} \lambda_0^{\mathbf{x}} \sigma\left(\frac{\|\Psi(t;\mathbf{z}) - \mathbf{x}\|}{r}\right)\right| && (5.2.13) \\
&+ \exp\left\{-\int_0^t \nabla_{\mathbf{x}} \cdot \mathbf{v}_s(\Phi(s;\Psi(t;\mathbf{z})))\mathrm{d}s\right\} \times \\
&\qquad \sum_{\mathbf{x}\in\{\mathbf{x}^k\}_{k=1}^N} |\lambda_0^{\mathbf{x}}| \left|\sigma\left(\frac{\|\Psi(t;\mathbf{z}) - \mathbf{x}\|}{r}\right) - \sigma\left(\frac{\|\mathbf{z} - \Phi(t;\mathbf{x})\|}{r}\right)\right| && (5.2.14) \\
&+ \sum_{\mathbf{x}\in\{\mathbf{x}^k\}_{k=1}^N} |\lambda_0^{\mathbf{x}}| \sigma\left(\frac{\|\mathbf{z} - \Phi(t;\mathbf{x})\|}{r}\right) \times \\
&\qquad \left|\exp\left\{-\int_0^t \nabla_{\mathbf{x}} \cdot \mathbf{v}_s(\Phi(s;\mathbf{x}))\mathrm{d}s\right\} - \exp\left\{-\int_0^t \nabla_{\mathbf{x}} \cdot \mathbf{v}_s(\Phi(s;\Psi(t,\mathbf{z})))\mathrm{d}s\right\}\right|. && (5.2.15)
\end{aligned}
$$

This error function shows three error sources in the RBF approach. The first one, Eq. (5.2.13), accounts for the interpolation error at the initial condition; that is, the error introduced by Eq. (5.2.12) at $t = 0$, which we use for forward-in-time advection. The second part, seen in Eq. (5.2.14) accounts for particle displacement rate between 0 and t, which affects the RBF particle coverage. Finally, the third error, in Eq. (5.2.15), shows the dependency on the divergence of the system, $\nabla_{\mathbf{x}} \cdot \mathbf{v}_t$. Because of the complexity of the error function, we can only analyze simple, specific cases such as $\nabla_{\mathbf{x}} \cdot \mathbf{v}_t = K$, $\forall t \geq t_0$ everywhere in $\mathcal{D}$ for some constant K. If $K = 0$, both Eq. (5.2.14) and Eq. (5.2.15) disappear. In this case, the interpolation procedure is the only error source. Also, if $K \neq 0$, only the last term Eq. (5.2.15) disappears since particle distances will vary with constant rate in space and time.

Solving a system of ODEs is (usually) computationally faster than solving full PDEs. However, to use the characteristic equation approach, we must decide what initial points $\{\mathbf{x}^j\}_j$, with their corresponding values $\{\rho_{t_0}(\mathbf{x}^j)\}_j$,

will evolve. The AMR procedure determines this part: From the initial PDF ρ_{t_0}, the AMR determines the most relevant points in the PDF domain and their respective values. These points are now considered particles that will evolve over a certain time according to the system of characteristic equations. Now, to approximate the evolution of ρ_t we will consider the value at the center of each ζ_t^j; that is, $\zeta_t^j(\Phi(t;\mathbf{x}^j)) = \lambda_t^j$. Finally, we reinitialize the PDF ρ_t following Eq. (5.2.7), although we will give a note on that later.

Remark 5.2.1. *Knowledge about how the numerical integrator's time step affects the RBF particle coverage (as seen in Figure 5.2) is crucial for a correct simulation. The evolution of the initial PDF could become useless if particles become too separated or too close to each other.*

Consider particles $\mathbf{x}_0^i$, $\mathbf{x}_0^j$ *with the initial distance between them* $r_0 = \|\mathbf{x}_0^i - \mathbf{x}_0^j\|$. *Let us compute some bounds of the separation between them as a function of time. At time* t, *we denote the squared distance between them as* $\alpha_t = \left\|\mathbf{x}_t^i - \mathbf{x}_t^j\right\|^2$, *where* $\mathbf{x}_t^k := \Phi(t;t_0,\mathbf{x}^k)$. *Since we assume that both particles are under the effect of the same vector field, the time derivative of* α_t *gives:*

$$\partial_t \alpha_t = 2\left\langle \mathbf{v}_t(\mathbf{x}_t^i) - \mathbf{v}_t(\mathbf{x}_t^j), \mathbf{x}_t^i - \mathbf{x}_t^j \right\rangle \Rightarrow -2K(\mathbf{v}_t)\alpha_t \leq \partial_t \alpha_t \leq 2K(\mathbf{v}_t)\alpha_t, \tag{5.2.16}$$

where $K(\mathbf{v}_t) := \sup_{\mathcal{D}\times[0,t]} \|D_t\|_2$, *and* D_t *is the Jacobian matrix of the vector field* $\mathbf{v}_t$. *Assuming* $K(\mathbf{v}_t) < \infty$ *for all* t *and using Gronwall's inequality, we obtain:*

$$r_0^2 \exp\left(-2\,K(\mathbf{v}_t)t\right) \leq \alpha_t \leq r_0^2 \exp\left(2\,K(\mathbf{v}_t)t\right). \tag{5.2.17}$$

Now, (5.2.17) *gives bounds on the squared distance. If we want our particles to have a bounded separation* $r_{\min} < r_0 < r_{\max}$, *solving for* t *we will give us*

bounds on the time step length to do so:

$$\alpha_t \leq r_0^2 \exp\left(2K(\mathbf{v}_t)t\right) < r_{\max}^2 \longrightarrow$$
$$0 \leq t_1 < \frac{1}{2K(\mathbf{v}_t)} \log\left(\frac{r_{\max}^2}{r_0^2}\right) = \frac{1}{K(\mathbf{v}_t)} \log\left(\frac{r_{\max}}{r_0}\right). \tag{5.2.18}$$
$$\alpha_t \geq r_0^2 \exp\left(-2K(\mathbf{v}_t)t\right) > r_{\min}^2 \longrightarrow$$
$$0 \leq t_2 < -\frac{1}{2K(\mathbf{v}_t)} \log\left(\frac{r_{\min}^2}{r_0^2}\right) = -\frac{1}{K(\mathbf{v}_t)} \log\left(\frac{r_{\min}}{r_0}\right). \tag{5.2.19}$$

Finally, we choose the maximum time step as $\min\{t_1, t_2\}$*. The next section will explain how this idea can be used for a better simulation (see also [89]). We will give more details about the choice of the time step in Section 5.4 devoted to examples.*

This section was explained assuming a deterministic vector field because the case of the random vector field amounts to solving the case of the deterministic vector field for several parameter realizations as shown in Equation (2.2.9). Indeed, recall that in Chapter 2, we showed that when we consider a vector field subject to random parameters, we have to solve a family of Liouville equations that return the conditional PDF of $\mathbf{X}(t, \omega)$, subject to the deterministic vector field $\mathbf{v}_t(\mathbf{x}\,;\,\mathbf{a})$, for a set of realizations $\mathbf{a}$ of the parameter random vector $\mathbf{A}$. Therefore, to obtain the PDF of $\mathbf{X}(t)$ independently of the realizations of $\mathbf{A}$, we used the law of total probability:

$$\rho_t(\mathbf{x}) = \int_{\mathbb{R}^m} \rho_t(\mathbf{x} \,|\, \mathbf{a}) f_A(\mathbf{a}) \mathrm{d}\mathbf{a} = \mathbb{E}_{\mathbf{A}}[\rho_t(\mathbf{x} \,|\, \mathbf{A})]. \tag{5.2.20}$$

For the computational approximation of this expectation operator, we consider the following approach:

$$\rho_t(\mathbf{x}) = \mathbb{E}_{\mathbf{A}}[\rho_t(\mathbf{x} \,|\, \mathbf{A})] \simeq \frac{\sum_{i=1}^{N_{\mathbf{A}}} \rho_t(\mathbf{x} \,|\, \mathbf{a}^i) f_{\mathbf{A}}(\mathbf{a}^i)}{\sum_{i=1}^{N_{\mathbf{A}}} f_{\mathbf{A}}(\mathbf{a}^i)}, \tag{5.2.21}$$

where the approximation is obtained by considering the following discretization of the parameter vector's joint PDF:

$$f_{\mathbf{A}} \simeq \sum_{i=1}^{N_{\mathbf{A}}} \frac{f_{\mathbf{A}}(\mathbf{a}^i)}{\sum_{k=1}^{N_{\mathbf{A}}} f_{\mathbf{A}}(\mathbf{a}^k)} \delta_{\mathbf{a}^i},$$

where $\delta_{\mathbf{a}^i}$ is the Dirac delta measure centered at $\mathbf{a}^i$.

5.3 Complete scheme and computational approach

This section will show how all the concepts and techniques seen in Section 5.2 will be used to compute the time evolution of the PDF of the solution to a system of RDEs. We will see how we have extended these concepts to the complete case (random vector field) and exploited GPUs' parallelism to tackle the complete problem. Fig. 5.3 shows the full procedure in a single iteration of the numerical method. We will explain each step in full detail.

As stated in the abstract and introduction sections, our numerical approach benefits from massively parallel computational architectures. SIMT (Single Instruction, Multiple Thread) is a computational model that allows for parallel execution of the same instructions across multiple threads. Modern GPUs commonly use it to handle highly parallel workloads efficiently, such as matrix multiplication or particle simulations [106]. Fig. 5.4 shows a diagram comparing the architecture of a GPU and a CPU. Although a detailed analysis between them is far more complicated than depicted in Fig. 5.3, we can see that GPUs possess massive parallel computing capabilities.

GPU memory is distributed in several levels and types. In this implementation, we have used two: global memory and registers. On the one hand, global memory is where we store the information that any of the GPU threads can access (GPU DRAM in Fig. 5.4). This memory is moderately large (several GBs in modern GPUs) but has a high access latency; that is, reading values from global memory takes a noticeable amount of time. On the other hand, registers are thread-private variables that have a very low access latency.

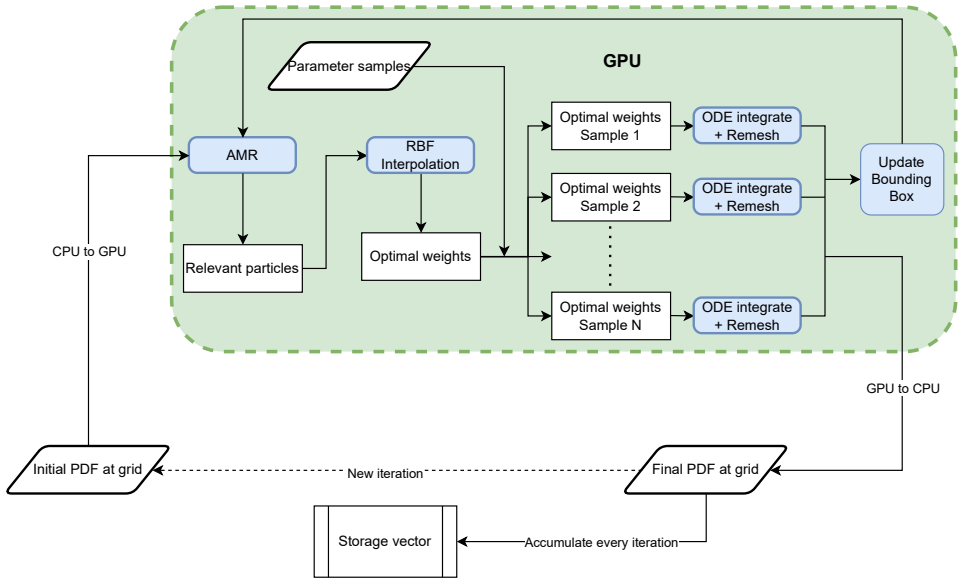

Figure 5.3: Flow chart for each iteration in the numerical method for the Liouville equation. The flow starts in `Initial PDF at grid` (bottom left), and ends at `Final PDF at grid`. Although `Parameter samples` appears as initialized in the GPU, it is actually created in the CPU and transferred to the GPU before the simulation's beginning. Also, `Storage vector` is separated from the main flow because this step is done concurrently (while the simulation is running).

However, this type of memory can only be accessed by the thread performing the computation, and the total capacity of registers is usually quite low (Purple rectangles/L1 Cache in Fig. 5.4). In short, to achieve efficient implementation, we must minimize access to the global memory and maximize intra-thread operations using registers.

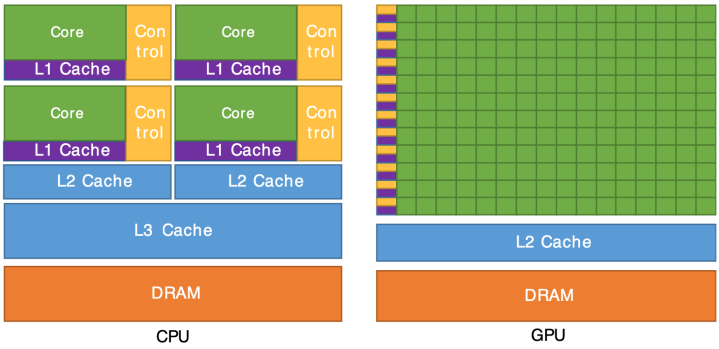

Figure 5.4: Comparison of the architecture of a CPU and a GPU. The cores (single green rectangles) are responsible for computations, and each core can make computations in parallel. Modern GPUs have thousands (or even tens of thousands) of cores. The DRAM in the GPU is also called VRAM (Video RAM) to make a distinction with the CPU DRAM. Image taken from [107].

5.3.1 Adaptive mesh refinement: finding the relevant particles

As explained in Subsection 5.2.3, the main building stone of our computational procedure is the system of characteristic equations associated with the Liouville equation. Specifically, we have seen that we can obtain the solution by solving this ODE system for many points in phase space. Now, the choice of the specific particles for which we will solve this system will be chosen by the AMR procedure.

We only use wavelet compression to find the areas with higher gradients; no reconstruction is considered. Therefore, we have used the simplest of wavelets:

the Haar wavelet defined as follows:

$$g(x) := \begin{cases} 1, & 0 \leq x < 1/2, \\ -1, & 1/2 \leq x < 1, \\ 0, & \text{otherwise.} \end{cases} \tag{5.3.1}$$

This wavelet is not commonly used because there are entire families of wavelets (Daubechies, for example) of a higher order that allows for much better compression and decompression of signals (see [85, Sec.42.3] for a detailed discussion). However, we are not interested in obtaining the optimal compression of the signal, but in finding grid nodes where there is a considerable gradient of the PDF surface; therefore, we can use this very fast wavelet transform together with the translation and dilation equation (5.2.1). The idea that this wavelet is enough for our purposes has been checked heuristically on several examples in multiple dimensions.

Although computing the discrete wavelet transform with the Haar wavelet is fast, the procedure does not scale well with dimensionality. In fact, the number of computations is $\mathcal{O}(N_{\text{Mesh}}^d)$, where N_{Mesh} is the number of mesh nodes per dimension at the finest level[2]. Regarding memory usage, this method requires two N_{Mesh}^d-size arrays: one for storing the mesh indices and the other for storing the decision variable (whether the node is considered relevant or not).

In an attempt to dampen the computational burden, at each iteration, we store the bounding box of the advected particles, which is a fair approximation of the support region of the PDF. Then, we compute the wavelet transform in this smaller domain at the next iteration. Afterward, we divide the bounding box into blocks with 2^d points per block. We assign each block to a GPU thread to compute a d-dimensional tensor wavelet transform (see Fig. 5.5). After computing the wavelet transform, each thread will pass over each of the assigned grid nodes of its block and will *activate* each detail-associated node with a value greater than the prescribed threshold (see Fig. 5.1). This is done recursively, from the finest discretization level up to the coarsest level,

[2] Actually, one may obtain the exact number of computations: $\frac{2^{d(L-L_0-1)}-1}{2^{d(L-L_0-1)}(2^d-1)} N_{\text{Mesh}}^d$, where L is the finest level, and L_0 is the coarsest level.

as shown in Section 5.2.1. Finally, we collect the most relevant points for the particle's advection, denoted by $\mathcal{G}_A$. In most practical applications for AMR, we take $\varepsilon \in [10^{-5}, 5 \cdot 10^{-3}]$.

To collect the most relevant nodes, we do two operations. The first one consists in counting the number of relevant nodes. Since they are stored as binary integers (1 or 0), summing the elements of the decision array gives $\#\mathcal{G}_A$. This is done via a parallel reduce operation whose time complexity is $\mathcal{O}(N/N_{\text{Threads}} + \log(N_{\text{Threads}}))$, where N is the number of elements, and N_{Threads} is the number of threads in which we parallelize the computation. The second part is sorting the nodes by setting the selected nodes' indices first. This part has a time complexity of $\mathcal{O}(N)$. Finally, we keep the first $\#\mathcal{G}_A$ elements of the index array.

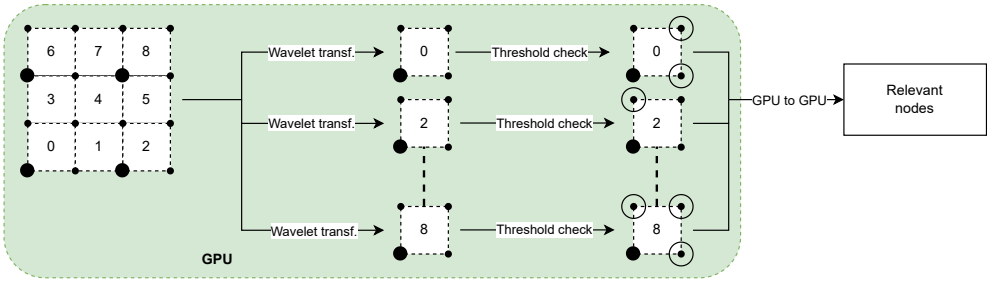

Figure 5.5: This flowchart shows the AMR procedure in a 2-dimensional, 16-node mesh for a 1-level refinement. Bigger nodes are the approximation nodes; smaller ones are the detail nodes. Circled nodes are the relevant ones. For more levels, we do the procedure in the GPU for all desired levels, and then we collect the relevant nodes in GPU memory.

5.3.2 Interpolation: finding the weight of each particle

Now, once we have built the set of relevant nodes $\mathcal{G}_A$ from the AMR procedure, we want to initialize the RBF weights to evolve them according to what is shown in the Subsection 5.2.3. This part is fairly straightforward: we have the relevant points $\{\mathbf{x}^i\}_{i=1}^{N_P} = \mathcal{G}_A$ and the PDF values at those points $\{\rho_t^i =$

$\rho_t(\mathbf{x}^t)\}_{i=1}^{N_P}$. We have to find $\Lambda_t = (\lambda_t^1, \ldots, \lambda_t^{N_P})$ such that

$$\begin{bmatrix} \sigma(\mathbf{x}^1) \\ \sigma(\mathbf{x}^2) \\ \vdots \\ \sigma(\mathbf{x}^{N_P}) \end{bmatrix} \Lambda = \underbrace{\begin{bmatrix} \sigma\left(\frac{\|\mathbf{x}^1-\mathbf{x}^1\|}{r}\right) & \sigma\left(\frac{\|\mathbf{x}^1-\mathbf{x}^2\|}{r}\right) & \cdots & \sigma\left(\frac{\|\mathbf{x}^1-\mathbf{x}^N\|}{r}\right) \\ \sigma\left(\frac{\|\mathbf{x}^2-\mathbf{x}^1\|}{r}\right) & \sigma\left(\frac{\|\mathbf{x}^2-\mathbf{x}^2\|}{r}\right) & \cdots & \sigma\left(\frac{\|\mathbf{x}^2-\mathbf{x}^N\|}{r}\right) \\ \vdots & \vdots & \ddots & \vdots \\ \sigma\left(\frac{\|\mathbf{x}^N-\mathbf{x}^1\|}{r}\right) & \sigma\left(\frac{\|\mathbf{x}^N-\mathbf{x}^2\|}{r}\right) & \cdots & \sigma\left(\frac{\|\mathbf{x}^N-\mathbf{x}^N\|}{r}\right) \end{bmatrix}}_{=:A_\sigma} \begin{bmatrix} \lambda_t^1 \\ \lambda_t^2 \\ \vdots \\ \lambda_t^{N_P} \end{bmatrix} = \begin{bmatrix} \rho_t^1 \\ \rho_t^2 \\ \vdots \\ \rho_t^{N_P} \end{bmatrix}.$$

On the computational side, this part consists of two steps. The first one consists of performing fixed-radius nearest neighbors to find particle-to-particle distances. The second one consists of iteratively solving the linear system. Both procedures can be very time and resource-intensive if not done properly.

To do so, we assign a particle to each GPU thread, which then checks the distance between that particle and all the other particles. This algorithm has a very bad asymptotic limit of $\mathcal{O}(N_P^2/N_{\text{Threads}})$; however, since no trees or new arrays are involved, this algorithm is the fastest and the most memory-efficient in all tested cases.

As for memory usage, at this step we create two $N_P \cdot N_{\text{Max.Neighbors}}$-sized arrays, one for storing the indices of the nearby particles and one for storing the particle-to-particle distances. $N_{\text{Max.Neighbors}}$ is the maximum number of neighbors each particle can have, which is trivially given by the radius of the RBF kernel chosen: $N_{\text{Max.Neighbors}} = (2[R_{\text{RBF}}/h] + 1)^d$, where h is the discretization length (assumed equal in all dimensions).

Finally, regarding the system solution, we mentioned in Subsection 5.2.2 that the interpolation matrix is sparse, symmetric, and positive definite. Therefore, we can use the conjugate gradient method with COO-style indexing. This indexing method is directly obtained from the neighbor search procedure, thus resulting in a very fast step.

5.3.3 Particle advection: evolving the relevant particles

Let us recall that when the vector field $\mathbf{v}_t$ depends on some random parameter $\mathbf{A}(\omega)$, the joint PDF of the solution is given by the law of total probability, as seen in Equation (2.2.9). Writing this integral as an expectation shows that we can solve the Liouville equation repeatedly for several realizations of the vector field's parameters and then compute its expectation according to the parameters' random vector joint PDF. Although this may sound straightforward, a naive implementation could leave many GPU threads idle, wasting significant computational resources and making the simulation much slower.

Going deeper into the previous paragraph, we have to integrate the characteristics of the same particles for every realization of a set of samples from the vector field's parameters. To do so, we can concatenate the particles assigned for each vector field parameters' realization and evolve all of them at once, using the full massive parallelization capability of GPUs. That is, we consider the a finite number of realizations $\{\mathbf{a}^i\}_{i=1}^{N_\mathbf{A}}$ of the random parameter vector $\mathbf{A}$[3], then the array of particles to be advected is:

$$\{\mathbf{z}_i\}_{i=1}^{N_\mathbf{A}N_P} = \{\overbrace{\underbrace{\mathbf{x}^1,\ldots,\mathbf{x}^{N_P}}_{N_P},\mathbf{x}^1,\ldots,\mathbf{x}^{N_P},\ldots,\mathbf{x}^1,\ldots,\mathbf{x}^{N_P}}^{N_\mathbf{A}N_P}\},\quad \{\mathbf{x}^j\}_{j=1}^{N_P} = \mathcal{G}_A.$$

The first N_P points, $\{z_i\}_{i=1}^{N_P}$, will be evolved/updated using the vector field with the realization $\mathbf{a}^1$; the next N_P points, $\{z_i\}_{i=N_P+1}^{2N_P}$ will be evolved using $\mathbf{a}^2$ and so on. This step requires solving (numerically) the system of characteristic equations (5.2.9), whose updated values we define by $\{\mathbf{q}_i\}_{i=1}^{N_\mathbf{A}N_P} := \{\Phi(\Delta t;\,\mathbf{z}_i)\}_{i=1}^{N_\mathbf{A}N_P}$. The time complexity of this step is $\mathcal{O}(N_P/N_{\text{Threads}})$, where N_P is the number of particles to advect. The error bound depends on the specific numerical integrator used. Regarding memory usage, no new arrays are created because the particle advections are done in-place.

[3]In the examples used in this chapter, we consider $\{\mathbf{a}^i\}_{i=1}^{N_\mathbf{A}} = \{a_1^i\}_{i=1}^{N_{A_1}} \otimes \{a_2^i\}_{i=1}^{N_{A_2}} \otimes \cdots \otimes \{a_M^i\}_{i=1}^{N_{A_M}}$, where $N_\mathbf{A} = N_{A_1}N_{A_2}\cdots N_{A_M}$, and each $\{a_k^i\}_{i=1}^{N_{A_k}}$ is an equidistant partition of the domain of A_k.

Depending on the nature of the problem at hand, different families of numerical integrators can be used for obtaining $\{\mathbf{q}_k\}_{k=1}^{N_P N_A}$, each one shining in specific applications. For example, there are general numerical methods such as Runge–Kutta methods (e.g., the Runge–Kutta [105] method of order 4 used for numerical experiments in this work) that allow obtaining fairly good approximations for generic systems; numerical integrators that are designed for stiff ODEs where explicit Runge–Kutta methods may fail; symplectic integrators for Hamiltonian systems, known as symplectic integrators, that preserve physical constants such as mechanical energy (see, e.g. [108–110]), etc.

In order to obtain the updated RBF weights $\{\lambda_{\Delta t}^j\}_{j=1}^{N_P N_A}$, we use the simple Simpson's rule. To get the midpoint value, we use Hermite interpolation.

Our approach uses only one memory transfer from RAM to VRAM (see Fig. 5.4), optimizing the available GPU memory bandwidth. Furthermore, the CUDA kernel written for this purpose only uploads a grid node and its corresponding PDF value from global memory. All other auxiliary variables for the numerical integrator particle update are thread-private registers, allowing fast read/write operations. Finally, the particle position and value are rewritten in the global memory. This approach allows each thread to update its position in its reserved memory location, eliminating any possible race condition between threads (two threads trying to access the same memory address) and the need to use shared memory or repeated access to higher-latency global memory [106].

5.3.4 Reinitialization: projecting particles onto the grid

After the evolution of the AMR-chosen particles has been completed, we reinterpolate the particles back onto the starting grid. As discussed earlier, this consists of a simple sparse matrix-vector multiplication. Let $\{\mathbf{y}_k\}_{k=1}^{N_G}$ be the

grid nodes. Then, the updated PDF at each node will finally be given by:

$$\begin{aligned}\rho_{\Delta t}(\mathbf{y}_k) = \mathbb{E}_{\mathbf{A}}[\rho_{\Delta t}(\mathbf{y}_k \,|\, \mathbf{A})] &\simeq \frac{1}{\sum_{i=1}^{N_{\mathbf{A}}} f_{\mathbf{A}}(\mathbf{a}^i)} \left(\sum_{i=1}^{N_{\mathbf{A}}} f_{\mathbf{A}}(\mathbf{a}^i) \rho_{\Delta t}(\mathbf{y}_k \,|\, \mathbf{a}^i) \right) \\ &\simeq \sum_{i=1}^{N_{\mathbf{A}}} \underbrace{\frac{f_{\mathbf{A}}(\mathbf{a}^i)}{\sum_{l=1}^{N_{\mathbf{A}}} f_{\mathbf{A}}(\mathbf{a}^l)}}_{:=w_i} \left(\sum_{j=1}^{N_P} \sigma \left(\frac{\|\mathbf{y}_k - \mathbf{q}_{j+N_P\,(i-1)}\|}{r} \right) \lambda_{\Delta t}^{j+N_P\,(i-1)} \right).\end{aligned} \tag{5.3.2}$$

Joining the computation for all the grid nodes, we have the following procedure:

$$\begin{bmatrix} \rho_{\Delta t}(\mathbf{y}_1) \\ \rho_{\Delta t}(\mathbf{y}_2) \\ \vdots \\ \rho_{\Delta t}(\mathbf{y}_{N_G}) \end{bmatrix} = \begin{bmatrix} \sigma(\mathbf{y}_1) \\ \sigma(\mathbf{y}_2) \\ \vdots \\ \sigma(\mathbf{y}_{N_G}) \end{bmatrix} \begin{bmatrix} (\lambda_{\Delta t}^{j})_{j=1}^{N_P}\, w_1 \\ (\lambda_{\Delta t}^{j+N_P})_{j=N_P}^{2N_P}\, w_2 \\ \vdots \\ (\lambda_{\Delta t}^{j+N_P(N_A-1)})_{j=1}^{N_P}\, w_{N_{\mathbf{A}}} \end{bmatrix}.$$

Observe that this part also includes a point search: we have to either find all the grid nodes within r distance from each advected particle or find all the advected particles within the same distance r from a fixed grid node. Following the latter idea, as in the point search at the interpolation step, would be a mistake because now we will have many more particles, and an exhaustive search approach would take too much time. However, following the first idea gives an easy way to find the nearest grid nodes with respect to a given advected particle.

Indeed, we know the finest grid discretization length h and the *bottom* corners of our computational domain. Therefore, for each particle $\mathbf{q}_j \in \{\mathbf{q}_k\}_{k=1}^{N_P\,N_{\mathbf{A}}}$, we can find the index of the nearest grid node just by dividing each dimensional component of v_i with h and then summing each index accordingly. Once we have its nearest grid node, we can easily know all the grid nodes within R distance from the particle $\mathbf{v}_i$ without having to do any kind of point search, resulting in a very fast procedure.

Regarding the computational aspects, we assign each $\mathbf{q}_j \in \{\mathbf{q}_k\}_{k=1}^{N_P N_\mathbf{A}}$ to a GPU thread. We only call $\mathbf{q}_j$ and the relative weight $w_i \in \{w_k\}_{k=1}^{N_\mathbf{A}}$ from global memory. We then divide the components, add them correspondingly to find the nearest grid node's index, and write the relative chapter of $\mathbf{q}_j$ to the corresponding grid node as in (5.3.2). This multiplication is relatively lightweight, computationally speaking. As a downside to this approach, we have to introduce the chapter of each particle to each node's memory address via atomic functions; that is, maybe there is more than one thread trying to write a value at a certain grid node, but this can only be done by serializing the memory access which will degrade the performance of the GPU kernel. However, we have seen experimentally that this does not happen so often; therefore, the performance is not degraded as much as it might look.

With regard to time complexity, it is $\mathcal{O}(N_P(2[R_{\text{RBF}}/h]+1)^d/N_{\text{Threads}})$, where $[\cdot]$ is the rounding function and R_{RBF} is the radius of the chosen RBFs. However, note that the atomic-adding step could slightly degrade performance. Regarding memory usage, no new arrays are created because the results are written back onto the original array containing the values of the PDF on the fine grid.

5.4 Numerical examples

This section is devoted to showcasing the performance of the numerical method with respect to RDE versions of several relevant mathematical models appearing in physics and epidemiology:

- The simple harmonic oscillator, a 2D linear model whose PDF can be obtained exactly. So, it is presented as a test example;
- The Van der Pol oscillator, a 2D model from physics with nonlinearity;
- The Mathieu equation, a similar 2D nonlinear model from physics exhibiting parametric resonance phenomena;
- The SIR model, a 3D nonlinear model from epidemiology.

In the numerical experiments, we contrast the results of the proposed Liouville equation solver with Monte Carlo simulations. For these problems, we use different types of integrators to demonstrate that the algorithm is integrator-agnostic. However, we do not aim to compare different types of numerical integrators for a specific problem because —when considering the solution per trajectory— the relation between the classes of integrators is well-researched [109, 110]. Nonetheless, to limit the scope of this work, we use ODE integrators that are *CUDA-friendly*, that is, methods which do not require nonlinear solvers.

Also, regarding the specific choice of RBF used, we use the Wendland function $\phi_{3,1}(r) = \max(1-r,0)^4(4r+1) \in \mathrm{C}^2([0,1])$ in all cases. This function is the first smooth CS-RBF for dimensions 2 and 3 (see [94, Tab. 3.2]). Since each problem has different dynamics, we do not want to force any extra smoothness. Also, if the RBF centers become too close to each other in a given system, the using a smoother RBF could negatively impact the matrix condition number (see Equation (5.2.5)).

All computations were performed in a desktop PC with 40GB of DDR4 RAM, an i9-10900K CPU and an RTX4000 (8GB) GPU. The source code is written in C++ and CUDA and is freely available for download ([111, Version 4.0.0]). The compiler used is `NVCC 12.2` for the CUDA code. In all cases, the operating system is Windows 10 Pro; however, it can also be built and run on Linux. Monte Carlo simulations are carried out using Julia 1.10.3 with the OrdinaryDiffEq.jl 6.78.0 [112], and the density plots are obtained using the kernel smoothing functions of StatsPlots.jl 0.15.7.

5.4.1 Harmonic oscillator: error analysis

Oscillator models are fundamental in science and engineering, representing various periodic motions in natural and artificial systems. The simple harmonic oscillator, characterized by constant amplitude and frequency, serves as the foundational model for such analyses. Though dynamically simple, it is of interest for its closed-form solution to the Liouville equation (denoted by

ρ_t^{REF}), providing a benchmark for comparing the joint PDFs computed by our Liouville solver (denoted by ρ_t).

We consider the following form of the harmonic oscillator with random initial conditions but deterministic frequency [12]:

$$\ddot{X}(t,\omega) = -\nu^2 X(t), \quad X(0,\cdot) = X_0 \in \mathrm{L}^2(\Omega,\mathbb{P}), \quad \dot{X}(0,\cdot) = \dot{X}_0 \in \mathrm{L}^2(\Omega,\mathbb{P}), \tag{5.4.1}$$

where ν is known as the angular frequency of the system, which we consider to be a deterministic value, and the initial conditions for position and velocity (X_0, $\dot{X}_0$, respectively) are random variables with finite variance.

The related Liouville IBVP is the following:

$$\partial_t \rho_t(x_1,x_2) + x_2 \partial_{x_1}\rho_t(\mathbf{x}) - \nu^2 x_1\, \partial_{x_2}\rho_t(\mathbf{x}) = 0, \qquad (t,x_1,x_2) \in (t_0,t_F)\times\mathcal{D}, \tag{5.4.2}$$

$$\rho_0(x_1,x_2) = f_0(x_1,x_2), \qquad (x_1,x_2) \in \overline{\mathcal{D}}, \tag{5.4.3}$$

$$\rho_t \mathbf{v}_t \cdot \mathbf{n}(x_1,x_2) = 0, \qquad (t,x_1,x_2) \in [t_0,t_F]\times\partial\mathcal{D}, \tag{5.4.4}$$

where $\mathcal{D}$ (computational domain) and t_F (final time) are defined in Table 5.1b. Its exact solution is:

$$\rho_t^{\mathrm{REF}}(x_1,x_2) = f_0\left(\cos(\nu t)x_1 - \frac{1}{\nu}\sin(\nu t)x_2, \nu\sin(\nu t)x_1 + \cos(\nu t)x_2\right).$$

Our analysis focuses on two key parameters: the RBF radius and $\Delta t_{\mathrm{Reinit}}$, with corresponding plots provided for each (see Figs. 5.6a,5.6b). We plot the quadratic error of the computed joint PDFs, $\rho_{t_{\mathrm{F}}}$, in the integration domain with discretization step h at the end of the integration time interval, that is,

$$\mathrm{Error} \coloneqq \sum_{i,\,j} \left(\rho_{t_{\mathrm{F}}}^{\mathrm{REF}}(x_0+ih, y_0+jh) - \rho_{t_{\mathrm{F}}}(x_0+ih, y_0+jh)\right)^2. \tag{5.4.5}$$

For the first test, we consider the RBF radius factor r/h between 0.5 and 16, while $\Delta t_{\mathrm{Reinit}}$ is set to the minimal value of Δt (that is, the reinitialization happens at every integration time step). For the second experiment, we fix the

best radius to discretization factor, $r/h = 15$, obtained on the previous step, and increase Δt_{Reinit} as powers of 2 (see parameters in Tables 5.1a and 5.1b).

On the one hand, Figure 5.6a shows the error curve for varying RBF radius, and we can clearly see a super-linear shape curve, which indicates an $\mathcal{O}((r/h)^q)$ asymptotic error curve, with $q > 1$. In fact, according to theory, the interpolation error is $\mathcal{O}((r/h)^{\frac{3}{2}})$ for the chosen RBF kernel, and this agrees with the error function Eqs. (5.2.13) to (5.2.15): since the divergence function of Eq. (5.4.2) is 0 everywhere, the only error source will be the interpolation procedure. Fig. 5.6c shows the exact solution to the Liouville boundary-IVP in Eqs. (5.4.2) to (5.4.4), while Figs. 5.6d to 5.6f shows the joint PDFs computed by our Liouville solver at the final time $t_F = 4$.

On the other hand, Fig. 5.6b shows something that may appear counter-intuitive: a larger reinitialization timestep results in lower error. This is not true in general (see Theorem 5.2.1), but in cases with zero divergence, such as our simple harmonic oscillator, where error only stems from the interpolation step, a larger reinitialization timestep means that less error will be accumulated because we will reinitialize less often.

As discussed previously via Eqs. (5.2.5) and (5.2.6), we expect both curves to be U-shaped: in the case of the error from the r/h choice, it is expected to decrease as the factor grows; but as discussed in Section 5.2.2, a very large radius will involve more particle chapters at interpolation, which will result in matrix condition deterioration. Also, regarding the error from the $\Delta t_{\text{Reinit.}}$ choice, particle distances will vary when the system has a non-zero divergence, and the RBF coverage (thus, the PDF value approximation) will also deteriorate.

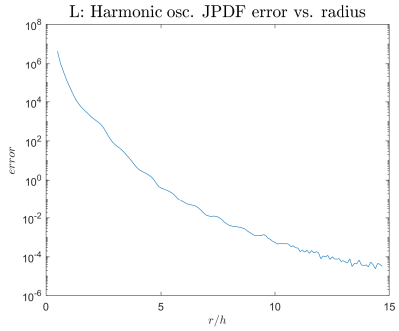

(**a**) Dependence of the quadratic error in the joint PDFs vs. the RBF radius for the harmonic oscillator.

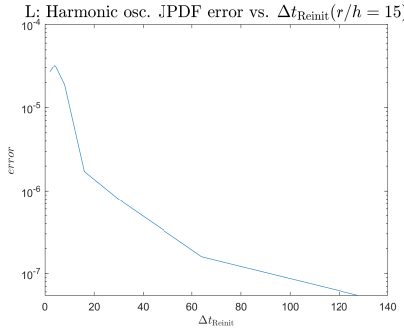

(**b**) Dependence of the quadratic error in the joint PDFs vs. the Δt_{Reinit} (the RBF radius $r/h = 15$) for the harmonic oscillator.

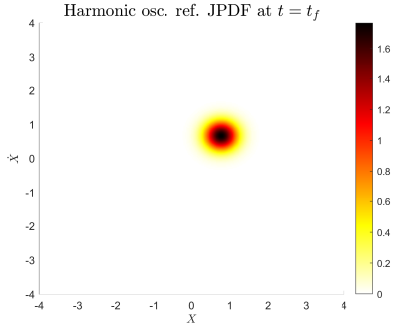

(**c**) Reference joint PDFs of the harmonic oscillator.

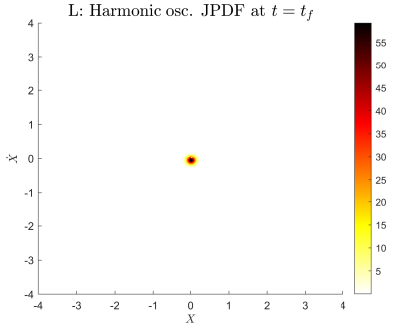

(**d**) joint PDFs of the harmonic oscillator for $r/h = 1$.

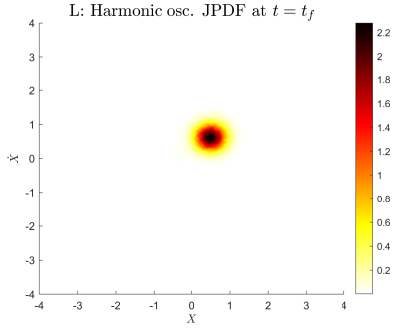

(**e**) joint PDFs of the harmonic oscillator for $r/h = 2.5$.

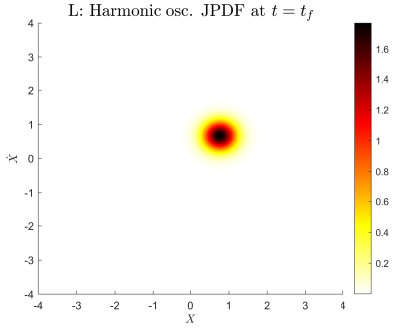

(**f**) joint PDFs of the harmonic oscillator for $r/h = 5$.

Figure 5.6: Comparison of the joint PDFs of the solutions to the harmonic oscillator by the Liouville method with different parameters. Here, $t_f = 4$ as defined in Table 5.1b.

Par.	Distr.	Mean	Var.
X_0	N	1.00	0.30
$\dot{X}_0$	N	-1.00	0.30

a Random parameters' statistical information. All parameters are pairwise independent. Initial conditions are truncated in the corresponding problem domain (see right table).

Input	Descr.
Δt	$2 \cdot 10^{-3}$
Δt_{Reinit}	$2^k,\ k = 1, \dots, 7$
Time span	$[0, 4]$
Domain	$[-8, 8] \times [-8, 8]$
Points	$2^9 \times 2^9$
AMR threshold	$1 \cdot 10^{-5}$
RBF radius	$0.5h$–$15h$

b List of the input parameters of the algorithm.

Table 5.1: Parameters of the random harmonic oscillator.

5.4.2 Van der Pol oscillator

The Van der Pol system holds importance in various fields due to its ability to simulate real-world behaviors like oscillations and irregular patterns. When varying the system parameter, μ, the Van der Pol oscillator shifts from orderly periodic oscillations to chaotic dynamics via a period-doubling route. This intricate behavior stems from the interaction between nonlinearity and damping, giving rise to complex patterns with implications in diverse domains like electronics, physics, and biology.

We consider the following form for the randomized Van der Pol oscillator:

$$\begin{aligned} &\ddot{X}(t,\omega) - \mu(\omega)\left(1 - X^2(t,\omega)\right)\dot{X}(t) + 5X(t,\omega) = 0, \quad t \geq 0, \\ &X(0,\omega) = X_0(\omega) \in \mathrm{L}^2 \cap \mathrm{L}^\infty(\Omega, \mathbb{P}), \\ &\dot{X}(0,\omega) = \dot{X}_0(\omega) \in \mathrm{L}^2 \cap \mathrm{L}^\infty(\Omega, \mathbb{P}). \end{aligned} \tag{5.4.6}$$

To launch the simulations, we set the simulation parameters specified in Table 5.2a. Using these we have seen (numerically) that the PDF total mass is always concentrated inside $\mathcal{D} = [-5.5, 5.5] \times [-5.5, 5.5]$. To compute the range of possible timesteps, we compute the Jacobian matrix for the Van der Pol

oscillator Eq. (5.4.6):

$$D_t(x_1,\, x_2) = \begin{bmatrix} 0 & 1 \\ -5 - 2\mu x_1 x_2 & \mu(1 - x_1^2) \end{bmatrix} \quad \Rightarrow \quad \sup_{\mathcal{D}\times\mathrm{supp}\{\mu(\omega)\}} \|D_t\|_2 \simeq 197.11040. \tag{5.4.7}$$

The comparison shown in the set of figures shown below (Figs. 5.7 and 5.8) were computed with an RBF radius of $7.49h$, where h denotes the discretization length of the domain. Using the results of Remark 5.2.1, we obtain the maximal reinitialization timestep of $\Delta t_{\mathrm{Reinit}} = 0.0102$, which corresponds to ~ 5 integration steps using Δt as defined in Table 5.2b.

Figure 5.7 shows the joint PDF obtained via the Liouville equation with the proposed solver and Montecarlo simulations with spatial binning. It can be seen that the Liouville solver provides a smooth evolution of the joint PDF and, contrarily to the MC simulations, it maintains a proper form without the severe particle distortion that affects the joint PDF's structure in phase space (compare Figs. 5.7e and 5.7f). This may result from MC being very sensitive to nonlinear phenomena when choosing a low-to-moderate number of particles. Particles are scattered easily throughout the phase space, where the Liouville equation solver can preserve the location of the most *relevant* particles due to the particle reinitialization at the underlying mesh and AMR. We may conclude that more particles must be chosen for a better, comparable, MC-based simulation.

Also, Fig. 5.8 shows the computed marginals from the Liouville equation and the MC simulations. We can see that the Liouville-based marginal PDFs achieve higher values than their MC counterparts, at least in the position component (compare Figs. 5.8a and 5.8b or Figs. 5.8c and 5.8d). This is the same as discussed in the previous paragraph: MC is very sensitive to nonlinear phenomena when choosing a low-to-moderate number of particles. However, there is a smaller difference than with the joint PDFs since we are

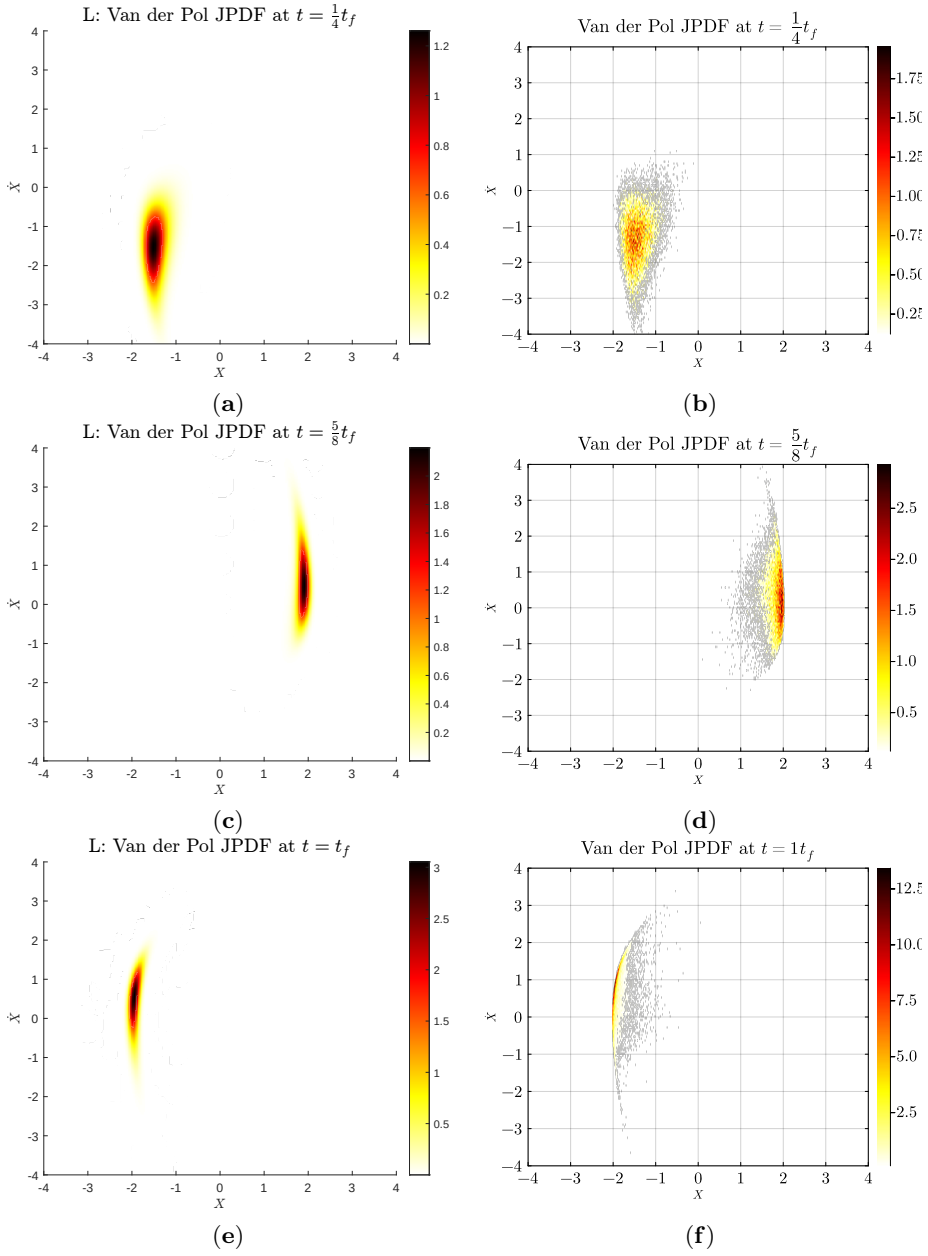

Figure 5.7: Comparison of the joint PDFs of the solution to the Van der Pol oscillator by the Liouville method (left) and the Monte Carlo simulation with $m = 2^{14}$ samples (right). Here, $t_f = 4$ as defined in Table 5.2b.

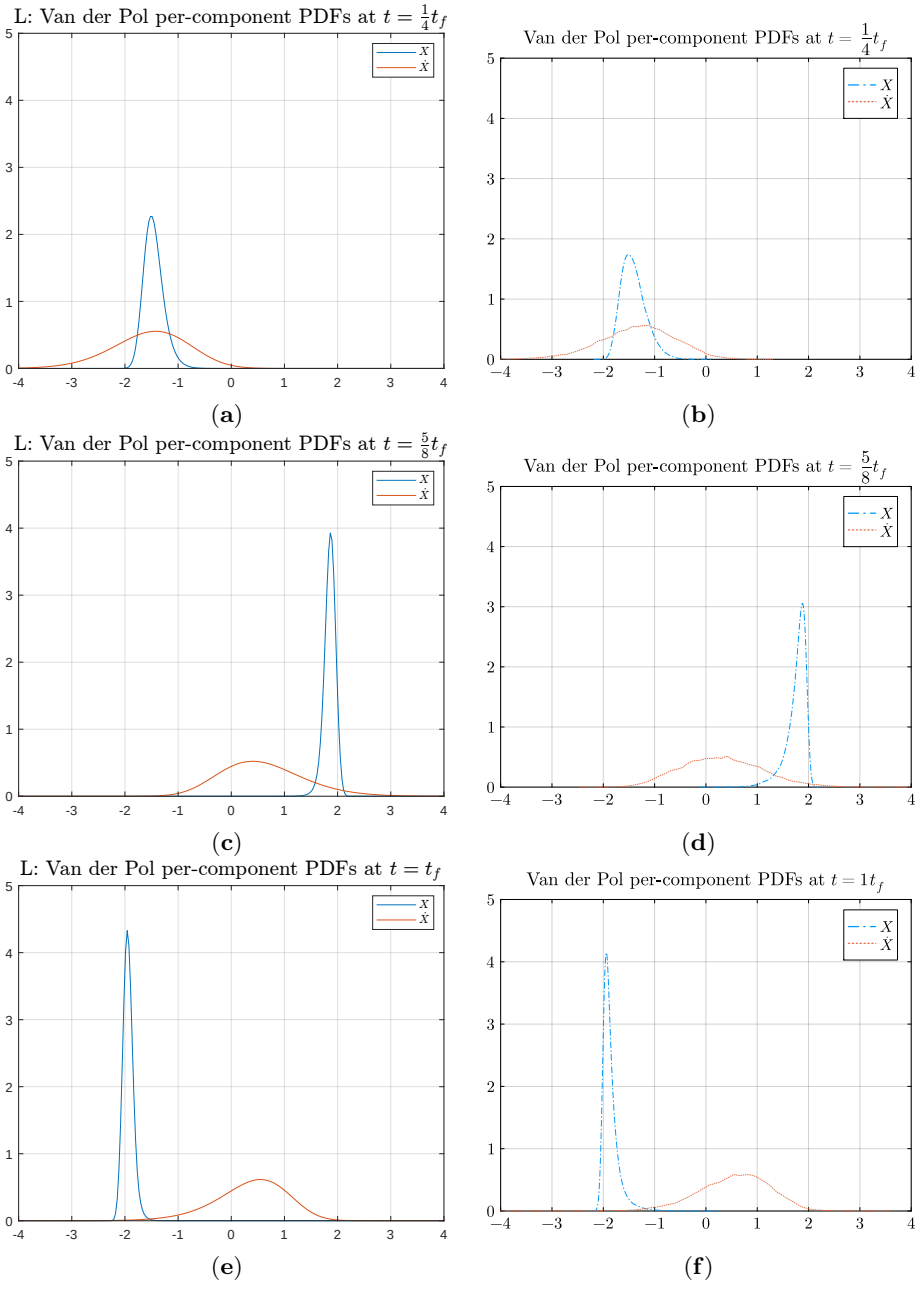

Figure 5.8: Comparison of the PDFs of the components of the solution to the random Van der Pol oscillator by the Liouville method (left) and the Monte Carlo simulation with $m = 2^{14}$ samples (right). Here, $t_f = 4$ as defined in Table 5.2b.

Par.	Distr.	Mean	Var.
X_0	N	1.00	0.30
$\dot{X}_0$	N	-1.00	0.30
μ	N	1.00	0.30

a Random parameters' statistical information. All parameters are pairwise independent. Initial conditions are truncated in the corresponding problem domain (see right table). We consider 64 samples for μ.

Input	Descr.
Δt	$2 \cdot 10^{-3}$
Δt_{Reinit}	0.01
Time span	$[0, 4]$
Domain	$[-8, 8] \times [-8, 8]$
Points	$2^9 \times 2^9$
AMR threshold	$1 \cdot 10^{-5}$
RBF radius	$1 \cdot 10^{-5}$

b List of the input parameters of the algorithm.

Table 5.2: Parameters of the random Van der Pol oscillator.

accumulating particles in the marginal components; therefore, the sensitivity to particles is slightly dampened.

5.4.3 Mathieu equation

Let us consider the Mathieu equation, in a sense similar to the Van der Pol model:

$$\ddot{X}(t,\omega) + (a(\omega) - 2q\cos(2t))\, X(t,\omega) = 0. \tag{5.4.8}$$

The Mathieu equation is characterized by periodic coefficients and it describes parametric resonance, where perturbations can lead to large oscillations. This model and similar ones find applications to periodically variable systems and their control [113–115] in areas such as mechanical vibrations, electromagnetic waves, and quantum mechanics, as it helps in understanding the stability and behavior of systems with periodic parameters. An interesting question is how does the Mathieu equation behave if some of its parameters are considered random variables. If one strives to define the regions of stability numerically, it is beneficial to use geometric integrators [109, 116]. Table 5.3b shows the statistical information for the system's and simulation's parameters. For this problem, we use the geometric Runge–Kutta–Munthe-Kaas Euler method [117] instead of the classical RK method $X_{n+1} = \exp(hA(t_n, X_n))\, X_n$[4].

Figure 5.9 shows similar features to the Van der Pol case. The Liouville equation solver can smoothly track the PDF evolution, while the MC samples are scattered throughout the phase space. However, the situation is better than in the Van der Pol case. This is also seen in the marginal PDFs in Fig. 5.10; the corresponding marginals are always very alike.

The situation is completely different in the unstable case, which shows one of the limitations of the current implementation of the Liouville equation solver. As the system evolution domain is set beforehand, the chosen window in the phase space cannot correctly track the system's resonant exploding growth (case $q_{\text{resonant}} = -8$) with the variance reaching the order of 10^3.

However, our solver forces the total density preservation inside the window, while in the resonant case, most of the density's mass should eventually escape the window. Nonetheless, this is not a fundamental limitation of the method

[4]For simplicity of implementation in CUDA and due to the low impact of the integrator's order in the resulting simulation, we have used a Taylor series approximation of the matrix exponential. However, it is favorable to use diagonal Padé approximants.

and can be alleviated by moving (and expanding, if necessary) the window alongside the system trajectories, that is one of the points of the future research.

Par.	Distr.	Mean	Var.
X_0	N	0.00	0.09
$\dot{X}_0$	N	-1.00	0.09
a	N	3.00	0.09
q_{stable}	D	-1.00	—
q_{resonant}	D	-8.00	—

a Random parameters' statistical information. All parameters are pairwise independent. Initial conditions are truncated in the corresponding problem domain (see right table). We consider 64 samples for random parameter a.

Input	Descr.
Δt	$\pi/500(\sim 0.0063)$
Δt_{Reinit}	$\pi/250$
Time span	$[0, 2\pi]$
Domain	$[-8, 8] \times [-8, 8]$
Points	$2^9 \times 2^9$
AMR threshold	$1 \cdot 10^{-6}$

b List of the input parameters of the algorithm.

Table 5.3: Parameters of the random Mathieu equation.

5.4.4 Susceptible-Infected-Recovered epidemiological model

The SIR model plays a crucial role in epidemiology, providing a framework to understand and predict the spread of infectious diseases within a population. Its simplicity allows for exploring various scenarios related to disease transmission, recovery rates, and vaccination strategies. The model helps estimate the potential impact of interventions and public health measures by categorizing individuals into susceptible, infectious, or recovered groups. Its application extends beyond infectious diseases, serving as a foundational tool for analyzing diverse phenomena in network dynamics, behavioral sciences, and risk assessment, offering valuable insights to guide health policies and interventions.

We consider a randomized SIR model with vital dynamics (birth and death) for the three-dimensional case. The SIR model is a well-known compartmental model in epidemiology. It is a nonlinear model that admits a closed solu-

tion only under certain circumstances. Particularly, we consider the following model:

$$S'(t,\omega) = \Delta(\omega) - \mu(\omega)S(t,\omega) - \beta(\omega)S(t,\omega)I(t,\omega), \qquad S(t_0,\omega) = S_0(\omega), \tag{5.4.9}$$

$$I'(t,\omega) = \beta(\omega)S(t,\omega)I(t,\omega) - \big(\gamma(\mu) + \mu(\omega)\big)I(t,\omega), \qquad I(t_0,\omega) = I_0(\omega), \tag{5.4.10}$$

$$R'(t,\omega) = \gamma(\omega)I(t,\omega) - \mu(\omega)R(t,\omega), \qquad R(t_0,\omega) = R_0(\omega), \tag{5.4.11}$$

where S, I and R denote the susceptible, infected, and recovered populations, respectively, Δ, μ denote the birth and death rates; and β, γ denote the susceptible–infected and infected–recovered transfer rates, respectively. We assume all parameters and the initial condition vector (S_0, I_0, R_0) are independent random variables.

With the SIR model definition Eqs. (5.4.9) and (5.4.11) and the distribution information from Table 5.4a, we may compute the maximum time step via the relations in Eqs. (5.2.18) and (5.2.19):

$$\sup\{\|D_t\|_2 : t \geq t_0,\, (S, I, \Lambda, \mu, \beta, \gamma) \in \tilde{\mathcal{D}}\} \simeq 0.77703,$$

where $\tilde{\mathcal{D}}$ denotes the joint positively invariant domain for all the random variables in the SIR model. Considering a RBF support radius of $6.49h$, we get the following time step bounds:

$$0 \leq \Delta t_{\max} \leq \frac{1}{0.77703}\log(6) \Rightarrow \Delta t_{\max} \simeq 2.31, \tag{5.4.12}$$

$$0 \leq \Delta t_{\min} \leq -\frac{1}{0.77703}\log\left(\frac{1}{6}\right) \Rightarrow \Delta t_{\min} \simeq 2.31, \tag{5.4.13}$$

which means that $\Delta t_{\text{Reinit}} \leq 2.31$, which is considerably larger than the previous examples.

Figures 5.11 show the difference between the marginal PDFs computed via MC and the Liouville equation solver. Once again, we can see that the MC

simulation tends to separate particles more giving higher-variance PDFs, although the expected values and general structure of the PDF are very similar. We expect that a much higher number of samples would be needed to lead similar results.

Also, Figures 5.12 show the 95% prediction surface of the PDF given by the Liouville equation solver and the MC version of the prediction surface for several time instants [5]. Once again, the Liouville equation solver improves the MC simulations giving a smooth surface, as expected by the nature of the random SIR model and showing the superiority of the Liouville equation in this kind of problems. The entire simulation in the [0, 30] timespan has been computed in ~ 4 minutes.

Par.	Distr.	Mean	Var.
S_0	N	0.7500	0.0001
I_0	N	0.1500	0.0001
R_0	N	0.1000	0.0001
Δ	D	0.0250	—
μ	D	0.0250	—
β	N	0.3000	0.0001
γ	Ga	0.2000	0.0001

a Random parameters' statistical information for the SIR model. The initial condition components do not have a prescribed number of random samples as the AMR procedure defines them. All parameters are pairwise independent. For the random parameters, we consider the cartesian product of 8 samples for β and 8 samples for γ.

Input	Descr.
Δt	0.5
Δt_{Reinit}	1.0
Time span	$[0, 30]$
Domain	$[0,1] \times [0,1] \times [0,1]$
Points	$2^8 \times 2^8 \times 2^8$
AMR threshold	$1 \cdot 10^{-3}$

b List of the input parameters of the algorithm.

Table 5.4: List of parameters for the random SIR model.

[5] Further details about the prediction region finder can be found in [118]

5.5 Conclusion

This chapter introduces and analyzes a novel numerical approach for efficiently solving the Liouville equation in the context of RDEs using General-Purpose Graphics Processing Units (GPGPUs). Our methodology integrates wavelet compression-based adaptive mesh refinement, Lagrangian particle methods, and radial basis function approximation to develop a versatile, accurate and computationally efficient numerical algorithm.

We validated the performance of our approach through several mathematical models, including the van der Pol oscillator, Mathieu equation, and SIR model. These examples demonstrate the method's applicability to various problems and its compatibility with various numerical integrators for the underlying systems. Not to be overlooked are the illustration of the limitation of the method in its current implementation. Future research directions include:

- Investigating the interconnection of the method's parameters to enable their automatic adjustment for specific problems.
- Developing a moving and adaptive window for domain integration representation.
- Implementing an inverse refining algorithm that begins with coarse approximations and progressively refines them.
- Finding an appropriate approach for higher dimensional systems ($d \geq 5$).

Our findings suggest that the numerical method described in the present chapter holds significant potential for quantifying forward uncertainty in random differential equations via probability density evolution, greatly improving on the information obtained by simply performing Montecarlo simulations.

Publications

The results presented in this thesis chapter have been published in [119]. In regard to this chapter, the PhD candidate has contributed by working on

its complete development with more emphasis on the theoretical results and preparing the visualization of the numerical examples.

Also, some results of this chapter have been presented at two conferences. The first one is the SIAM UQ24: SIAM Conference in Uncertainty Quantification, held in Trieste (Italy) from 27th February-1st March, 2024. The talk was titled *Forward Uncertainty Evolution of General Random Differential Equation Systems*. The second congress is the International Conference in Mathematical Analysis and Applications in Science and Engineering (ICMA2SC'22), held in Porto (Portugal), from 27-29th 2022. The talk was titled *Probability Density Evolution and its Applications in Random Differential Equations*, and was published in the conference proceedings with ISBN 978-989-53496-3-0.

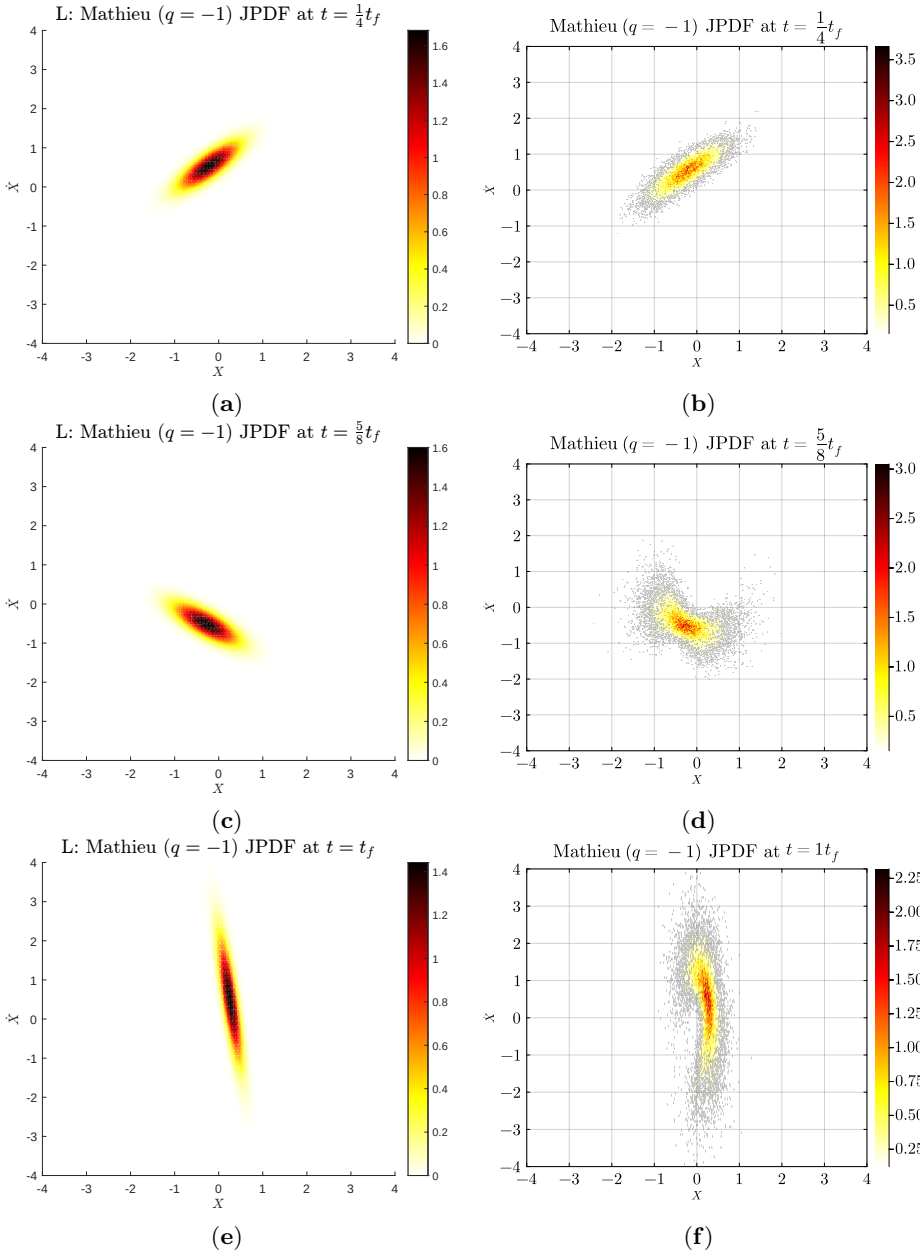

Figure 5.9: Comparison of the joint PDFs of the solution to the Mathieu equation (stable case with $q = -1$) by the Liouville method (left) and the Monte Carlo simulation with $m = 2^{14}$ samples (right). Here, $t_f = 2\pi$ as defined in Table 5.3b.

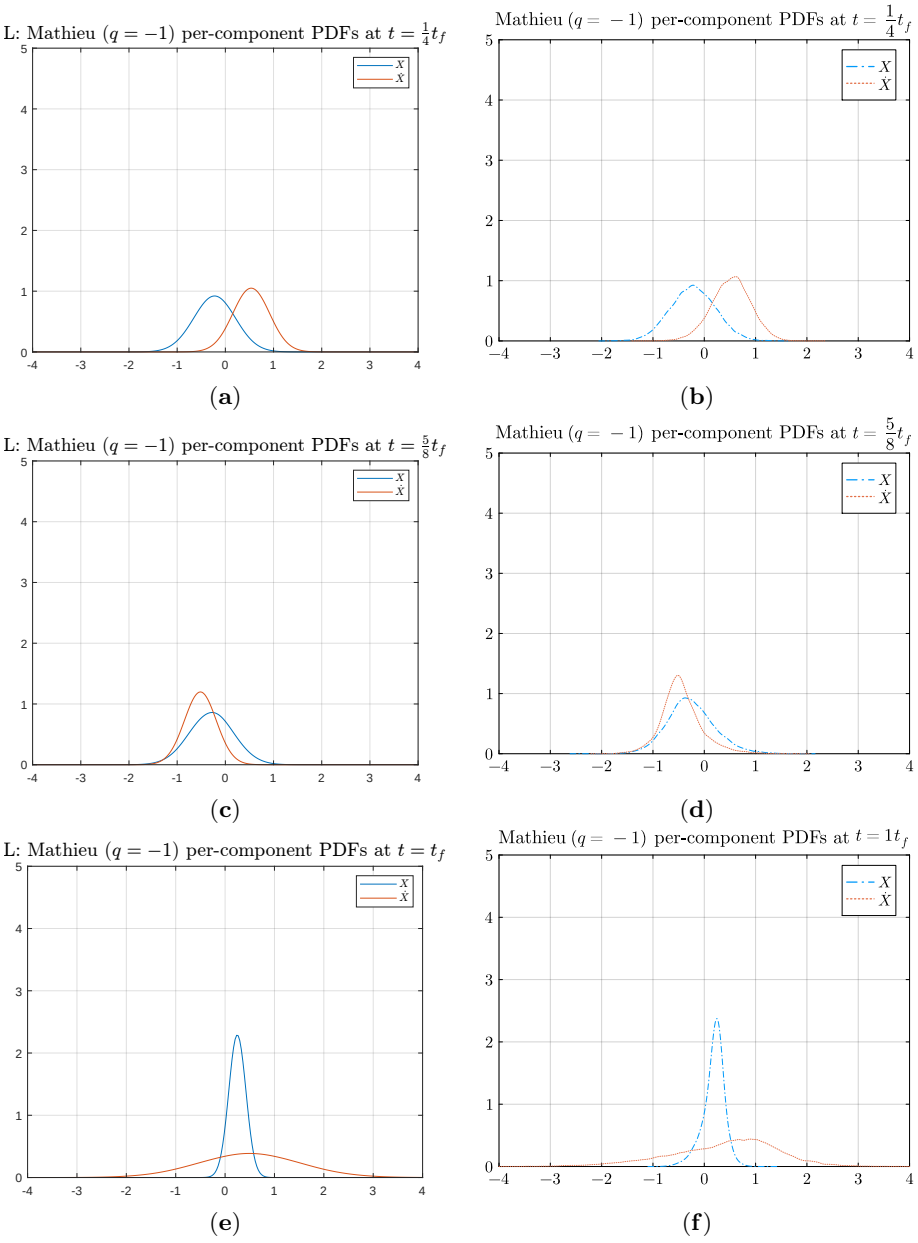

Figure 5.10: Comparison of the PDFs of the components of the solution to the Mathieu equation (stable case $q = -1$) by the Liouville method (left) and the Monte Carlo simulation with $m = 2^{14}$ samples (right). Here, $t_f = 2\pi$ as defined in Table 5.3b.

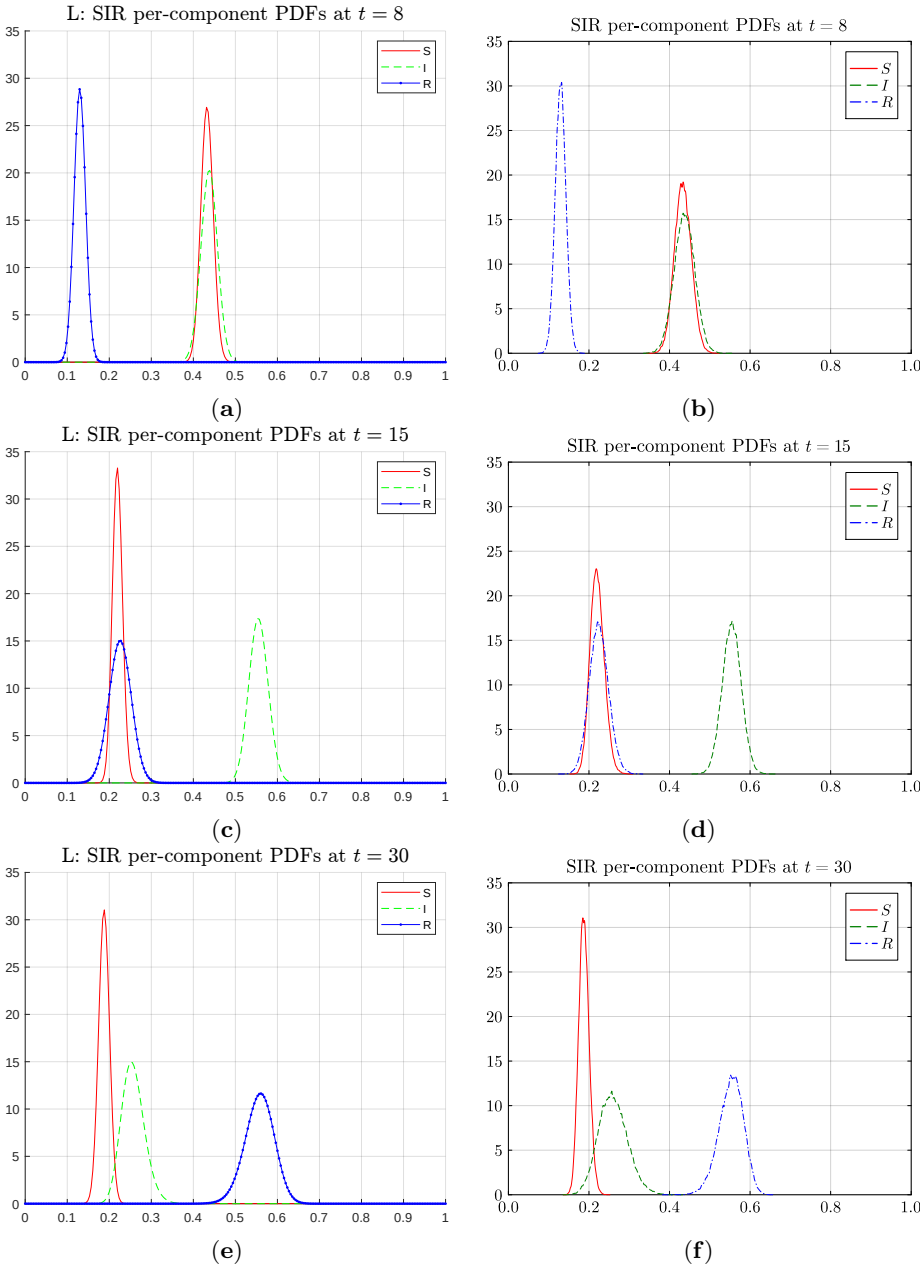

Figure 5.11: Comparison of the marginal PDFs of the components of the solution to the SIR system by the Liouville method (left) and the Monte Carlo simulation with $m = 2^{16}$ samples (right). Here, $t_f = 30$ as defined in Table 5.4b.

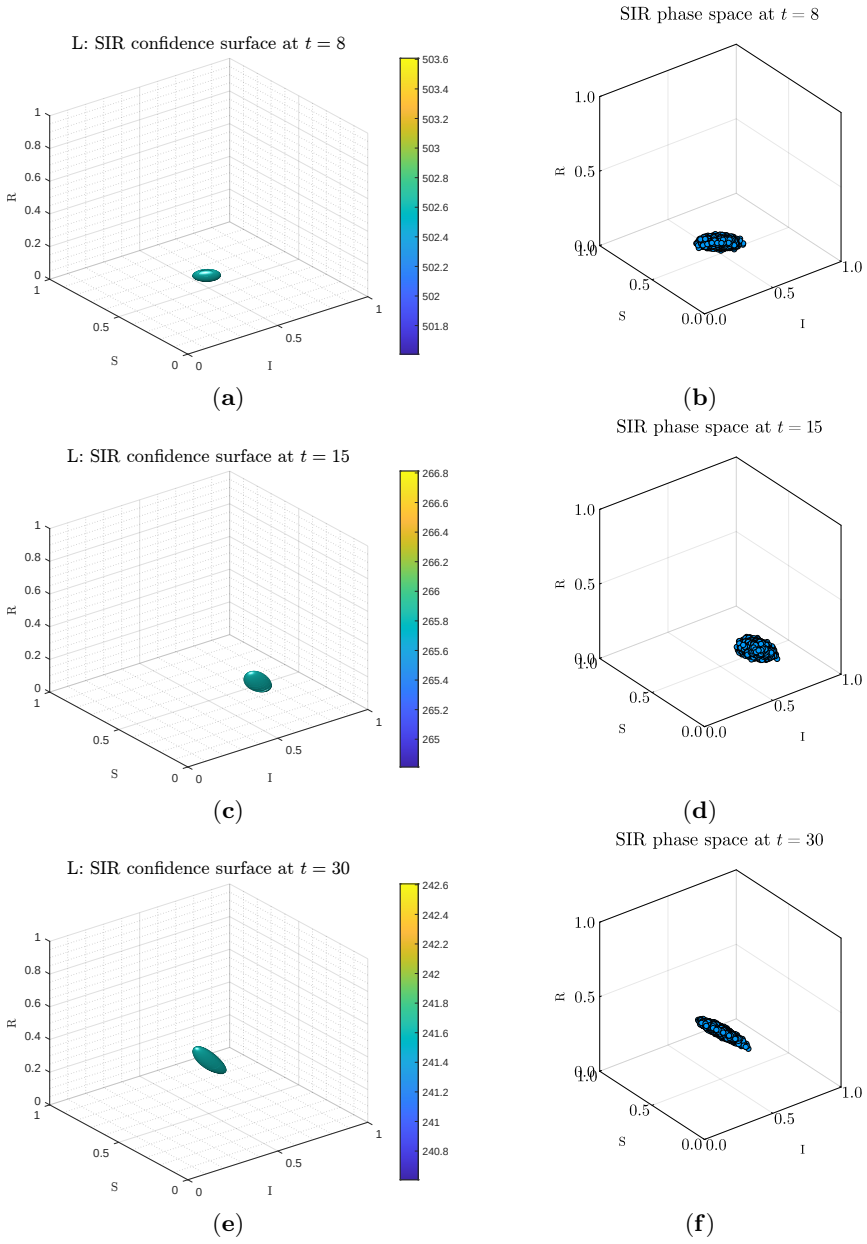

Figure 5.12: Prediction ellipsoid for the SIR system solution by the Liouville method (left) and the phase space by the Monte Carlo simulation with $m = 2^{16}$ samples (right). Here, $t_f = 4$ as defined in Table 5.4b.

Chapter 6

Generalized logistic equation

Based on existing literature about the random logistic and Gompertz models, this chapter aims to extend the investigations to the generalized logistic differential equation in the random setting. First, this is done by rigorously constructing its solution in two ways: the sample-path approach and the mean-square calculus. Secondly, the probability density function at each time instant is derived in two ways: by applying the random variable transformation technique and solving the associated Liouville equation. We also prove that the stochastic solution and its density function converge under specific conditions to the corresponding solution and density function of the logistic and Gompertz models, respectively. The investigation finishes by showing some examples where some computational techniques described in the previous chapter are combined to construct reliable approximations of the probability density of the stochastic solution. In particular, we show how our findings can be applied to a real-world problem.

The logistic differential equation has been generalized in different senses to better model the dynamics of real-world phenomena where it has been applied. This generalization has included its reformulation in terms of fractional derivatives, the substitution of the contagion rate term by a power-law function, etc. [120–122]. In this chapter, we deal with the following generalization of the logistic differential equation

$$Y'(t) = AY(t)\left(1 - \left(\frac{Y(t)}{K}\right)^B\right),\ t \geq t_0, \quad Y(t_0) = Y_0. \tag{6.0.1}$$

As usual, t is interpreted as the time. The parameter A is the growth rate, K is the carrying capacity, and B is a power that controls how fast the limiting number K is approached.

When $B = 1$, the classical logistic differential equation is obtained. And when B tends to 0, the Gompertz equation is given. Indeed, given $A, B > 0$, we put $\hat{A} = AB$, and then (7.2.10) can be written as

$$Y'(t) = \frac{\hat{A}}{B}Y(t)\left(1 - \left(\frac{Y(t)}{K}\right)^B\right). \tag{6.0.2}$$

Now, let us calculate the limit as $B \to 0^+$ of the following term that defines the right-hand side of the above equation:

$$\lim_{B\to 0^+} \frac{\left(1 - \left(\frac{Y(t)}{K}\right)^B\right)}{B} = \lim_{B\to 0^+} -\left(\frac{Y(t)}{K}\right)^B \ln\left(\frac{Y(t)}{K}\right) = -\ln\left(\frac{Y(t)}{K}\right) = \ln\left(\frac{K}{Y(t)}\right).$$

As a consequence, as $B \to 0^+$, the differential equation (7.2.10) can be expressed as

$$Y'(t) = \hat{A}Y(t)\ln\left(\frac{K}{Y(t)}\right),$$

which corresponds to the Gompertz model [123, 124].

The incorporation of the power B allows for more flexible S-shaped curves to model growth phenomena over time. Examples of application include tumor

growth [125–128] and diseases such as SARS [129, 130], dengue fever [131], influenza H1N1 [132], Zika [133], Ebola [134], and COVID-19 [135–138].

We investigate the random counterpart of (7.2.10) in order to extend the previous literature on the logistic random differential equation [44, 73] and the Gompertz random differential equation [26]. It is assumed that $B > 0$, $K > 0$, $Y_0 \in [0, K]$ (almost surely), and A are random variables on a common underlying and complete probability space $(\Omega, \mathcal{F}, \mathbb{P})$. Due to uncertainty propagation, the solution $Y(t)$ is a differentiable stochastic process. The randomness of the parameters arises from the uncertainty inherent to the problem that, in principle, cannot be reduced by additional knowledge [2].

The organization of the remaining part of the chapter is as follows: In Section 6.1, the sample-path and mean-square solution to (7.2.10) is rigorously found. In Section 6.2, the PDF of the solution is obtained in two ways: by the RVT technique and by solving Liouville's PDE. In Section 6.3, the behavior of the solution, when the power tends to 1 or 0, is examined (through the mean-square convergence and via the convergence of the densities) to replicate the deterministic counterpart. In Section 6.4, we illustrate our main findings with two examples that include a real-world application. Finally, in Section 6.5, the main conclusions are drawn.

6.1 Stochastic solution

In this section, we investigate the existence and uniqueness of a stochastic solution to the generalized logistic random differential equation model (7.2.10). Two notions of solution are treated: sample-path solution and mean-square solution.

6.1.1 Sample-path solution

By definition, $Y(t)$ is a sample-path solution to (7.2.10) if Y is a stochastic process and its trajectories solve (7.2.10) on $[t_0, \infty)$ in a deterministic sense [139, Chapter 3], [12, Appendix I]. The construction of the sample-path solution is usually straightforward; one merely solves the deterministic problem and checks that the conditions for being a sample-path solution (measurability and common time domain for the trajectories) are satisfied.

In the present case, model (7.2.10) corresponds to a Bernoulli differential equation. After the standard change of variables $X = Y^{-B}$, a linear differential equation is derived for X. At the end, the solution to (7.2.10) becomes

$$Y(t) = \frac{K}{\left[1 + \left(-1 + \left(\frac{K}{Y_0}\right)^B\right) \mathrm{e}^{-AB(t-t_0)}\right]^{1/B}}. \tag{6.1.1}$$

When $0 \leq Y_0 \leq K$ almost surely $Y(t)$, which is defined by (6.1.1), is the sample-path solution and it lies within $[0, K]$ almost surely, for every $t \geq t_0$.

6.1.2 Mean-square solution

By definition, $Y(t)$ is a mean-square solution to (7.2.10) when the derivative in (7.2.10) (and in general any limit) is considered in the metric of the Lebesgue space $\mathrm{L}^2(\Omega, \mathbb{P})$ [139, chapter 4], [12, 140]. Mean-square convergence is of great interest because convergence in this setting implies convergence of the two most sought moments of a stochastic process: the mean and the variance [12].

Let us see that the sample-path solution defined by (6.1.1) is also the mean-square solution on $[t_0, \infty)$, whenever $\|A\|_\infty < \infty$, $B > 0$ almost surely, $\|B\|_\infty < \infty$, $0 \leq Y_0 \leq K$ almost surely, and $0 < \kappa_0 \leq K \leq \kappa_1 < \infty$ almost surely, where κ_0 and κ_1 are constant.

Let

$$F(Y, \omega) = A(\omega) Y \left(1 - \left(\frac{Y}{K(\omega)}\right)^{B(\omega)}\right), \quad Y \in [0, K(\omega)], \quad \omega \in \Omega.$$

Fix an $\omega \in \Omega$. By the triangular inequality and the mean value theorem, it is easy to see that $F(\cdot,\omega)$ is Lipschitz on $[0, K(\omega)]$, with Lipschitz constant $\|A\|_\infty(1+\kappa_1\|B\|_\infty/\kappa_0)$:

$$\begin{aligned}
|F(Y_1,\omega)-F(Y_2,\omega)| = &\left|A(\omega)Y_1\left(1-\left(\frac{Y_1}{K(\omega)}\right)^{B(\omega)}\right)-\right.\\
&\left.A(\omega)Y_2\left(1-\left(\frac{Y_2}{K(\omega)}\right)^{B(\omega)}\right)\right|\\
&\le |A(\omega)||Y_1-Y_2|\left(1-\frac{Y_1}{K(\omega)}\right)^{B(\omega)}\\
&+|A(\omega)|Y_2\left|\left(1-\frac{Y_1}{K(\omega)}\right)^{B(\omega)}-\left(1-\frac{Y_2}{K(\omega)}\right)^{B(\omega)}\right|\\
&\le \|A\|_\infty|Y_1-Y_2|+\|A\|_\infty|Y_2|\frac{\|B\|_\infty}{\kappa_0}|Y_1-Y_2|\\
&\le \|A\|_\infty\left(1+\frac{\kappa_1\|B\|_\infty}{\kappa_0}\right)|Y_1-Y_2|.
\end{aligned}$$

By Tietze extension theorem [141, Th. 1], $F(\cdot,\omega)$ can be extended to a Lipschitz map $\tilde{F}(\cdot,\omega):\mathbb{R}\to\mathbb{R}$ with Lipschitz constant $\|A\|_\infty(1+\kappa_1\|B\|_\infty/\kappa_0)$. Consider $Y'(t)=\tilde{F}(Y(t))$. By [139, Th. 4.3], [12, Th. 5.1.2], the Lipschitz condition on the whole $\mathbb{R}$ implies that the problem $Y'(t)=\tilde{F}(Y(t))$, $Y(t_0)=Y_0$, possesses a unique mean-square solution on $[t_0,\infty)$. Any mean-square solution is equivalent to the sample-path solution [142, Th. 3(a)], which is (6.1.1) precisely. Then (6.1.1) is the mean-square solution. This completes the proof.

6.2 Two methods for computing the PDF of the solution stochastic process

In this section, we compute the PDF of $Y(t)$, denoted as $f_{Y(t)}(y)$. Two complementary techniques are employed: the application of the RVT method and the resolution of Liouville's PDE. The former requires the computation of a Jacobian, while the latter needs the resolution of the Liouville equation.

6.2.1 First method: RVT technique

Let (Y_0, K, A, B) be an absolutely continuous random vector with a certain joint probability distribution, $f_{(Y_0,K,A,B)}$. Fix $t \geq t_0$. To apply the technique, we need a transformation that relates the inputs, (Y_0, K, A, B), to the output, $Y(t)$. The transformation mapping is the following:

$$v(Y_0, K, A, B) = \left(\frac{K}{\left[1 + \left(-1 + \left(\frac{K}{Y_0}\right)^B\right) \mathrm{e}^{-AB(t-t_0)}\right]^{1/B}}, K, A, B \right),$$

where the auxiliary components K, A and B have been conveniently chosen. The inverse mapping is computed easily:

$$h(Y, K, A, B) = \left(\frac{K}{\left[1 + \left(-1 + \left(\frac{K}{Y}\right)^B\right) \mathrm{e}^{AB(t-t_0)}\right]^{1/B}}, K, A, B \right).$$

The Jacobian of h is the determinant of the matrix of first partial derivatives of h:

$$Jh(Y, K, A, B) = \frac{\partial Y_0}{\partial Y} = \frac{K^{1+B}\mathrm{e}^{AB(t-t_0)}}{Y^{B+1}\left[1 + \left(-1 + \left(\frac{K}{Y}\right)^B\right) \mathrm{e}^{AB(t-t_0)}\right]^{1/B+1}} > 0.$$

Such positivity holds because $0 < Y < K$ and $B > 0$ almost surely. By the RVT formula [34], [78, Th. 2.1.5], and after marginalizing with respect to K, A and B, the PDF of $Y(t)$ is obtained in a semi-implicit manner through a triple integral:

$$f_{Y(t)}(y) = \int_{\mathcal{D}_{(K,A,B)}} f_{(Y_0,K,A,B)} \left(\frac{K}{\left[1 + \left(-1 + \left(\frac{K}{Y}\right)^B\right) \mathrm{e}^{AB(t-t_0)}\right]^{1/B}}, K, A, B \right) \times \frac{K^{1+B}\mathrm{e}^{AB(t-t_0)}}{Y^{B+1}\left[1 + \left(-1 + \left(\frac{K}{Y}\right)^B\right) \mathrm{e}^{AB(t-t_0)}\right]^{1/B+1}} \,\mathrm{d}K\,\mathrm{d}A\,\mathrm{d}B. \qquad (6.2.1)$$

Here $\mathcal{D}_{(K,A,B)}$ denotes the support of (K, A, B).

The PDF (6.2.1) is the general formula. Sometimes, it may be simplified. First, if Y_0, K, A and B are independent random variables, then the joint PDF $f_{(Y_0,K,A,B)}$ factorizes:

$$f_{(Y_0,K,A,B)} = f_{Y_0} \times f_K \times f_A \times f_B.$$

In consequence, the PDF of the solution can be expressed via an expectation

$$f_{Y(t)}(y) = \mathbb{E}_{K,\,A,\,B}\left[f_{Y_0}\left(\frac{K}{\left[1 + \left(-1 + \left(\frac{K}{y}\right)^B\right) \mathrm{e}^{AB(t-t_0)}\right]^{1/B}} \right) \times \frac{K^{1+B}\mathrm{e}^{AB(t-t_0)}}{y^{B+1}\left[1 + \left(-1 + \left(\frac{K}{y}\right)^B\right) \mathrm{e}^{AB(t-t_0)}\right]^{1/B+1}} \right].$$

Note that this is a parametric approximation of the PDF because it is obtained as an expectation of a transformation of the input random variables (A, B, K). This PDF representation is beneficial since Monte Carlo simulation can be easily applied by sampling the involved random variables and then computing the expectation that approximates the PDF [143].

Secondly, if an input random variable (Y_0, K, A or B) is discrete, rather than absolutely continuous, its PDF may be viewed in a generalized sense. For example, if K is discrete, then

$$f_K(k) = \sum_i k_i \delta_0(k - k_i),$$

where $k_i > 0$ are the mass points of the discrete random variable K and δ_0 is the Dirac delta function (everywhere zero but with infinite value at the origin and integral equal to 1). The integral over $\mathcal{D}_K$ would become a sum over the points $\{k_i\}_i$.

6.2.2 Second method: Liouville's PDE

Let us denote model (7.2.10) as

$$Y'(t) = v(Y(t), K, A, B),$$

where

$$v(Y, K, A, B) = AY\left(1 - \left(\frac{Y}{K}\right)^B\right). \tag{6.2.2}$$

The Liouville equation for $Y(t)$ independently from the system's parameters can be obtained by applying Equations (2.2.7) and (2.2.9). In this case, the explicit solution to the Liouville's equation is [12, Chapter 6]

$$f(t, y) = \mathbb{E}_{(K,A,B)}\left[f_{(Y_0,K,A,B)}(Y_0, K, A, B)\exp\left(-\int_{t_0}^{t} \frac{\partial v}{\partial y}(Y(\tau), K, A, B)\,\mathrm{d}\tau\right)\right], \tag{6.2.3}$$

where $Y(t) = h(Y_0, K, A, B, t)$ is the input-output relation and

$$Y_0 = h^{-1}(Y, K, A, B, t) = \frac{K}{\left[1 + \left(-1 + \left(\frac{K}{Y}\right)^B\right)\mathrm{e}^{AB(t-t_0)}\right]^{1/B}}$$

is the inverse relation, in terms of the initial condition. The partial derivative of g with respect to Y is

$$\frac{\partial v}{\partial Y} = A\left(1 - \left(\frac{Y}{K}\right)^B\right) - \frac{AB}{K^B}Y^B.$$

An important term in the solution of Liouville's PDE is

$$\exp\left(-\int_{t_0}^{t} \frac{\partial v}{\partial Y}(Y(\tau), K, A, B)\,\mathrm{d}\tau\right) = \mathrm{e}^{-A(t-t_0)}\frac{\left(K^B + (-1 + \mathrm{e}^{AB(t-t_0)})Y_0^B\right)^{(1+B)/B}}{K^{1+B}}.$$

Then the Jacobian of the RVT formula is retrieved as

$$\exp\left(-\int_{t_0}^{t}\frac{\partial v}{\partial Y}(Y(\tau),K,A,B)\,\mathrm{d}\tau\right)\Big|_{Y_0=h^{-1}(y,K,A,B,t)}=\frac{K^{1+B}\mathrm{e}^{AB(t-t_0)}}{Y^{B+1}\left[1+\left(-1+\left(\frac{K}{Y}\right)^{B}\right)\mathrm{e}^{AB(t-t_0)}\right]^{1/B+1}}.$$

Thus, the PDF obtained via the Liouville equation as Equation (6.2.3) is equal to the PDF (6.2.1) after computing the expectation in the system's parameters $\mathbb{E}_{(K,\,A,\,B)}[\cdot]$.

6.3 Convergence when the power tends to 1 or 0

By the deterministic theory, it is known that the classical logistic and Gompertz differential equations are retrieved when $B=1$ and $B\to 0$, respectively. The aim of the present section is to extend those results to the random scenario. Different convergence measures for $Y(t)$ are used: mean-square convergence and convergence of densities.

6.3.1 Mean-square convergence

We investigate the mean-square convergence of $Y(t)$. Two cases are distinguished, according to the probabilistic convergence of B:

- Case $B\to 1$ or $B\to 0$ almost surely. By the deterministic theory, it is known that $Y(t)$ converges to the logistic curve or the Gompertz curve almost surely when $B\to 1$ or $B\to 0$ almost surely, respectively. It is also known that $0\leq Y(t)\leq K\in \mathrm{L}^1(\Omega,\mathrm{d}\mathbb{P})$, and analogously for the logistic and the Gompertz curves. By the dominated convergence theorem [144, result 11.32, p. 321], the almost sure convergence of $Y(t)$ translates into mean-square convergence. In conclusion, $Y(t)$ converges to the logistic curve or the Gompertz curve in the mean-square sense when $B\to 1$ or $B\to 0$ almost surely.

- Case $B \to 1$ or $B \to 0$ in the mean-square sense. Pick any sequence $\{B_n\} \to 1$ or $\{B_n\} \to 0$ in the mean-square sense. There exists a subsequence such that $\{B_{n_l}\} \to 1$ or $\{B_{n_l}\} \to 0$ almost surely. By the previous item, the corresponding $\{Y_{n_l}(t)\}$ converges in mean-square to the logistic curve or to the Gompertz curve, respectively. At the end, this implies that $Y(t)$ converges to the logistic curve or the Gompertz curve in the mean-square sense when $B \to 1$ or $B \to 0$ in mean-square.

6.3.2 Convergence of densities

We prove that, if $B \to 1$ or $B \to 0$ almost surely, then $f_{Y(t)}(y)$ converges to the PDF of the logistic curve or the PDF of the Gompertz curve almost everywhere, respectively. Almost everywhere convergence of densities is a strong mode of convergence, as it implies convergence in $\mathrm{L}^1(\mathbb{R}, \mathrm{d}y)$ by Scheffé's lemma [145, p. 55], [146].

For the proof, it is assumed that Y_0 and (K, A, B) are independent, $A > 0$ almost surely (increasing trend), $Y_0 \geq z > 0$ almost surely (z constant), $\|B\|_\infty < \infty$, there exists $C > 0$ such that $f_{Y_0}(y) \leq \min\{C/y, C/y^{1+\|B\|_\infty}\}$ for all $y > 0$, and $\mathbb{E}[\mathrm{e}^{A\|B\|_\infty(t-t_0)}] < \infty$ (finite moment-generating function of A). Due to the independence, the PDF (6.2.1) is rewritten as

$$f_{Y(t)}(y) = \mathbb{E}\left[f_{Y_0}(R_B)(R_B)^{1+B}\mathrm{e}^{AB(t-t_0)}\frac{1}{y^{B+1}}\right],$$

where

$$R_B = \frac{K}{\left[1 + \left(-1 + \left(\frac{K}{Y}\right)^B\right)\mathrm{e}^{AB(t-t_0)}\right]^{1/B}}$$

and the domain is $y \geq z$. Now,

$$0 \leq f_{Y_0}(R_B)(R_B)^{1+B}\mathrm{e}^{AB(t-t_0)}\frac{1}{y^{B+1}} \leq C\mathrm{e}^{A\|B\|_\infty(t-t_0)}\min\left\{\frac{1}{z}, \frac{1}{z^{1+\|B\|_\infty}}\right\},$$

where such upper bound is a constant that, in consequence, belongs to $\mathrm{L}^1(\Omega, \mathrm{d}\mathbb{P})$. The dominated convergence theorem [144, result 11.32, p. 321] allows for interchanging the limit on B and the expectation.

6.4 Numerical examples and real data

In this section, the previous theoretical findings will be applied to analyze the dynamics of the solution stochastic process to the random generalized logistic model (7.2.10), through its PDF and main moments (mean and variance). This analysis is first performed via two numerical examples, and afterward using real-world data. As several numerical challenges may appear when solving model (7.2.10), we shall also recall a number of deterministic and probabilistic tools that will be used in the examples.

Subsection 6.4.1 gives a brief summary of the numerical scheme used, previously described in Chapter 5, used to solve the Liouville equation. Afterward, in Subsections 6.4.2 and 6.4.3, a brief presentation of a metaheuristic optimization algorithm (Particle Swarm Optimization algorithm) and a method to construct reliable PDFs from sampled information (Principle of Maximum Entropy) will be given, respectively. Finally, in Subsections 6.4.4 and 6.4.5, an application of the numerical procedures to some numerical examples and a full study of a real-world case of microbial growth data will be discussed, respectively.

6.4.1 Solving the Liouville equation numerically

We analyze the numerical evolution of the PDF as the solution to the Liouville equation through its characteristic curves (see Equations (2.2.4) to (2.2.6)) [47, Sec. 3.2]. We have used the Runge-Kutta 4 (RK4) integrator to approximate the characteristic curves, and the Simpson rule for the computation of the integral in (2.2.6) [105]. Each specific example 6.4.4 and 6.4.5 will include the particular time step used in the respective example.

Also, in order to accelerate computations, we have used AMR as described in Chapter 5. Finally, instead of the RBF interpolation, we used linear interpolation because of its simplicity and availability in 1D models.

6.4.2 PSO algorithm

The Particle Swarm Optimization (PSO) algorithm is an optimization algorithm widely used in cases where the parameters to be optimized are not in a discrete set. In short, it generates a number of particles (combinations of possible optimal values) where a certain fitness function (FF) is evaluated. Taking into account the values of the FFs at those points, the particles are updated by imitating the behavior of birds when searching for food [147]. We will take advantage of this optimization technique to search for the best estimates for model parameters in the subsequent examples.

6.4.3 PME

There are various ways of assigning distributions to random variables or vectors. One of them is the so-called Principle of Maximum Entropy (PME [62] or MaxEnt [148]). This data-driven method seeks to obtain a PDF that captures the maximum uncertainty (which is measured by the so-called *Shannon Entropy functional*) from the available sampled information (usually described via the moments such as the mean, variance, etc.) about the random variable [61]. In this chapter we will only use the mean and variance, since adding more moments does not change the resulting PDF noticeably in this case. In Subsection 5.6, this method is applied to assign a PDF to a set of real data.

Mathematically speaking, we want to compute the following:

$$f_{\text{sample}} = \arg\max \left\{ \int_{\mathcal{D}} f(y) \log(f(y)) \mathrm{d}y \,|\, f \in \mathrm{L}^1(\mathcal{D}),\ f \geq 0 \right\},$$

subject to the following constraints

$$\begin{aligned} \textstyle\int_{\mathcal{D}} f(y)\mathrm{d}y &= 1, \\ \textstyle\int_{\mathcal{D}} y\, f(y)\mathrm{d}y &= \mu_{\text{sample}}, \\ \textstyle\int_{\mathcal{D}} y^2\, f(y)\mathrm{d}y &= \sigma^2_{\text{sample}} + \mu^2_{\text{sample}}. \end{aligned}$$

Here $\mathcal{D}$ denotes the domain of the random variable Y. Using the Lagrange multiplier method, it can be shown that the PDF has the following form [65]

$$f_{\text{sample}}(y) = \exp\{-1 - \lambda_0 - \lambda_1\, y - \lambda_2\, y^2\},$$

where λ_0, λ_1 and λ_2 are the *Lagrange multipliers*. These values are determined by solving the system defined by the constraints, which usually requires numerical methods since it is often nonlinear in λ_0, λ_1 and λ_2.

6.4.4 Numerical Example

In this section, we will take advantage of the mathematical tools summarized in Subsections 6.4.1–6.4.3 to compute and visualize the dynamical behavior of the PDF of the solution stochastic process for the generalized logistic model (7.2.10). We will assume that $t_0 = 0$ and that t is measured in hours. First, two numerical examples will be shown in order to introduce a brief idea about how the numerical solution performs. Then we will solve an inverse problem with real-world data. All computations in the following sections have been performed in an AMD Ryzen 5800H-based laptop computer with 16 GB of RAM.

Deterministic coefficients

Only the initial condition is assumed a random variable which follows a symmetric triangular distribution with parameters 1.1, 1.3, whose mode is located at 1.2. It can be seen in Figure 6.1. The rest of model parameters, A, B and K, are assumed deterministic. We have considered two scenarios, Case 1 and Case 2, where only the value of B differs (see Table 6.1). In this way, we can better observe the role that parameter B plays in the model (this can repeated for the rest of model parameters). It is important to note, however, that the support of the PDF must be contained inside the interval $[0, K]$ in all times; that is, $\text{supp}\{f([0, +\infty), \cdot)\} \subset [0, K]$. This is due to the nature of the model, which assumes that K is the carrying capacity, or asymptotic equilibrium state. We have chosen our initial high resolution grid to consist of 4096

points. Figures 6.2 and 6.3 show the time evolution of the PDF in Cases 1 and 2, respectively, along with the expectation and standard deviation functions. The whole computation took about 0.6 seconds.

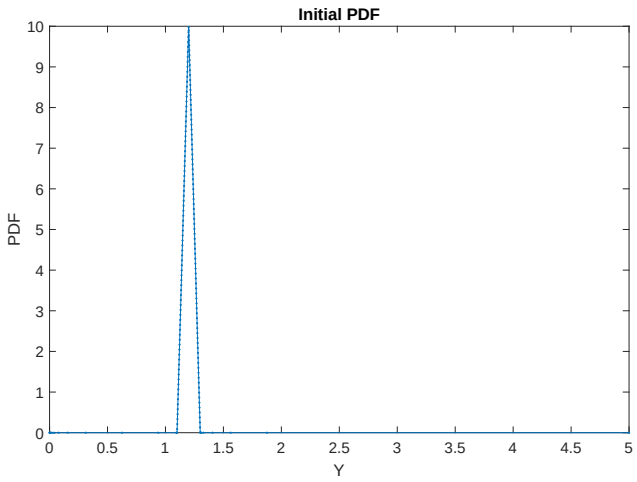

Figure 6.1: Triangular distribution PDF used as initial condition for both numerical examples in Section 6.4.4.

	Case 1			Case 2		
Parameter	A_1	B_1	K_1	A_2	B_2	K_2
Value	0.33	1	5	0.33	2.5	5

Table 6.1: Parameter values used in Case 1 (A_1, B_1, K_1) and Case 2 (A_2, B_2, K_2), respectively. Numerical Example.

Note that there are some similarities between both simulations. In particular, we can see that both simulations converge to a stationary value (the carrying capacity, $K = 5$) and their standard deviations decay to zero as this happens. This is to be expected because of the fact that the mean-square solution of the random IVP is also a pathwise solution of the random IVP. The carrying capacity is a globally asymptotically stable state of both the logistic and the generalized logistic equations. This means that, independently of the initial

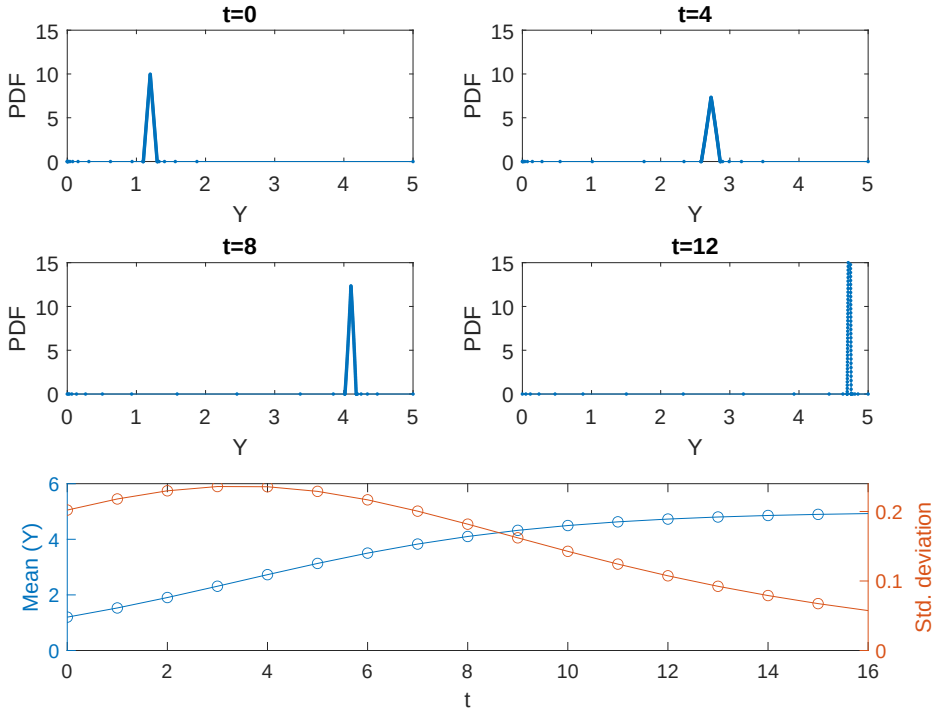

Figure 6.2: Top four panels: PDF of the solution stochastic process to the generalized logistic equation model (7.2.10) at different time instants (in hours). Bottom panel: Mean (blue, left axis) and standard deviation (orange, right axis) of the solution stochastic process. Case 1 (Numerical Example). Maximum absolute error in the PDF total mass: $\sim 5.3 \cdot 10^{-4}$.

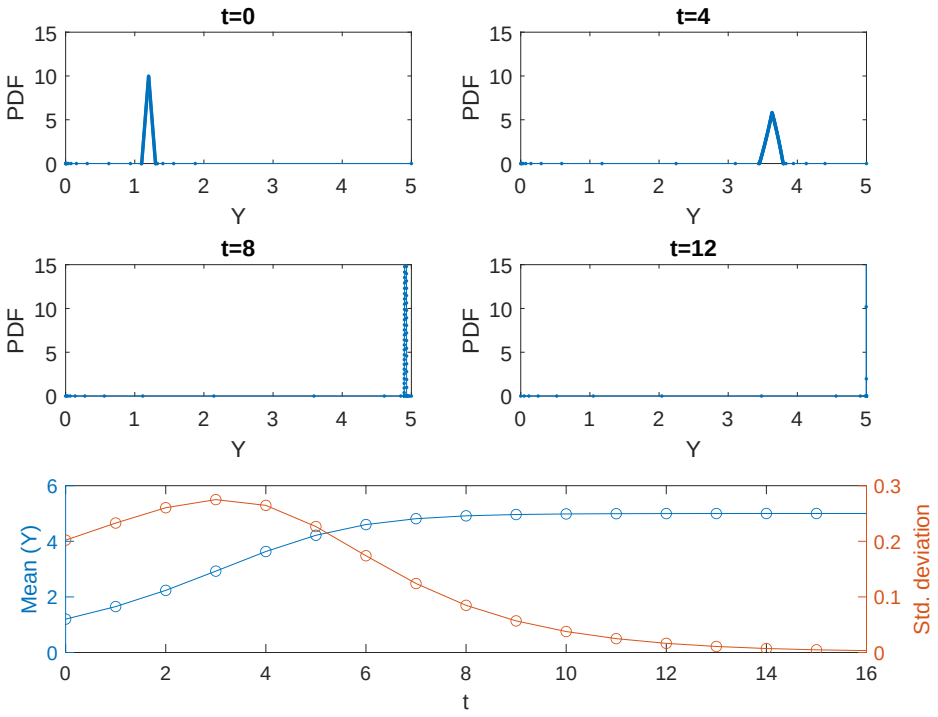

Figure 6.3: Top four panels: PDF of the solution stochastic process to the generalized logistic equation model (7.2.10) at different time instants (in hours). Bottom panel: Mean (blue, left axis) and standard deviation (orange, right axis) of the solution stochastic process. Case 2 (Numerical Example). Maximum absolute error in the PDF total mass: $\sim 6.1 \cdot 10^{-3}$.

value and the values for $A > 0$ and $B > 0$, all paths corresponding to the realizations of both the initial condition and the coefficients will approximate the carrying capacity value as time goes on. It is also noteworthy that the integral of the PDF, in the whole domain, is very close 1 at every timestep. This property of the PDF has been used to check the numerical approximations of the PDF when solving the Liouville's PDE are reliable at every timestep.

There also are some differences between both scenarios. In Case 1, it can be seen how standard deviation has a smooth growth and posterior decay to zero. Also, the mean curve shows a very gentle logistic-type curve, as it was expected due to the theoretical development in previous sections. However, Case 2, where the deceleration parameter is increased to 2.5, shows a sharper growth and decay of the standard deviation. Correspondingly, the mean curve stabilizes much faster than in Case 1.

6.4.5 Real-world Example

In this subsection, we are going to apply the theoretical and numerical concepts and findings discussed in previous sections to a real data set regarding the growth of a biological culture studied at [66]. Measurements were obtained by specialized fluorescent imaging techniques whose measurement units are known as Optical Density (OD). The means of the measurements at each measured time can be seen in Table 6.2. All details about the biological and experimental procedures can be found at [66].

By applying the PME technique to the data regarding the set of measurements at time $t_0 = 0$, we assign an initial PDF with the form described in Section 6.4.3. Particularly, we remind that the PDF has the form

$$f_0(y) = \exp\{-1 - \lambda_0 - \lambda_1\, y - \lambda_2\, y^2\}, \tag{6.4.1}$$

where the λ_i are the ones defined in Table 6.3. In Figure 6.4, we have plotted this PDF. It has been calculated by the wavelet compression-based adapted

Time (h.)	Mean (OD)	Time (h.)	Mean (OD)
0.000	0.286	3.547	0.527
0.233	0.308	3.828	0.547
0.465	0.331	4.061	0.558
0.698	0.354	4.294	0.569
1.001	0.383	4.527	0.581
1.234	0.403	4.759	0.590
1.466	0.416	4.992	0.597
1.839	0.437	5.275	0.608
2.072	0.450	5.508	0.612
2.304	0.464	5.740	0.616
2.537	0.476	6.039	0.616
2.849	0.486	6.271	0.617
3.081	0.500	6.503	0.617
3.315	0.514	6.803	0.619

Table 6.2: Time at which measurements are taken with the mean of the measurements. 28 measurements were taken at each time. The variance was only computed in the first time, in order to use the PME. Measurements were obtained by specialized fluorescent imaging techniques whose measurement units are known as Optical Density (OD). More details about the data and how it was collected in [66]. Real-world Example.

λ_0	λ_1	λ_2
443.84321	-3132.90787	5470.16958

Table 6.3: Lagrange's multipliers obtained in the PME method (see Subsection 6.4.3 for further details about the computation of the Lagrange's multipliers). Real-world Example.

mesh. It can clearly be seen where there is a higher concentration of points. These points are obtained exactly where the function has a larger gradient.

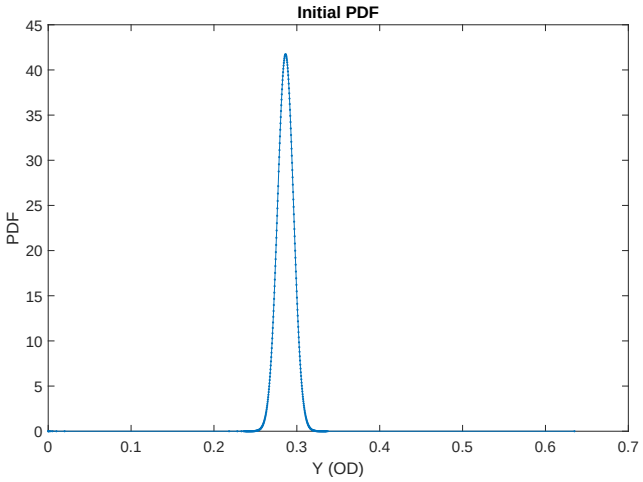

Figure 6.4: PDF at $t_0 = 0$ used as the initial condition for the Liouville's PDE (see expression 6.4.1 and Table 6.3). Initial high resolution grid of 4096 points. Adapted grid with 330 points. Real-world Example.

Deterministic coefficients

First, the deterministic parameter values are determined in order to have a first, expected representation of the sample data. Since the PDE computation time is relatively fast, we can use the PSO algorithm directly from the PDE itself. The computational procedure used for this purpose consists of the following steps, and it is shown in the flowchart depicted in Figure 6.5:

1. Extract growth data from the data set, $\mathbf{Y}_i$, at each time measurement t_i. At this point we have a collection of 24 measurements per time instant, with a total of 28 measurements; that is, we have $\{(t_i, \mathbf{Y}_i)\}_{i=1}^{28}$, where $\mathbf{Y}_i = (Y_i^1, \ldots, Y_i^{24})$.
2. Compute the initial density, f_0, in its adapted grid $\mathcal{G}_0$, using the PME. Also, compute the mean of the measurement vectors, $\overline{Y}_i = \frac{1}{24}\sum_{j=1}^{24} Y_i^j$

at each time instant t_i, $i = 1, \ldots, 28$. At this point, we have the initial PDF, $f_0(\mathcal{G}_0)$, and the curve of the sample means $\{(t_i, \overline{Y}_i)\}_{i=1}^{28}$.

3. We now enter the PSO algorithm (see Subsection 6.4.2). In the present work, we have used 60 particles and a maximum of 100 iterations. The parameter values used for the evaluation of the error function may be computed in two different ways depending on whether it is the first iteration or not.
   - In the first case, 60 points are generated at random positions in the parameter space; that is, $\{(A_l, B_l, K_l)\}_{l=1}^{60}$.
   - In the latter case, the same number of points are generated following a very specific set of rules [147], returning the updated set of parameter values $\{(A'_l, B'_l, K'_l)\}_{l=1}^{60}$.
4. After the set of parameter values has been defined (let it be at the first iteration or after an update), we compute the numerical solution of the PDF at each of the time instants $\{t_i\}_{i=1}^{28}$ using the Lagrangian approach (see Subsection 6.4.1). At this point we have a family of PDFs and their corresponding adapted grids; that is, $\{f(\mathcal{G}_i, t_i \,|\, A, B, K)\}_{i=1}^{28}$ for each tuple of parameter values $(A, B, K) \in \{(A_l, B_l, K_l)\}_{l=1}^{60}$. Note that we have dropped the conditional PDF notation in the following steps for the sake of simplicity.
5. For each of the PDFs defined as in the previous step, we compute their respective expectations, denoted by $\{\overline{f(\mathcal{G}_i, t_i)}\}_{i=1}^{28}$, and compute its absolute error respect to the sample mean $\overline{Y}_i$ at each time instant t_i. We then compute the sum of these absolute errors; that is

$$\text{Error} = \sum_{i=1}^{28} |\overline{f(\mathcal{G}_i, t_i)} - \overline{Y}_i|.$$

6. Now, if the following absolute error

$$\text{Error} = \sum_{i=1}^{28} |\overline{f(\mathcal{G}_i, t_i)} - \overline{Y}_i|$$

varies below a given threshold, among all generated (A, B, K), which the authors have chosen as 10^{-9}, we keep the tuple of parameter values with

the best fitness function value, (A^*, B^*, K^*). If not, we update the set of parameter values and we start at point (3) of the present description.

The optimal values obtained as the PSO procedure output, as defined in Figure 6.5, can be found in Table 6.4. Figure 6.6 shows the numerically computed PDF using the optimal values collected in Table 6.4. 60 particles were used in order to compute an optimum and the PSO ended after 100 iterations with an error tolerance of 10^{-9}. It is worth noting that the whole optimization procedure takes about 9 minutes to compute in an AMD Ryzen 7 5800H, whereas the simulation itself takes around 0.4 seconds to carry out calculations. Both cases were simulated with a $\Delta t = 0.005$ time step in the Lagrangian method. We refer to Figure 6.6 for more information.

Note that the objective function to be minimized by the PSO is not necessarily convex, so no global minimum is assured. Therefore, the parameter tuple given by the PSO algorithm may not be the global minimum of the error function defined in step 6 of the procedure explanation. However, as seen in Figures 6.6-6.8, they provide a parameter vector that allows approaching the real data with reasonable accuracy. In Figure 6.7 we have plotted the average or sample mean of the sample data together with the mean and a confidence interval constructed as mean plus/minus 3 standard deviations both obtained from repeatedly solving the Liouville's PDE sampling the initial condition from its PDF, $f_0(y)$. We can observe that this confidence interval captures most of the uncertainty at every time instant and, when computing the integral in the corresponding intervals, we obtain values of approximately 0.9, so we are representing a confidence interval of 90%.

Finally, in Figure 6.8, absolute and relative errors between the mean computed from sampled data and the Liouville's PDF are shown. Notice that graphical representations shown in Figures 6.7 and 6.8 are in full agreement. It is interesting to see the oscillation of the error functions in Figure 6.8 which shows that, for this particular data set, we have an appropriate fit given by the generalized logistic model. We have obtained a parameter vector that allows us to represent the expected behavior of the biological population under study. Non-oscillatory error functions would be given by a fit that is always

above (over-predicting), or below (under-predicting), the mean curve. This would mean that the generalized logistic model is incapable of representing the dynamics of this data set appropriately. Moreover, as the biological culture approaches its steady state, we will have a lower variability and, in theory, the amplitude will eventually decrease and stabilize.

A^*	B^*	K^*
0.4911	1.5212	0.635

Table 6.4: Optimal model parameters. Real-world Example with deterministic parameters.

Random coefficients

In order to perform realistic simulations taking into account the uncertainty in model parameters, probability distributions are assigned in such a way that the expectation of these distributions match their corresponding deterministic optimal values collected in Table 6.4. In our subsequent calculations, this will be assumed for model parameters A and B, that is,

$$A^* = \int_\Omega A(\omega)\,\mathrm{d}\mathbb{P}(\omega), \quad B^* = \int_\Omega B(\omega)\,\mathrm{d}\mathbb{P}(\omega),$$

while $K = K^* = 0.635$ will be taken as the deterministic optimal value (see Table 6.4) since from its own biological interpretation its variability is negligible with respect to the one of A and B.

Probability distributions for A and B have been assigned following particular biological reasons. They are assigned a priori in such a way that the support of their corresponding PDFs makes sense in this biological problem; for example $A > 0$ and $B > 0$. Particularly, we have chosen $A \sim \mathrm{Exp}(1/A^*)$ and $B \sim \mathrm{Unif}(B^*(1-0.15), B^*(1+0.15))$; that is, an Exponential distribution whose expectation is A^* (recall that the mean of an exponential distribution is the

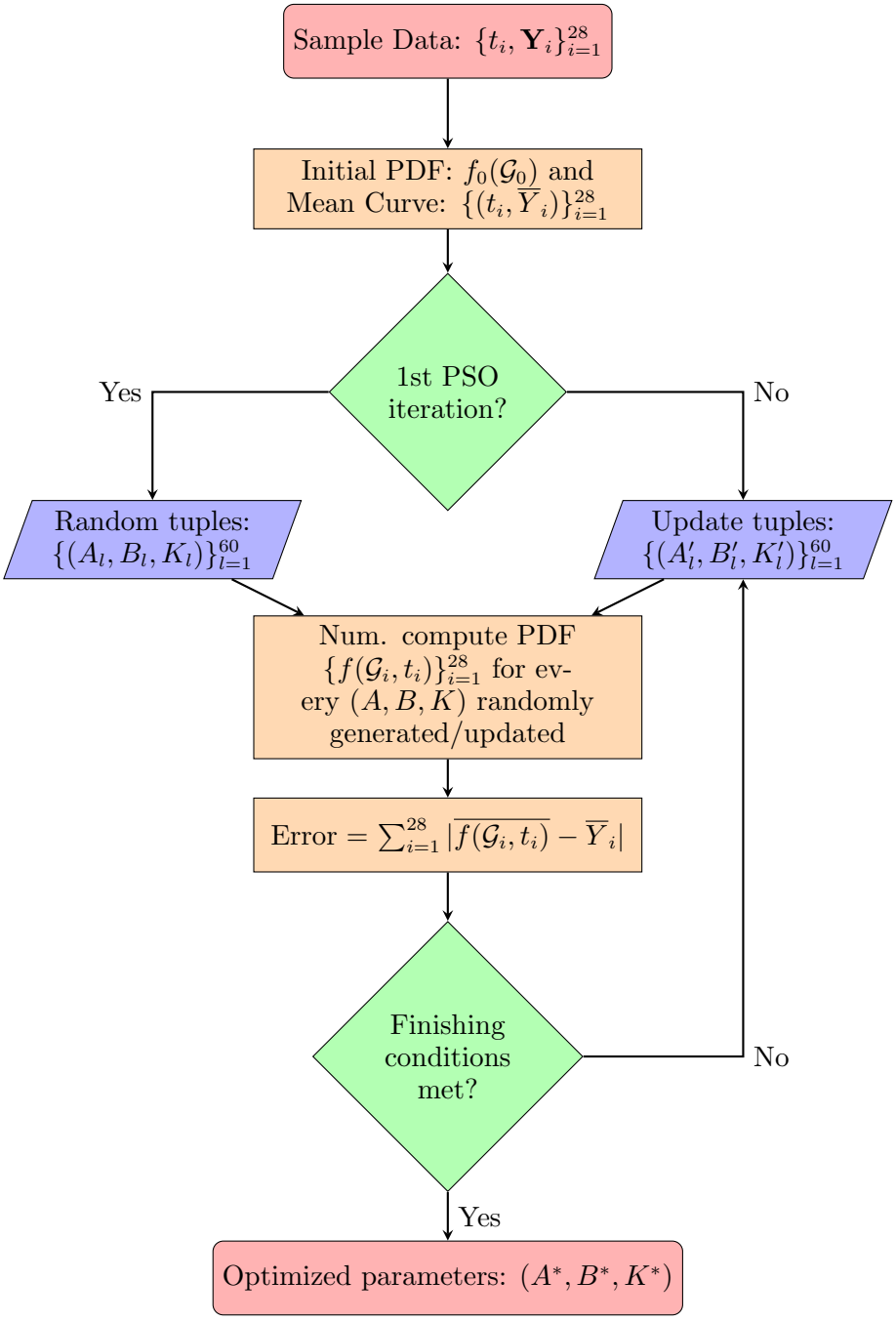

Figure 6.5: Flowchart describing the entire PSO-based optimization procedure for deterministic parameters. Real-world Example with deterministic parameters.

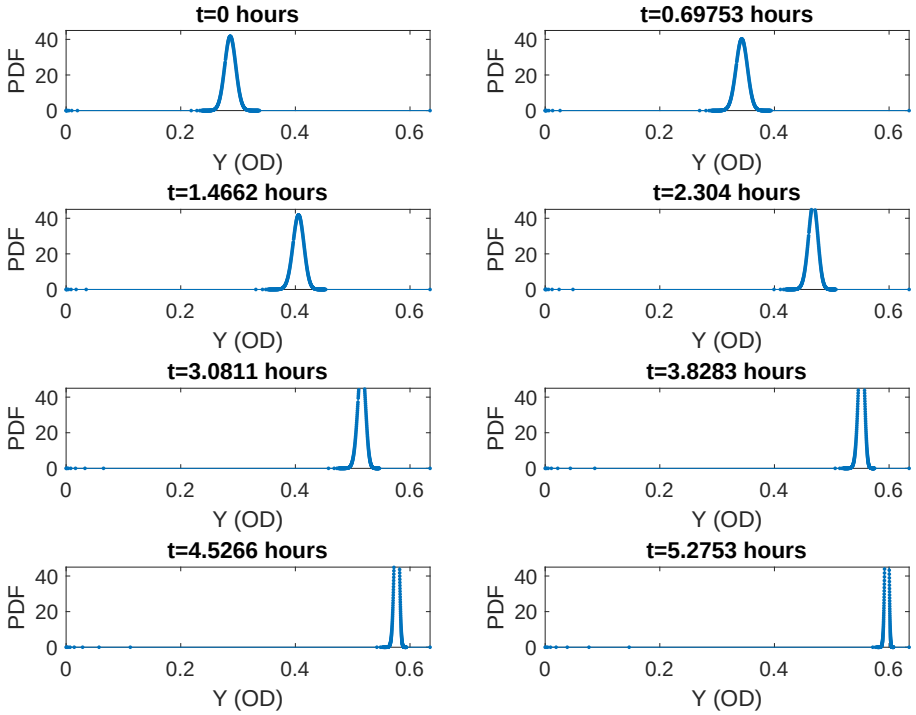

Figure 6.6: Time evolution of the PDF with model parameters given in Table 6.4. Real-world Example with deterministic parameters. Maximum absolute error in the PDF total mass: $\sim 6.7 \cdot 10^{-4}$.

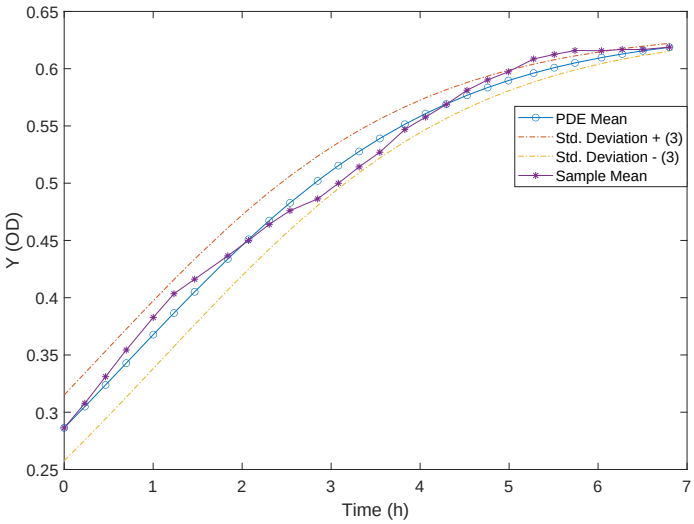

Figure 6.7: Mean of the PDF obtained by solving the Liouville PDE along with a confidence interval centered at the mean with a 3 standard deviation radius. Starry points denote the sample mean at each of the time instants. Real-world Example with deterministic parameters.

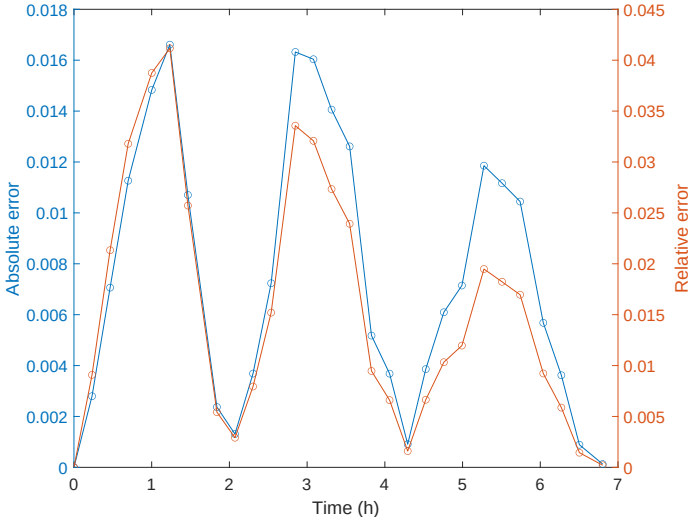

Figure 6.8: Absolute error (left axis, blue curve) and relative error (right axis, orange curve) of the mean of the PDF computed by the Liouville PDE with respect to the sample data. Real-world Example with deterministic parameters.

inverse of its parameter) and a Uniform distribution centered at B^* with a 15% support radius interval, respectively.

Now, simulations of the full 28 time values of Table 6.2, that is, up to time 6.803 hours, are computed. Figure 6.9 shows the simulated PDFs at several time instants. Full simulation with random coefficients and a 4096-point base grid was performed in just over 37 minutes, with a timestep of $\Delta t = 0.005$.

As previously indicated, note that we have assumed the carrying capacity to be a constant, $K = K^* = 0.635$. Also note in Figures 6.10 and 6.11 that the optimization procedure returned a set of parameters that allows a very good description of the sample data with the distributions chosen for A and B. As in the case of the deterministic coefficients, we can observe an oscillation of the error functions which again is a sign of a coherent fit to the mean data curve. Notice that there is a slight difference in the amplitude of the oscillations. This difference is natural and it is because of the nature of both problems. The case of deterministic coefficients consists in obtaining the PDF of a stochastic process depending on a single random variable, that is, the initial condition. The second case, which is represented in Figures 6.10 and 6.11, consists in obtaining the PDF of a stochastic process where 3 of its parameters are random variables. Moreover, the relationship between the solution stochastic process and its parameters is nonlinear. This is reflected in the evolution of its PDF as it can be seen when comparing Figures 6.7 and 6.8 with 6.10 and 6.11.

6.5 Conclusion

With the aim of extending recent studies performed for the logistic random differential equation and the Gompertz random differential equation, in this chapter we have investigated the generalized logistic random differential equation. This equation includes a power term into the classical logistic model, to better control how fast the limiting capacity is approached. We have as-

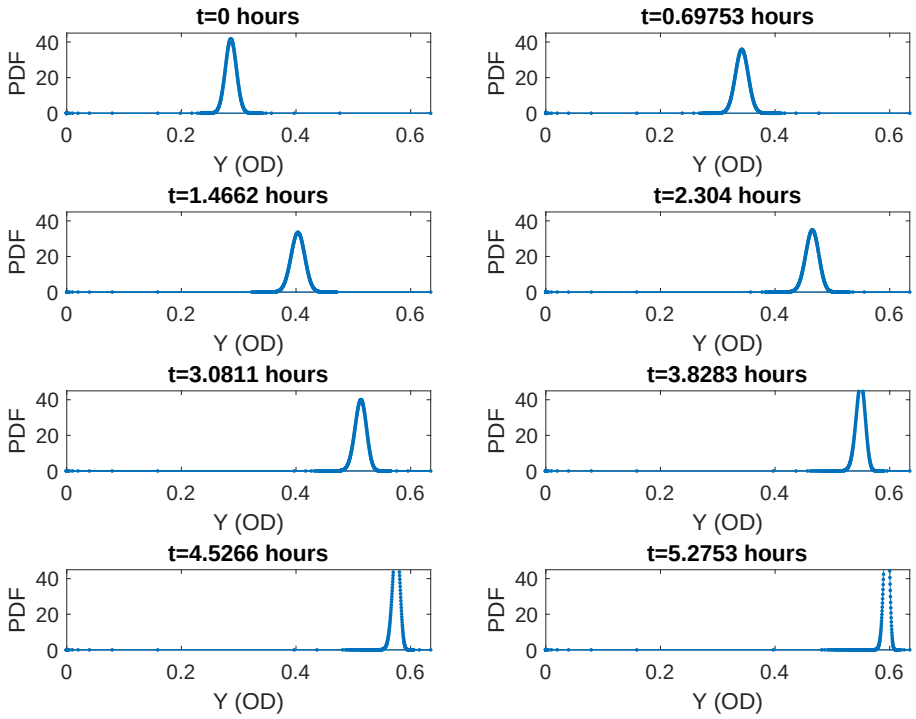

Figure 6.9: Time evolution of the PDF. Real-world Example with random parameters. Maximum absolute error in PDF mass: $\sim 4.8 \cdot 10^{-5}$.

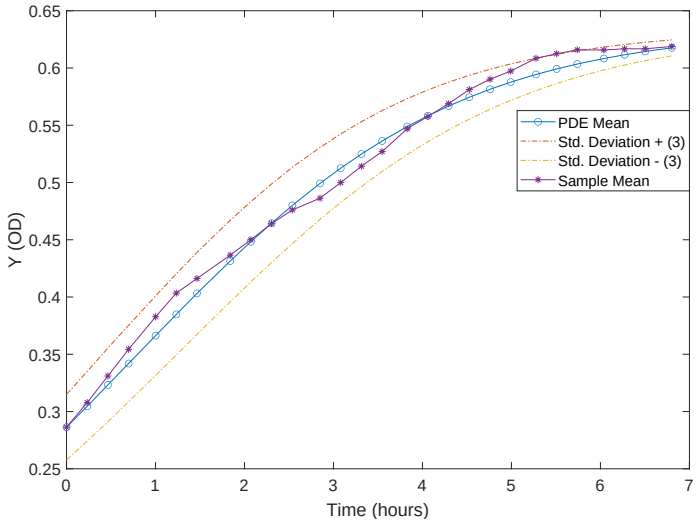

Figure 6.10: Mean of the PDF obtained by solving the Liouville PDE along with a confidence interval centered at the mean with a 3 standard deviation radius. Starry points denote the sample mean at each time instant. Real-world Example with random parameters.

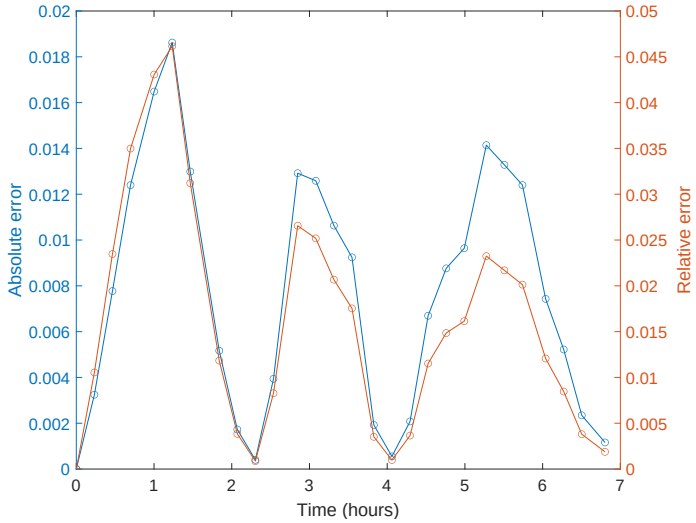

Figure 6.11: Absolute error (left axis, blue curve) and relative error (right axis, orange curve) of the mean of the PDF computed by the Liouville PDE with respect to the sample data. Real-world Example with random parameters.

sumed that the parameters are random variables. Then, we have obtained the sample-path and mean-square solution rigorously, and we have computed its Probability Density Function by applying the Random Variable Transformation technique and the Liouville's equation. We have analyzed how the model reduces to the classical logistic equation and the Gompertz equation when the power tends to 1 and 0 in a probabilistic sense.

Furthermore, we have made use of a type of numerical methods specially suited for the computation of the solution of partial differential equations such as Liouville's equation, where convection is the main dynamical behavior of the solution. It has first been applied to a case with deterministic coefficients and it has been extended to the scenario where coefficients are given by random variables. Afterwards, an optimization procedure based on the Particle Swarm Optimization algorithm has been implemented. Its objective has been to obtain the deterministic coefficient values which allow describing the mean behavior of the biological culture growth data set.

Publications

The results presented in this thesis chapter have been published in [149]. In regard to this chapter, the PhD candidate has contributed by working on its complete development with more emphasis on the theoretical results and preparing the visualization of the numerical examples.

Some results of this chapter have also been presented at the Mathematical Modeling in Engineering and Human Behavior in Valencia (Spain) from June 14-16th, 2021. The talk, titled *Density-based uncertainty quantification in a generalized Logistic-type model*, was published in the conference proceedings with ISBN: 978-84-09-36287-5. A similar work, using the techniques and approach seen in this chapter was presented at the GECCO conference in Boston (USA) and was published as a conference paper [150].

Chapter 7

Random systems with impulses

This chapter aims at studying a general class of random differential equations with Dirac-delta impulse terms at a finite number of time instants via its probability density function. We consider the case of additive impulses and multiplicative impulses. We combine the Liouville equation and the random variable transformation method to conduct our study. Finally, all our theoretical findings are illustrated on two stochastic models, widely used in mathematical modeling, for which numerical simulations are carried out using the computational approach described in Chapter 5.

Most natural phenomena can be mathematically described as a function evolving smoothly with respect to time, solving a differential equation. The models studied previously in Chapters 3, 4 and 6 are good examples of such smoothly-evolving systems. However, there are cases where the system suddenly changes its state. For example, one may be interested in the dynamical response of a spring-damper system on a train when advancing from one set of rails to the next. The system could be destroyed if the oscillations are near its resonant frequencies. Analyzing these dynamics requires special mathematical tools; we must consider differential equations with impulses.

This chapter is organized as follows. Section 7.1 is divided into two parts; in Subsection 7.1.1, we rigorously build pathwise solutions of two kinds of RDEs with impulses: systems with additive impulses and systems with state-dependent impulses. Then, in Subsection 7.1.2, we apply the Liouville equation to obtain the corresponding 1-PDF of the solution of the abovementioned two classes of RDEs. We will place particular emphasis on determining the 1-PDF behavior at the interface of the discontinuities due to the application of the impulses. We will do so without any knowledge of the explicit form of the field function of the corresponding RDE. This results in the application of the Liouville equation approach to general RDEs. To illustrate this latter fact, in Section 7.2, we apply the theoretical findings to devise a computational procedure for some relevant linear and nonlinear models widely used in biology, medicine, and engineering. Conclusions are drawn in Section 7.3.

Note that in all cases $t_0 \geq 0$ denotes the initial time of the system, $\mathbf{X}^0(\omega) = (X_1^0(\omega), \ldots, X_d^0(\omega)) \in \mathrm{L}_2^d(\Omega, \mathbb{P})$, $\mathbf{A}(\omega) := (A_1(\omega), \ldots, A_m(\omega)) \in \mathrm{L}_2^m(\Omega, \mathbb{P})$ and $\{\mathbf{\Gamma}^k(\omega) = (\Gamma_1^k(\omega), \ldots, \Gamma_d^k(\omega))\}_{k=1}^N \subset \mathrm{L}_2^d(\Omega, \mathbb{P})$ are assumed to be real-valued pairwise independent absolutely continuous random vectors. The $\delta(t - t_k)$ stands for the Dirac delta function [85] acting at the prefixed time instants $t = t_k$, $k = 1, \ldots, N$ and $\mathbf{v}$ is the *(vector) field function* satisfying the same conditions stated in Equation (2.1.8). For simplification, the ω-dependence notation will be omitted when convenient.

7.1 Theory

This section will deal with the theoretical probabilistic analysis of the following class of impulsive random IVPs:

$$\begin{cases} \dfrac{\mathrm{d}\mathbf{X}}{\mathrm{d}t}(t,\omega) &= \mathbf{v}(\mathbf{X}(t,\omega),t,\mathbf{A}(\omega)) - \displaystyle\sum_{k=1}^{N} \mathbf{\Gamma}^k(\omega)\delta(t-t_k), \quad t > t_0, \\ \mathbf{X}(t_0,\omega) &= \mathbf{X}^0(\omega), \end{cases} \tag{7.1.1}$$

and

$$\begin{cases} \dfrac{\mathrm{d}\mathbf{X}}{\mathrm{d}t}(t,\omega) &= \mathbf{v}(\mathbf{X}(t,\omega),t,\mathbf{A}(\omega)) - \displaystyle\sum_{k=1}^{N} \mathbf{\Gamma}^k(\omega) \odot \mathbf{X}(t,\omega)\delta(t-t_k), \quad t > t_0, \\ \mathbf{X}(t_0,\omega) &= \mathbf{X}_0(\omega), \end{cases} \tag{7.1.2}$$

where $\odot$ is the Hadamard product applied to vectors $\mathbf{\Gamma}^k$ and $\mathbf{X}(t,\omega)$, both defined in $\mathbb{R}^{d1}$.

Observe that we set the impulse terms with the negative sign because, in most practical cases, one is often interested in the instantaneous change of the system's state in a way opposite to its *natural* dynamics.

The existence and uniqueness properties of solutions to the random IVPs defined by Equations (7.1.1) and (7.1.2) have some dependence on the realizations of the parameter random vector $\mathbf{A}(\omega), \omega \in \Omega$ (see [12, Appendix I]). One can guarantee the existence and uniqueness of solutions *between* the impulses $t = t_k$ generated by the Dirac delta function $\delta(t - t_k)$ in the sample/pathwise sense by imposing classical regularity assumptions on the regularity of $\mathbf{v}(\cdot, t, \mathbf{A}(\omega))$. Let us recall the ones considered in Equation (7.1.1): we can assume that the event $\tilde{\Omega} = E_1 \cap E_2$, where

$$E_1 = \{\omega \in \Omega : \mathbf{v}(\cdot, t, \mathbf{A}(\omega)) \text{ is Lipschitz in } \mathbb{R} \text{ uniformly in } t\},$$
$$E_2 = \{\omega \in \Omega : \mathbf{v}(\mathbf{x}, \cdot, \mathbf{A}(\omega)) \text{ is continuous in } [t_0, \infty) \text{ for all } \mathbf{x} \in \mathbb{R}\},$$

[1] The Hadamard product between two matrices $\mathbf{A}, \mathbf{B} \in \mathbb{R}^{M\times N}$ is defined as the element-wise product; that is, a matrix $\mathbf{C} \in \mathbb{R}^{M\times N}$ such that $C_{ij} = A_{ij}B_{ij}$.

has probability 1, i.e., $\mathbb{P}[\tilde{\Omega}] = 1$. One can then guarantee the existence of a global solution between the impulses sequence $\{t_k\}_{k=1}^{N}$. In particular, this behavior implies the following conditions (see Figure 7.1):

1. Continuous differentiability in (t_{k-1}, t_k), $k = 1, \ldots, N$.
2. Existence and finiteness of $\mathbf{X}(t_k^+) := \lim_{t \to t_k^+} \mathbf{X}(t)$ for all $k = 0, \ldots, N$ and $\mathbf{X}(t_k^-) := \lim_{t \to t_k^-} \mathbf{X}(t)$ for $k = 1, \ldots, N$.
3. Uniqueness of the solution in (t_{k-1}, t_k) given $\mathbf{X}(t_{k-1}^+)$, $\mathbf{X}(t_k^-)$ or some $\mathbf{X}(t^*)$, with $t^* \in (t_{k-1}, t_k)$, for $k = 1, \ldots, N$.

In summarizing, a *priori*, we can not guarantee the existence or uniqueness of a solution to the random IVPs defined by Equations (7.1.1) and (7.1.2). However, as shown in the following section, classical regularity assumptions are sufficient to ascertain each sample trajectory's global existence.

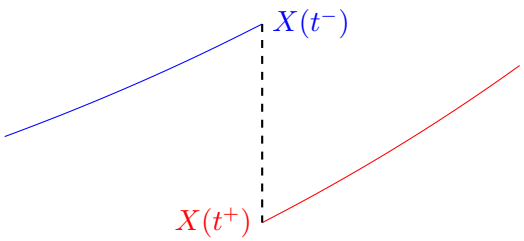

Figure 7.1: Path solution to (7.1.1) in a neighborhood of an impulse time. Conditions (1)-(3) are clearly reflected in this example.

7.1.1 Pathwise (weak) solution

We will first build a pathwise solution for the random IVP (7.1.1) considering the previous paragraphs' comments. The proof for (7.1.2) is very similar to this one, but there are some details that we will point out later.

Additive impulse

Let us fix $\omega \in \tilde{\Omega}$ and compute the deterministic Laplace transform [151] to the corresponding IVP (7.1.1)[2]. Denoting $\lambda(s) = \mathcal{L}[\mathbf{X}(\cdot, \omega)](s)$, $\mathbf{X}^0 = \mathbf{X}^0(\omega)$, $\mathbf{a} = \mathbf{A}(\omega)$ and, momentarily dropping the ω notation, we obtain

$$s\lambda(s) - \mathbf{X}^0 = \mathcal{L}[\mathbf{v}(\mathbf{X}(\cdot), \cdot, \mathbf{a})](s) - \sum_{k=1}^{N} \mathbf{\Gamma}^k \mathrm{e}^{-st_k}.$$

Solving for $\lambda(s)$:

$$\lambda(s) = \frac{1}{s}\mathbf{X}^0 + \frac{1}{s}\mathcal{L}[\mathbf{v}(\mathbf{X}(\cdot), \cdot, \mathbf{a})](s) - \sum_{k=1}^{N} \mathbf{\Gamma}^k \frac{\mathrm{e}^{-st_k}}{s}. \tag{7.1.3}$$

Computing the inverse Laplace transform of (7.1.3) gives

$$\mathbf{X}(t) = \mathbf{X}^0 + \int_{t_0}^{t} \mathbf{v}(\mathbf{X}(s), s, \mathbf{a})\mathrm{d}s - \sum_{k=1}^{N} \mathbf{\Gamma}^k \mathrm{H}(t - t_k), \tag{7.1.4}$$

where $\mathrm{H}(\cdot)$ is the Heaviside function, defined as

$$\mathrm{H}(u) = \begin{cases} 1 & u \geq 0, \\ 0 & u < 0. \end{cases} \tag{7.1.5}$$

Notice that expression (7.1.4) is the integral form of Equation (7.1.1), where $\delta(\cdot)$ acts as a measure [153]. Substituting $t = t_1$ and taking into account

[2] See [152] for a useful table on Laplace transforms, some of which have been used in the present discussion.

(7.1.5), yields

$$\mathbf{X}(t_1) = \mathbf{X}^0 + \int_{t_0}^{t_1} \mathbf{v}(\mathbf{X}(s), s, \mathbf{a})\mathrm{d}s - \mathbf{\Gamma}^1 = \lim_{t \to t_1^-} \mathbf{X}(t) - \mathbf{\Gamma}^1 := \mathbf{X}(t_1^-) - \mathbf{\Gamma}^1.$$

Now, let us see what happens after the impulse. From (7.1.4) and the previous relation for $\mathbf{X}(t_1)$, we can compute the jump induced in the paths by the impulse term

$$\mathbf{X}(t_1^+) - \mathbf{X}(t_1^-) = \int_{t_1^-}^{t_1^+} \mathbf{v}(\mathbf{X}(s), s, \mathbf{a})\mathrm{d}s - \mathbf{\Gamma}^1.$$

The integral term in the previous equation is the $\mathbf{0}$ vector:

$$\begin{aligned}\left\| \int_{t_1^-}^{t_1^+} \mathbf{v}(\mathbf{X}(s), s, \mathbf{a})\mathrm{d}s \right\| &\leq \lim_{\varepsilon \to 0} \left(\int_{t_1-\varepsilon}^{t_1} \|\mathbf{v}(\mathbf{X}(s), s, \mathbf{a})\|\mathrm{d}s + \int_{t_1}^{t_1+\varepsilon} \|\mathbf{v}(\mathbf{X}(s), s, \mathbf{a})\|\mathrm{d}s \right) \\ &\leq \lim_{\varepsilon \to 0} \left(\sup_{t \in [t_1-\varepsilon, t_1)} \|\mathbf{v}(\mathbf{X}(t), t, \mathbf{a})\|\varepsilon + \sup_{t \in (t_1, t_1+\varepsilon]} \|\mathbf{v}(\mathbf{X}(t), t, \mathbf{a})\|\varepsilon \right) \\ &= 0,\end{aligned}$$

because both supremum terms are finite due to the regular behavior of the solution between the impulse times. Summarizing, we have the following relations:

$$\mathbf{X}(t_1^+) - \mathbf{X}(t_1^-) = -\mathbf{\Gamma}^1 \iff \mathbf{X}(t_1^+) = \mathbf{X}(t_1) = \mathbf{X}(t_1^-) - \mathbf{\Gamma}^1. \tag{7.1.6}$$

The general solution (7.1.4) is right-continuous at the first impulse. Recovering the ω-notation, the previous identity is stated as

$$\mathbf{X}(t_1, \omega) = \mathbf{X}(t_1^+, \omega) = \mathbf{X}(t_1^-, \omega) - \mathbf{\Gamma}^1(\omega), \tag{7.1.7}$$

which shows that, for every sample $\omega \in \tilde{\Omega}$, the paths are right-continuous at $t = t_1$. We can proceed similarly for the following impulse times. For example,

for all $t \in [t_1, t_2]$, the solution process is given by

$$\mathbf{X}(t) = \mathbf{X}^0 + \int_{t_0}^{t} \mathbf{v}(\mathbf{X}(s), s, \mathbf{a})\mathrm{d}s - \mathbf{\Gamma}^1 \mathrm{H}(t - t_1) - \mathbf{\Gamma}_2 \mathrm{H}(t - t_2). \tag{7.1.8}$$

Now, by using (7.1.4), we see that, at time $t = t_2$, (7.1.8) can be written as:

$$\mathbf{X}(t_2) = \mathbf{X}(t_1) + \int_{t_1}^{t_2} \mathbf{v}(\mathbf{X}(s), s, \mathbf{a})\mathrm{d}s - \mathbf{\Gamma}_2,$$

which yields

$$\mathbf{X}(t_2) = \mathbf{X}(t_1) + \int_{t_1}^{t_2} \mathbf{v}(\mathbf{X}(s), s, \mathbf{a})\mathrm{d}s - \mathbf{\Gamma}_2 = \lim_{t \to t_2^-} \mathbf{X}(t) - \mathbf{\Gamma}_2 := \mathbf{X}(t_2^-) - \mathbf{\Gamma}_2.$$

Following the same reasoning we used to obtain relation (7.1.6), the value after the impulse will be

$$\mathbf{X}(t_2^+) - \mathbf{X}(t_2^-) = -\mathbf{\Gamma}_2 = \Longleftrightarrow \ \mathbf{X}(t_2^+) = \mathbf{X}(t_2^-) - \mathbf{\Gamma}_2.$$

The steps followed for analyzing the first and second impulse times can be easily generalized for any finite number of impulse times. Particularly, at a given impulse time t_k, and recovering the ω-notation one gets

$$\mathbf{X}(t_k^+, \omega) = \mathbf{X}(t_k, \omega) = \mathbf{X}(t_k^-, \omega) - \mathbf{\Gamma}^k(\omega), \tag{7.1.9}$$

for all $k = 1, \ldots, N$.

Summarizing, we have constructed a right-continuous pathwise solution of the random IVP (7.1.1), given by

$$\mathbf{X}(t, \omega) = \mathbf{X}^0(\omega) + \int_{t_0}^{t} \mathbf{v}(\mathbf{X}(s, \omega), s, \mathbf{A}(\omega))\mathrm{d}s - \sum_{k=1}^{N} \mathbf{\Gamma}^k(\omega)\mathrm{H}(t - t_k), \quad t \geq t_0, \tag{7.1.10}$$

$$\mathbf{X}(t_k^+, \omega) = \mathbf{X}(t_k, \omega) = \mathbf{X}(t_k^-, \omega) - \mathbf{\Gamma}^k(\omega), \quad k = 1, \ldots, N, \ \omega \in \tilde{\Omega}. \tag{7.1.11}$$

Multiplicative case

In this case, we will see the proof in the scalar equation case, although the same properties occur in higher-dimensional systems because of the behavior of the Hadamard product. That is, we will build a solution for the following scalar random IVP:

$$\begin{cases} \dfrac{\mathrm{d}X}{\mathrm{d}t}(t,\omega) &= v(X(t,\omega),t,\mathbf{A}(\omega)) - \displaystyle\sum_{k=1}^{N} \Gamma^k(\omega)\delta(t-t_k)X(t,\omega), \quad t > t_0, \\ X(t_0,\omega) &= X^0(\omega). \end{cases} \tag{7.1.12}$$

Once again, fixing $\omega \in \tilde{\Omega}$ and using the Laplace transform used to obtain Equation (7.1.4), one gets

$$X(t) = X^0 + \int_{t_0}^{t} v(X(s),s,\mathbf{a})\mathrm{d}s - \sum_{k=1}^{N} \Gamma^k X(t_k)H(t-t_k), \tag{7.1.13}$$

where $X^0 = X^0(\omega)$ and $\mathbf{a} = \mathbf{A}(\omega)$.

Now, the equivalent of (7.1.9) for this case would be:

$$X(t_1) = \frac{X^0 + \int_{t_0}^{t_1} v(X(s),s,\mathbf{a})\mathrm{d}s}{1+\Gamma^1} = \frac{\lim_{t\to t_1^-} X(t)}{1+\Gamma^1} := \frac{X(t_1^-)}{1+\Gamma^1}.$$

Let us emphasize the interesting transformations given by the previous equation. We have the following transformations:

1. The transformation will be well-defined (and invertible) if $\Gamma^1(\omega) \neq -1$.
2. If $\Gamma^1(\omega) = 0$, the identity transformation applies; that is, $X(t_1,\omega) = X(t_1^-,\omega)$.
3. If $\Gamma^1(\omega) \in (0,\infty)$, we will have $X(t_1,\omega) < X(t_1^-,\omega)$.
4. If $\Gamma^1(\omega) \in (-1,0)$, we will have $X(t_1,\omega) > X(t_1^-,\omega)$.
5. If $\Gamma^1(\omega) \in (-2,-1)$, we will have $X(t_1,\omega) < -X(t_1^-,\omega)$.
6. If $\Gamma^1(\omega) \in (-\infty,-2)$, we will have $X(t_1,\omega) > -X(t_1^-,\omega)$.

Note that the first condition in the previous list occurs almost surely (i.e., with unit probability) when Γ^1 is an absolutely continuous random variable.

Using the same reasoning as in Equation (7.1.7), and recovering the ω-notation, we arrive at the following relation between the states of the system at the first impulse time:

$$X(t_1^+, \omega) = X(t_1, \omega) = \frac{X(t_1^-, \omega)}{1 + \Gamma^1(\omega)}. \tag{7.1.14}$$

Following the same procedure as in the additive impulse case, we finally obtain:

$$X(t_k^+, \omega) = X(t_k, \omega) = \frac{X(t_k, \omega)}{1 + \Gamma^k(\omega)}, \qquad k = 1, \ldots, N. \tag{7.1.15}$$

We can easily generalize this to the general multidimensional system case because what we have shown will happen for each dimensional component of the solution. Thus, we have built a general solution to the random IVP given by Equation (7.1.2), which is:

$$\begin{aligned} \mathbf{X}(t, \omega) = \mathbf{X}^0(\omega) &+ \int_{t_0}^{t} \mathbf{v}(\mathbf{X}(s, \omega), s, \mathbf{A}(\omega)) \mathrm{d}s \\ &- \sum_{k=1}^{N} \mathbf{\Gamma}^k(\omega) \odot \mathbf{X}(t_k, \omega) \mathrm{H}(t - t_k), \quad t \geq t_0, \end{aligned} \tag{7.1.16}$$

$$\mathbf{X}(t_k^+, \omega) = \mathbf{X}(t_k, \omega) = \left(\frac{X_j(t_k, \omega)}{1 + \Gamma_j^k(\omega)} \right)_{j=1}^{d}. \tag{7.1.17}$$

7.1.2 Probability Density Function evolution

Let us recall the Liouville theorem from Theorem 2.2.3: we can assure the global-in-time existence of a solution to the Liouville equation when the field function $\mathbf{v}(\cdot, t)$ is Lipschitz continuous, uniformly in t. However, the fields under consideration, $\mathbf{v}(\mathbf{x}, t) - \sum_{k=1}^{N} \mathbf{\Gamma}^k \delta(t - t_k)$ and $\mathbf{v}(\mathbf{x}, t) - \sum_{k=1}^{N} \mathbf{\Gamma}^k \odot \mathbf{x}\, \delta(t - t_k)$, do not verify the hypotheses at the impulse times $\{t_k\}_{k=1}^{N}$. In this section, we aim at obtaining a condition such as the jump conditions gathered in Equations (7.1.11) and (7.1.17) for the PDF. This will allow the computation of the

evolution of f_0, accurately capturing the discontinuities at the impulse times. In the following subsections, we consider $\mathcal{D} \subset \mathbb{R}^d$ such that no trajectories of the system ever exit the domain; that is, we consider $\mathcal{D}$ such that:

$$\mathbb{P}\left[\{\omega \in \tilde{\Omega} : \mathbf{X}(t,\omega) \in \mathcal{D}\}\right] = 1 \iff \int_{\mathcal{D}} f(\mathbf{x},t)\mathrm{d}\mathbf{x} = 1,$$

for all $t \geq t_0$. Here f is the PDF of $\mathbf{X}(t,\cdot)$.

PDF transformation at the impulse times

Let us return to the set of conditions gathered in Equations (7.1.11) and (7.1.17). Note that these are equalities between random variables where the density of $\mathbf{X}(t_k^-,\cdot)$ can be known: its density verifies the Liouville equation from the previous impulse time up to t_k^-. To get the PDF at the impulse time, and thus the PDF for future evolution, we can use the RVT stated in Theorem 2.2.2.

As in the case of the pathwise solution analysis, let us consider the first transformation in detail and then we will write the result for the general case. Let $f(\cdot,t_1)$ be the PDF of the stochastic process solution at a given impulse time t_1; that is, the PDF of $\mathbf{X}(t_1,\cdot)$ (which is unknown). Let $f(\cdot,t_1^-)$ be the PDF before the jump; that is, the PDF of $\mathbf{X}(t_1^-,\cdot)$ (which is known because it verifies the Liouville equation in (t_0,t_1)). With this in mind, let us now consider each case.

Additive impulse

Recalling the jump conditions given in Equation (7.1.9), we have:

$$\mathbf{X}(t_1,\omega) + \boldsymbol{\Gamma}^1(\omega) = \mathbf{X}(t_1^-,\omega) \iff \left|\frac{\partial \mathbf{X}(t_1^-,\omega)}{\partial \mathbf{X}(t_1,\omega)}\right| = 1.$$

Denoting the joint PDFs of $\mathbf{X}(t,\cdot)$ and $\boldsymbol{\Gamma}^1$ by $f_{(\mathbf{X}(t),\boldsymbol{\Gamma}^1)}$, for $t \in \{t_1^-, t_1\}$, the application of the RVT theorem leads to

$$f_{(\mathbf{X}(t_1),\boldsymbol{\Gamma}^1)}(\mathbf{x},\boldsymbol{\gamma}^1,t_1) = f_{(\mathbf{X}(t_1^-),\boldsymbol{\Gamma}^1)}\left(\mathbf{x}+\boldsymbol{\gamma}^1,\boldsymbol{\gamma}^1,t_1^-\right)\cdot 1 = f\left(\mathbf{x}+\boldsymbol{\gamma}^1,t_1^-\right) f_{\boldsymbol{\Gamma}^1}(\boldsymbol{\gamma}^1),$$

where $\mathbf{x} \in \mathcal{D}$ and $\boldsymbol{\gamma}^1 = (\gamma_1^1, \ldots, \gamma_d^1)$ is an arbitrary sample of $\boldsymbol{\Gamma}^1$. The density factorization is justified because $\mathbf{X}(t_1^-, \cdot)$ is independent from $\boldsymbol{\Gamma}^1$, which only appears at the impulse time. Finally, to obtain the PDF of $\mathbf{X}(t_1, \cdot)$, we marginalize respect to $\boldsymbol{\Gamma}^1$

$$f(\mathbf{x}, t_1) = \int_{\mathcal{D}(\boldsymbol{\Gamma}^1)} f\left(\mathbf{x} + \boldsymbol{\gamma}, t_1^-\right) f_{\Gamma^1}(\boldsymbol{\gamma}) \mathrm{d}\boldsymbol{\gamma} = \mathbb{E}_{\boldsymbol{\Gamma}^1}[f\left(\mathbf{x} + \boldsymbol{\Gamma}^1, t_1^-\right)], \tag{7.1.18}$$

for all $\mathbf{x}$, which shows that, at the jump, there is a translation of the PDF for every realization of $\boldsymbol{\gamma}^1$. The average of these translations gives the PDF of $\mathbf{X}(t_1, \cdot)$. Note that, in (7.1.18), $\mathcal{D}(\boldsymbol{\Gamma}^1)$ denotes the domain of random vector $\boldsymbol{\Gamma}^1(\omega)$.

Now, the Liouville equation describes the evolution of the PDF (7.1.18) until the following impulse time t_2. Clearly, at any other impulse time, we will have the same case as for t_1:

$$f(\mathbf{x}, t_k) = \mathbb{E}_{\boldsymbol{\Gamma}_k}[f\left(\mathbf{x} + \boldsymbol{\Gamma}_k, t_k^-\right)], \quad \forall \mathbf{x} \in \mathcal{D}, \quad k = 1, \ldots, N. \tag{7.1.19}$$

Multiplicative impulse

In this case, since the state of the system is affected both by the impulse and the system's state before the impulse, as seen in Equation (7.1.15), we get a more interesting effect (see Figure 7.2):

$$\mathbf{X}(t_1, \omega) \odot (\mathbf{1} + \boldsymbol{\Gamma}^1(\omega)) = \mathbf{X}(t_1^-, \omega) \Longrightarrow \left| \frac{\partial \mathbf{X}(t_1^-, \omega)}{\partial \mathbf{X}(t_1, \omega)} \right| = \prod_{j=1}^{d} |1 + \Gamma_j^1(\omega)|, \tag{7.1.20}$$

where $\mathbf{1} = (1, \ldots, 1) \in \mathbb{R}^d$. Denoting the joint PDFs of $\mathbf{X}(t, \cdot)$ and $\mathbf{\Gamma}^1$ by $f_{(\mathbf{X}(t),\Gamma^1)}$, for $t \in \{t_1^-, t_1\}$, the application of the RVT theorem leads to

$$\begin{aligned} f_{(\mathbf{X}(t_1),\mathbf{\Gamma}^1)}(\mathbf{x}, \boldsymbol{\gamma}^1, t_1) &= f_{(\mathbf{X}(t_1^-),\mathbf{\Gamma}^1)}\left(\mathbf{x} \odot (\mathbf{1} + \boldsymbol{\gamma}^1), \boldsymbol{\gamma}^1, t_1^-\right) \prod_{j=1}^{d} |1 + \gamma_j^1(\omega)| \\ &= f\left(\mathbf{x} \odot (\mathbf{1} + \boldsymbol{\gamma}^1), t_1^-\right) f_{\mathbf{\Gamma}^1}(\boldsymbol{\gamma}^1) \prod_{j=1}^{d} |1 + \gamma_j^1(\omega)|, \end{aligned}$$

because $\mathbf{X}(t_1^-, \cdot)$ is independent from $\mathbf{\Gamma}^1$, which only appears at the impulse time. Finally, to obtain the PDF of $\mathbf{X}(t_1, \cdot)$, we have to marginalize respect to $\mathbf{\Gamma}^1$:

$$\begin{aligned} f(\mathbf{x}, t_1) &= \int_{\mathcal{D}(\mathbf{\Gamma}^1)} f\left(\mathbf{x} \odot\ (\mathbf{1} + \boldsymbol{\gamma}), t_1^-\right) \prod_{j=1}^{d} |1 + \gamma_j| f_{\mathbf{\Gamma}^1}(\boldsymbol{\gamma}) \mathrm{d}\boldsymbol{\gamma} \qquad (7.1.21) \\ &= \mathbb{E}_{\mathbf{\Gamma}^1}\left[f\left(\mathbf{x} \odot (\mathbf{1} + \mathbf{\Gamma}^1), t_1^-\right) \prod_{j=1}^{d} |1 + \Gamma_j^1| \right], \end{aligned}$$

for all $\mathbf{x}$, which shows that, at the jump, there is a rescaling of $f(\cdot, t_1^-)$, **both in its argument and value**, for every realization of $\mathbf{\Gamma}^1$ (see Figure 7.2). The average of these transformations gives the PDF of $\mathbf{X}(t_1, \cdot)$. Note that, in (7.1.21), $\mathcal{D}(\mathbf{\Gamma}^1)$ denotes the domain of random variable $\mathbf{\Gamma}^1$.

Now, the Liouville equation describes the evolution of the PDF (7.1.21) until the following impulse time t_2. Clearly, at any other impulse time, we will have the same case as for t_1:

$$f(\mathbf{x}, t_k) = \mathbb{E}_{\mathbf{\Gamma}^k}\left[f\left(\mathbf{x} \odot (\mathbf{1} + \mathbf{\Gamma}^k), t_k^-\right) \prod_{j=1}^{d} |1 + \Gamma_j^k| \right], \quad k = 1, \ldots, N. \quad (7.1.22)$$

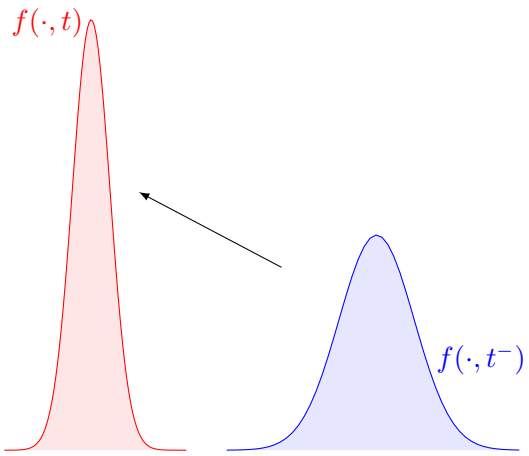

Figure 7.2: PDF transformation at the impulse times for the multiplicative case. An illustrative example concerning the case of a $\Gamma > 0$ sample. In the additive impulse case, we only have a translation of the PDF (same height), however, in the multiplicative case, we also have rescaling.

Full evolution simulation

Summarizing, the PDF evolution of the random IVPs given by Equations (7.1.1) and (7.1.2) can be split into the following steps:

1. Define f_0, the PDF of the random initial condition $\mathbf{X}^0$.
2. Compute its evolution for several realizations of the random parameter vector $\mathbf{A}$ via the Liouville equation, using Equations (2.2.7) and (2.2.9), until the first impulse time t_1. We now have a family of PDFs at time t_1 before the impulse, which we denote by $\{f(\cdot, t_1^- \,|\, \mathbf{a})\}_{\mathbf{a}\in\mathbf{A}(\Omega)}$.
3. Compute the approximation to the expected PDF with respect to the random parameter distribution, which we denote by $f(\cdot, t_1^-)$.
4. Transform $f(\cdot, t_1^-)$ via Equations (7.1.9) and (7.1.15), obtaining the PDF $f(\cdot, t_1)$.
5. Repeat Steps 1-4, but with $f_0(\cdot) = f(\cdot, t_1)$ until the following impulse time t_2.
6. Repeat Steps (1)-(5) until the last impulse time, t_N.

7. Evolve $f(\cdot, t_N)$ until wanted.

7.2 Examples

This section is aimed at showing the applicability of the theoretical findings stated in the previous sections to some relevant random mathematical models where jumps are a key feature in the mathematical formulation. We will show three examples:

1. A scalar linear RDE with additive impulse.
2. An additive impulse nonlinear oscillator system based on the Duffing oscillator.
3. A multiplicative generalized logistic equation applicable to biomedical problems.

In this section, we use the computational approach described in Chapter 5: In all cases, we use wavelet-compression based AMR and the interpolation-remeshing step is done using RBFs. Details about the specific parameters chosen will be detailed in each example's subsection.

7.2.1 Scalar linear RDE

Linear ODEs are the simplest and among the most successful types of ODEs. This kind of ODEs verifies many properties, making them relatively easy to work with. Although most natural phenomena are modeled by nonlinear ODEs, there are some cases where one can consider the *linearization* of the ODE; that is, a linear ODE whose dynamic properties are the same as the original nonlinear ODE in a neighborhood of some time where the linearization is done. For example, when studying growth processes in biology or medicine, a linear model can be used to predict the growth at the initial stages, despite the fact that nonlinear behavior appears after some time and ends up governing the growth process asymptotically. A typical example is the logistic model, which is nonlinear but behaves like the Malthusian model, which is linear, at the initial times.

We consider the following impulsive random IVP:

$$\dot{X}(t,\omega) = A(\omega)\,X(t,\omega) + B(\omega) - \Gamma \sum_{i=1}^{N} \delta(t - T_i), \quad t > 0, \tag{7.2.1}$$

$$X(0,\omega) = X_0(\omega), \tag{7.2.2}$$

where $\omega \in \Omega$ and X_0, B and $A \neq 0$ a.s. are finite-variance random variables with preassigned PDFs denoted by f_0, f_B and f_A, respectively. Also, $\Gamma \neq 0$ a.s. is a random variable with a known PDF, f_Γ. For the sake of simplicity, we assume that X_0, A, B, and Γ are mutually independent.

Obtaining the pathwise flow is a relatively easy task. Let us fix $\omega \in \Omega$ and denote $x_0 = X_0(\omega)$, $a = A(\omega)$, $b = B(\omega)$, $\gamma = \Gamma(\omega)$. Using the well-known solution expression of linear ODEs, for $t \in [T_k, T_{k+1})$, we get

$$\phi(t; x_0, a, b) = \mathrm{e}^{at}\left(x_0 + \frac{b}{a} - \gamma \sum_{i=1}^{k} \mathrm{e}^{-aT_i}\mathrm{H}(t - T_i)\right) - \frac{b}{a},$$

which can be easily proven to be a solution of the random IVP (7.2.1)-(7.2.2) (classical between impulse times and weak globally). Analogously, solving the previous equation for x_0, the inverse flow has the following expression:

$$\psi(t; x, a, b) = \mathrm{e}^{-at}\left(x + \frac{b}{a} + \gamma \sum_{i=1}^{k} \mathrm{e}^{a(t-T_i)}\mathrm{H}(t - T_i)\right) - \frac{b}{a}. \tag{7.2.3}$$

The Liouville equation for this case is then easily obtained

$$\partial_t f(x,t \,|\, a,b) + (ax + b)\partial_x f(x,t \,|\, a,b) = -a f(x,t \,|\, a,b),$$

and its solution, conditioned to every pair of realizations (a,b), is given by

$$f(x,t \,|\, a,b) = f_0(\psi(t; x, a, b))\mathrm{e}^{-at}, \tag{7.2.4}$$

where ψ is defined in (7.2.3).

To obtain the final 1-PDF, we have to compute the conditional expectation of (7.2.4) with respect to A and B as shown in expression (2.2.9):

$$f(x,t) = \mathbb{E}_{A,B}[f(x,t \mid A,B)] = \int_{\mathcal{D}(B)} \int_{\mathcal{D}(A)} f_0(\psi(t;x,a,b))\mathrm{e}^{-at} f_A(a) f_B(b) \mathrm{d}a\mathrm{d}b, \tag{7.2.5}$$

where $\mathcal{D}(A)$ and $\mathcal{D}(B)$ denote the domains of the random variables A and B, respectively.

Table 7.1 shows the chosen distributions, mean, and standard deviation (*Std* for short) of the parameter random variables. Note that these distributions have been selected just to illustrate the versatility of the Liouville equation method. Indeed, any other combination of probability distributions could have been chosen for the same purpose. We have considered 3 impulse times, at instants $T_1 = 15$, $T_2 = 25$ and $T_3 = 35$, with the same impulse strength distribution Γ.

Variable	Distribution	Mean	Std
X_0	Normal	0.17	0.015
A	Gamma	0.03	0.02
B	Uniform	0.04	0.02
Γ	Uniform	0.5	0.02

Table 7.1: Statistical information about the random model parameters in the linear impulsive random IVP (7.2.1)–(7.2.2).

Figure 7.3 shows the evolution of the mean function and the 95% confidence interval. We can see the characteristic exponential growth of the linear ODE (7.2.1) and the sharp decreases of the solution at the impulse times. We can also observe that the confidence interval size remains almost the same before and after the impulse, as expected from (7.1.19). This implies that there is almost no difference in the uncertainty of the system before and after a given impulse. Figure 7.4 shows the PDF at several time instants together with the information from Figure 7.3. This figure clearly shows the effect of the exponential growth determined by the linear ODE; indeed, as time goes on, each "slice" of the PDF becomes lower and wider (platykurtic) until it becomes a small lump when compared with the initial PDF where is leptokurtic. At

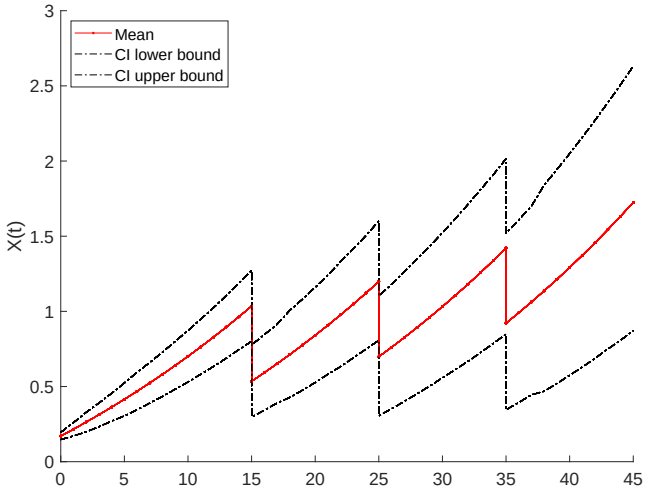

Figure 7.3: Mean function (red solid curve) of the solution process and the boundaries of the 95% probabilistic interval (black dashed curves). Linear impulsive random IVP (7.2.1)–(7.2.2) with random model parameters listed in Table 7.1.

$t = 15$, there is a sharp translation of the PDF, which is the effect of a Dirac impulse term. This fact can be further seen in Figure 7.5, which shows the transformations of the PDFs at each impulse time. Notice there is a translation of the PDF and a slight rescaling of the PDF, as expected by relation (7.1.19).

For the simulation shown in Figures 7.3-7.4, we have used a 0.25 time-step, with re-interpolation every 4 time-steps. The grid is formed by 1024 equispaced nodes. It was computed using 150 samples (15 for parameter A and 10 for parameter B). Jumps were resolved using 30 samples for Γ (other combinations of samples can also be used).

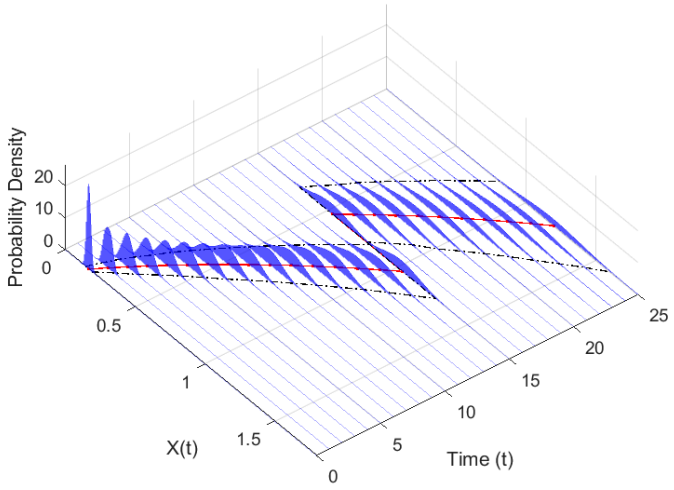

Figure 7.4: Waterfall plot of the evolution of the PDF (blue slices) with the mean function (red solid curve) and the probabilistic intervals (black dashed curves) in the time interval $[0, 25]$. Linear impulsive random IVP (7.2.1)–(7.2.2) with random model parameters listed in Table 7.1.

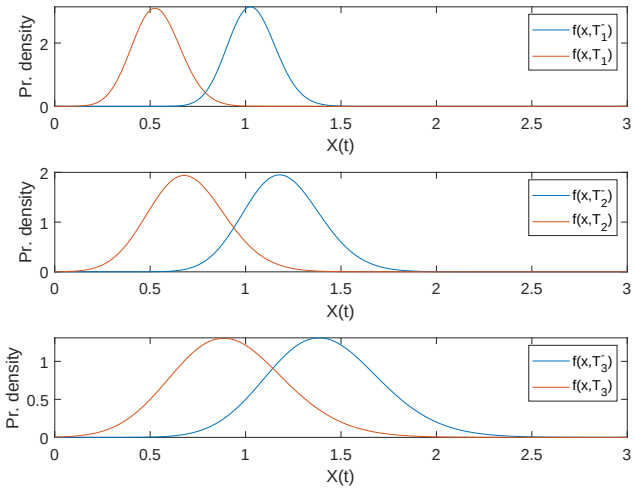

Figure 7.5: PDFs before and after each of the 3 impulse times: $T_1 = 15$, $T_2 = 25$ and $T_3 = 35$. Linear impulsive random IVP (7.2.1)–(7.2.2) with random model parameters listed in Table 7.1.

7.2.2 Random Duffing oscillator

Nonlinear oscillators have been thoroughly studied due to their rich dynamical behavior and ability to model a wide variety of natural and engineering phenomena. For example, Hooke's law states that there is a linear relationship between the deformation and the force exerted by a spring. However, when the deformation becomes large enough, the response becomes nonlinear. Also, elastic pendulums, mechanical isolators, beams with non-linear stiffness, cable vibrations, and some electrical circuits can be modeled via the nonlinear oscillator equation known as the Duffing equation [154–156].

We here consider the following impulse-forced Duffing equation

$$\ddot{X}(t,\omega) + 2\Xi(\omega)\dot{X}(t) + X(t,\omega) + \Lambda(\omega)X(t,\omega)^3 = \sum_{i=1}^{N} \Gamma_i(\omega)\delta(t-T_i), \quad t>0, \tag{7.2.6}$$

$$X(0,\omega) = X_0(\omega),\ \dot{X}(0,\omega) = \dot{X}_0(\omega), \tag{7.2.7}$$

where the model parameters $\Xi > 0$ and $\Lambda > 0$, as well as the initial conditions X_0 and $\dot{X}_0$, are assumed to be mutually independent finite-variance random variables with pre-assigned PDFs f_Ξ, f_Λ, f_{X_0} and $f_{\dot{X}_0}$, respectively. Also, the random variables $\{\Gamma_i\}_{i=1}^N$ are assumed to be mutually independent with known PDFs, denoted by f_{Γ_i}, $i = 1,\ldots,N$.

Contrarily to the previous example, the Duffing model does not have an "easily manageable" closed-form solution, and furthermore, the cases where such a solution expression exists are rare [157]. Therefore, this case will be treated numerically. In this context, combining the RVT method and the Liouville equation is particularly useful rather than only applying the RVT method.

First, let us transform the Duffing equation into a first-order two-dimensional ODE. Consider the vector $\mathbf{Y}(t,\omega) = [Y_1, Y_2]^\mathsf{T} := [X(t,\omega), \dot{X}(t,\omega)]^\mathsf{T}$, $t \geq 0$, whose components represent position and velocity, respectively. Now, dropping the ω-notation, the Duffing equation can be written as

$$\dot{\mathbf{Y}}(t) = \begin{bmatrix} Y_2(t) \\ -2\Xi Y_2(t) - Y_1(t) - \Lambda Y_1(t)^3 + \sum_{i=1}^N \Gamma_i \delta(t-T_i) \end{bmatrix}, \quad \mathbf{Y}(0) = \begin{bmatrix} X_0 \\ \dot{X}_0 \end{bmatrix}$$

where $\dot{\mathbf{Y}}$ can be rewritten as

$$\dot{\mathbf{Y}}(t) = \overbrace{\begin{bmatrix} Y_2(t) \\ -2\Xi Y_2(t) - Y_1(t) - \Lambda Y_1(t)^3 \end{bmatrix}}^{\mathbf{g}(\mathbf{Y}(t),t,\Xi,\Lambda)} + \sum_{i=1}^{N} \delta(t-T_i) \overbrace{\begin{bmatrix} 0 \\ \Gamma_i \end{bmatrix}}^{\mathbf{\Gamma}_i}.$$

As we will simulate the initial PDF evolution numerically, we have to build the Liouville equation to be solved between the impulse times and then translate

the PDF as shown in (7.1.19). Let us fix $\omega \in \Omega$ and consider the pair of arbitrary realizations $\xi = \Xi(\omega)$ and $\lambda = \Lambda(\omega)$. Indeed, the vector field and divergence terms for the Liouville equation are

$$\mathbf{g}(y_1, y_2, t, \xi, \lambda) = (y_2, -2\xi y_2 - y_1 - \lambda y_1^3), \quad \nabla_{\mathbf{y}} \cdot \mathbf{g}(y_1, y_2, t, \xi, \lambda) = -2\xi,$$

respectively. Therefore, the Liouville equation related to the random IVP (7.2.1)-(7.2.2) between the impulse times is

$$\partial_t f(\mathbf{y}, t \,|\, \xi, \lambda) +$$
$$y_2 \partial_{y_1} f(\mathbf{y}, t \,|\, \xi, \lambda) - (2\xi y_2 + y_1 + \lambda y_1^3)\partial_{y_2} f(\mathbf{y}, t \,|\, \xi, \lambda) = 2\xi f(\mathbf{y}, t \,|\, \xi, \lambda), \quad (7.2.8)$$
$$f(\mathbf{y}, 0 \,|\, \xi, \lambda) = f_0(\mathbf{y}) := f_{X_0}(y_1) f_{\dot{X}_0}(y_2). \quad (7.2.9)$$

To solve this PDE, we will use the Lagrangian particle and AMR techniques described in Subsections 5.2.3 and 5.2.1, respectively. Finally, all that would be left is to compute the PDF marginalizing the model parameters Ξ and Λ using expression (2.2.9) with the identification $\mathbf{A} = (\Xi, \Lambda)$.

Variable	Mean	Var.
X_0	1.75	0.025
$\dot{X}_0$	0	0.025
Ξ	0.2	0.02
Λ	3	0.3
Γ_1	2.5	0.02
Γ_2	1	0.02
Γ_3	1.2	0.02

Table 7.2: Statistical information about the random model parameters in the Duffing equation. In all the cases, random variables are assumed to be independent and have Normal distributions with the specified values for the mean and the variance. Due to their physical meaning, the random variables Ξ and Λ are truncated to positive values. Random Duffing oscillator 7.2.6–7.2.7.

To carry out the computations, we have assumed the probability distributions listed in Table 7.2 for each random variable. Note that we have considered 3 impulse terms, which have been chosen at the following time values: $T_1 = 0.6$, $T_2 = 1.2$, and $T_3 = 2.4$. Furthermore, in Figures 7.6–7.12, we show the

evolution of the initial PDF for the corresponding parameter distributions before and at the corresponding impulse times.

These simulations show the fascinating dynamics induced by the Duffing oscillator. The complete sequence of Figures 7.6–7.12 (left figures) show the initial joint PDF for the position and velocity (that is shown in Figure 7.6 (left)) begins to decay in a counter-clockwise spiral-like fashion toward the origin, which is its trivial equilibrium point. As it is shown in the right panel in Figures 7.6, 7.8, 7.10 and 7.12, the AMR technique selects relatively few points as the particles that will be evolved using the corresponding characteristic equations (5.2.9). These points carry the most information about the values of the PDF in the underlying 512×512-point grid.

Figure 7.7 shows the joint PDF of position and velocity before the first impulse time $T_1 = 0.6$ (left figure) and its transformation after applying the impulse (left figure). We can see that the transformation (all of them) consists of a translation and a subtle rescaling due to the distribution of the impulse random variable Γ_1. If the impulse were deterministic, the transformation would consist of a translation only (compare with Equation (7.1.19)).

As explained in Section 7.1.2, the simulation continues by performing the AMR of the transformed PDF and smoothly evolving the PDF until the next impulse time. As it can be seen in Figure 7.8, the PDF starts to lose its ellipse-like shape because the points that are further away from the origin carry more velocity than those where the PDF is concentrated. This fact is clearly observable when we arrive at the next impulse time, $T = 1.2$ (Figure 7.9). Now, the aforementioned rescaling property is visible on the plot. There is a greater difference between the PDF before and after the impulse time than in the first impulse (compare Figures 7.7 and 7.9).

Once again, the AMR is performed, and the PDF evolves from its new state according to the Duffing oscillator dynamics. Figure 7.10 shows the interesting form that the PDF is attaining. Finally, the last impulse transformation at time $T = 2.4$ is shown in Figure 7.11, and Figure 7.12 shows the peculiar form of the PDF at time $t = 2.6$. Figure 7.13 shows the marginal PDF of position at time $t = 2.6$, assuming a fixed value for velocity 0.6 (compare

with Figure 7.12) whereas Figure 7.14 shows the marginal PDF of velocity at time $t = 2$, assuming that position is in the interval $[0.4, 0.6]$. As mentioned in the introduction, by knowing the joint PDF of a stochastic process, we can understand its behavior at every time instant. The figures shown in this example are a clear example where knowing the joint and marginal PDFs gives key statistical information that would not be attainable by computing only the mean and variance of the stochastic process, as is usually done in the literature.

As a final note regarding the interpolation procedure used in this particular case, we have used compactly-supported RBF interpolation based on the Wendland C^2 kernels [94]. Although there may be faster methods for interpolating scattered points in 2D, RBF-based interpolation allows for a stable, easily implementable, and general interpolation approach, independently of the dimensionality of the RDE system. Also, the time step used for the numerical solution via the Runge-Kutta integrator is 0.05, and we have re-interpolated the particles every 2 steps, according to the theory in Chapter 5. In this case, we used 98 samples (7 for Ξ and 14 for Λ, although other combinations can be used). Jumps were resolved using 20 samples each.

7.2.3 Generalized logistic equation

In [158, 159], similar problems have been studied in the setting of the logistic equation, a classical and widely used mathematical model that appears in several areas of science. In this chapter, we are going to deal with the impulse-

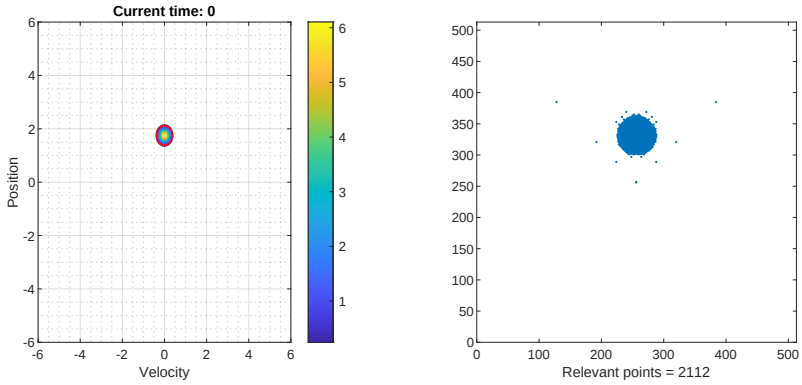

Figure 7.6: Left: Level curves of the initial PDF f_0 (view color-bar) of the Duffing equation model, and the 95% confidence region (curve in red). Right: Scatter view of the grid points that will be used to compute the evolution of the PDF. We obtain a 99.43% compression with respect to the underlying fine grid. Random Duffing oscillator (7.2.6)–(7.2.7) with random model parameters listed in Table 7.2.

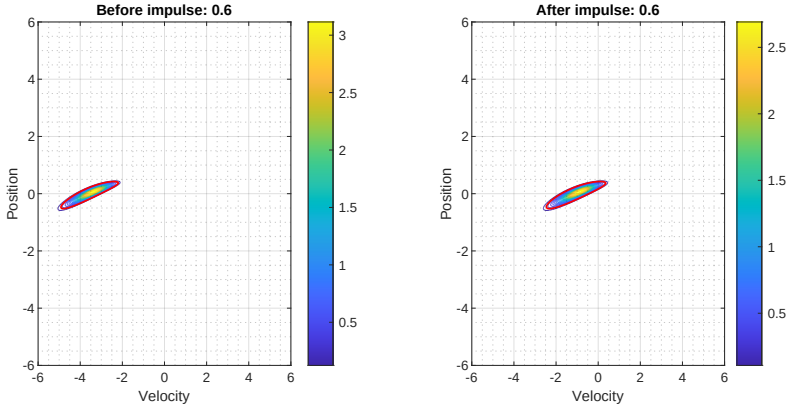

Figure 7.7: Left: PDF approaching the first impulse time from the left; that is, $f(\cdot, 0.6^-)$. Right: PDF at the transformation; that is, $f(\cdot, 0.6) = f(\cdot, 0.6^+)$. Random Duffing oscillator (7.2.6)–(7.2.7) with random model parameters listed in Table 7.2.

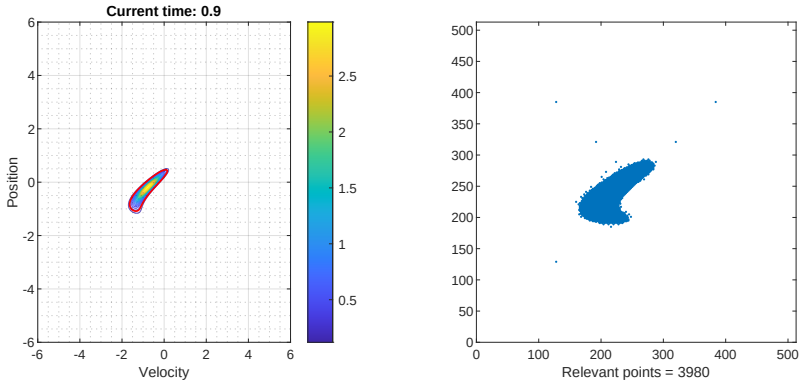

Figure 7.8: Left: Level curves of the PDF at time $t = 0.9$ (view color-bar) and the 95% confidence region (curve in red). Right: Scatter view of the relevant grid points for the computation of the evolution of the PDF. We obtain a 98.79% compression with respect to the underlying fine grid. Random Duffing oscillator (7.2.6)–(7.2.7) with random model parameters listed in Table 7.2.

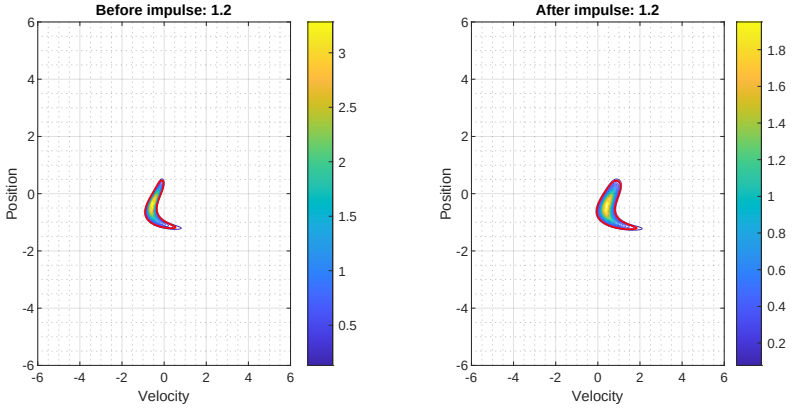

Figure 7.9: Left: PDF approaching the second impulse time from the left; that is, $f(\cdot, 1.2^-)$. Right: PDF at the transformation; that is, $f(\cdot, 1.2) = f(\cdot, 1.2^+)$. Random Duffing oscillator (7.2.6)–(7.2.7) with random model parameters listed in Table 7.2.

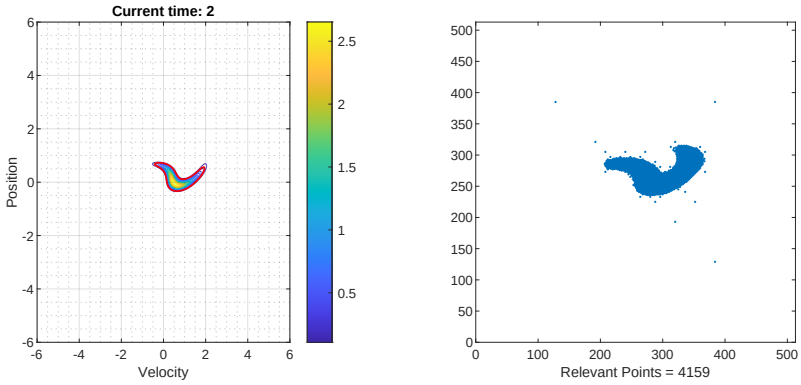

Figure 7.10: Left: Level curves of the PDF at time $t = 2$ (view color-bar) and the 95% confidence region (curve in red). Right: Scatter view of the relevant grid points for the computation of the evolution of the PDF. We obtain a 98.72% compression with respect to the underlying fine grid. Random Duffing oscillator (7.2.6)–(7.2.7) with random model parameters listed in Table 7.2.

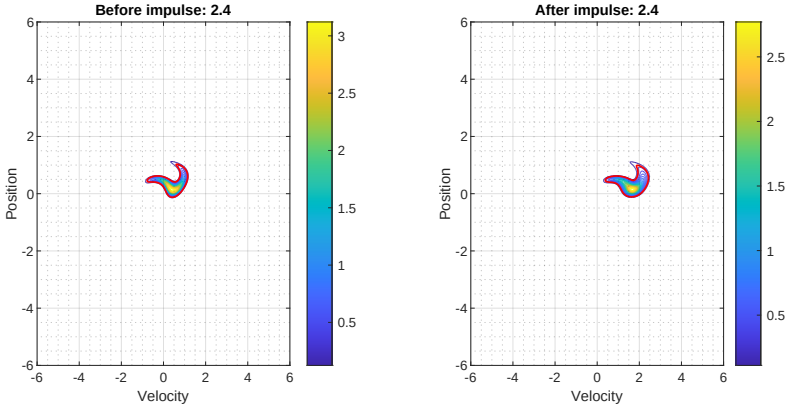

Figure 7.11: Left: PDF approaching the third impulse time from the left; that is, $f(\cdot, 2.4^-)$. Right: PDF at the transformation; that is, $f(\cdot, 2.4) = f(\cdot, 2.4^+)$. Random Duffing oscillator (7.2.6)–(7.2.7) with random model parameters listed in Table 7.2.

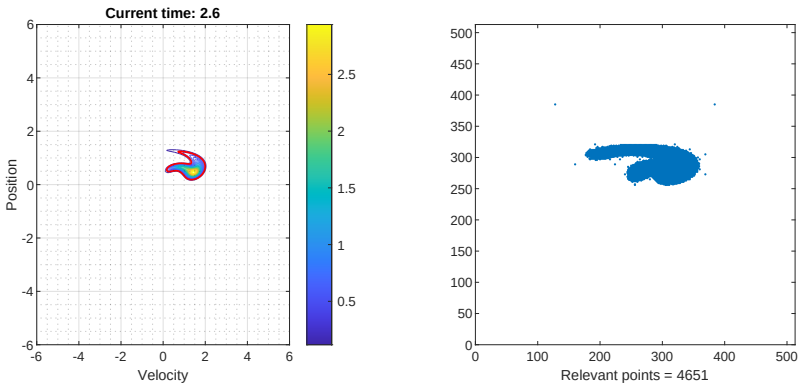

Figure 7.12: Left: Level curves of the PDF at time 2.6 (view color-bar) and the 95% confidence region (curve in red). Right: Scatter view of the relevant grid points for the computation of the evolution of the PDF. We obtain a 98.48% compression with respect to the underlying fine grid. Random Duffing oscillator (7.2.6)–(7.2.7) with random model parameters listed in Table 7.2.

harvest generalized logistic model with a finite number of captures, say N,

$$X'(t,\omega) = \alpha(t)\, r(\omega) X(t,\omega) \left(1 - \left(\frac{X(t,\omega)}{K(\omega)}\right)^{\nu(\omega)}\right) - \sum_{n=1}^{N} \Gamma_n(\omega)\delta(t-t_n)X(t,\omega), \tag{7.2.10}$$

$$X(t_0,\omega) = X^0(\omega),$$

where $t \geq t_0$ and $\omega \in \tilde{\Omega}$. As usual, t is interpreted as the time, the parameter r is the growth ($r > 0$) or decay ($r < 0$) rate, and K is the carrying capacity. The differential equation is generalized by adding two terms: a positive, monotonically growing function $\alpha(\cdot)$ and a constant positive term ν. The first term, $\alpha(\cdot)$, allows controlling the so-called *lag phase*, which is the growth phase in which the population under study has not yet achieved fully exponential

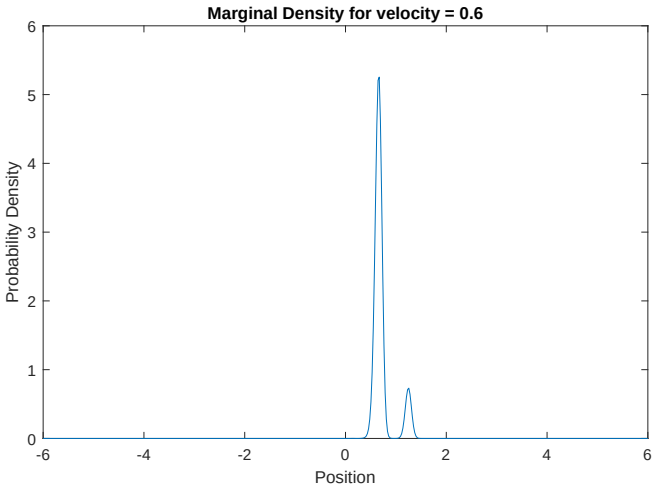

Figure 7.13: Marginal PDF of position at time $t = 2.6$, that is, $X(2.6)$, subject to $\dot{X}(2.6) = 0.6$. Random Duffing oscillator (7.2.6)–(7.2.7) with random model parameters listed in Table 7.2.

growth. In particular, we have chosen [66]:

$$\alpha(t) := \frac{q(\omega)}{q(\omega) + \mathrm{e}^{-m(\omega)\, t}}, \quad q, m > 0 \text{ a.s.}$$

The latter, ν, is a power that controls how fast the carrying capacity K is approached and is known as *deceleration* term. When $\nu = 1$, the classical logistic differential equation is obtained. And when ν tends to 0, the Gompertz equation is given. The incorporation of both the function $\alpha(\cdot)$ and the power ν allows for more flexible S-shaped curves to model growth phenomena over time.

The field function of the generalized logistic equation under study (7.2.10) verifies all the conditions of Theorem 2.2.3, where the set $\mathcal{D}$ in Theorem 2.2.3 for the generalized logistic model (7.2.10) is going to be $\mathcal{D} = [0, ||K||_{\mathrm{L}^\infty}]$, with $||K||_{\mathrm{L}^\infty} = \sup\{K(\omega) : \omega \in \tilde{\Omega}\}$. Furthermore, it is smooth in space and time variables, so the use of the Liouville equation as in (2.2.3) is available.

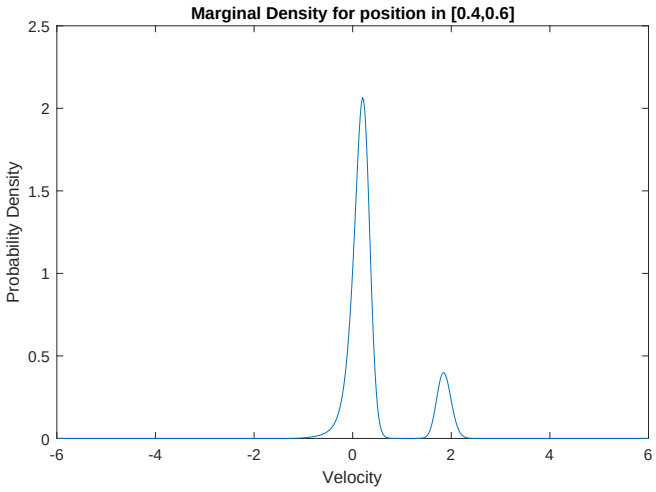

Figure 7.14: Marginal PDF of velocity at time $t = 2$, that is, $\dot{X}(2)$, subject to $X(2.6) \in [0.4, 0.6]$. Random Duffing oscillator (7.2.6)–(7.2.7) with random model parameters listed in Table 7.2.

Therefore, its corresponding Liouville equation between impulse times is:

$$\partial_t f(x,t\,|\,\mathbf{a}) + \alpha(t)\, rx \left(1 - \left(\frac{x}{K}\right)^{\nu}\right) \partial_x f(x,t\,|\,\mathbf{a}) \\ = -f(x,t\,|\,\mathbf{a})\alpha(t)\, r \left(1 - (1+\nu)\left(\frac{x}{K}\right)^{\nu}\right).$$

We remind the computation of the marginal PDF with respect to $\mathbf{A}$ as in equation (2.2.9). Using this final PDF, we will compute the statistical information given by the mean $\mathbb{E}[X(t,\omega)]$, and the variance $\mathbb{V}[X(t,\omega)] = \mathbb{E}[(X(t,\omega))^2] - (\mathbb{E}[X(t,\omega)])^2$ at a certain prefixed time instant, say t.

Application to tumor removal

There are many ways of treating cancer, such as radiotherapy, chemotherapy, and in some cases, direct retrieval of a fraction of the tumor mass. The first two treatments have a prolonged effect of tumor destruction, whereas the latter intervention can be modeled via a delta-type impulse function because of the sudden extraction of the tumor mass with respect to the total treatment. Regarding un-altered tumor growth, it is well known that Malthus-type models of exponential growth only work when studying initial growth stages. Just as an illustrative example of the application of Equation (7.2.10) to model this kind of medical problem, we choose the parameter vectors as follows:

- The initial tumor size $X^0 \sim \mathrm{N}|_{(0,1)}(0.15, 0.01)$, where $\mathrm{N}|_{(0,1)}$ is a normal distribution truncated on the interval $(0, 1)$.
- Variables q and m will be given the same deterministic values as in the previous example: $q = 1$ and $m = 4$.
- We consider $r \sim \mathrm{N}|_{(0,1)}(0.15, 0.0075)$, $\nu \sim \mathrm{Unif}(1, 1.25)$ and $K \sim \mathrm{Unif}(0.9, 1)$.
- We are going to consider 5 removals with equally distributed intensity given by $\Gamma^1 = \ldots = \Gamma_5 = \Gamma \sim \mathrm{N}|_{\mathbb{R}^+}(2, 0.01)$, at times $T_{\mathrm{Tumor}} = \{t_1 = 15, t_2 = 25, t_3 = 35, t_4 = 45, t_5 = 55\}$.

In Figure 7.15, we have plotted the mean and 95%-confidence intervals according to the prefixed parameters and removal times. It can be seen how, after each removal, the tumor size starts growing according to the un-removed size of the tumor. Interestingly, the confidence interval amplitude before each removal is higher than the uncertainty after the removal. Indeed, since all removals are distributed as $\Gamma \sim \mathrm{N}|_{\mathbb{R}^+}(2, 0.01)$, it can be easily seen that each removal takes away half of the tumor (in average), thus reducing the uncertainty after each removal time. Contrary to the previous example, this case allows having a long-time prediction with a reduced level of uncertainty while still considering random impulses. This can be further seen in Figure 7.17, where the PDF given as the solution of the Liouville equation in this particular problem setting is shown in every simulated time in T_{Tumor}.

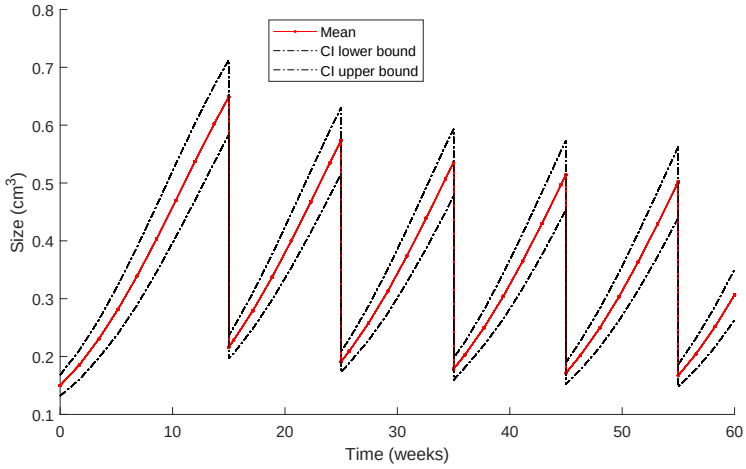

Figure 7.15: Time evolution of the mean tumor size and a 95% confidence interval with several extractions.

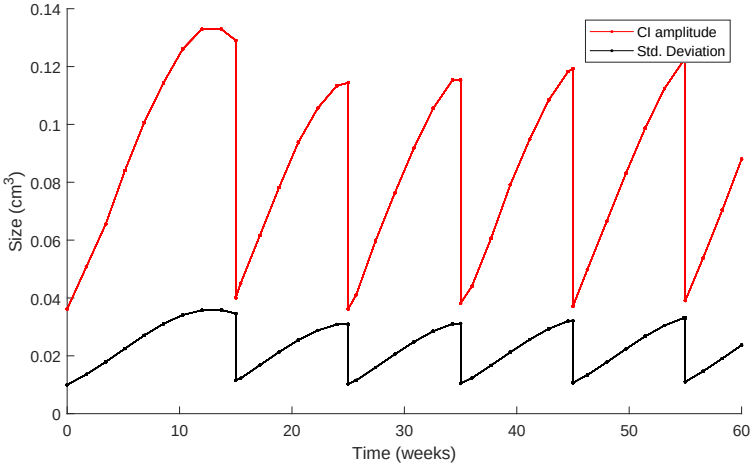

Figure 7.16: Time evolution of the 95% confidence interval amplitude and the standard deviation of the tumor growth with extractions.

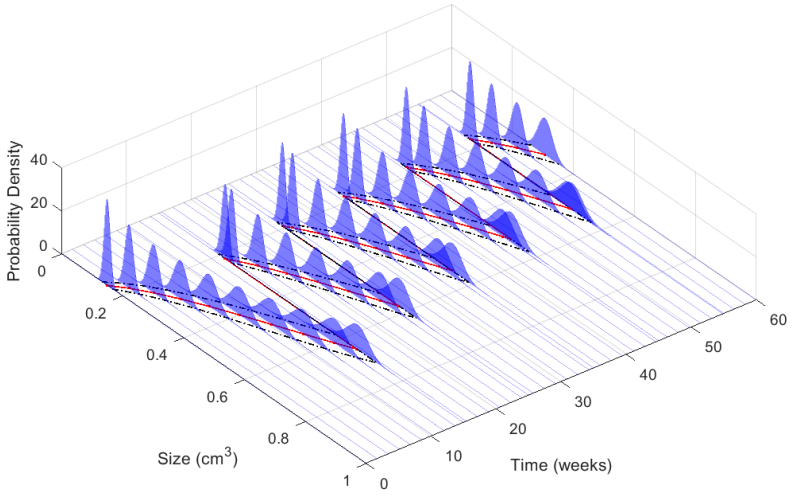

Figure 7.17: Full view of the PDF evolution simulations of the tumor growth problem 7.2.3 at the corresponding time values in T_{Tumor}, together with the mean (red) and 95% confidence intervals (dashed, black). Compare with Figure 7.15.

7.3 Conclusions and future work

In this chapter, we have rigorously obtained a pathwise solution to a general random differential equation with a finite number of random-intensity impulsive terms, with the usual assumptions on the regularity of the field function. Furthermore, we have determined the evolution of the first probability density function of the solution stochastic process by combining the Liouville equation and the Random Variable Transformation technique. After some brief comments on the numerical approach for the simulation of the probability density function evolution, we have applied our general theoretical findings to several mathematical models. Indeed, two of these examples emerge from the generalized logistic model with natural decay and growth, respectively, being both altered by additive and multiplicative impulsive terms acting contrarily to their respective natural dynamics. The other example is based on a randomization of the Duffing oscillator, whose external input is defined via a train of random additive impulses. This has been done to showcase the wide range of applicability of the theoretical findings obtained throughout this chapter.

Publications

The results presented in this thesis chapter have been published in [118, 160]. Regarding this chapter, the PhD candidate has contributed by working on its complete development with more emphasis on the theoretical results and preparing the visualization of the numerical examples.

Also, some results of this chapter have been presented at two international conferences. The first one is the 2022 Mathematical Modeling in Engineering and Human Behavior (MMEHB-22), held in Valencia (Spain) from 14-16th of July, 2022. The talk, titled *Probabilistic analysis of scalar random differential equations with state-dependent impulsive terms via probability density functions* was published in the conference proceedings, with ISBN: 978-84-09-47037-2. The second congress was the Uncertainties 2023 conference, held in Fortaleza (Brazil) from July 30th-August 4th, 2023. The talk was titled *Uncertainty Quantification in Impulsive Random Differential Equations.*

Chapter 8

Conclusions and future work

In this thesis, we have tackled the problem of estimating the PDF and the related probabilistic information from a stochastic process verifying some RDE system in the pathwise or mean square sense. We have discussed several methods throughout the dissertation, but we have emphasized the usage of the RVT Theorem and the Liouville equation. Indeed, several computational techniques were combined to obtain a procedure to quantify uncertainty evolution in mathematical models given by RDE systems under general assumptions. We now give a brief reminder on the main keys from each chapter.

Chapter 3 studies, from a probabilistic standpoint, the fully randomized Gompertz model. This important model plays a key role in describing the dynamics of biological and biophysical parts of complex systems, which often involve uncertainties. The study has been conducted under very general hypotheses regarding the probability distributions of model parameters, which confers a wide range of applicability to our theoretical findings. The numerical experiments and modeling carried out in our examples show very good results.

This chapter shows the valuable information that can be gained from having a closed-form solution for the mathematical model under study, where both the Liouville equation and the RVT theorem can be directly applied. It also discusses the great improvement in considering random models instead of deterministic models when dealing with real-world data.

Chapter 4 defines a procedure to quantify uncertainty in a random biological system. Specifically, we have used the Liouville equation, whose solution at every instant was obtained using a finite volume numerical scheme. Using real data from experiments performed in the literature and the Principle of Maximum Entropy, we assigned a reliable probability density to the initial condition of the dynamical system. We successfully optimized two key model parameters, representing the growth rates of both strains of bacteria so that the mean of the solution stochastic process is as close as possible to the real sample mean. The optimal values were obtained using the Particle Swarm Optimization algorithm.

This chapter highlights the main advantage of the Liouville equation over the RVT theorem: the availability of numerical methods from deterministic PDEs to estimate the PDF without having a closed-form solution for the underlying stochastic process. However, it also highlights two issues that are addressed in the following chapter: 1) Not any numerical approach is valid for the kind of problem defined by the Liouville equation: we must choose one designed for advection-dominated problems; 2) we must use advanced computational techniques to define a numerical method that can compute the PDF efficiently and in a reasonable amount of time.

Chapter 5 introduces and analyzes a novel numerical approach for efficiently solving the Liouville equation in the context of RDEs using General-Purpose Graphics Processing Units (GPGPUs). Our methodology integrates wavelet compression-based adaptive mesh refinement, Lagrangian particle methods, and radial basis function approximation to develop a versatile, accurate, and computationally efficient numerical algorithm. We validated the performance of our approach through several mathematical models, including the van der Pol oscillator, Mathieu equation, and SIR model. These examples demonstrate

the method's applicability to various problems and its compatibility with various numerical integrators for the underlying systems. Not to be overlooked is the illustration of the method's limitations in its current implementation.

Our findings suggest that the numerical method described in the chapter holds significant potential for quantifying forward uncertainty in random differential equations via probability density evolution, greatly improving the information obtained by simply performing Montecarlo simulations. However, more research must be done to determine the effect of the several parameters that define the computational on the quality of the simulation.

Chapter 6 investigates the generalized logistic random differential equation. This equation includes a power term in the classical logistic model to better control how fast the limiting capacity is approached. We have assumed that the parameters are random variables. Then, we rigorously obtained the sample path and mean-square solution and computed its Probability Density Function by applying the Random Variable Transformation technique and Liouville's equation. We have analyzed how the model reduces to the classical logistic equation and the Gompertz equation when the power tends to 1 and 0 in a probabilistic sense.

We applied the numerical method defined in Chapter 5 to a case with deterministic coefficients, and then it was extended to the scenario where coefficients are given by random variables. Afterward, an optimization procedure was implemented based on the Particle Swarm Optimization algorithm. Its objective has been to obtain the deterministic coefficient values that describe the mean behavior of the biological culture growth data set. This chapter points out that a wise combination of our Liouville solver with state-of-the-art optimization techniques can provide a valuable tool for inverse uncertainty quantification and posterior prediction information in real-world scenarios.

Finally, in Chapter 7 we have rigorously obtained a pathwise solution to a general random differential equation with a finite number of random-intensity impulsive terms, with the usual assumptions on the regularity of the field function. Furthermore, we have determined the evolution of the first probability

density function of the solution stochastic process by combining the Liouville equation and the Random Variable Transformation theorem.

This chapter provides novel results in the vibrant area of Dirac-forced additive and impulsive RDE systems. Specifically, using the pathwise Laplace transform, we can use both the Liouville equation and the RVT theorem in the same framework to determine the PDF evolution at all times, including the impulse instant. Once again, it shows the versatility of these methods and the numerical techniques considered in the thesis.

Regarding future work, we believe that the numerical approach for solving the Liouville equation can still be improved in accuracy and computational efficiency. We are currently researching the interplay of the solver's parameters, which are very intricate. There is also the possibility of using a neural network-based approach to improve and automate the solution-finding process and computing the PDF evolution in higher dimensions while minimizing memory usage. In relation to the applications, a significant challenge lies in assigning appropriate probability distributions to the model parameters. This ensures that the response of the differential equation accurately reflects the uncertainty inherent in the physical phenomena being studied. While this issue has not been directly addressed in this thesis, it may influence the methods developed in this dissertation when applied to real-world scenarios

We are also aware of the interesting challenges of random boundary value problems, where we already have some theoretical results and expect numerical results soon. Finally, random delay equations and fractional RDEs are also under the radar. In these cases, all we need to do is find the corresponding Liouville equation, the corresponding characteristic equations and modify the numerical method appropriately.

Appendix A

Relating the Liouville equation with RDEs

In this appendix, we include several proofs regarding the relationship between the PDF of an RDE system and the Liouville equation. In all cases, we consider the general RDE from Chapter 2, given by the following initial value problem:

$$\begin{cases} \dfrac{\mathrm{d}\mathbf{X}}{\mathrm{d}t}(t) &= \mathbf{v}(\mathbf{X}(t),t), \quad t > t_0, \\ \\ \mathbf{X}(t_0) &= \mathbf{X}_0 \in \mathrm{L}^2_d(\Omega,\mathbb{R}^d), \end{cases} \tag{A.0.1}$$

and $\mathbf{X}(t) = \mathbf{X}(t,\omega)$, $t \geq t_0$, $\omega \in \Omega$ is the stochastic process that verifies the equation. Since we will consider three different approaches, we will specify the specific sense in which $\mathbf{X}(t)$ verifies the RDE.

A.0.1 Classical theorem proof

In the context of dynamical systems, the Liouville-Gibbs theorem states that the PDF, $f(t, \mathbf{x})$, of the solution stochastic process, $\mathbf{X}(t)$, of IVP (2.1.7) is an invariant of motion, i.e., the integral

$$\mathcal{J}(t) = \int_{D_t} f(t, \mathbf{x}) \, \mathrm{d}\mathbf{x} \tag{A.0.2}$$

is independent of t for any domain $D_t \subset \mathbb{R}^d$ (defined in terms of t), i.e.,

$$\frac{\mathrm{d}\mathcal{J}(t)}{\mathrm{d}t} = 0. \tag{A.0.3}$$

In this case, we assume that $\mathbf{X}(t)$ verifies Equation (A.0.1) in the pathwise sense. Let us consider

$$\mathcal{J}(t+h) = \int_{D_{t+h}} f(t+h, \mathbf{y}) \, \mathrm{d}\mathbf{y}. \tag{A.0.4}$$

Using the theorem of change of variables for integrals, expression (A.0.4) can be written on the domain D_t as

$$\mathcal{J}(t+h) = \int_{D_t} f(t+h, \mathbf{y}) \left| \frac{\partial \mathbf{y}}{\partial \mathbf{x}} \right| \mathrm{d}\mathbf{x} \tag{A.0.5}$$

Let us now calculate the two factors, $f(t+h, \mathbf{y})$ and the jacobian $\left| \dfrac{\partial \mathbf{y}}{\partial \mathbf{x}} \right|$, appearing in the previous integral. For the former, let us observe using Taylor's expansion of order 2 that

$$\begin{aligned} f(t+h, \mathbf{y}) &= f(t, \mathbf{x}) + h \left(\partial_{x_1} f \frac{\mathrm{d}x_1}{\mathrm{d}t} + \ldots + \partial_{x_d} f \frac{\mathrm{d}x_d}{\mathrm{d}t} + \partial_t f \right) + \mathcal{O}(h^2) \\ &= f + h \left(\partial_{x_1} f v_1 + \ldots + \partial_{x_d} f v_d + \partial_t f \right) + \mathcal{O}(h^2), \end{aligned} \tag{A.0.6}$$

where in the last step we have used the shorter notation $f = f(t, \mathbf{x})$ and that $\mathbf{x} = (x_1, \ldots, x_d)$ satisfies the differential equation in (A.0.1), so $\dfrac{\mathrm{d}x_i}{\mathrm{d}t} = v_i$, $v_i = v_i(t, x_1, \ldots, x_d)$, $1 \leq i \leq d$. To compute the jacobian, we apply again

Taylor's expansion of order 2 for each component,

$$y_i = x_i + h\frac{\mathrm{d}x_i}{\mathrm{d}t} + \mathcal{O}(h^2) = x_i + hv_i + \mathcal{O}(h^2), \quad 1 \le i \le d.$$

Then the jacobian $\dfrac{\partial \mathbf{y}}{\partial \mathbf{x}}$ in (A.0.5) can be calculated as

$$\begin{aligned}
\frac{\partial \mathbf{y}}{\partial \mathbf{x}} &= \det \begin{bmatrix} \partial_{x_1} y_1 & \cdots & \partial_{x_1} y_d \\ \vdots & \ddots & \vdots \\ \partial_{x_d} y_1 & \cdots & \partial_{x_d} y_d \end{bmatrix} \\
&= \det \begin{bmatrix} 1 + h\partial_{x_1} v_1 + \mathcal{O}(h^2) & \cdots & h\partial_{x_1} v_d + \mathcal{O}(h^2) \\ \vdots & \ddots & \vdots \\ h\partial_{x_d} v_1 + \mathcal{O}(h^2) & \cdots & 1 + h\partial_{x_d} v_d + \mathcal{O}(h^2) \end{bmatrix} \\
&= 1 + h\left(\partial_{x_1} v_1 + \cdots + \partial_{x_d} v_d\right) + \mathcal{O}(h^2).
\end{aligned}$$

Therefore, using (A.0.6) and this last expression for the jacobian one gets

$$\begin{aligned}
f(t+h, \mathbf{y})\frac{\partial \mathbf{y}}{\partial \mathbf{x}} &= \left[f + h\left(\partial_{x_1} f v_1 + \ldots + \partial_{x_d} f v_d + \partial_t f\right) + \mathcal{O}(h^2)\right] \\
&\quad \cdot \left[1 + h\left(\partial_{x_1} v_1 + \cdots + \partial_{x_d} v_d\right) + \mathcal{O}(h^2)\right] \\
&= f + h\left(\partial_{x_1} f v_1 + \ldots + \partial_{x_d} f v_d + \partial_t f\right. \\
&\quad \left. + f\partial_{x_1} v_1 + \cdots + f\partial_{x_d} v_d\right).
\end{aligned}$$

Now, we use the rule for the derivative of a product $\partial_{x_i}(f v_i) = v_i \partial_{x_i} f + f\partial_{x_i} v_i$, $1 \le i \le d$. Then, the last expression can be written as

$$f(t+h, \mathbf{y})\frac{\partial \mathbf{y}}{\partial \mathbf{x}} = f(t, \mathbf{x}) + h\left(\partial_t f + \sum_{i=1}^{n} \partial_{x_i}(f v_i)\right),$$

i.e.,

$$\frac{f(t+h, \mathbf{y})\dfrac{\partial \mathbf{y}}{\partial \mathbf{x}} - f(t, \mathbf{x})}{h} = \partial_t f + \sum_{i=1}^{n} \partial_{x_i}(f v_i), \tag{A.0.7}$$

where, for convenience, we have recovered the notation $f = f(t, \mathbf{x})$. Finally, we subtract (A.0.2) from (A.0.4), then divide by h and take limits as $h \to 0$,

and use (A.0.7), one gets

$$0 = \frac{\mathrm{d}\mathcal{J}(t)}{\mathrm{d}t} = \lim_{h\to 0} \frac{\mathcal{J}(t+h) - \mathcal{J}(t)}{h} = \int_{D_t} \frac{f(t+h,\mathbf{y})\dfrac{\partial \mathbf{y}}{\partial \mathbf{x}} - f(t,\mathbf{x})}{h}\,\mathrm{d}\mathbf{x}$$
$$= \int_{D_t} \left(\partial_t f + \sum_{i=1}^{n} \partial_{x_i}(f v_i) \right) \mathrm{d}\mathbf{x}.$$

Therefore, if the PDF $f = f(t,\mathbf{x})$ of the solution stochastic process of (A.0.1) satisfies the following PDE

$$\partial_t f + \sum_{i=1}^{n} \partial_{x_i}(f v_i) = \partial_t f + \nabla_{\mathbf{x}} \cdot [f\mathbf{v}] = 0, \tag{A.0.8}$$

then it is an invariant of motion of the dynamical system (A.0.1).

A.0.2 L2 case

In this case, we consider that $\mathbf{X}(t)$ verifies Equation (A.0.1) in the $\mathrm{L}^2_d(\Omega,\mathbb{P})$, or *mean square*, sense. Let us fix $t \in [t_0,\infty)$ and consider the definition of the characteristic function of the random vector $\mathbf{X}(t) = (X_1(t),\ldots,X_d(t))^{\mathsf{T}}$,

$$\Phi(t,\mathbf{u}) = \mathbb{E}\left[\mathrm{e}^{\mathrm{i}\mathbf{u}^{\mathsf{T}}\mathbf{X}(t)}\right] = \int_{\mathbb{R}^d} \mathrm{e}^{\mathrm{i}\mathbf{u}^{\mathsf{T}}\mathbf{x}} f(t,\mathbf{x})\,\mathrm{d}\mathbf{x} = (2\pi)^d \mathcal{F}[f(t,\mathbf{x})](\mathbf{u}), \tag{A.0.9}$$

where $\mathbf{u} = (u_1,\ldots,u_d)^{\mathsf{T}} \in \mathbb{R}^d$ and $\mathcal{F}[\cdot]$ is the Fourier Transform operator.

Now, we differentiate expression (A.0.9) with respect to t and apply the commutation between the mean square derivative and the expectation operator

(see [12, Eq. 4.128]). This yields

$$\partial_t \Phi(t,\mathbf{u}) = \partial_t \mathbb{E}\left[\mathrm{e}^{\mathrm{i}\sum_{k=1}^{d} u_k X_k(t)}\right] = \mathbb{E}\left[\partial_t\left(\mathrm{e}^{\mathrm{i}\sum_{k=1}^{d} u_k X_k(t)}\right)\right] \tag{A.0.10}$$

$$= \mathbb{E}\left[\mathrm{i}\sum_{k=1}^{d} u_k \dot{X}_k(t)\mathrm{e}^{\mathrm{i}\mathbf{u}^\intercal \mathbf{X}(t)}\right] = \mathrm{i}\sum_{k=1}^{d} u_k \mathbb{E}[\dot{X}_k(t)\mathrm{e}^{\mathrm{i}\mathbf{u}^\intercal \mathbf{X}(t)}]$$

$$= \mathrm{i}\sum_{k=1}^{d} u_k \mathbb{E}[v_k(t,\mathbf{X}(t))\mathrm{e}^{\mathrm{i}\mathbf{u}^\intercal \mathbf{X}(t)}] = \sum_{k=1}^{d} \mathrm{i}u_k \int_{\mathbb{R}^n} \mathrm{e}^{\mathrm{i}\mathbf{u}^\intercal \mathbf{x}} v_k(t,\mathbf{x}) f(t,\mathbf{x})\,\mathrm{d}\mathbf{x}.$$

On the one hand, according to [85, Prop. 17.2.1] and (A.0.9), each addend in the last sum can be expressed in terms of the Fourier transform,

$$\mathrm{i}u_k \int_{\mathbb{R}^n} \mathrm{e}^{\mathrm{i}\mathbf{u}^\intercal \mathbf{x}} v_k(t,\mathbf{x}) f(t,\mathbf{x})\,\mathrm{d}\mathbf{x} = (2\pi)^d \mathcal{F}\left[-\partial_{x_k}(v_k(t,\mathbf{x})f(t,\mathbf{x}))\right](\mathbf{u}).$$

Then, using this latter representation together with the linearity of the Fourier transform operator, expression (A.0.10) can be written as

$$\partial_t \Phi(t,\mathbf{u}) = (2\pi)^d \mathcal{F}\left[-\sum_{k=1}^{d} \partial_{x_k}(v_k(t,\mathbf{x})f(t,\mathbf{x}))\right](\mathbf{u}). \tag{A.0.11}$$

On the other hand, if we directly differentiate (A.0.9) under the integral sign with respect to t, one gets

$$\partial_t \Phi(t,\mathbf{u}) = \int_{\mathbb{R}^n} \mathrm{e}^{\mathrm{i}\mathbf{u}^\intercal \mathbf{x}} \partial_t f(t,\mathbf{x})\mathrm{d}\mathbf{x} = (2\pi)^d \mathcal{F}\left[\partial_t f(t,\mathbf{x})\right](\mathbf{u}). \tag{A.0.12}$$

Finally, subtracting (A.0.11) and (A.0.12) and using the Fourier inversion transform [85, Th. 18.1.1], one obtains the Liouville-Gibbs equation

$$\partial_t f(t,\mathbf{x}) + \sum_{k=1}^{d} \partial_{x_k}(v_k(t,\mathbf{x})f(t,\mathbf{x})) = 0. \tag{A.0.13}$$

A.0.3 Relating Stokes' theorem/divergence theorem

The following motivation and concepts come from the area of fluid dynamics. In this case, the RDE (A.0.1) describes the movement of a random particle or molecule in a fluid that evolves according to the *flow field* $\mathbf{v}$. Thus, we consider that $\mathbf{X}(t)$ satisfies Equation (A.0.1) in the pathwise sense. We will consider the physical intuition and the corresponding probabilistic concepts at each step.

Let $f = f(t, \mathbf{x})$ be the *fluid density* at time t, and position $\mathbf{x}$. The *quantity of fluid* at a region V is denoted by

$$F(t) = \int_V f(t, \mathbf{x}) \mathrm{d}\mathbf{x}$$

for some region $V \subseteq \mathbb{R}^d$. In probabilistic terms, the *fluid density* is the PDF at time t, whereas the *fluid quantity* is the distribution function (see Theorem 2.2.1).

Now, the *density flow in* V is defined as the net gain/loss of fluid in a region V per unit time. Mathematically, this can be represented as:

$$\int_{\partial V} f(t, \mathbf{x}) \mathbf{v}(t, \mathbf{x}) \cdot \mathbf{n}(\mathbf{x}) \mathrm{d}\mathbf{x},$$

where $(f\,\mathbf{v})(t, \mathbf{x})$ is referred to as the *fluid flux*. Thus a simple fluid conservation argument for the fluid quantity evolution gives the following relation:

$$\frac{\mathrm{d}F}{\mathrm{d}t}(t) + \int_{\partial V} f(t, \mathbf{x}) \mathbf{v}(t, \mathbf{x}) \cdot \mathbf{n}(\mathbf{x}) \mathrm{d}\mathbf{x} = \eta(t), \tag{A.0.14}$$

where $\eta(t)$ denotes the net rate at which $F(t)$ is being generated inside V per unit time. If $\eta(t) > 0$, then there is a *source* of fluid inside V. If $\eta(t) < 0$, there is a *sink* inside V. The same idea applies to the probabilistic scenario.

Systems such as Equation (A.0.1) describe the evolution of a fluid that doesn't have any sinks or sources. Indeed, for any randomly chosen fluid particle (any random sample of the initial condition), Equation (A.0.14) describes a (possibly) smooth movement through the phase space; no generation or

reduction of the quantity of fluid, both locally and globally. Therefore, $\eta(t) = 0$ at all times and Equation (A.0.14) now reads:

$$\partial_t \int_V f(t, \mathbf{x}) \mathrm{d}\mathbf{x} + \int_{\partial V} f(t, \mathbf{x}) \mathbf{v}(t, \mathbf{x}) \cdot \mathbf{n}(\mathbf{x}) \mathrm{d}\mathbf{x} = 0.$$

Using the divergence theorem, we have

$$\int_V \left(\partial_t f(t, \mathbf{x}) + \nabla_{\mathbf{x}} \cdot [f\, \mathbf{v}](t, \mathbf{x})\right) \mathrm{d}\mathbf{x} = 0,$$

and since this was done for an arbitrary V, then the integrand must be zero almost everywhere in $\mathbb{R}^d$ for the Lebesgue measure. Since we assume that the PDF is smooth inside its domain, we get

$$\partial_t f(t, \mathbf{x}) + \nabla_{\mathbf{x}} \cdot [f\, \mathbf{v}](t, \mathbf{x}) \mathrm{d}\mathbf{x} = 0, \quad \mathbf{x} \in \mathbb{R}^d, t > t_0.$$

Appendix B

Direct relation between the Liouville equation solution and the RVT theorem

In this brief appendix, we show that there is a direct relationship between the jacobian matrix from Theorem 2.2.2, the RVT Theorem, and the Liouville equation solution Equation (5.2.10).

As in the previous appendix, we assume that the vector field $\mathbf{v}$ verifies the conditions considered in Chapter 2. Once again we consider $\mathbf{X}(t)$ the stochastic process that verifies the general RDE in the pathwise sense.

We know that, for any random initial condition realization, $\mathbf{x}^0 = \mathbf{X}^0(\omega)$ for some $\omega \in \Omega$, the solution path must have the following form:

$$\mathbf{X}(t, \mathbf{x}^0) = \mathbf{x}^0 + \int_0^t \mathbf{v}(s, \mathbf{X}(s, \mathbf{x}^0))ds.$$

Let us consider $\nabla_{\mathbf{x}} X_i(t, \mathbf{x}^0)$ for every $i = 1, \dots, d$. The simple application of the chain rule and differentiating under the integral sign gives:

$$\nabla_{\mathbf{x}} X_i(t, \mathbf{x}^0) = \mathbf{e}_i + \int_0^t \nabla_{\mathbf{x}} v_i(s, \mathbf{X}(s, \mathbf{x}^0)) \mathrm{D}\mathbf{X}(s, \mathbf{x}^0) ds, \tag{B.0.1}$$

where D is the *differential matrix* (or *jacobian* matrix) of $\mathbf{X}$; that is

$$\mathrm{D}\mathbf{X}(t, \mathbf{x}^0) = \begin{bmatrix} \partial_{x_1} X_1(t, \mathbf{x}^0) & \cdots & \partial_{x_d} X_1(t, \mathbf{x}^0) \\ \vdots & \ddots & \vdots \\ \partial_{x_1} X_d(t, \mathbf{x}^0) & \cdots & \partial_{x_d} X_d(t, \mathbf{x}^0) \end{bmatrix}.$$

Now, by considering the time derivative of Equation (B.0.1), and considering all components of $\nabla_{\mathbf{x}} X_i$ we get the equation

$$\frac{\mathrm{d}}{\mathrm{d}t} \mathrm{D}\mathbf{X}(t, \mathbf{x}^0) = \mathrm{D}\mathbf{v}(t, \mathbf{X}(t, \mathbf{x}^0)) \mathrm{D}\mathbf{X}(t, \mathbf{x}^0).$$

Now, [161, Th, 18.4] states that the previous relation implies:

$$\frac{\mathrm{d}}{\mathrm{d}t} \det[\mathrm{D}\mathbf{X}](t, \mathbf{x}^0) = \mathrm{tr}[\mathrm{D}\mathbf{v}](t, \mathbf{X}(t, \mathbf{x}^0)) \det[\mathrm{D}\mathbf{X}](t, \mathbf{x}^0). \tag{B.0.2}$$

Writing $\mathrm{J}\mathbf{X} = \det[\mathrm{D}\mathbf{X}]$, and using $\mathrm{tr}[\mathrm{D}\mathbf{v}] = \nabla_{\mathbf{x}} \cdot \mathbf{v}$, Equation (B.0.2) now reads:

$$\frac{\mathrm{d}}{\mathrm{d}t} \mathrm{J}\mathbf{X}(t, \mathbf{x}^0) = \nabla_{\mathbf{x}} \cdot \mathbf{v}(t, \mathbf{X}(t, \mathbf{x}^0)) \mathrm{J}\mathbf{X}(t, \mathbf{x}^0).$$

The solution to this linear equation, using that $\mathrm{J}\mathbf{X}(0, \mathbf{x}^0) = \mathbf{Id}_d$, is

$$\mathrm{J}\mathbf{X}(t, \mathbf{x}^0) = \exp\left\{ \int_0^t \nabla_{\mathbf{x}} \cdot \mathbf{v}(s, \mathbf{X}(s, \mathbf{x}^0)) \mathrm{d}s \right\}. \tag{B.0.3}$$

Let us see some notes about the relation we just obtained. Equation (B.0.3) says that, provided the appropriate conditions are verified on $\mathbf{v}$ (such as the ones considered in 2), the transformation always exists and is invertible. Also, the inverse matrix is precisely the one considered in the right-hand-side of the

RVT Theorem 2.2.2 and is

$$\mathrm{J}\mathbf{X}(t,\mathbf{x}^0)^{-1} = \exp\left\{-\int_0^t \nabla_{\mathbf{x}}\cdot\mathbf{v}(s,\mathbf{X}(s,\mathbf{x}^0))\mathrm{d}s\right\},$$

which is precisely the multiplicative term found on the solution of the Liouville equation in the characteristic curves (Equation (5.2.10)).

Bibliography

[1] A. Der Kiureghian and O. Ditlevsen. "Aleatory or Epistemic? Does It Matter?" In: *Structural Safety* 31.2 (2009), pp. 105–112. ISSN: 0167-4730. DOI: 10.1016/j.strusafe.2008.06.020.

[2] R.C. Smith. *Uncertainty Quantification: Theory, Implementation and Applications*. Computational Science and Engineering. New York: SIAM, 2014. ISBN: 9781611973211.

[3] L. Arnold. *Stochastic Differential Equations: Theory and Applications*. New York: Krieger Publishing Company, 1992. ISBN: 9780471033592.

[4] B. Øksendal. *Stochastic Differential Equations: An Introduction with Applications*. Berlin-Heidelberg: Springer-Verlag, 2003. ISBN: 9783540047582.

[5] P.E. Kloeden and E. Platen. *Numerical Solution of Stochastic Differential Equations*. Applications of Mathematics. Berlin: Springer, 1992. ISBN: 9783540540625. DOI: 10.1007/978-3-662-12616-5.

[6] D. Henderson and D. Plaschko. *Stochastic Differential Equations in Science and Engineering*. Singapore: World Scientific, 2006. DOI: 10.1142/5806.

[7] D. Nualart. *The Malliavin Calculus and Related Topics*. Berlin: Springer-Verlag, 2006. ISBN: 9783540283287. DOI: 10.1007/3-540-28329-3.

[8] E. Allen. *Modeling with Itô Stochastic Differential Equations: Theory and Applications*. Springer Dordrecht, 2007. ISBN: 9781402059520. DOI: 10.1007/978-1-4020-5953-7.

[9] G. Di Nunno, B. Oksendal, and F. Proske. *Malliavin Calculus for Lèvy Processes and Applications to Finance*. Universitext. Berlin: Springer-Verlag, 2009. ISBN: 9783540785712. DOI: 10.1007/978-3-540-78572-9.

[10] C.A. Braumann. *Introduction to Stochastic Differential Equations with Applications to Modelling in Biology and Finance*. NJ: Wiley & Sons Ltd., 2019. ISBN: 9781119166061.

[11] Dongbin Xiu. *Numerical Methods for Stochastic Computations: A Spectral Method Approach*. Computational Science and Engineering. New Jersey: Princeton University Press, 2010. ISBN: 9780691142128. DOI: 10.2307/j.ctv7h0skv.

[12] T. T. Soong. *Random Differential Equations in Science and Engineering*. Mathematics in Science and Engineering. New York: Academic Press, 1973. ISBN: 9780126548501. DOI: 10.1016/s0076-5392(08)x6011-4.

[13] H. Evans and P.E. Kloeden. *Random Ordinary Differential Equations and Their Numerical Solution*. Probability Theory and Stochastic Modelling. Springer Singapore, 2017. ISBN: 9789811062643. DOI: 10.1007/978-981-10-6265-0.

[14] T. Neckel and F. Rupp. *Random Differential Equations in Scientific Computing*. München: De Gruyter Open, 2013. ISBN: 9788376560250. DOI: 10.2478/9788376560267.

[15] M. Loève. *Probability Theory I*. New York: Springer New York, NY, 1977. ISBN: 9780387902104. DOI: 10.1007/978-1-4684-9464-8.

[16] J. Peano. "Démonstration de l'intégrabilité des équations différentielles ordinaires." In: *Mathematische Annalen* 37 (1890), pp. 182–228. DOI: 10.1007/BF01200235.

[17] G. Teschl. *Ordinary Differential Equations and Dynamical Systems*. American Mathematical Society, 2012. ISBN: 9780821883280. DOI: 10.1090/gsm/140.

[18] R.P. Agarwal and V. Lakshmikantham. *Uniqueness and Nonuniqueness Criteria for Ordinary Differential Equations*. World Scientific, 1993. ISBN: 9789810213572. DOI: 10.1142/1988.

[19] T. Caraballo et al. "A way to model stochastic perturbations in population dynamics models with bounded realizations". In: *Communications in Nonlinear Science and Numerical Simulation* 77 (2019), pp. 239–257. DOI: 10.1016/j.cnsns.2019.04.019.

[20] T. Caraballo, J. López-de-la-Cruz, and A. Rapaport. "Modeling bounded random fluctuations in biological systems: application to the chemostat model with two species". In: *IFAC-PapersOnLine* 52.26 (2019), pp. 187–192. DOI: 10.1016/j.ifacol.2019.12.256.

[21] K. F. Nipa, S. R.-J. Jang, and L. J. S. Allen. "The effect of demographic and environmental variability on disease outbreak for a dengue model with a seasonally varying vector population". In: *Mathematical Biosciences* 331.108516 (2021). DOI: 10.1016/j.mbs.2020.108516.

[22] D. P. Kroese et al. “Why the Monte Carlo method is so important today”. In: *Wiley Interdisciplinary Reviews: Computational Statistics* 6.6 (2014), pp. 386–392. ISSN: 1939-0068. DOI: 10.1002/wics.1314.

[23] R.E. Caflisch. “Monte Carlo and quasi-Monte Carlo methods”. In: *Acta Numerica* 7 (1998), pp. 1–49. ISSN: 0962-4929. DOI: 10.1017/S0962492900002804.

[24] W. J. Morokoff and R. E. Caflisch. “Quasi-Monte Carlo Integration”. In: *Journal of Computational Physics* 122.2 (1995), pp. 218–230. ISSN: 0021-9991. DOI: 10.1006/jcph.1995.1209.

[25] M. Jornet et al. “Variance reduction methods and multilevel Monte Carlo strategy for estimating densities of solutions to random second-order linear differential equations”. In: *International Journal for Uncertainty Quantification* 10.5 (2020), pp. 467–497. DOI: 10.1615/Int.J.UncertaintyQuantification.2020032659.

[26] V.J. Bevia et al. “Uncertainty quantification analysis of the biological Gompertz model subject to random fluctuations in all its parameters”. In: *Chaos, Solitons & Fractals* 138 (2020), p. 109908. ISSN: 0960-0779. DOI: 10.1016/j.chaos.2020.109908.

[27] V.I. Bogachev. *Measure Theory*. Berlin, Heidelberg: Springer Berlin Heidelberg, 2007. ISBN: 9783540345145. DOI: 10.1007/978-3-540-34514-5_3.

[28] J. C. Cortés et al. “A full solution of random autonomous first-order linear systems of difference equations. Application to construct random phase portrait for planar systems”. In: *Applied Mathematics Letters* 68 (2017), pp. 150–156. DOI: 10.1016/j.aml.2016.12.015.

[29] J. C. Cortés et al. “Solving the random Pielou logistic equation with the random variable transformation technique: Theory and applica-

tions". In: *Mathematical Methods in the Applied Sciences* 42 (17 2019), pp. 5708–5717. DOI: 10.1002/mma.5440.

[30] M. C. Casabán et al. "Computing probabilistic solutions of the Bernoulli random differential equation". In: *Journal of Computational and Applied Mathematics* 309 (2017), pp. 396–407. DOI: 10.1016/j.cam.2016.02.034.

[31] B. Kegan and R. W. West. "Modeling the simple epidemic with deterministic differential equations and random initial conditions". In: *Mathematical Biosciences* 195 (5 2005), pp. 179–193. DOI: 10.1016/j.mbs.2005.02.004.

[32] A. Hussein and M.M. Selim. "Solution of the stochastic generalized shallow-water wave equation using RVT technique". In: *The European Physical Journal Plus* 130.12 (2015), p. 249. ISSN: 2190-5444. DOI: 10.1140/epjp/i2015-15249-3.

[33] H. Slama et al. "Solution of the finite Milne problem in stochastic media with RVT Technique". In: *The European Physical Journal Plus* 132 (505 2017). DOI: 10.1140/epjp/i2017-11763-6.

[34] A. Hussein and M.M. Selim. "A general probabilistic solution of randomized radioactive decay chain (RDC) model using RVT technique". In: *The European Physical Journal Plus* 135.5 (2020), p. 418. DOI: 10.1140/epjp/s13360-020-00389-6.

[35] F. A. Dorini and M. C. C. Cunha. "On the linear advection equation subject to random velocity fields". In: *Mathematics and Computers in Simulation* 82 (4 2011), pp. 679–690. DOI: 10.1016/j.matcom.2011.10.008.

[36] V.J. Bevia, J. Calatayud, and J.C. Cortés. "Probabilistic analysis of a class of 2D-random heat equations via densities". In: *Applied Mathe-*

matics Letters 146 (2023), p. 108828. ISSN: 0893-9659. DOI: 10.1016/j.aml.2023.108828.

[37] A. Hussein and M. M. Selim. "A general analytical solution for the stochastic Milne problem using Karhunen–Loeve (K–L) expansion". In: *Journal of Quantitative Spectroscopy and Radiative Transfer* 125 (2013), pp. 84–92. DOI: 10.1016/j.jqsrt.2013.03.018.

[38] A. Hussein and M. M. Selim. "A complete probabilistic solution for a stochastic Milne problem of radiative transfer using KLE-RVT technique". In: *Journal of Quantitative Spectroscopy and Radiative Transfer* 232 (2019), pp. 54–65. DOI: 10.1016/j.jqsrt.2019.04.034.

[39] J. C. Cortés et al. "Random Airy type differential equations: Mean square exact and numerical solutions". In: *Computers and Mathematics with Applications* 60.5 (2010), pp. 1237–1244. DOI: 10.1016/j.camwa.2010.05.046.

[40] Z. Bekiryazici, M. Merdan, and T. Mesemen. "Modification of the random differential transformation method and its applications to compartmental models". In: *Communications in Statistics: Theory and Methods* (2020). DOI: 10.1080/03610926.2020.1713372.

[41] A. K. Golmankhaneh, N. A. Porghoveh, and D. Baleanu. "Mean square solutions of second-order random differential equations by using homotopy analysis method". In: *Romanian Reports in Physcis* 65 (2 2013), pp. 350–362.

[42] M. A. El-Tawil. "The approximate solutions of some stochastic differential equations using transformations". In: *Applied Mathematics and Computation* 164 (1 2005), pp. 167–178. DOI: 10.1016/j.amc.2004.04.062.

[43] J. Calatayud et al. "Constructing reliable approximations of the probability density function to the random heat PDE via a finite difference scheme". In: *Applied Numerical Mathematics* 151 (2020), pp. 413–424. DOI: 110.1016/j.apnum.2020.01.012.

[44] F.A. Dorini, M.S. Cecconello, and L.B. Dorini. "On the logistic equation subject to uncertainties in the environmental carrying capacity and initial population density". In: *Communications in Nonlinear Science and Numerical Simulation* 33 (2016), pp. 160–173. ISSN: 1007-5704. DOI: 10.1016/j.cnsns.2015.09.009.

[45] S. Howida et al. "An approximate probabilistic solution of a random SIR-type epidemiological model using RVT technique". In: *Applied Mathematics and Computation* 361 (2019), pp. 144–156. ISSN: 0096-3003. DOI: 10.1016/j.amc.2019.05.019.

[46] F. Santambrogio. *Optimal Transport for Applied Mathematicians. Calculus of Variations, PDEs and Modeling.* Progress in Nonlinear Differential Equations and Their Applications. Birkhäuser Cham, 2015. ISBN: 9783319208275. DOI: 10.1007/978-3-319-20828-2.

[47] L. C. Evans. *Partial differential equations.* Providence, R.I.: American Mathematical Society, 2010. ISBN: 9780821849743. DOI: 10.1090/gsm/019.

[48] A. T. Bharucha-Reid. *Probabilistic Analysis and Related Topics.* Vol. 1. London: Academic Press, 1978. ISBN: 9780120956029.

[49] M. Zak, J. P. Zbilut, and R. E. Meyers. *From Instability to Intelligence: Complexity and Predictability in Nonlinear Dynamics.* Germany: Springer, 1997. ISBN: 9783540630555. DOI: 10.1007/978-3-540-69121-1.

[50] T. L. Saaty. *Modern Nonlinear Equations*. New York: Dover Publ., 1981. ISBN: 9780486642321.

[51] F. Kozin. "On the probability densities of the output of some random systems". In: *J. Appl. Mech.* 28.2 (1961), pp. 161–165. ISSN: 0021-8936. DOI: 10.1115/1.3641646.

[52] T. Saaty. *Modern Nonlinear Equations*. New York: Dover Publications, 1981.

[53] M. Ehrendorfer. "The Liouville equation and its potential usefulness for the prediction of forecast skill. Part II: Applications". In: *Mon. Weather Rev.* 122.4 (1994), pp. 714–728. ISSN: 0027-0644. DOI: 10.1175/1520-0493(1994)122%3C0714:TLEAIP%3E2.0.CO;2.

[54] J.B. Chen and J. Li. "A note on the principle of preservation of probability and probability density evolution equation". In: *Probabilist. Eng. Mech.* 24.1 (2009), pp. 51–59. ISSN: 0266-8920. DOI: 10.1016/j.probengmech.2008.01.004.

[55] A. Halder and R. Bhattacharya. "Dispersion analysis in hypersonic flight during planetary entry using stochastic Liouville equation". In: *Journal of Guidance, Control, and Dynamics* 34.2 (2011), pp. 459–474. DOI: 10.2514/1.51196.

[56] V.J. Bevia et al. "Analysing Differential Equations with Uncertainties via the Liouville-Gibbs Theorem: Theory and Applications". In: *Computational Mathematics and Applications*. Ed. by D. Zeidan et al. Singapore: Springer Singapore, 2020, pp. 1–23. ISBN: 9789811584985. DOI: 10.1007/978-981-15-8498-5_1.

[57] V.J. Bevia et al. "Uncertainty Quantification of Random Microbial Growth in a Competitive Environment via Probability Density Functions". In: *Fractal and Fractional* 5.2 (2021). DOI: 10.3390/fractalfract5020026.

[58] L. Hörmander. *The Analysis of Linear Partial Differential Operators I: Distribution Theory and Fourier Analysis*. Springer Berlin, Heidelberg, 2003. ISBN: 9783540006626.

[59] P. Rabinowitz P.J. Davis. *Methods of Numerical Integration*. Dover Books, 2007. ISBN: 9780122063602. DOI: 10.1016/C2013-0-10566-1.

[60] M.B. Giles. "Multilevel Monte Carlo Methods". In: *Acta Numerica* 24 (2015), pp. 259–328. ISSN: 0962-4929. DOI: 10.1017/s096249291500001x.

[61] J.V. Michalowicz, J.M. Nichols, and F. Bucholtz. *Handbook of Differential Entropy*. 1st. New York: Chapman and Hall/CRC, 2013. ISBN: 9781466583177.

[62] C. Burgos-Simón et al. "Modeling breast tumor growth by a randomized logistic model: A computational approach to treat uncertainties via probability densities". In: *Eur. Phys. J. Plus* 135 (2020), p. 826. DOI: 10.1140/epjp/s13360-020-00853-3.

[63] C. Burgos et al. "Random fractional generalized Airy differential equations: A probabilistic analysis using mean square calculus". In: *Applied Mathematics and Computation* 352 (2019), pp. 15–29. ISSN: 0096-3003. DOI: 10.1016/j.amc.2019.01.039.

[64] C. Burgos et al. "Mean square convergent numerical solutions of random fractional differential equations: Approximations of moments and density". In: *Journal of Computational and Applied Mathematics* 378 (2020), p. 112925. ISSN: 0377-0427. DOI: 10.1016/j.cam.2020.112925.

[65] David G. Luenberger. *Optimization by Vector Space Methods*. 1st. USA: John Wiley & Sons, Inc., 1997. ISBN: 047155359X.

[66] Y. Ram et al. "Predicting microbial growth in a mixed culture from growth curve data". In: *Proceedings of the National Academy of Sciences* 116.29 (2019), pp. 14698–14707. DOI: 10.1073/pnas.1902217116.

[67] L.J.S. Allen. *An Introduction to Mathematical Biology*. New Jersey: Pearson Education, 2007. ISBN: 9780130352163.

[68] P. Turchin. *Complex Population Dynamics: A Theoretical/Empirical Synthesis*. Monographs in Population Biology. New Jersey: Princeton University Press, 2003. ISBN: 9780691090214.

[69] M. Patel, J. P. Zbilut, and R. E. Nagl. *The Role of Model Integration in Complex Systems Modelling: An Example from Cancer Biology*. Understanding Complex Systems. Berlin Heidelberg: Springer: Complexity, 2010. ISBN: 9783642156038. DOI: 10.1007/978-3-642-15603-8.

[70] J. Golec and S. Sathananthan. "Stability analysis of a stochastic logistic model". In: *Mathematical and Computer Modelling* 38.5–6 (2003), pp. 585–593. DOI: 10.1016/S0895-7177(03)90029-X.

[71] E.K. Moummou et al. "A stochastic Gompertz model highlighting internal and external therapy function for tumour growth". In: *Applied Mathematics and Computation* 246 (2003), pp. 1–1. DOI: 10.1016/j.amc.2014.08.008.

[72] J. C. Cortés, L. Jódar, and L. Villafuerte. "Random linear-quadratic mathematical models: Computing explicit solutions and applications". In: *Mathematics and Computers in Simulation* 79.7 (2009), pp. 2076–2090. DOI: 10.1016/j.matcom.2008.11.008.

[73] F. A. Dorini, N. S. Bobko, and L. B. Dorini. "A note on the logistic equation subject to uncertainties in parameters". In: *Computational and Applied Mathematics* 37 (2018), pp. 1496–1506. DOI: 10.1007/s40314-016-0409-6.

[74] J. Calatayud, J.C. Cortés, and M. Jornet. "Uncertainty quantification for random parabolic equations with nonhomogeneous boundary conditions on a bounded domain via the approximation of the probability density function". In: *Mathematical Methods in the Applied Sciences* 42 (17 2019), pp. 5649–5667. ISSN: 0170-4214. DOI: 10.1002/mma.5333.

[75] M. C. Casabán et al. "Probabilistic solution of the homogeneous Riccati differential equation: A case-study by using linearization and transformation techniques". In: *Journal of Computational and Applied Mathematics* 79 (2016), pp. 20–35. DOI: 10.1016/j.cam.2014.11.028.

[76] A. Laird. "Dynamics of Tumour Growth: Comparison of Growth Rates and Extrapolation of Growth Curve to One Cell". In: *British journal of cancer* 19 (1965), pp. 278–91. DOI: 10.1038/bjc.1965.32.

[77] S. Nahashon et al. "Growth characteristics of Pearl Gray Guinea Fowl as predicted by the Richards, Gompertz, and Logistic Models". In: *Poultry Science* 85 (3 2006), pp. 359–363. DOI: 10.1093/ps/85.2.359.

[78] R.L. Berger G. Casella. *Statistical Inference*. 4th. Cengage Learning, 2008. ISBN: 9788131503942. DOI: 10.1201/b11551-8.

[79] B. S. Goh. "Global Stability in Many-Species Systems". In: *The American Naturalist* 111.977 (1977), pp. 135–143. ISSN: 00030147, 15375323. DOI: 10.1086/283144.

[80] P. Waltman et al. *Competition Models in Population Biology*. CBMS-NSF Regional Conference Series in Applied Mathematics. Society for Industrial and Applied Mathematics, 1983. ISBN: 9780898711882.

[81] B. S. Goh. "Stability in Models of Mutualism". In: *The American Naturalist* 113.2 (1979), pp. 261–275. ISSN: 00030147, 15375323.

[82] R.J. LeVeque. *Finite Volume Methods for Hyperbolic Problems*. Cambridge Texts in Applied Mathematics. Cambridge University Press, 2002. DOI: 10.1017/CBO9780511791253.

[83] N. Khemka and C. Jacob. "Exploratory Toolkit for Evolutionary and Swarm-Based Optimization". In: *The Mathematica Journal* 11 (2008). DOI: 10.3888/tmj.11.3-5.

[84] H.K. Khalil. *Nonlinear systems*. 3rd ed. Upper Saddle River, NJ: Prentice-Hall, 2002. ISBN: 9780130673893.

[85] C. Gasquet and P. Witomski. *Fourier Analysis and Applications. Filtering, Numerical Computation, Wavelets*. Springer, 1998. DOI: 10.1007/978-1-4612-1598-1.

[86] "Weak Convergence in Metric Spaces". In: *Convergence of Probability Measures*. John Wiley & Sons, Ltd, 1999. Chap. 1, pp. 7–79. ISBN: 9780470316962. DOI: 10.1002/9780470316962.ch1.

[87] K. Riley, M. Hobson, and S. Bence. "Mathematical Methods for Physics and Engineering - 3rd Edition". In: *American Journal of Physics* 67 (1999). DOI: 10.2277/0521861535.

[88] V.G. Weirs T. Plewa T. Linde. *Adaptive Mesh Refinement - Theory and Applications. Proceedings of the Chicago Workshop on Adaptive Mesh Refinement Methods*. Springer Berlin, Heidelberg, 2005. ISBN: 9783540211471. DOI: 10.1007/b138538.

[89] M. Bergdorf and P. Koumoutsakos. "A Lagrangian Particle-Wavelet Method". In: *Multiscale Modeling & Simulation* 5.3 (2006), pp. 980–995. ISSN: 1540-3459. DOI: 10.1137/060652877.

[90] F.A. Shah L. Debnath. *Wavelet Transforms and Their Applications*. 2nd. Springer Science + Business Media New York 2015, 2014. ISBN: 9780817684174. DOI: 10.1007/978-0-8176-8418-1.

[91] A. Cour-Harbo A. Jensen. *Ripples in Mathematics: The Discrete Wavelet Transform*. Springer Berlin, Heidelberg, 2001. ISBN: 9783540416623. DOI: 10.1007/978-3-642-56702-5.

[92] G.H. Cottet and P. Koumoutsakos. "High Order Semi-Lagrangian Particle Methods". In: *Spectral and High Order Methods for Partial Differential Equations ICOSAHOM 2016*. Ed. by M. L. Bittencourt, N. A. Dumont, and J. S. Hesthaven. Vol. 119. Cham: Springer International Publishing, 2017, pp. 103–117. ISBN: 9783319658704. DOI: 10.1007/978-3-319-65870-4_6.

[93] P. A. Bosler et al. "A Lagrangian particle method with remeshing for tracer transport on the sphere". In: *Journal of Computational Physics* 340 (2017), pp. 639–654. ISSN: 0021-9991. DOI: 10.1016/j.jcp.2017.03.052.

[94] A. Iske and V.I. Arnold. *Multiresolution Methods in Scattered Data Modelling*. Springer Verlag, 2004. ISBN: 9783540204794. DOI: 10.1007/978-3-642-18754-4.

[95] H. Wendland. "Piecewise polynomial, positive definite and compactly supported radial functions of minimal degree". In: *Advances in Computational Mathematics* 4.1 (1995), pp. 389–396. ISSN: 1019-7168. DOI: 10.1007/bf02123482.

[96] H. Wendland. "Error Estimates for Interpolation by Compactly Supported Radial Basis Functions of Minimal Degree". In: *Journal of Approximation Theory* 93.2 (1998), pp. 258–272. ISSN: 0021-9045. DOI: 10.1006/jath.1997.3137.

[97] R. Schaback and H. Wendland. “Using compactly supported radial basis functions to solve partial differential equations”. In: *Boundary Element Technology XIII*. Ed. by C. S. Chen, C. A. Brebbia, and D. W. Pepper. Southampton, Boston: WitPress, 1999, pp. 311–324. URL: http://num.math.uni-goettingen.de/schaback/research/papers/UCSRBFtSPDE.pdf.

[98] M. Neumann. *Lecture 13: Radial Basis Function networks*. https://www.cse.wustl.edu/~m.neumann/sp2016/cse517/lecturenotes/lecturenote13.html. Accessed: 2023-07-31.

[99] G. Dimarco et al. “An efficient numerical method for solving the Boltzmann equation in multidimensions”. In: *Journal of Computational Physics* 353 (2018), pp. 46–81. ISSN: 0021-9991. DOI: 10.1016/j.jcp.2017.10.010.

[100] G.K. Batchelor. *An Introduction to Fluid Dynamics*. Cambridge University Press, 1973. ISBN: 9780521098175. DOI: 10.1017/CBO9780511800955.

[101] T. T. Warner. *Numerical Weather and Climate Prediction*. Cambridge, UK: Cambridge University Press, 2012. ISBN: 9780511763243. DOI: 10.1002/met.1309.

[102] S. Koshizuka et al. “Chapter 1 - Introduction”. In: *Moving Particle Semi-implicit Method*. Ed. by S. Koshizuka et al. Academic Press, 2018, pp. 1–23. ISBN: 9780128127797. DOI: 10.1016/B978-0-12-812779-7.00001-1.

[103] P. Schreurs, J. Mewis, and J. Havens. “Numerical aspects of a lagrangian particle model for atmospheric dispersion of heavy gases”. In: *Journal of Hazardous Materials* 17.1 (1987), pp. 61–80. ISSN: 0304-3894. DOI: 10.1016/0304-3894(87)85042-2.

[104] M. Bergdorf. "Multiresolution particle methods for the simulation of growth and flow". en. Doctoral Thesis. Zürich: ETH Zurich, 2007. DOI: 10.3929/ethz-a-005565040.

[105] J.C. Butcher. *Runge–Kutta Methods*. Numerical Methods for Ordinary Differential Equations. John Wiley & Sons, Ltd, 2016. ISBN: 9781119121534. DOI: 10.1002/9781119121534.ch3.

[106] S. Cook. *CUDA Programming: A Developer's Guide to Parallel Computing with GPUs*. 1st. San Francisco, CA, USA: Morgan Kaufmann Publishers Inc., 2012. ISBN: 9780124159334.

[107] NVIDIA, P. Vingelmann, and F.H.P. Fitzek. *CUDA Documentation, release: 12.2*. 2023. URL: https://developer.nvidia.com/cuda-toolkit.

[108] R.I. McLachlan and G.R.W. Quispel. "Geometric integrators for ODEs". In: *Journal of Physics A: Mathematical and General* 39.19 (2006), p. 5251. ISSN: 0305-4470. DOI: 10.1088/0305-4470/39/19/S01.

[109] S. Blanes and F. Casas. *A concise introduction to geometric numerical integration*. Chapman & Hall/CRC Monographs and Research Notes in Mathematics. Oakville, MO: Apple Academic Press, 2016. DOI: 10.1201/b21563.

[110] E. Hairer, C. Lubich, and G. Wanner. *Geometric numerical integration*. Berlin, Germany, 2006, pp. 805–882. DOI: 10.4171/owr/2006/14.

[111] V.J. Bevia. N-Dimensional Liouville Solver [Computer Software]. https://doi.org/10.5281/zenodo.7673678 [Accessed: September 2023]. 2023.

[112] C. Rackauckas and Q. Nie. "DifferentialEquations.jl – A Performant and Feature-Rich Ecosystem for Solving Differential Equations in Julia".

In: *The Journal of Open Research Software* 5.1 (2017). Exported from https://app.dimensions.ai on 2019/05/05. DOI: 10.5334/jors.151.

[113] W. Paul. "Electromagnetic traps for charged and neutral particles". In: *Reviews of Modern Physics* 62.3 (1990), pp. 531–540. ISSN: 1539-0756. DOI: 10.1103/revmodphys.62.531.

[114] J. M. Sanz-Serna. "Stabilizing with a hammer". In: *Stochastics and Dynamics* 08.01 (2008), pp. 47–57. ISSN: 1793-6799. DOI: 10.1142/s0219493708002263.

[115] I. Kovacic, R. Rand, and S. Mohamed-Sah. "Mathieu's Equation and Its Generalizations: Overview of Stability Charts and Their Features". In: *Applied Mechanics Reviews* 70.2 (2018). ISSN: 2379-0407. DOI: 10.1115/1.4039144.

[116] P. Bader et al. "Symplectic integrators for the matrix Hill equation". In: *Journal of Computational and Applied Mathematics* 316 (2017), pp. 47–59. ISSN: 0377-0427. DOI: 10.1016/j.cam.2016.09.041.

[117] H. Munthe-Kaas. "Runge-Kutta methods on Lie groups". In: *BIT Numerical Mathematics* 38.1 (Mar. 1998), pp. 92–111. ISSN: 1572-9125. DOI: 10.1007/bf02510919.

[118] V.J. Bevia, J.C. Cortés, and R.J. Villanueva. "Forward uncertainty quantification in random differential equation systems with delta-impulsive terms: Theoretical study and applications". In: *Mathematical Methods in the Applied Sciences* (2023), pp. 1–21. ISSN: 0170-4214. DOI: 10.1002/mma.9226.

[119] V.J. Bevia et al. "A GPU-accelerated Lagrangian method for solving the Liouville equation in random differential equation systems". In: *Applied Numerical Mathematics* (2024). ISSN: 0168-9274. DOI: https://doi.org/10.1016/j.apnum.2024.09.021.

[120] V. E. Tarasov. "Exact Solutions of Bernoulli and Logistic Fractional Differential Equations with Power Law Coefficients". In: *Mathematics* 8.12 (2020), p. 2231. DOI: 10.3390/math8122231.

[121] I. Area and J. J. Nieto. "Power series solution of the fractional logistic equation". In: *Physica A: Statistical Mechanics and its Applications* 573 (2021), p. 125947. ISSN: 0378-4371. DOI: 10.1016/j.physa.2021.125947.

[122] G. Consolini and M. Materassi. "A stretched logistic equation for pandemic spreading". In: *Chaos, Solitons & Fractals* 140 (2020), p. 110113. ISSN: 0960-0779. DOI: 10.1016/j.chaos.2020.110113.

[123] C. P. Winsor. "The Gompertz Curve as a Growth Curve". In: *Proceedings of the National Academy of Sciences* 18.1 (1932), pp. 1–8. DOI: 10.1073/pnas.18.1.1.

[124] P. Koya and A. Goshu. "Generalized Mathematical Model for Biological Growths". In: *Open Journal of Modelling and Simulation* 1 (2013), pp. 42–53. DOI: 10.4236/ojmsi.2013.14008.

[125] M. Marusic et al. "Tumor growth in vivo and as multicellular spheroids compared by mathematical models". In: *Bulletin of Mathematical Biology* 56 (1994), pp. 617–631. DOI: 10.1007/BF02460714.

[126] J. S. Spratt, J. S. Meyer, and J. A. Spratt. "Rates of growth of human neoplasms: Part II". In: *Journal of Surgical Oncology* 61.1 (1996), pp. 68–83. DOI: 10.1002/1096-9098(199601)61:1%3C68::aid-jso2930610102%3E3.0.co;2-e.

[127] C.P. Birch. "A new generalized logistic sigmoid growth equation compared with the Richards growth equation". In: *Annals of Botany* 83.6 (1999), pp. 713–723. DOI: 10.1006/anbo.1999.0877.

[128] R. K. Sachs, L. R. Hlatky, and P. Hahnfeldt. "Simple ODE models of tumor growth and anti-angiogenic or radiation treatment". In: *Mathematical and Computer Modelling* 33.12–13 (2001), pp. 1297–1305. DOI: 10.1016/S0895-7177(00)00316-2.

[129] Y. H. Hsieh, J. Y. Lee, and H. L. Chang. "SARS epidemiology modeling". In: *Emerging infectious diseases* 10.6 (2004), p. 1165. DOI: 10.3201%2Feid1006.031023.

[130] Y.H. Hsieh. "Richards Model: A Simple Procedure for Real-time Prediction of Outbreak Severity". In: *Modeling and Dynamics of Infectious Diseases*. World Scientific, 2009, pp. 216–236. DOI: 10.1142/9789814261265_0009.

[131] Y. H. Hsieh and S. Ma. "Intervention measures, turning point, and reproduction number for dengue, Singapore, 2005". In: *The American Journal of Tropical Medicine and Hygiene* 80.1 (2009), pp. 66–71. DOI: 10.4269/ajtmh.2009.80.66.

[132] Y. H. Hsieh. "Pandemic influenza A (H1N1) during winter influenza season in the southern hemisphere". In: *Influenza and Other Respiratory Viruses* 4.4 (2010), pp. 187–197. DOI: 10.1111%2Fj.1750-2659.2010.00147.x.

[133] G. Chowell et al. "Using phenomenological models to characterize transmissibility and forecast patterns and final burden of Zika epidemics". In: *PLoS Currents* 8 (2016). DOI: 10.1371/currents.outbreaks.f14b2217c902f453d9320a43a35b9583.

[134] B. Pell et al. "Using phenomenological models for forecasting the 2015 Ebola challenge". In: *Epidemics* 22 (2018), pp. 62–70. DOI: 10.1016/j.epidem.2016.11.002.

[135] E. Pelinovsky et al. "Logistic equation and COVID-19". In: *Chaos, Solitons & Fractals* 140 (2020), p. 110241. DOI: 10.1016/j.chaos.2020.110241.

[136] K. Wu et al. "Generalized logistic growth modeling of the COVID-19 outbreak: comparing the dynamics in the 29 provinces in China and in the rest of the world". In: *Nonlinear dynamics* 101.3 (2020), pp. 1561–1581. DOI: 10.1007/s11071-020-05862-6.

[137] E. Aviv-Sharon and A. Aharoni. "Generalized logistic growth modeling of the COVID-19 pandemic in Asia". In: *Infectious Disease Modelling* 5 (2020), pp. 502–509. DOI: 10.1016/j.idm.2020.07.003.

[138] S. Y. Lee, B. Lei, and B. Mallick. "Estimation of COVID-19 spread curves integrating global data and borrowing information". In: *PloS One* 15.7 (2020), e0236860. DOI: 10.1371/journal.pone.0236860.

[139] T. Neckel and F. Rupp. *Random Differential Equations in Scientific Computing*. Walter de Gruyter, 2013. ISBN: 9788376560267.

[140] L. Villafuerte et al. "Random differential operational calculus: Theory and applications". In: *Computers and Mathematics with Applications* 59.1 (2010), pp. 115–125. DOI: 10.1016/j.camwa.2009.08.061.

[141] E. J. McShane. "Extension of range of functions". In: *Bulletin of the American Mathematical Society* 40.12 (1934), pp. 837–842. URL: https://www.ams.org/journals/bull/1934-40-12/S0002-9904-1934-05978-0/.

[142] J.L. Strand. "Random ordinary differential equations". In: *Journal of Differential Equations* 7.3 (1970), pp. 538–553. DOI: 10.1016/0022-0396(70)90100-2.

[143] J. Calatayud and M. Jornet. "Extending the applicability of the RVT technique for the randomized radioactive decay chain model". In: *Eur. Phys. J. Plus* 137.405 (2022). DOI: 10.1140/epjp/s13360-022-02625-7.

[144] W. Rudin. *Principles of Mathematical Analysis*. Third. International Series in Pure & Applied Mathematics, 1976. ISBN: 9780070542358.

[145] D. Williams. *Probability with Martingales*. New York: Cambridge University Press, 1991. ISBN: 9780521406055.

[146] H. Scheffé. "A useful convergence theorem for probability distributions". In: *Annals of Mathematical Statistics* 18.3 (1947), pp. 434–438. URL: https://www.jstor.org/stable/2235739.

[147] D. Wang, D. Tan, and L. Liu. "Particle swarm optimization algorithm: an overview". In: *Soft Comput* 22 (2018), pp. 387–408. DOI: 10.1007/s00500-016-2474-6.

[148] E. T. Jaynes. "Information Theory and Statistical Mechanics". In: *The Physical Review* 106 (1957), pp. 620–630. DOI: 10.1103/PhysRev.106.620.

[149] V.J. Bevia et al. "On the generalized logistic random differential equation: Theoretical analysis and numerical simulations with real-world data". In: *Communications in Nonlinear Science and Numerical Simulation* 116 (2023), p. 106832. ISSN: 1007-5704. DOI: 10.1016/j.cnsns.2022.106832.

[150] V.J. Bevia et al. "Probability Density Function Computation in Evolutionary Model Calibration with Uncertainty". In: *Proceedings of the Genetic and Evolutionary Computation Conference Companion*. Ed. by Jonathan E. Fieldsend and Markus Wagner. GECCO '22. Boston, Mas-

sachusetts: Association for Computing Machinery, 2022, pp. 1902–1908. ISBN: 9781450392686. DOI: 10.1145/3520304.3534017.

[151] P. Dyke. *An Introduction to Laplace Transforms and Fourier Series*. Springer London, 2014. ISBN: 9781447163947. DOI: 10.1007/978-1-4471-6395-4.

[152] A. Jeffrey. "19 - Laplace Transformation". In: *Handbook of Mathematical Formulas and Integrals (Third Edition)*. Ed. by A. Jeffrey. Third Edition. Burlington: Academic Press, 2004, pp. 299–305. ISBN: 9780123822567. DOI: 10.1016/B978-012382256-7/50022-1.

[153] J.J. Benedetto. *Harmonic Analysis and Applications*. CRC Press, 1997. ISBN: 9781003068839.

[154] I. Kovacic and M. Brennan. *The Duffing Equation: Nonlinear Oscillators and their Behavior*. John Wiley & Sons, 2011. ISBN: 9780470715499. DOI: 10.1002/9780470977859.

[155] Y. Jia. "Review of nonlinear vibration energy harvesting: Duffing, bistability, parametric, stochastic and others". In: *Journal of Intelligent Material Systems and Structures* 31.7 (2020), p. 1045389X2090598. ISSN: 1045-389X. DOI: 10.1177/1045389X20905989.

[156] A. Zeni and J. Gallas. "Lyapunov exponents for a Duffing oscillator". In: *Physica D: Nonlinear Phenomena* 89.1-2 (1995), pp. 71–82. ISSN: 0167-2789. DOI: 10.1016/0167-2789(95)00215-4.

[157] S. Lenci. "Exact solutions for coupled Duffing oscillators". In: *Mechanical Systems and Signal Processing* 165 (2022), p. 108299. ISSN: 0888-3270. DOI: 10.1016/j.ymssp.2021.108299.

[158] J.C. Cortés et al. "Probabilistic analysis of a class of impulsive linear random differential equations forced by stochastic processes admitting

Karhunen-Loève expansions". In: *Discrete & Continuous Dynamical Systems - S* 15.11 (2022), p. 3131. ISSN: 1937-1179. DOI: 10.3934/dcdss.2022079.

[159] J.C. Cortés, A. Moscardó-García, and R.J. Villanueva. "Uncertainty quantification for hybrid random logistic models with harvesting via density functions". In: *Chaos, Solitons & Fractals* 155 (2022), p. 111762. DOI: 10.1016/j.chaos.2021.111762.

[160] V.J. Bevia et al. "Probabilistic analysis of a general class of nonlinear random differential equations with state-dependent impulsive terms via probability density functions". In: *Communications in Nonlinear Science and Numerical Simulation* 119 (2023), p. 107097. ISSN: 1007-5704. DOI: 10.1016/j.cnsns.2023.107097.

[161] K. Spindler. *Abstract Algebra with Applications. Vol. 1: Vector Spaces and Groups*. Marcel Dekker, Inc., 1994, 1993. ISBN: 9780824791445.

This PhD thesis aims to develop and extend analytical and computational techniques for quantifying uncertainty in random differential equation systems using a system's probability density function. By employing the random variable transformation theorem and the Liouville (continuity) equation, we tackle both forward and inverse uncertainty quantification problems in random systems with real-world data. We also design a computational method to efficiently estimate a system's probability density by solving the Liouville equation with GPU acceleration. Finally, we examine uncertainty evolution in a class of impulse-forced systems, providing new insights into the dynamics of their probability density functions.